
Preparation and Characterization of Solution-Processed Organic Semiconductor Interfaces:

Electronic Properties of Thiophene-Fullerene based Donor-Acceptor Systems

Zur Erlangung des akademischen Grades Doktor-Ingenieur (Dr.-Ing.)
genehmigte Dissertation von Julia Maibach aus Bad Homburg v.d.H.
Januar 2014 – Darmstadt – D 17



TECHNISCHE
UNIVERSITÄT
DARMSTADT



Preparation and Characterization of Solution-Processed Organic Semiconductor Interfaces:
Electronic Properties of Thiophene-Fullerene based Donor-Acceptor Systems

vom Fachbereich Material- und Geowissenschaften der Technischen Universität Darmstadt
zur Erlangung des Grades Doktor-Ingenieur (Dr.-Ing.)
genehmigte Dissertation von
Dipl.-Ing. Julia Maibach aus Bad Homburg v.d.H.

1. Gutachten: Prof. Dr. Wolfram Jaegermann

2. Gutachten: Prof. Dr. Heinz von Seggern

Tag der Einreichung: 06.12.2013

Tag der Prüfung: 22.01.2014

Darmstadt 2014 – D17

Contents

Abstract & Zusammenfassung	iv
1 Introduction	1
1.1 Scope of this Work	3
1.2 A Glance at Literature	4
2 Theoretical Background	7
2.1 Organic Semiconductors	7
2.2 Charge Carrier Interactions	11
2.3 Interfaces	14
3 Materials and Experimental Setups	21
3.1 Materials Used in this Work	21
3.2 Sample Preparation	24
3.3 Theory of Photoelectron Spectroscopy	32
3.4 Further Characterization Methods	45
I Breaking it Down	55
4 Characterizing a PCBM:P3HT Bulk Heterojunction Layer	57
4.1 PCBM	57
4.2 P3HT	61
4.3 Characterizing a Bulk Heterojunction Layer	67
4.4 Approaching the Interface	71
4.5 Motivating the Next Steps	77
5 Processing Possibilities of PCBM and DH6T	79
5.1 Thermal Evaporation of PCBM	79
5.2 Comparison of Drop-cast and Evaporated DH6T	98

6	Deciphering the Band Energy Diagram of a PCBM:DH6T BHJ	109
6.1	Interface Experiment	109
6.2	Blends	116
6.3	Derived Model	121
6.4	Conclusion	123
7	Evaluation of the Model Experiments	125
II	Building it Up	129
8	Developing the Nebulizer Deposition Method	131
8.1	Development Steps	131
8.2	Method Related Considerations	132
8.3	Substrate and Solvent Characteristics	134
8.4	Wetting of Ozone-Treated ITO by Chlorobenzene	141
8.5	Summary	143
9	Nebulization of DH6T	145
9.1	Chemical and Electronic Structure of Differently Prepared DH6T	145
9.2	Optical Microscopy	152
9.3	Summary	153
10	Nebulization of PCBM	155
10.1	Nebulizer Parameters	155
10.2	PCBM on ITO	155
10.3	PCBM on PEDOT:PSS	160
10.4	PCBM on PEI	167
10.5	Comparison and Evaluation of the Different Energy Level Alignments	173
10.6	Discussion of Valence Features	176
10.7	Optical Microscopy	180
10.8	Film Formation Properties	182
10.9	Summary	183
11	Evaluation of the Nebulizer Method	185

12 Concluding Remarks and Outlook	187
Bibliography	191
Appendix	201
A Additional Data to the Analysis of Evaporated PCBM	203
A.1 Difference XP Spectra of the Crucible Residue Sample	203
B Inelastic Mean Free Path Calculations	205
Publications & Conference Contributions	207
Danksagung	209



Abstract

Motivated by the increasing importance of organic optoelectronic devices produced via printing and other ink-based coating processes, this work focuses on the defined preparation and characterization of functional electronic interfaces of solution-processed organic semiconductors. Using donor/acceptor heterojunction interfaces from organic photovoltaic (OPV) devices as example systems, photoelectron spectroscopy (PES) is applied, which is an established and powerful method to decipher the chemical and electronic surface and interface properties of inorganic but also organic semiconductor contacts. In order to derive a band energy diagram containing energy level offset, interface dipole and induced band bending, controlled sample preparation conditions usually achieved through ultra high vacuum (UHV) and stepwise built-up of the targeted interface, starting with a monolayer or even below, are required. The implicit lack of methods for defined step-by-step deposition for most soluble organic molecules poses challenges for the photoelectron spectroscopic interface characterization of solution-processable heterojunction devices, which are to be overcome in this work.

The presented interfaces govern crucial processes in organic solar cells. Thus, understanding their electronic properties and how they are influenced by the processing conditions is of key importance. Targeting the donor/acceptor interface of an archetype bulk heterojunction between Poly(3-hexylthiophene) (P3HT) and Phenyl C₆₁ butyric acid methyl ester (PCBM), different preparative approaches of this interface are discussed and implications to an interface dipole between the two materials and possibly band bending in the donor are found. However, direct access to this interface has previously been hindered by the formation of a P3HT surface layer independent of the preparation technique. Therefore, thermal evaporation of PCBM was explored but has proven to be an inefficient method to produce chemically pure PCBM layers. For P3HT, a suitable replacement concerning stepwise deposition is found in α, ω -Dihexylsexithiophene (DH6T) as this small molecular thiophene can be deposited by physical vapor deposition as well as from solution. Through the substitution of the polymeric donor with DH6T, the interface between DH6T and PCBM could be characterized by an in-situ interface experiment based on stepwise

evaporation of DH6T on drop-cast PCBM. An interface dipole of 0.26 eV and band bending of 0.3 eV in the donor is found while the Fermi level position in PCBM remains unchanged. Combining these results with experimental findings of differently composed DH6T:PCBM blends processed entirely from solution, a model was developed, which describes the interface between donor and acceptor for solution-processed bulk heterojunctions with a donor capping layer.

To overcome the limitation of interface characterization using PES to UHV-integrated step-wise preparation, a novel ultra-clean wet deposition via an ultrasonic nebulizer unit is introduced. Design steps and method-related considerations such as wetting behavior are discussed and first results of the successful deposition of various organic inks are presented. In the case of DH6T, the perfect agreement between drop-cast, evaporated, and nebulized spectra shows the great potential of the newly developed method. In the case of PCBM on different inorganic and polymeric substrates, different thickness-dependent electronic interface properties indicating the formation of interface dipoles and space charge regions are observed for the first time. Therefore, the nebulizer method presents an innovative pathway to derive interface band energy diagrams for electronic devices deposited from inks.

The results of this work highlight the relevance of direct electronic interface characterization for solution-processed systems to gain fundamental understanding of solution-based functional organic interfaces relevant to achieve efficient OPV devices.

Zusammenfassung

Motiviert durch die zunehmende Bedeutung von optoelektronischen Bauteilen, die durch lösungsbasierte Beschichtungsverfahren wie z.B. Tintenstrahl- oder Tiefdruck realisiert werden, zielt diese Arbeit auf die definierte Präparation und Charakterisierung von funktionalen Grenzflächen von lösungsprozessierten organischen Halbleitern. Die Photoelektronenspektroskopie (PES) ist eine etablierte und aussagekräftige Methode für die Untersuchung der chemischen und elektronischen Ober- und Grenzflächeneigenschaften von anorganischen aber auch organischen Halbleiterkontakten und wird in dieser Arbeit beispielhaft auf Donor/Akzeptor-Grenzflächen organischer Solarzellen (OPV) angewendet. Voraussetzung für die Bestimmung eines kompletten Energiebanddiagramms, das die Anpassung der Energieniveaus, Grenzflächendipol und Bandverbiegung beinhaltet, sind jedoch kontrollierte Probenpräparationsbedingungen, die für gewöhnlich durch den schrittweisen Aufbau der zu untersuchenden Grenzfläche, beginnend bei (Sub-)Monolagen, im Ultrahochvakuum (UHV) erreicht werden. Für die meisten organischen Materialien, die für eine Flüssigprozessierung ausgelegt sind, ist eine definierte Schritt-für-Schritt-Deposition jedoch nicht möglich. Die daraus resultierenden Herausforderungen in Bezug auf PES-Grenzflächencharakterisierung aus Lösung werden im Rahmen dieser Arbeit erarbeitet.

Die vorgestellten Grenzflächen bestimmen wesentliche Prozesse innerhalb der Solarzellen. Daher ist das Verständnis ihrer elektronischen Eigenschaften und wie diese möglicherweise durch Herstellungsbedingungen beeinflusst werden von zentraler Bedeutung. Zur Charakterisierung der Donor/Akzeptor-Grenzfläche einer typischen „Bulk Heterojunction“ Solarzelle basierend auf Poly(3-hexylthiophen) (P3HT) und Phenyl-C₆₁-Buttersäure Methylester (PCBM) werden verschiedene Ansätze zur Präparation der Grenzfläche diskutiert. Aus den Ergebnissen konnten Hinweise auf einen Grenzflächendipol und eine Bandverbiegung im Donor abgeleitet werden. Bisher war der direkte Zugang aus der flüssigen Phase zu dieser Grenzfläche aufgrund einer sich ausbildenden P3HT-Deckschicht jedoch nicht möglich. Daher wurde die Abscheidung von PCBM durch thermisches Verdampfen untersucht. Die Ergebnisse zeigen jedoch, dass sich diese Methode nicht eignet, chemisch reine PCBM-Schichten herzustellen. Für das Polymer P3HT stellt α, ω -Dihexylsexithiophen

(DH6T) eine geeignete Alternative, da dieses molekulare Thiophen sowohl durch thermisches Verdampfen im UHV als auch aus Lösung abgeschieden werden kann. Durch das Austauschen von P3HT mit DH6T als Donor ist die Grenzfläche zwischen DH6T und PCBM durch ein in-situ Grenzflächenexperiment zugänglich geworden und konnte charakterisiert werden. Dabei wurde DH6T schrittweise auf eine durch Auftropfen hergestellte PCBM-Schicht aufgedampft, wodurch ein Grenzflächendipol von 0.26 eV und eine Bandverbiegung von 0.3 eV im Donor bestimmt werden konnten, wohingegen die Position des Fermi-Niveaus im Akzeptor unverändert blieb. Durch das Zusammenführen dieser Ergebnisse mit den Resultaten unterschiedlich zusammengesetzter, vollständig lösungsprozessierter DH6T:PCBM Mischsysteme ist ein Modell entwickelt worden, dass die elektronische Struktur der Grenzfläche zwischen Donor und Akzeptor in lösungsprozessierten „Bulk Heterojunctions“ mit einer Donor-Deckschicht beschreibt.

Um die Limitierung der Grenzflächencharakterisierung mittels PES auf UHV-integrierte schrittweise Präparation zu umgehen, ist eine neue Präparationstechnik basierend auf einer Ultraschall-Vernebelungseinheit erarbeitet worden. Dazu werden die Entwicklungsschritte sowie weitere Einflussfaktoren wie das Benetzungsverhalten diskutiert und erste Ergebnisse zu Abscheidungen verschiedener organischer Moleküle präsentiert. Am Beispiel des DH6T zeigt die große Übereinstimmung der Spektren für getropfte, genebelte und gedampfte Proben die umfassenden Möglichkeiten der neu entwickelten Methode. Durch eine Kombination aus Vernebelung und Tropfenabscheidung sind für PCBM erstmals schichtdickenabhängige elektronische Eigenschaften, die auf die Bildung von Grenzflächendipolen und Raumladungszonen hindeuten, an Grenzflächen zu verschiedenen anorganischen und organischen Substraten beobachtet worden. Die „Nebulizer“-Methode eröffnet somit eine neue Methode, sich den elektronischen Grenzflächeneigenschaften von lösungsprozessierten optoelektronischen Bauteilen zu nähern.

Die Ergebnisse dieser Arbeit verdeutlichen die Relevanz der direkten Charakterisierung der Grenzflächen von lösungsprozessierten Systemen, um ein grundlegendes Verständnis von flüssigprozessierten funktionalen organischen Grenzflächen zu erarbeiten und somit die Entwicklung effizienter Bauteile zu ermöglichen.

1 Introduction

The world's increasing energy demand combined with the limited resources on fossil fuels and the ongoing endeavor to minimize climate change pose urgent environmental, political, and social challenges. As the fifth Assessment Report (Working Group I) of the INTERGOVERNMENTAL PANEL ON CLIMATE CHANGE describes, the human influence especially through the release of greenhouse gases caused by the combustion of fossil fuels is most likely the origin of the present climate change [1]. This enforces the utilization of regenerative energy sources which in turn promotes research on sustainable energy conversion methods and energy efficient devices. Not only the energy consumption is increasing but also the number of electronic devices needed to maintain the high living standards achieved in the current Information Age. Therefore, it is of key importance to develop new as well as energy and material preserving devices and appliances. At this point, organic materials offer interesting opportunities and in many cases suitable or even outperforming alternatives to inorganic materials. Enabled by organic chemistry, it is possible to synthesize and customize organic materials in almost unlimited variety. The application of this class of materials as functional (semiconducting) materials for electronic applications is based on the discovery of the high electrical conductivity of halogen derivatives of polyacetylene by SHIRAKAWA ET AL. in 1977 [2].

Organic semiconductor materials are highly attractive, because the optical, electronic, chemical, and processing properties can be easily adjusted. An additional technological interest arises as cost and energy efficient production methods like evaporation and printing may be applied. Furthermore, flexible devices can be realized using organic semiconductor materials, which could be mass-produced in a continuous roll-to-roll process [3]. Scientifically, organic semiconductors are highly interesting as many processes in these complex materials and in their interactions are not yet fully understood. In order to achieve a better understanding, a multi-disciplinary approach is needed, because the interplay between chemistry, physics, and engineering enables efficient device development.

The first organic semiconducting devices emerged at the end of the last century. The most relevant representatives are organic field effect transistors (OFET), organic light emitting

diodes (OLED), and organic photovoltaic (OPV) devices. The first report on an OFET by TSUMURA ET AL. dates back to 1986 [4]. Research and development of OLEDs was triggered by the publication of TANG AND VAN SLYKE in 1987 [5]. As of today, OLEDs are commercially available both in display as well as lighting applications [6–9]. The first organic solar cell was presented by TANG in 1986 based on a planar heterostructure of an organic donor and acceptor combination [10]. The heterojunction in this device triggered further research on OPV devices, as efficient charge carrier separation was only achieved for large valence band (highest molecular orbital, HOMO) / conduction band (lowest unoccupied molecular orbital, LUMO) offsets. The introduction of an intermixed but phase-separated structure, the so called bulk heterojunction (BHJ), lead to a significant increase of the area of this critical interface between donor and acceptor. Additionally, the diffusion length of bound charge carrier pairs, so called excitons, to this charge carrier separating interface was reduced. This led to significantly improved solar cell efficiencies [11, 12]. The commercialization of organic OPV devices is still limited, although recently, efficiencies as high as 12 % have been reported for a multi junction solar cell [13] (meaning at least two solar cells stacked on top of each other in one device). Considering the increase in world wide energy need and the aim of reducing the dependence on fossil fuels, the further development of efficient OPV devices is very important.

Thus, focusing on the photovoltaic applications of organic semiconductors, the investigation and understanding of donor/acceptor interfaces is of high significance as critical processes in the solar cell are determined by this interface [14]. In particular, the determination of the interface band energy diagram representing frontier orbital energy level alignment and possible band bending due to formation of space charge regions at the internal donor/acceptor interfaces in BHJ solar cells plays a central role [15]. Therefore, in this work a detailed investigation of the donor/acceptor interfaces of the prototypical bulk heterojunction system based on thiophene donors and fullerene acceptors using photoelectron spectroscopy (PES) is presented. Challenges in characterizing these systems arise from the materials' deposition from solution and the implicit lack of methods for defined interface preparation. Hence, this work focuses on the influence of different preparation techniques on the electronic material properties to allow the use of model systems as well as on the development of new techniques to prepare defined interfaces in a controlled way directly from solution.

The work presented in this thesis is embedded in the MESOMERIE¹ project funded by the Bundesministerium für Bildung und Forschung (BMBF) and the research work was performed at the InnovationLab in Heidelberg as well as at the synchrotron facilities BESSY II at the Helmholtz Zentrum Berlin. The major focus of the research activities at the InnovationLab lies in the development and up-scaling of solution-processed organic electronic devices. This work therefore contributes to the ongoing development of printed electronics by providing valuable insights on solution-processed organic functional interfaces at a fundamental level.

1.1 Scope of this Work

In order to achieve highly efficient organic electronic devices, it is essential to understand the underlying material interactions at the different interfaces with respect to their fabrication process. Following the general approach of the Surface Science division, this work aims at understanding principal electronic surface and interface properties in organic solar cells, derived from an established device structure and adapting deposition and fabrication processes in such a way that detailed and undisturbed surface characterization is possible.

Photoelectron spectroscopy elucidates both the chemical and electronic structure of thin films and their interfaces. Due to the method-inherent high surface sensitivity, ultra-clean sample preparation conditions are required. BRILLSON summarized the important criteria to characterize interfaces on a fundamental level as follows: "(a) create surfaces with little or no structural damage and maintain them free of contamination for significant lengths of time, (b) modify them with the addition of new chemical species, on a scale of monolayers, and (c) analyze them with one or more surface sensitive methods of analysis." [16]. Although this was intended for metal/semiconductor interfaces it equally is true for organic semiconductor interfaces.

Considering that printing and coating techniques rely on ink deposition, the organic semiconducting materials used are designed for solution processing which makes them by implication not suitable for stepwise deposition via thermal evaporation. This obstacle arising from the lack of applicable interface preparation techniques for polymers and other solely

¹ Morphologie und elektronische Struktur von Organik/Organik und Organik/Metalloxid-Hybridsystemen

solution-processable materials might be a reason why the focus of ultraviolet photoelectron spectroscopy (UPS), which probes the occupied electronic states near the Fermi level, has not been on the energy level alignment directly at the interface [17]. In order to fill this gap in organic electronic interface characterization, two approaches are investigated in the course of this work:

In a first step the complex structure of the active layer of the electronically and spectroscopically well-characterized bulk heterojunction system Poly(3-hexylthiophene) (P3HT) : Phenyl-(C61)-butyric acid methyl ester (PCBM) [18–21] is simplified using a model system based on the small molecular thiophene α, ω -Dihexylsexithiophene (DH6T). The latter can be thermally evaporated and deposited from solution. Thus, through this breaking-down approach insights derived from UHV experiments can be transferred to solution-based systems.

To further explore the applicability of PES on organic semiconductors deposited from ink, a second emphasis of this work lies on the development of a method for step-by-step deposition of dissolved molecules. This way, it is intended to access interface properties directly from solution is intended. A piezoelectric nebulizer unit has been incorporated into the glass cell setup. The general suitability of this approach to build up interface in a step-wise manner from solution as well as the possibility to characterize thickness-dependent interface properties of the soluble small molecular organic materials is evaluated.

1.2 A Glance at Literature

Photoelectron spectroscopy is often used to characterize inorganic and organic semiconductors to determine interface band diagrams as e.g. exemplified in ref. [17, 22, 23]. The technique has also already been used on bulk heterojunction structures processed from solution. In the case of P3HT:PCBM blended active layers investigated by GUAN ET AL. [24] and XU ET AL. [20] the interface between the donor and acceptor could not be directly accessed due to the formation of a P3HT-enriched surface layer. While GUAN ET AL. used a lift-off technique to characterize the bottom side of the active layer to gain further insight in the electronic interaction between the two materials [24], XU ET AL. used varying concentration ratios of donor and acceptor to derive interface information [20]. Through their experimental approach GUAN ET AL. determined the energy gap between the PCBM lowest unoccupied molecular orbital (LUMO) and the P3HT highest occupied molecular orbital

(HOMO) to be 1.4 eV and an implied interface dipole between the two materials on the order of 0.5 eV. XU ET AL. found that the change in the energy level alignment in the top P3HT-layer is due to changes in the substrate work function and the PCBM concentration at the bottom surface of the film. In neither case a complete interface band diagram could be obtained.

In order to determine the interface dipole and characterize the band bending using PES one semiconductor should be stepwise deposited on top of the other [16]. However, as neither of the BHJ materials is intended to be deposited via thermal evaporation such a stepwise interface experiment has not been conducted for the P3HT:PCBM system. OSIKOWICZ ET AL. replaced the acceptor molecule PCBM with its unsubstituted parent molecule C₆₀ to determine the electronic band line up between a spin-cast film of P3HT and vapor-deposited C₆₀ [25]. For stepwise C₆₀ deposition onto spin-coated P3HT on a Si/SiO_x substrate a continuous increase in work function and an upward shift of C₆₀ valence orbitals were found in the UPS spectra and interpreted as the formation of an interface dipole of 0.6 eV due to electron transfer from the P3HT HOMO to the C₆₀ LUMO. Depending on the metal/metal oxide substrate different values for the P3HT/C₆₀ interface dipole were deduced (Al/Al_xO_y: 0.5 eV; Au/AuO_x: 0.15 eV).

Another approach is presented by FRISCH and co-workers [26]. They characterized the interface between P3HT and PEDOT:PSS (poly(3,4-ethylenedioxythiophene):poly(styrenesulfonate)) by varying the P3HT thickness by spin-coating from differently concentrated solutions and successive washing steps to further reduce the layer thickness. The results showed the formation of an interface dipole of around 0.5 eV at the contact between the electrode material and the donor polymer. One advantage in these experiments is the orthogonality of the solvents used to deposit the materials. While PEDOT:PSS is dissolved in water, chloroform was used to deposit P3HT, and thus intermixing is unlikely. However, the successive washing steps of P3HT in chloroform to reduce the layer thickness might alter the probed surface and introduce additional contaminations.

One approach, which directly targets the interface between P3HT and different contact materials, is presented by CASCIO ET AL. and LYON ET AL.. In their studies, electro-spray thin film deposition of P3HT is used to build up the contact step-by-step with intermediate PES characterizations performed without breaking the vacuum [27, 28]. Spray-coating techniques have also been applied for photovoltaic device fabrication. CHEN ET AL. used an airbrush technique to produce a bilayer P3HT/PCBM solar cell with an efficiency of 0.74 %

although the interface between the two materials was most likely not abrupt but rather an interdigitized interface [29]. STEIRER ET AL. used an ultrasonic sprayer as an easily scalable technique to produce P3HT:PCBM bulk heterojunction solar cells with power conversion efficiencies up to 3.2 % after annealing [30].

2 Theoretical Background

In this chapter the underlying theoretical concepts of organic semiconductors and heterojunctions will be briefly summarized. Detailed reviews can be found e.g. in references [31–33]. Here, the focus lies on the semiconducting and optoelectronic properties of organic materials and especially the interaction of donor and acceptor materials. As these properties are the results of the conjugated π -electron systems in the molecular building blocks the formation of these π -states is outlined. Since all optoelectronic devices are largely governed by their interface characteristics, the basic principles of interface formation between organic semiconductors are reviewed and put into the context of organic photovoltaic devices.

2.1 Organic Semiconductors

The electronic properties and interaction of organic semiconducting materials are commonly described using the principles of inorganic semiconductors. This might be applicable in many areas but there are major differences between the two material classes which will be elucidated in the following sections.

In principle, organic semiconductors can be divided into two classes: small molecules and polymers. This classification is based on mass, where typically small molecules have molar masses in the range of a few 100 g mol^{-1} while polymer mole masses are in the region of several $10\,000 \text{ g mol}^{-1}$. This division also has implications on the how the materials are processed. Due to their high mass, polymers cannot be deposited via thermal evaporation since decomposition takes place at rather low temperatures. Therefore, these materials are usually deposited via solution-based techniques. Depending on their size and functionalization small molecules usually can be deposited via thermal evaporation. In this work, both material classes are investigated as the influence of the preparation technique on the electronic properties is a central question in research on organic electronics.

Formation of Molecular Orbitals

Most organic materials are actually insulators but for certain compounds, semiconducting properties are observed. These arise from the bond formation characteristics of carbon atoms, which are the main building blocks of all organic materials. In the ground state a carbon atom has the electronic configuration $1s^2 2s^2 2p^2$. As the $2p$ subshell is not completely filled and contains only two electrons, carbon would thus be expected to be divalent. However, carbon can form up to four equivalent bonds. This is due to hybridization, which is the linear combination of electron wave functions of different character, e.g. of s - and p -functions. The hybridization is possible since the energetic difference between the $2s$ and $2p$ orbitals is small to begin with and can be overcome by an external potential such as an adjacent hydrogen or second carbon atom. In a first step one of the two $2s$ electrons is promoted into the empty $2p$ orbital. Secondly, the hybrid orbitals are formed. Depending on the number of participating p -electrons in this hybridization, carbon forms three different hybrid orbitals, namely sp , sp^2 , and sp^3 . The process is schematically shown in Figure 2.1.

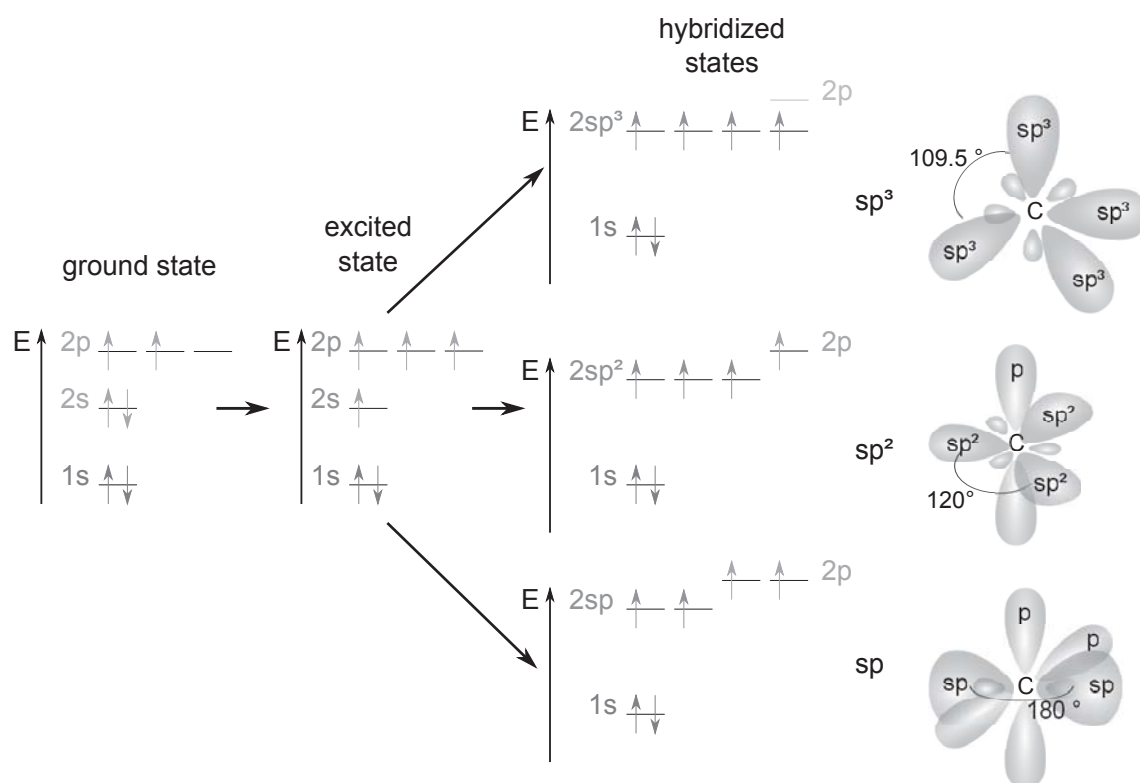


Figure 2.1: Mechanism of hybridization. (left) ground state of the carbon atom. (middle) excited state. (right) hybrid orbital formation of sp^3 (top), sp^2 (middle) and sp (bottom) and their geometric configuration.

The hybrid orbitals have a certain geometric arrangement with respect to each other (see Figure 2.1 on the very right). While the four equal sp^3 -orbitals form a tetrahedral structure with a bonding angle of 109.5° , the three sp^2 hybrid orbitals are all in plane separated by an angle of 120° with the remaining p orbital perpendicular to this plane. The sp orbitals form an angle of 180° and the two remaining p orbitals are oriented perpendicular to this orientation as well as to each other. These orientations result in two different types of bonds: A σ bond is formed if the charge density is centered along the bonding axis (see Figure 2.2). This is always the case if any of the sp^x hybrid orbitals overlap. A π bond is formed by overlapping p -orbitals which did not take part in the hybridization. Due to their dumbbell shape there is no electron density directly on the bonding axis but above and below (see Figure 2.2). These π bonds play an important role for the electronic properties as these electrons are generally only loosely bound.

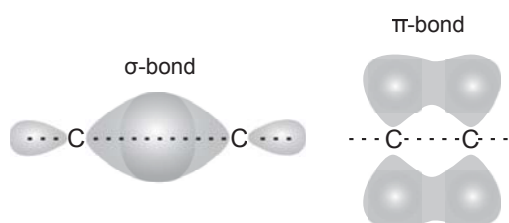


Figure 2.2: (left) σ -bond with the charge density located along the bonding axis. (right) π -bond with charge density above and below the bonding axis.

The formation of molecular orbitals (MOs) from these atomic and hybrid orbitals is schematically shown for Ethene (Figure 2.3), which is the smallest hydrocarbon molecule with sp^2 hybridized carbon atoms. The π molecular orbital is thus the highest occupied molecular orbital (HOMO). The lowest unoccupied molecular orbital (LUMO) is formed by the π^* states. The lowest electronic transition is therefore a $\pi - \pi^*$ transition and the energy gap between these states is typically in the range of 1 eV to 3 eV which results in absorption or emission in the visible (and neighboring near IR and UV) region [17, 32]. The color of organic materials thus directly relates to the π electron system. The values for HOMO and LUMO energies in this work are referenced to the Fermi energy. Their respective energies referenced to the vacuum level are given as ionization potential (IP) and electron affinity (EA).

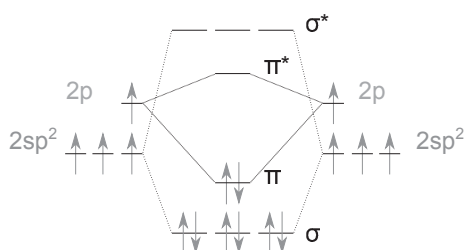


Figure 2.3: Formation of σ and π bonding and anti-bonding states from the valence orbitals in the case of Ethene.

Besides these direct relations to the electronic properties, the hybridization state of the involved carbon atoms becomes important in chapter 4.2.1 of this work as the hybridization affects the electronegativity of carbon and is therefore considered in peak assignment.

Formation of Organic (molecular) Solids

From the considerations on molecular orbitals, an important difference between organic and inorganic semiconductors is evident: With organic semiconductors, the electronically active states already exist on each individual molecule and are not formed by the formation of a crystalline solid as in inorganic semiconductors. Therefore, the electronic properties are largely governed by the individual building blocks, i.e. the molecule itself or the monomer repeat unit within a polymer. The transition from an atom to a molecule and finally to a molecular solid has been described in detail by ISHII ET AL. [17]. Following this approach the electronic structure is schematically represented by potential wells formed by the Coulomb potential of a nucleus, as shown in Figure 2.4. When the molecule or polyatomic monomer unit of a polymer is formed, the potential wells fuse in the upper part to form one broad well. The levels in this upper region are no longer specific to one single nucleus but form the above mentioned molecular orbitals. The core levels are in principle unaffected. If several molecules or monomer units now form an organic solid the individual molecular orbitals are still associated with the respective building blocks as these molecular orbitals only interact weakly via van der Waals forces.

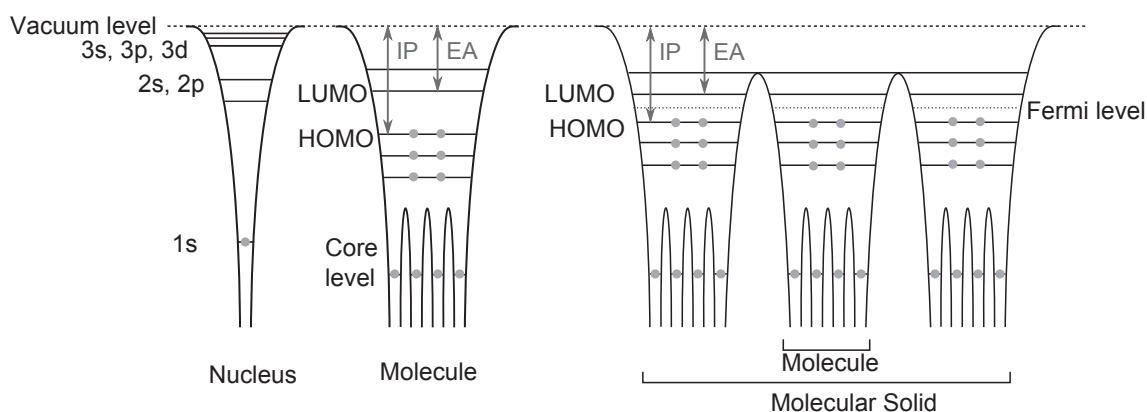


Figure 2.4: Representation of the electronic structure in coulombic potential wells. (left) Single atomic nucleus (Hydrogen). (middle) Polyatomic molecule. (right) Molecular solid. (reproduced from [17]).

2.2 Charge Carrier Interactions

Organic materials are typically soft materials (i.e. with the exception of diamond) and usually have a low charge carrier density and mobility. As a result, the molecular shape and lattice are deformed if an additional charge is introduced in the LUMO or a charge is removed from the HOMO, respectively. This is to compensate for the significant change in energy of the respective state. Additionally, the rather localized electronic states influence the charge carrier excitation and transport properties.

Polarons and Excitons

The values of the ionization potential and the electron affinity for a molecular solid differ from those of the individual molecules and monomer units, respectively. This is due to polarization and relaxation effects which stabilize the positive or negative ions. In principle, three contributions need to be considered:

Electronic polarization Upon ionization the valence electrons react to the presence of a charge by forming dipoles that stabilize the ion. The electronic polarization is extremely fast and occurs within approximately 10^{-16} s. The energetic contribution to the polarization is typically larger than 1 eV [34, 35].

Molecular relaxation After electronic polarization, intermolecular or intramolecular relaxation occurs to accommodate the redistribution of charge inducing slight atomic rearrangements within the molecules, e.g. changes in the bond lengths. This process is slightly slower than the electronic polarization and takes place within 10^{-14} s to 10^{-13} s after charge generation. The effect on the electronic levels is about 200 meV [34, 35].

Lattice relaxation Through a lattice distortion in the vicinity of the charged molecule the ion is further balanced. As this process involves movement of molecules it is rather slow ($t > 10^{-13}$ s) and contributes only about 10 meV to the total polarization [34, 35].

The combination of the charge and the polarization and relaxation of its surrounding is called polaron. The different polarization effects are important in PES as well as in charge

transport as charged molecules are involved in both processes. The time scale of the photoionization process is on the order of the molecular relaxation and thus slower than the electronic polarization. Therefore, the contribution of the electronic polarization (P_{el}) is included in PES and thus in the HOMO-LUMO energy distance obtained from a combination of direct and inverse photoemission, the PES gap. The lattice relaxation is too slow compared to the photoionization while the molecular relaxation may or may not be included. Since the hopping transport occurs on a time scale of 10^{-12} s, the fully relaxed state including lattice relaxation is probed with charge transfer methods giving the transport gap [34].

In the case of optical excitation, upon excitation the molecule is still neutral and a Coulomb bound electron hole pair, an exciton is formed. Compared to inorganic semiconductors, excitons have a high binding energy in organic materials which is due to their low dielectric constant ϵ_r (typically $\epsilon_r = 3$ [36]). Additionally, the excitons are localized on a single molecule because of the limited extension of the electronic wave function [36]. Common values for the exciton binding energy are in the order of 0.5 eV to 1 eV [32]. The implications of the high exciton binding energy on the device performance and structure will be exemplified in the case of organic solar cells later in section 2.3.

From this discussion, it follows that the HOMO-LUMO gap measured by PES differs from the transport gap as well as from the optical gap. The different gaps are schematically represented in Figure 2.5.

Transport Phenomena

The charge carrier mobility within one molecule arises from the overlap of the π orbitals and the loosely bound electrons therein. In systems with alternating single and double bonds (i.e. conjugated bonds), these are not localized between two atoms but delocalized over the complete π -electron system. Not only carbon atoms can contribute to the π -electron system but also e.g. oxygen or sulphur can contribute with their free electron pairs [39]. The σ bonds form the molecular backbone. The conjugation length, i.e. the extension of the π -electron system, is therefore crucial for charge transport properties. Especially in the case of polymers, the conjugation length can be reduced due to twisting and kinks. Hence, the molecule or monomer arrangements have significant effects on the charge carrier transport in organic semiconductors.

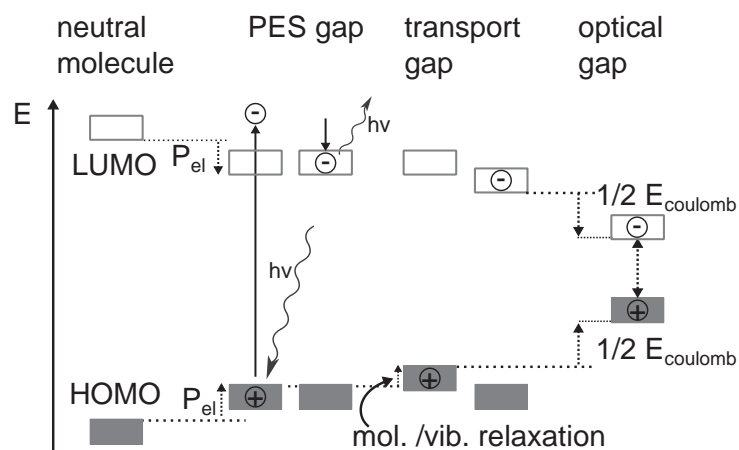


Figure 2.5: Schematic representation of the energy gaps in organic semiconductors. The gap probed by PES differs from the gap of the neutral molecule (at least) by the electronic polarization. The transport gap describes the fully relaxed state for either the hole in the HOMO or the electron in the LUMO. The optical gap is further reduced due to the Coulomb attraction of electron-hole pair. Adapted from [35, 37, 38].

In the transition from a single molecule to an organic solid the degree of molecular ordering determines the overlap between the molecular orbitals. For highly ordered and purified molecular systems band transport is observed at rather low temperatures. The bandwidth in these crystals, however, is only in the range of 100 meV which is small compared to inorganic materials [32].

For amorphous systems the orbital overlap between the individual molecules is small. Additionally, the molecules only interact via relatively weak van der Waals forces. Therefore charge transport from one molecule to the next can only be achieved through hopping transport [40]. The distribution of the HOMO and LUMO states for an amorphous material is Gaussian (see Figure 2.6 a). The different molecules experience different surrounding potentials. In this case the individual HOMO-LUMO gaps do not differ and the values of the maxima of HOMO and LUMO should be taken as a measure for the transport levels. If additionally, polarization effects occur also the individual molecular gaps vary (see Figure 2.6 b). Ultimately, this will also lead to a Gaussian broadening of the density of states for the amorphous solid. In this case however, the onset values of HOMO and LUMO, respectively, are representative for transport levels as they describe the smallest possible gap.

From a PES perspective the onset value of the measured orbitals should be taken since for many organic materials the first spectral feature which is attributed to the HOMO consists

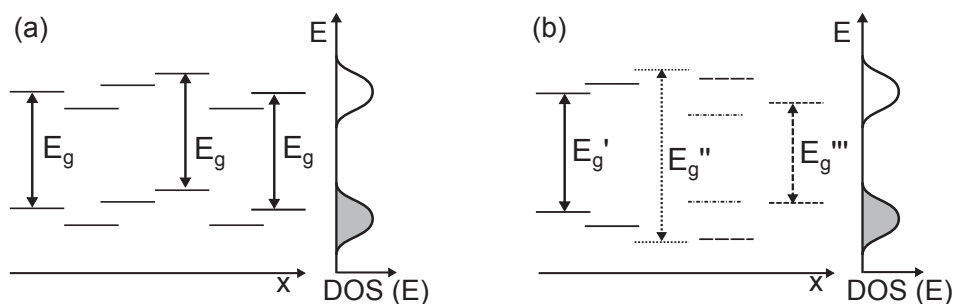


Figure 2.6: Model distribution of molecular orbital energies in an amorphous organic solid. (a) Lacking long range order leads to different energetic positions of the molecular orbitals but the energy gap (E_g) stays constant. (b) Through polarization effects the energy gaps is varied. Both molecular orbital distributions lead to a Gaussian density of states (DOS). Adapted from [38].

of more than one molecular orbital. In case of PCBM the feature is formed by five states of which three and two, respectively, are degenerate. The energy difference between these states however is so small that they cannot be resolved by UPS. Additionally, their intensity can vary with different excitation energies which would result in a shift of the maximum. However, the onset value is influenced by the measurement technique and setup. This specific contribution is rather small (as discussed in section 3.3.3), therefore, in the course of this work the $\text{HOMO}_{\text{onset}}$ value is used.

2.3 Interfaces

In organic solar cells a donor material is combined with an acceptor material to provide the energy necessary for exciton splitting. The donor material is a hole conducting material with a low ionization potential. As the ionization potential describes the energy required to remove one electron from the HOMO, it also determines the electron donating power of the material in question. The electron acceptor and thus electron transport material is vice versa characterized by a high electron affinity.

In principle, two aspects considering the interfacial electronic structure are relevant: (i) the energy level alignment at the interface and (ii) band bending in the bulk region [17, 41]. The interfaces between donor, acceptor and the contact materials govern the processes of charge injection, charge extraction, and charge separation.

Contact Formation Models

How the electronic levels arrange at the organic-organic interfaces is still under debate as the general models derived for inorganic semiconductors are not applicable in all cases due to the above presented differences in electronic structure in organic semiconductors. However, due to the lack of a comprehensive theory describing the contact formation in organic semiconductors, the inorganic interface models are a valid starting point.

The Schottky model describes the rectifying metal-semiconductor contact [42, 43]. The barriers responsible for this behavior are formed according to SCHOTTKY due to the alignment of the vacuum levels in a first step followed by the matching of the Fermi levels [42, 43]. As charge neutrality holds, the number of exchanged charges in order to achieve electronic equilibrium is the same on the metal and semiconductor side. What differs is the special distribution of charges. Due to the high density of charge carriers in a metal, the exchanged charge is shielded within about 0.1 Å. In a semiconductor an extended space charge region is formed due to the limited number of free charge carriers. The model describes ideal interfaces at thermal equilibrium. Interface states are thus neglected, which can cause deviations at real interfaces.

The Anderson model is based on the Schottky model and describes the inorganic semiconductor-semiconductor interface in thermal and electronic equilibrium [44, 45]. Again, the contact is formed firstly by vacuum level alignment and followed by Fermi level alignment. As now on both sides the density of free charge carriers is reduced (compared to a metal) a space charge region forms in either semiconductor. A barrier results at both the valence and conduction band levels are obtained from the differences of the electron affinities (EA) and the ionization potentials (IP):

$$\Delta E_{CBM} = EA(A) - EA(B) \quad (2.1)$$

$$\Delta E_{VBM} = IP(A) - IP(B) \quad (2.2)$$

In the Anderson model the formation of interface dipoles is not included. Therefore the so called electron affinity rule (after equation 2.1) only applies for contacts, where no interface dipole due to charged surface states is obtained.

Within certain limitations, theories for the contact formation of organic-organic and organic-inorganic interfaces have been presented. For contacts where only weak interac-

tion is assumed as in most cases of organic-organic interfaces, the integer charge transfer (ICT) model was developed by SALANECK ET AL. [46]. To be more specific, weak interaction means that no hybridization occurs between the π -electron system of the organic semiconductor and the wave functions of the substrate material.

The integer charge transfer model is based on the formation of charge transfer states within the band gap of an organic semiconductor. As previously described, organic semiconductors relax electronically and geometrically if a charge carrier is removed or injected. With respect to the ICT model, these polaronic states are referred to as the ICT+ state formed close to the HOMO edge if a charge is removed and the ICT- state formed close to the LUMO edge, if an additional charge is introduced. The energy difference between the ICT state and the respective MO edge describes the energy necessary to fully relax the organic semiconductor after charge extraction/injection.

Upon contact formation the position of the respective ICT state to the substrate Fermi level in the case of an inorganic substrate or the substrate ICT states in the case of organic semiconductors need to be considered. In the following, the contact formation with an inorganic substrate will be described in detail and the result of transferring the model to all organic interfaces will be only briefly summarized. For a more elaborate description the reader is referred to Ref. [46].

Depending on the position of the substrate Fermi level with respect to the ICT states three regimes are distinguished [46]:

$\Phi_{Sub} > E_{ICT+}$: The work function of the substrate (Φ_{Sub}) is larger than the energy of the positive ICT state (E_{ICT+}). Thus, electrons will flow from the organic material to the substrate. This results in Fermi level pinning at the ICT+ state and an interface dipole Δ of $\Phi_{Sub} - E_{ICT+}$. The work function of the organic is independent of the substrate, only the dipole potential changes (see Figure 2.7 a).

$\Phi_{Sub} < E_{ICT-}$: The work function of the substrate is smaller than the energy of the negative ICT state (E_{ICT-}). Therefore, electrons from the substrate will be injected into the organic material. Comparable to the first case, the Fermi level of the substrate pins to the ICT- state. Hence, an interface dipole Δ of $E_{ICT-} - \Phi_{Sub}$ is formed. Again, the work function of the organic is independent of the substrate (see Figure 2.7 b).

$E_{ICT-} < \Phi_{Sub} < E_{ICT+}$: The work function of the substrate is larger than the energy of the negative ICT state but smaller than the positive ICT state. This means, that no spontaneous electron transfer either from the organic to the substrate or vice versa will occur. Therefore, vacuum level alignment will be observed, meaning that the work function of the adsorbed organic is dependent on the work function of the substrate (see Figure 2.7 c). In this case in particular, one drawback in the model becomes obvious, as the position of the Fermi level in the organic is not discussed, or better said it is simply predefined by the Fermi level position of the substrate. However (for a reasonably well doped semiconductor), there can only be one position of the Fermi level in a material, and thus upon contact formation the Fermi level needs to align between two materials. This discrepancy was already discussed by C. HEIN [38] where she proposed an alignment of the Fermi level via a Fermi level movement in the organic material as depicted in Figure 2.7 c on the right. The ICT model then describes the energy alignment at the interface for the limiting cases of an infinitely extended space charge region (at low doping level) or very thin layers.

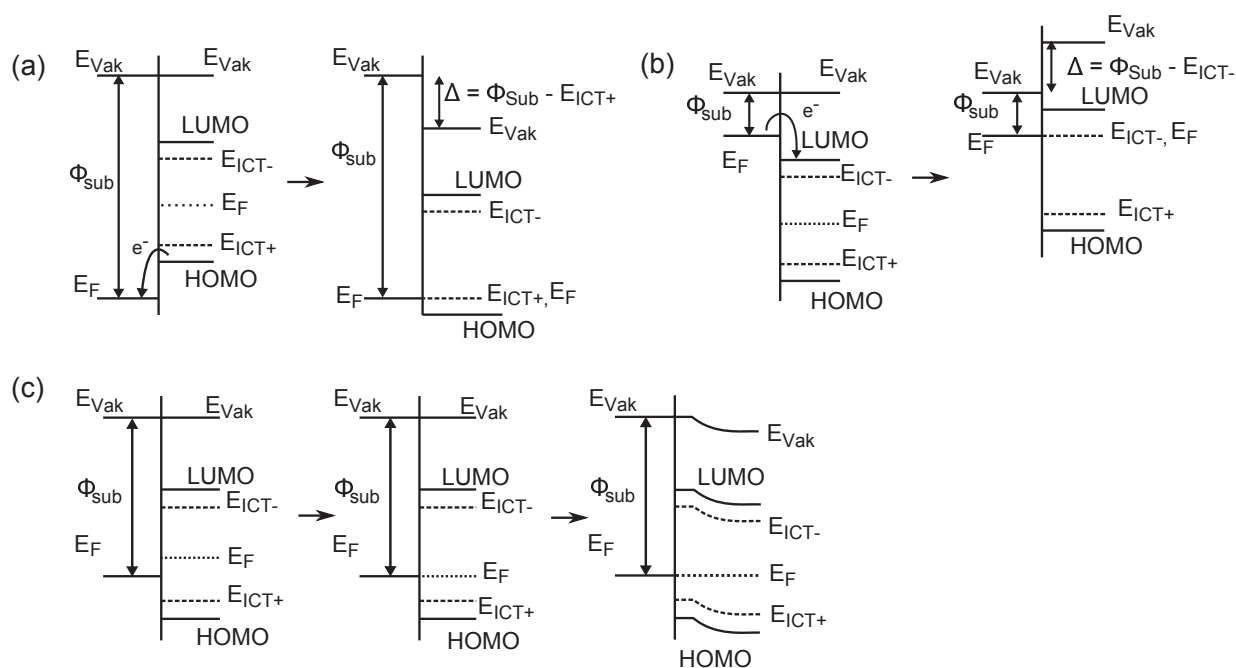
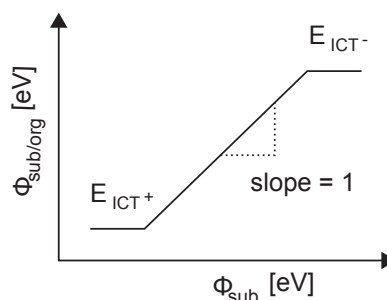


Figure 2.7: Schematic representation of the energy level alignment according to the ICT model (a) in the case of $\Phi_{Sub} > E_{ICT+}$, (b) in the case of $\Phi_{Sub} < E_{ICT-}$, and (c) for $E_{ICT-} < \Phi_{Sub} < E_{ICT+}$ including an extension of the model considering the Fermi level position in this case. Adapted from [38, 46].

The three regimes can be summarized in a plot of the work function of the adsorbed organic material $\Phi_{Org/Sub}$ over the work function of the substrate Φ_{Sub} as can be seen in

Figure 2.8. For small substrate work functions, the work function of the organic material is independent of the former. In the intermediate regime, vacuum level alignment is observed, resulting in a dependency of the organic work function on the substrate work function which is characterized by the slope = 1. For high substrate work functions, the organic work function is again independent of the substrate work function (i.e. Fermi level pinning). The transition points between the three regimes mark the energies of the negative/positive ICT states. This behavior could be shown experimentally for several organic materials (see Ref. [46] and the references therein) including P3HT and PCBM [20].

Figure 2.8: Dependence of the work function of the adsorbed molecule with respect to the work function of the substrate. Adapted from [46].



The ICT model can be transferred to organic/organic interfaces as well, if the precondition of only weak interaction is fulfilled. During contact formation, the relative position of the ICT states between the two organic materials needs to be considered. In a first step, the interaction of the first organic material with the substrate is determined according to the ICT model. The obtained work function is then taken as the starting point for the energy level alignment with the ICT states of the second, adsorbed organic material.

However, a general theory to describe or even predict energy level alignment at organic hetero contacts does not yet exist. KAHN and co-workers have proposed the induced density of interface states (IDIS) model which describes the contact formation of strongly interacting substrates and adsorbates [47]. In the case of metal/organic interfaces the alignment is determined by the relative positions of the metal work function and the so called charge neutrality level (CNL) in the organic material as well as the interface parameter S which describes the screening of the potential difference due to polarization. Additionally, charge redistribution effects influence the alignment. The so called push-back or pillow effect describes the reduced extension of the metal surface electron density tail upon adsorption of organic molecules [48, 49]. Even a combination of the pillow effect and the IDIS model has been proposed to describe the electronic interaction at organic-organic interfaces [50].

The Role of Donor/Acceptor Interfaces in Organic Solar Cells

The efficiencies of organic solar cells are typically below those of inorganic PV devices. A comprehensive overview of the state of the art for single cells or submodules is given in the solar cell efficiency tables [51] but generally crystalline inorganic PV devices achieve efficiencies around or above 20% while organic solar cells range in the region of 10% with the current world record of 12% [13]. One reason lies in the high exciton binding energy in organic materials. The necessary driving force for the exciton dissociation in organic solar cells is only provided at the interface of donor and acceptor due to their different electronic potentials. Thus, the excitons have to diffuse to these interfaces without recombining. The typical exciton diffusion length is on the order of 10 nm [32]. Although organic materials have high absorption coefficients equal or even larger than 10^5 cm^{-1} [31, 52] and thus required absorber layer thicknesses in the range of a few 100 nm completely transform the incident light into charge carriers, this thickness is well beyond the exciton diffusion length. Therefore, device architectures other than bilayer cells are often employed. One way to realize the intimate blending of donor and acceptor material is the bulk heterojunction structure. This structure has the advantage of increased exciton splitting interface area and simultaneously reduced exciton diffusion lengths to reach these interfaces. A schematic of such an OPV device is shown in Figure 2.9. In the case of P3HT:PCBM this interpenetrating network is formed during film deposition. Both materials are dissolved in the same solution with a given weight ratio and due to diffusion and crystallization forces the blend structure develops.

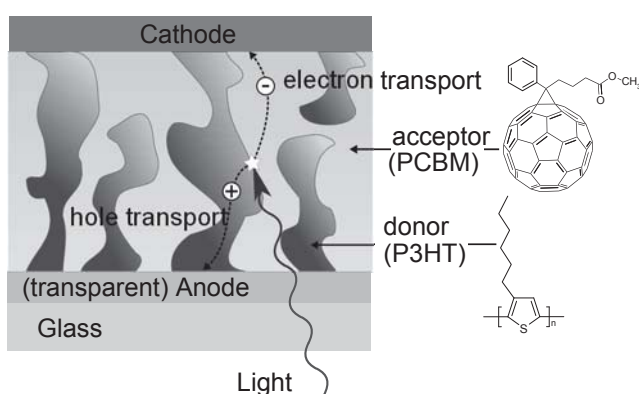
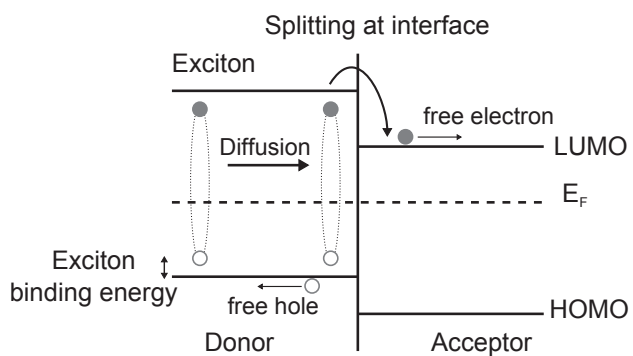


Figure 2.9: Schematic representation of a bulk heterojunction solar cell. The exciton is created by irradiation of light and split at the donor:acceptor interface into free charge carriers. The electron is transported through the acceptor to the cathode and the hole moves through the donor to the anode. Adapted from [32].

The energy level alignment at the interface governs the charge carrier separation and also determines the photovoltage: The driving force for exciton splitting is the energy difference of the electron (hole) in the excitonic states of the donor LUMO (acceptor HOMO)

and in the acceptor LUMO (donor HOMO) state as depicted in Figure 2.10 [53, 54]. However, the energy difference of the donor HOMO and acceptor LUMO represents an upper (never reached) limit of the photovoltage [55, 56]. Therefore, a compromise in energy level alignment needs to be achieved as the photo current is increased by shifting the energy of the acceptor's frontier orbital states down relative to the donor states and the photovoltage is increased by shifting the acceptor states up.

Figure 2.10: Schematic representation of the exciton splitting at the donor-acceptor interface.



3 Materials and Experimental Setups

While in the previous chapter the general properties of organic semiconductors have been described, in this chapter the donor and acceptor materials used in this work are introduced. Furthermore, an overview of the applied characterization methods is given. The focus lies on photoelectron spectroscopy as this is the major measurement techniques used in this work.

3.1 Materials Used in this Work

The materials applied in this work can be classified according to their functionality within OPV devices. The electron donor materials investigated in this work are thiophene-based whereas the acceptor molecules are fullerene-based. The latter class of materials such as C_{60} and Phenyl-(C61)-butyric acid methyl ester (PCBM) are widely used acceptor molecules since they have very suitable electronic properties. Due to their low lying LUMO [24, 57] and thus high electron affinity they are compatible with a large variety of donor materials [58]. Ultra-fast charge transfer on the time scale of 45 fs for numerous fullerene-polymer blends has been observed [59]. For both C_{60} as well as for PCBM rather high charge carrier mobilities of $0.4\text{--}11\text{ cm}^2\text{ V}^{-1}\text{ s}^{-1}$ and $0.05\text{--}0.2\text{ cm}^2\text{ V}^{-1}\text{ s}^{-1}$, respectively, have been determined in transistor geometry [60–62]. Thiophenes are commonly used as donor materials because they have a strong tendency to form highly ordered structures which enables efficient π stacking [63, 64]. In the case of Poly(3-hexylthiophene) (P3HT) charge transport can occur efficiently both inter- as well as intramolecular [65]. Alkylated thiophenes show good solubility and processability and are generally environmentally stable [66, 67]. In combination, P3HT:PCBM bulk heterojunctions are one of the most widely studied representatives in the field of organic solar cells (see e.g. ref. [18, 68, 69]).

With respect to photoelectron spectroscopy, donor acceptor systems based on thiophenes and PCBM can be well examined as both molecules contain elements which are characteristic for the respective material. The major element in both materials is carbon but only the thiophenes contain sulphur atoms while oxygen is only present in PCBM. This facilitates

material identification in mixed systems with PES. The chemical structure of the donor and acceptor materials is given in Figure 3.1.

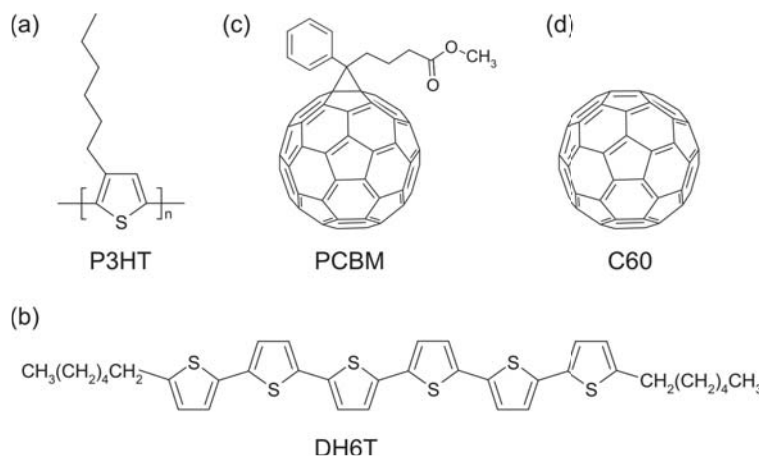


Figure 3.1: Chemical structures of the thiophene based donors P3HT (a) and DH6T (b) as well as the fullerene acceptor materials PCBM (c) and C₆₀ (d).

3.1.1 Substrate Materials

Photoelectron spectroscopy is applied in this work as the major characterization technique. Therefore, the substrates were chosen with respect to a prerequisite of this method, which is sufficient sample conductivity. Therefore, commercial indium doped tin oxide (ITO) covered glass substrates (Merck) were primarily used. ITO belongs to the class of transparent conductive oxides which are currently one of the standard contact materials both in organic as well as inorganic optoelectronic applications. These oxides are suitable contact materials due to their low lying electronic levels which makes them selective for holes and efficiently blocks electrons. Additionally, ITO has a low sheet resistance of below 20 Ω/sq [70]. With transparencies larger than 80% in the visible region they allow for light in- or out-coupling depending on the device requirement. Different substrate surface treatments such as argon sputter cleaning and ozone surface activation have been applied mainly to remove residual carbon contaminations after the solvent substrate cleaning with acetone and isopropyl alcohol. These treatments can additionally alter surface properties such as polarity which can be beneficial for subsequent material deposition. The effects of these surface treatments have been thoroughly studied in ref. [71]. Experiments requiring high IR transparency necessitated the use of substrates such as lightly doped to undoped silicon

(Siltronix, SiMat) with a specific resistance of larger than 5000 Ωcm (according to the manufacturers).

Additionally, some polymer-covered ITO substrates were used to obtain non-reactive substrates with varying work functions. To achieve this, ITO was coated with poly(3,4-ethylenedioxythiophene) poly(styrenesulfonate) (PEDOT:PSS, Heraeus). This material is very common as an interlayer in OPV devices as it improves the hole selectivity and additionally smooths the ITO surface [72]. To fabricate low work function substrates, ITO was covered with branched Polyethylenimine (PEI, Sigma Aldrich) [73].

3.1.2 P3HT

A widely used donor polymer in OPV research is Poly(3-hexylthiophene) (P3HT). The molecular structure of a monomer unit is shown in Figure 3.1 a. The electronic properties of the material are mainly governed by the thiophene units while the hexyl side chains enable solution processing. Details about the synthesis and properties of thiophenes in general and P3HT in particular can be found in the HANDBOOK OF OLIGO- AND POLYTHIOPHENES [67].

There are in principle two modifications of P3HT depending on the orientation of the hexyl groups: regio-regular possessing an ordered structure of the side chains and regio-random where no long range order of the side chains applies. With increasing regio-regularity the mobility increases up to two orders of magnitude due to self-organization of the polymer chains [74]. The material used in this work (Honeywell, 70510) has a regio-regularity of 94.7% and a mean molecular weight of 30 000 g mol^{-1} . As for all polymeric materials the degree of polydispersity can vary strongly which needs to be considered when discussing reproducibility. The experiments presented in this work were therefore all performed using material from a single batch.

3.1.3 DH6T

α, ω -Dihexylsexithiophene (DH6T) also belongs to the class of thiophene compounds but in contrast to P3HT it is a small molecule. The synthesis, electric properties and thin film structure of the material are described in [75]. The chemical structure is depicted in Figure 3.1 b. Through the addition of the hexyl-chains at the ends, the molecule becomes

soluble in chlorobenzene. This functionalization, however, does not change the vacuum processability of the molecule. This leads to the main reason why this molecule is used in the following experiments: All preparation techniques discussed in this work ranging from UHV thermal evaporation to the newly developed nebulizer deposition can be applied to DH6T. Thus, direct comparison of the deposition routes and their potential influence on the electronic properties of the material is possible. Additionally, this material offers better reproducibility as the issues of molecular weight distribution and purity are less pronounced in small molecular systems.

The molecule itself is mainly used in transistor configurations (see e.g. [76]) but its application in both bilayer as well as bulk-heterojunction solar cells has been shown in literature [77]. In this work DH6T was obtained from Sigma Aldrich and used as received.

3.1.4 PCBM & C₆₀

C₆₀ was first discovered in 1985 by KROTO ET AL. [78] and named fullerene after the architect Richard Buckminster Fuller. The first efficient synthesis was described in 1990 by KRÄTSCHMER ET AL. [79] marking the starting point of the widespread application of C₆₀ as an acceptor/n-type conducting material in organic electronics.

The fullerene-derived material [6,6]-phenyl C₆₁ butyric acid methyl ester (PCBM) consists of a C₆₀-cage structure as well as a side chain (see Figure 3.1 c). This side chain contains a phenyl ring and an ester group. The latter makes the molecule soluble in many organic solvents while the phenyl group is only needed due to synthesis reasons. The complete synthesis is reported in ref. [80]. PCBM was purchased at Nano-C as well as at American Dye Source. The purity in both cases was specified to be larger than 99.5%. Through the addition of the side chain the electronic properties of the C₆₀ core are almost unchanged. Therefore C₆₀ (Dynamic Enterprises, 99.5%) was used as a reference or substitute material in some cases. PCBM and C₆₀ were used as received.

3.2 Sample Preparation

Different preparation techniques, namely physical vapor deposition under vacuum conditions and solution-based methods at ambient pressure, are employed to evaluate their

possible influence on the electronic properties of the resulting film. The different processes applied and developed during this work are schematically represented in Figure 3.2.

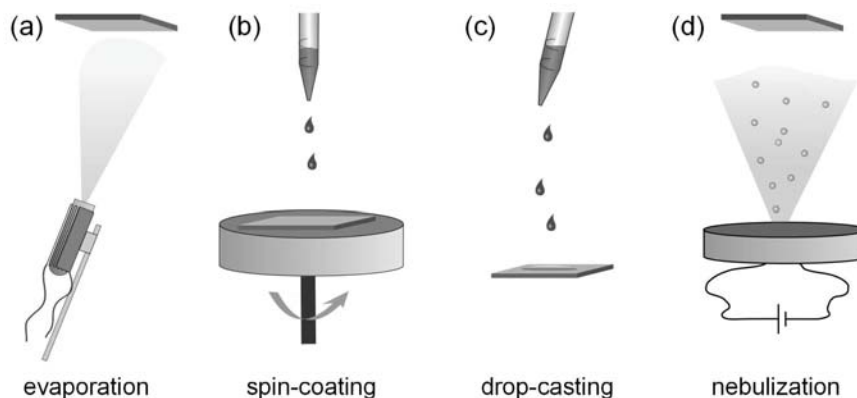


Figure 3.2: Sketch of the different preparation techniques: (a) Thermal evaporation. (b) Spin-Coating. (c) Drop-casting. (d) "Nebulization".

For thermal evaporation home-made effusion cells were used (see Figure 3.2 a). These consist of aluminum oxide crucibles with a tantalum wire wrapped around for resistive heating. The evaporation temperature can be controlled with the help of a thermocouple in contact with the crucible. The advantage of physical vapor deposition is the possibility to perform both a step-by-step deposition as well as deposition of mixed systems through co-evaporation. The former is exploited in this work when conducting interface experiments. In such an experiment the contact between two materials is built up sequentially with repeated PES measurements after each deposition step. This allows the tracking of the electronic properties as a function of layer thickness which corresponds to the distance to the contact area. However, the method is only applicable to small molecules as most polymers decompose before the evaporation temperature is reached.

As liquid-based techniques spin-coating (Figure 3.2 b) and drop-casting (Figure 3.2 c) have been applied as established film deposition methods. Additionally, the so called nebulizer technique (Figure 3.2 d) has been developed in this work to achieve a step-by-step deposition from solution. This method and its development will be discussed in full detail in part II of this thesis. Spin-coating experiments are performed in the nitrogen glove box using a Spin150-NPP spin-coater from SPS Europe. The coating process can be challenging as many factors such as the pollution of the N_2 -atmosphere might affect the film properties. Especially, when preparing samples for photoelectron spectroscopy characterization, a high level of cleanliness and accuracy is required to achieve samples with sufficiently low

contamination suitable for surface characterization. Some spin-coating experiments have been performed ex-situ either because of the lack of a glovebox or because the required solvent could not be used in a glovebox as it contained water. In order to maintain a very low level of contamination and water adsorption, these samples were placed on a hot plate after the spin-coating process (at temperatures of around 100 °C) and screwed onto a hot sample holder. The samples were then placed in the load lock while still warm.

Spin-coating can lead to inhomogeneous films due to remaining liquid at the sample edges and corners. However, spin-coating generally produces more homogeneous films than drop-casting. The advantage of the latter deposition route with respect to photoelectron spectroscopy is that it can be done inside the glass cell which offers better control of possible contamination sources. For drop casting experiments several droplets of the organic solution are deposited on the substrate. The film is then dried in the glass cell, if necessary, by using a low pressure argon stream. The complete glass cell setup and its features are described in detail in section 3.2.2.

3.2.1 UHV Systems

All experiments were performed at two integrated systems, namely the Solid Liquid Analysis System (SoLiAS) and the Clustertool. The setups unite sample preparation and characterization in one ultra high vacuum (UHV) system. These are required when using PES as a characterization tool for two reasons: One is process-inherent as the emitted photoelectrons could interact undesirably with extraneous matter such as gas molecules. Thus, as the ambient pressure increases the mean free path of the electrons is drastically reduced. This would lead to reduced count rates or even no signal at all if the emitted electrons scatter so much that they do not reach the analyzer anymore. However, pressures in the high vacuum regime, i.e. 10^{-5} mbar, are sufficient for the electrons to reach the analyzer [81].

Another and more important reason lies in the high surface sensitivity of photoelectron spectroscopy which implies that contaminations need to be avoided as much as possible to allow for analyzing the actual material properties and not the surface contamination. The direct combination of sample preparation and characterization in one UHV system reduces contamination processes to a level suitable for PES. At a base pressure of 10^{-6} mbar and a sticking probability of 1 a monolayer of adsorbates forms on the surface within seconds.

Thus, by reducing the pressure even further (and since polymers and other organic materials usually exhibit a sticking coefficient much less than 1) acceptable times for surface investigations can be achieved [81].

SoLiAS

The Solid Liquid Analysis System (SoLiAS) is a movable UHV endstation located at the synchrotron light source BESSY II at the Helmholtz Center Berlin. The basic setup is shown in Figure 3.3. In principle, the system can be divided into three levels: Analysis, UHV preparation and Solid/Liquid preparation. On the analysis level (1) the SXPS experiments are performed. SoLiAS is equipped with a Phoibos 150 hemispherical analyzer (SPECS) and a nine channel detector. The achievable resolution deduced from the silver Fermi edge for the chosen excitation energies between 90 eV to 600 eV is in the range of 220 meV to 300 meV. The pressure in the analysis chamber is typically in the low 10^{-10} mbar range. At level 2 the UHV sample preparation is performed. This includes sputter cleaning of the substrates, if necessary, and deposition via thermal evaporation. The base pressure in the deposition chamber is kept in the between 10^{-8} to 10^{-6} mbar. The solution-based deposition steps in the glass cell (for details see section 3.2.2) were performed at level 3.

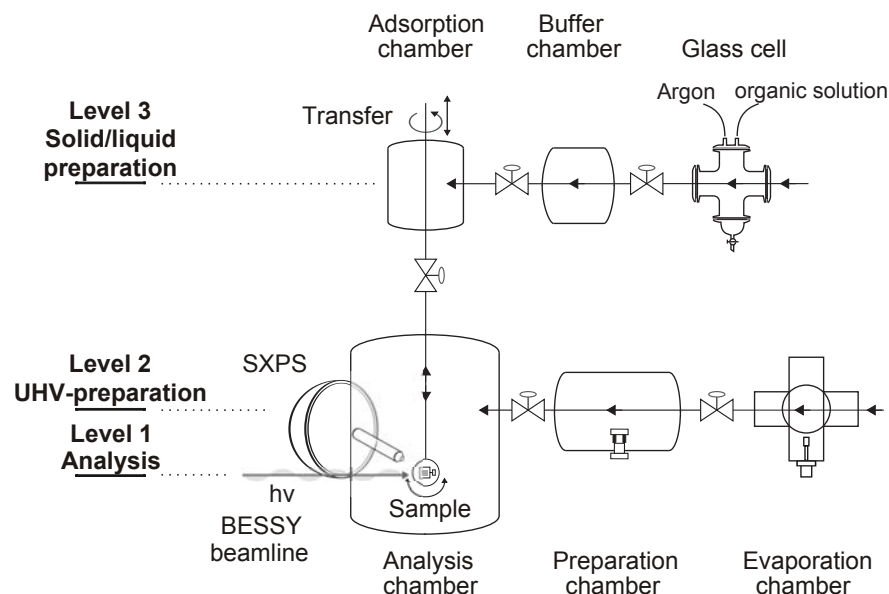


Figure 3.3: Sketch of the experimental end station SoLiAS at BESSY II in Berlin.

The central equipment of the joint research activities of the TU Braunschweig, the University of Heidelberg, and the TU Darmstadt at the InnovationLab within the MESOMERIE project is the UHV preparation and characterization setup Clustertool. This system unites three functionalities, namely sample preparation, sample transfer, and sample characterization without breaking vacuum.

Preparation and Transfer

The layout of the system is shown in Figure 3.4. The backbone of the system are three interconnected circular distribution chambers. At the first handler almost all preparation units are attached. For solution-based depositions at ambient pressure as well as sample handling in inert atmosphere a glovebox is connected to the UHV system via the load lock. The glovebox is equipped with a spin-coater and hot plates for solution-based substrate coating. Also at *Handler I* three larger deposition chambers are located. Two of these chambers are built for organic film deposition via thermal evaporation while the third chamber is reserved for metal deposition. In all chambers the deposition processes can be controlled through shutters and micro-balances.

The deposition concept allows for the preparation of up to four identical samples which can then be distributed to the incorporated characterization tools. At *Handler II* the *IR spectroscopy* setup is positioned. Between *Handler II* and *Handler III* a smaller organic deposition chamber is located. This chamber holds up to eight evaporation sources. Due to the smaller crucibles used in these sources as well as the possibility to evaporate material on a single sample holder this chamber is very suitable for material testing. Additionally, shorter transfer times to the PES unit are beneficial for extended surface and interface characterization. *Handler III* connects the preparation units to the *Photoelectron Spectroscopy* as well as to the *Scanning Probe* setup. Also at *Handler III* a buffer chamber with glass cell is built in close proximity to the PES equipment for ultra-clean solution-based deposition. As this specific setup was built up, optimized, and customized as part of this work it will be described in more detail in section 3.2.2.

The distribution chambers are equipped with motorized transfer arms which allow sample placement in all attached chambers. The handing-over of the samples between the

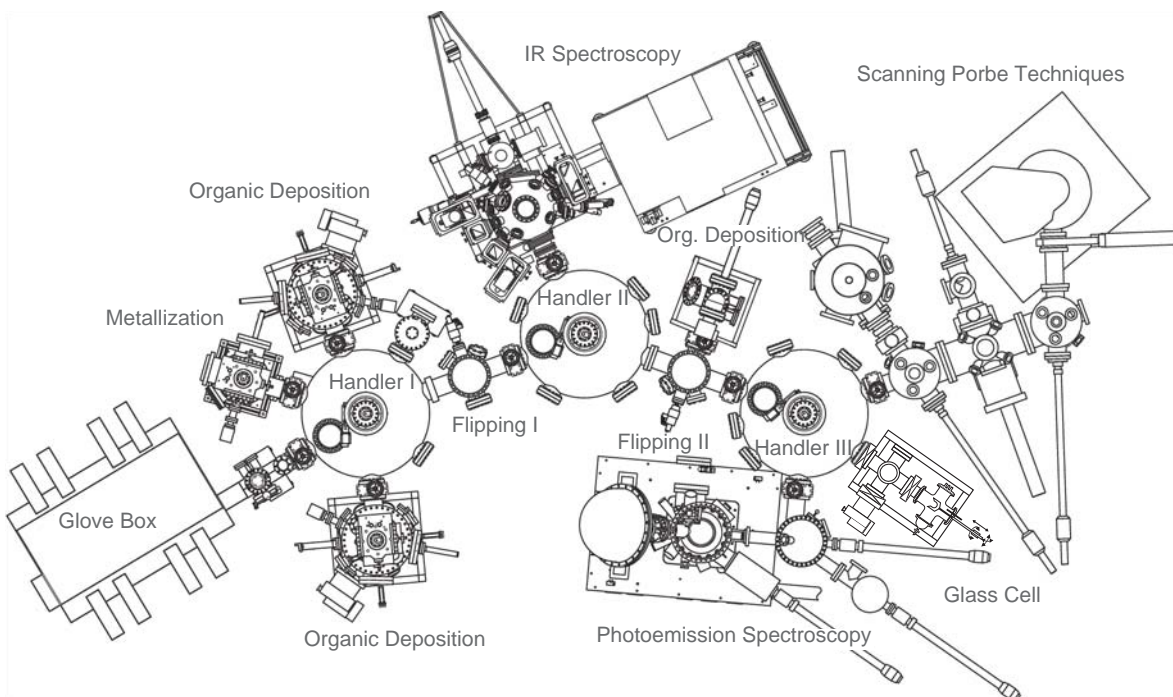


Figure 3.4: Top view of the UHV system Cluster Tool of the analytics competence center at the InnovationLab Heidelberg. This image was created from a VG CAD drawing and adapted from [82].

different arms is established through wobble sticks located in the flipping stations. These chambers are specially designed to change the sample cassette orientation from face-down to face-up as well as for sample individualization as up to four samples can be prepared and transferred simultaneously.

Characterization

The three major characterization setups *Scanning Probe Techniques*, *IR Spectroscopy*, and *Photoelectron Spectroscopy* are united in one UHV system to promote the understanding of charge and energy transport in organic electronics through joint research efforts. The individual features and benefits of each method are briefly described in the following:

Scanning probe techniques Morphological studies of surfaces and sample cross sections can be performed under defined conditions with an Auriga Crossbeam system from Zeiss. A focused ion beam (FIB) is combined with a scanning electron microscope (SEM) within one HV chamber. An exchangeable door system by DME enables the incorporation of other scanning probe techniques such as atomic force microscopy,

scanning tunneling microscopy and scanning Kelvin probe microscopy. This unique combination allows also the lateral investigation of electrical potentials with high spacial resolution. These techniques are complemented by an UHV scanning probe setup.

Fourier transform infrared spectroscopy The Fourier transform infrared (FT-IR) spectroscopy unit is based on a Bruker Vertex 80v spectrometer. This is attached to a custom made UHV chamber which enables controlled deposition of thin films via thermal evaporation while simultaneously measuring IR spectra. The combination of two different excitation sources and six detectors covers the spectral region of 20 to $12\,800\text{ cm}^{-1}$. The details of this setup are described in ref. [82].

Photoemission spectroscopy The photoelectron spectrometer incorporated into the Clustertool is a PHI VersaProbe II Scanning XPS Microprobe equipped with a hemispherical analyzer and a 16 channel detector. The base pressure in the analysis chamber is in the low 10^{-9} mbar region. A setup for inverse photoemission spectroscopy (IPES) is also incorporated. The details of photoelectron spectroscopy including instrumentation will be explained in detail in section 3.3.

3.2.2 The Glass Cell

The basic setup for solution-based deposition techniques suitable for sample preparation for photoelectron spectroscopy is the so called glass cell. This specific setup is unique to the Surface Science division and is built-up from a KF50 glass double cross. Despite the two ports required for sample transfers this allows for the addition of specially tailored flanges that enable both continuous gas flow and material deposition. A key requirement of this setup is that it is constantly rinsed with ultra-clean inert gas such as argon 5.0 or 6.0 or nitrogen.

The incorporation of the glass cell into the UHV systems is established through a buffer chamber which is designed to bridge the gap between UHV characterization conditions and normal pressure solution-based deposition. The buffer chamber is kept at vacuum conditions (base pressure below 5×10^{-9} mbar) to introduce a sample from the UHV side. The chamber is then vented with ultra pure inert gas such as argon 5.0 or 6.0. The pressure in the buffer chamber is set in such a way that it is slightly higher than the pressure in the glass cell to allow gas flow from the buffer chamber to the glass cell. This way possible

contaminations of the UHV system are minimized. This becomes especially important during back transfer after the sample preparation because the pumping down time of the buffer chamber depends very much on solvent residues in the sample but also on the ambient gas environment. Pumping time is additionally reduced by a rough vacuum bypass from the turbo pump rough vacuum line directly to the buffer chamber. The basic components of this setup at the Clustertool are schematically represented in Figure 3.5.

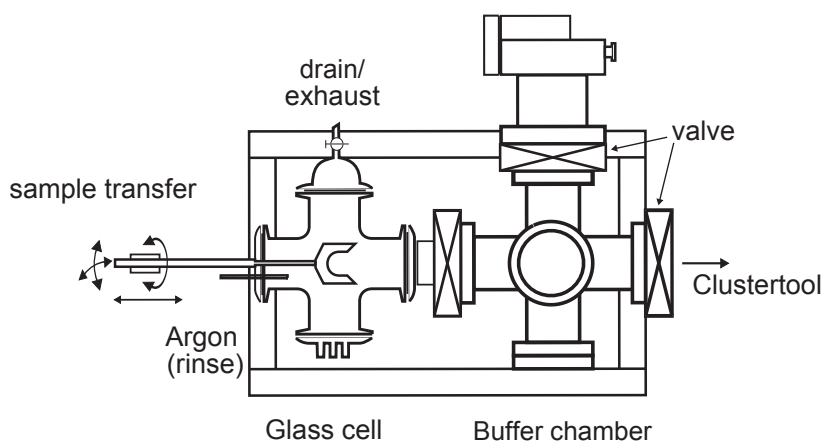


Figure 3.5: Top view of the glass cell setup as incorporated to the UHV system Clustertool in Heidelberg. The two stage chamber system is in principal equivalent to the setup used at SoLiAS in Berlin.

In principle, at least one argon gas inlet as well as a drain/exhaust structure are needed for glass cell operation. Depending on the chosen deposition technique further adjustments need to be made. For drop casting experiments a glass port inlet is required at the top position of the glass cell through which the respective solution can be deposited on the substrate. An additional argon nozzle also inserted from the top can be applied to burst the deposited liquid drop to prevent possible surface contaminations resulting from the possibly polluted outer droplet membrane. Furthermore, this argon jet is useful for removing residual solvents both from the sample as well as from the sample holder prior to transferring the sample back into UHV. For the nebulizer setup, the exhaust is moved to a side position since the nebulizer components are positioned at the bottom flange of the glass cell. An additional inlet port is installed at a side flange through which argon is led into the nebulae steering unit. The development of these components will be discussed later on (see chapter 8.1). The following sketch illustrates the individual glass cell components and their usage during the two solution-based deposition techniques discussed in this work, namely drop-casting and nebulizer deposition (Figure 3.6).

Generally, the glass cell provides much better control in terms of environmental contamination sources than a glovebox. Additionally, the gas composition in the glass cell can be tuned to the specific experimental requirements. Even an oxidizing environment could be

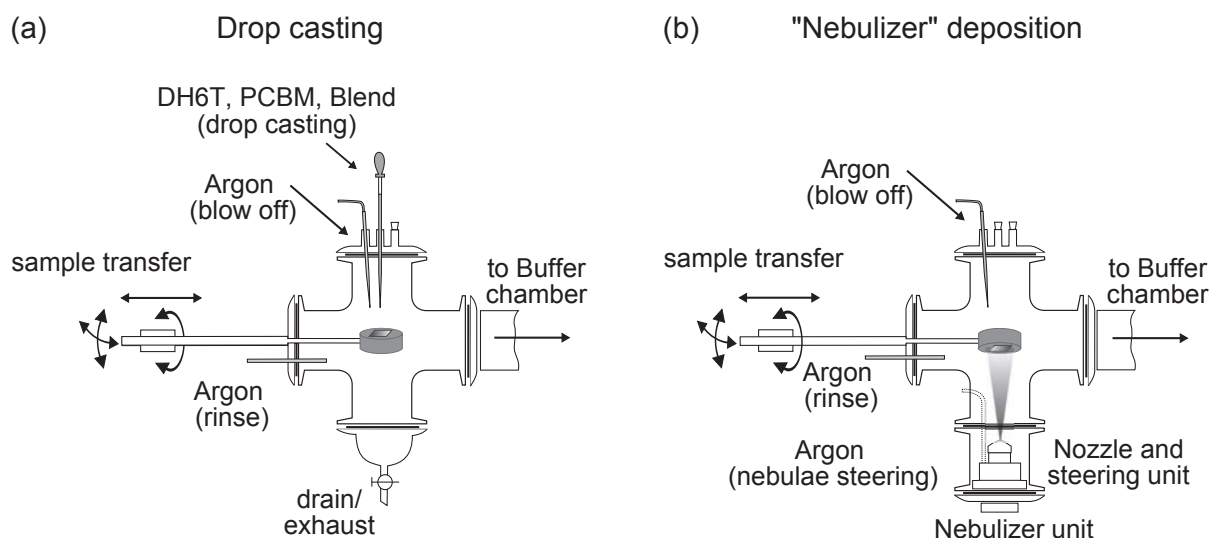


Figure 3.6: (a) The glass cell in the configuration used to perform drop casting experiments. (b) The glass cell in the configuration used to deposit solutions by the nebulizer method.

set to study degradation phenomena. However, the possibility to vary the deposition and drying conditions is limited. E.g. spin- or blade-coating is not yet possible and controlled and reproducible drying can be further optimized.

3.3 Theory of Photoelectron Spectroscopy

Photoelectron spectroscopy (PES) is a powerful, versatile, and non-destructive method for surface and interface characterization. The underlying physical principle is the photoelectric effect discovered by HERTZ in 1887. With this method, it is possible to investigate the electronic structure of surfaces and interfaces. Additionally, information on the chemical composition as well as bonding states of individual atoms can be derived. In the field of organic electronics the method is routinely applied as it provides information about the energetic position of frontier electronic orbitals which are involved in charge transfer processes. Detailed descriptions of the processes, instrumentation, and spectral information can be found e.g. in references [81], [83], [84], and [85].

3.3.1 Working Principle

Through the irradiation of a sample with high energy photons, an electron can be removed from a bound state. As the photoemission process is an elastic scattering process the energy

of the photon is transferred completely to the excited electron. If the energy of the incident photon ($h\nu$) is sufficient to overcome the binding energy of the electron E_{bind} as well as the work function ϕ of the sample the electron can leave the sample with a certain kinetic energy E_{kin} . The basic equation describing this process is:

$$E_{\text{kin}} = h\nu - E_{\text{bind}} - \phi_{\text{sample}}. \quad (3.1)$$

As sample and spectrometer are in electrical contact the Fermi levels are aligned which results in a contact potential. This is the difference between the work function of the sample (ϕ_{sample}) and the work function of the spectrometer (ϕ_{spec}). The emitted electrons have to overcome this potential difference and thus have a kinetic energy according to equation 3.2 when they reach the detector:

$$E_{\text{kin}} = h\nu - E_{\text{bind}} - \phi_{\text{sample}} + (\phi_{\text{sample}} - \phi_{\text{spec}}) = h\nu - E_{\text{bind}} - \phi_{\text{spec}}. \quad (3.2)$$

The kinetic energy of the detected electrons is therefore independent of the sample work function. The reference point for the binding energy is the Fermi level (E_{F}) which is at 0 eV per definition. Therefore, the work function of the spectrometer can be directly determined with the help of a metallic sample.

The photoelectron spectrum is generated by detecting the emitted electrons according to their kinetic energy and counting their intensity. The binding energy is then calculated via equation 3.2. The discrete and characteristic emissions from core or valence levels are superimposed by a diffuse background which rises with decreasing kinetic energy. This background is caused by inelastically scattered and secondary electrons. In addition to photoelectrons Auger electrons can leave the sample. These electrons are the result of a non-radiative decay process in which the photohole is filled by an electron from a higher shell and the excess energy is then transferred to an additional electron which can then leave the sample. The energy of this electron is independent of the incident photon energy. Both the photoemission process as well as the Auger process are schematically represented in Figure 3.7.

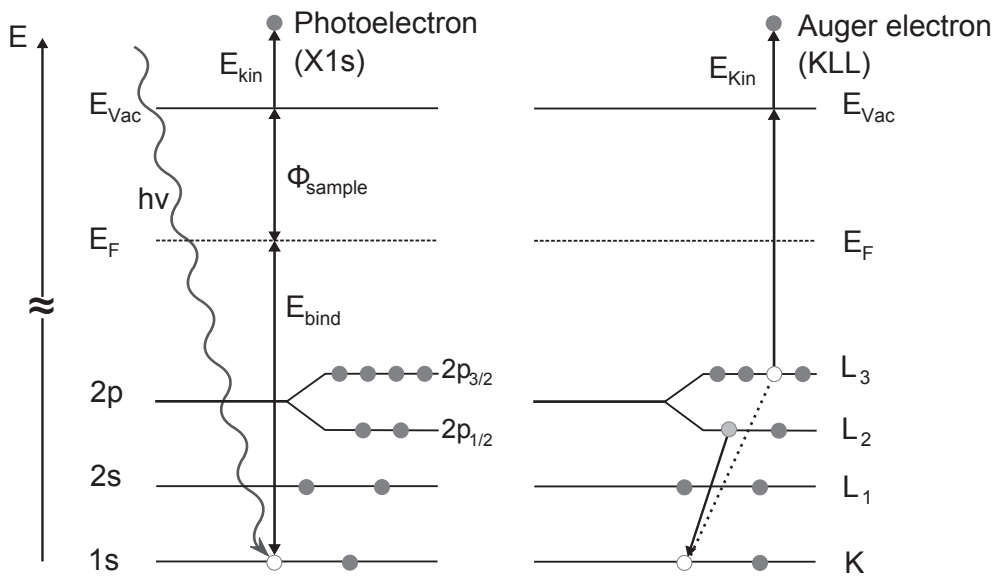


Figure 3.7: (left) Schematic representation of the photoemission process. The incident photon excites an electron from the 1s core shell to an unbound state above the vacuum level (E_{Vac}). (right) Schematic representation of the Auger process. The photohole in the K shell is filled by an electron of the L2 sub shell and the resulting energy is transferred to an electron in the L3 sub shell which then leaves the sample.

Photoelectron spectroscopy is a surface sensitive probing technique. The information depth is usually limited to a range of several Ångströms up to few nanometer. It is determined by the excitation energy which in turn governs the mean free path of the photogenerated electrons within the sample. The penetration depth of the incident photons is much larger than the escape depth of the electrons. The correlation of the kinetic energy and the mean free path of the photoelectrons (λ) within the material is depicted in Figure 3.8. The kinetic energies resulting from the excitation energies used in this work are marked. The overall probing depth is determined as low as 3λ .

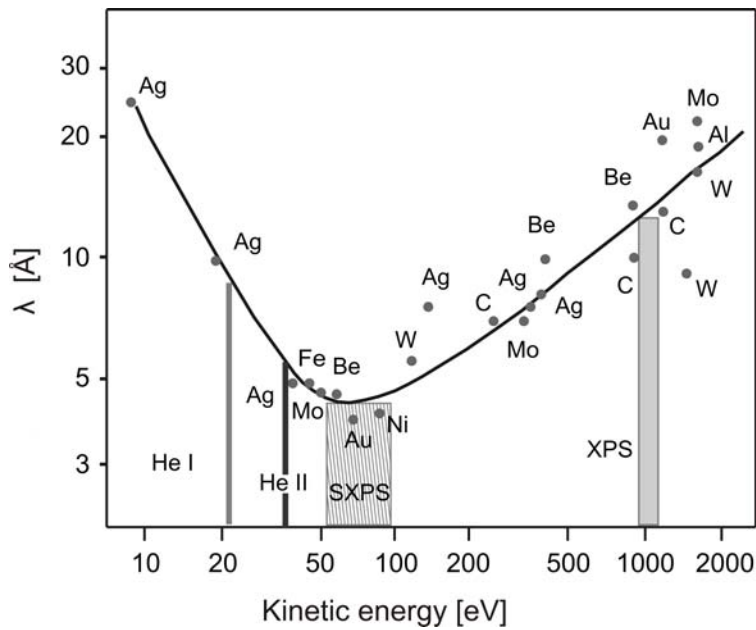


Figure 3.8: Relation between mean free path λ and the kinetic energy of the emitted photoelectrons within the material. The approximate kinetic energies (energy regions) resulting from the photon sources used are indicated.

3.3.2 Instrumentation

Depending on the used excitation source three types of photoelectron spectroscopy will be applied in this thesis: synchrotron-induced photoelectron spectroscopy (SXPS), x-ray photoelectron spectroscopy (XPS), and UV photoelectron spectroscopy (UPS). The basic components of a photoelectron spectrometer are the photon source, the sample, the electron energy analyzer, and the detector (Figure 3.9).

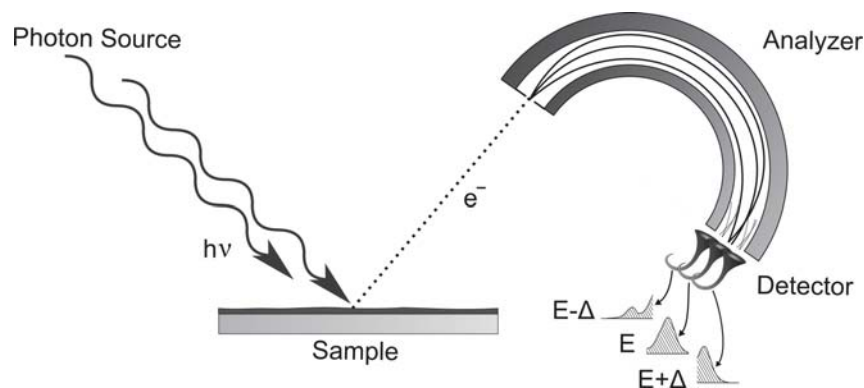


Figure 3.9: Schematic representation of the basic components of a photoelectron spectrometer. The light is generated in the photon source and hits the sample where electrons are emitted. These electrons are separated according to their kinetic energy in the analyzer and finally counted in the detector.

Radiation Sources

SXPS offers the unique possibility of tuning the excitation energy. At the undulator beam line U49/PGM-2 at BESSY II at the Helmholtz Zentrum Berlin, where all SXPS experiments presented in this work were performed, the energy can be varied from 86 eV to 1890 eV. From the continuous spectrum of synchrotron radiation a certain light energy can be chosen according to the electronic level of interest. The optimal excitation energy was determined according to the photoionisation cross section, the possible overlap with Auger lines and maximum surface sensitivity. The high intensity of synchrotron radiation furthermore improves the signal-to-noise ratio. The drawback of the high flux density, however, is the increased probability of radiation induced changes in the material. As the probing depth depends on the kinetic energy of the photoelectrons within the material (see section 3.3.1), the variation of the excitation energy additionally provides a possibility to achieve thickness-dependent information in a non-destructive manner.

The photoelectron spectrometer at the Clustertool in Heidelberg is equipped with a monochromatized scanning micro focused x-ray source for XPS. In this configuration an aluminum cathode is used giving an x-ray energy of 1486.6 eV with a line width of about 0.4 eV. Due to the focused x-ray beam, micro area spectroscopy with x-ray spot sizes from $10\ \mu\text{m}$ to $200\ \mu\text{m}$ can be achieved. Additionally, the x-ray beam can be scanned over the sample surface which allows large area analysis of up to 0.5 mm. In the presented measurements the typical x-ray spot size on the sample is about $200\ \mu\text{m}$ which also defines the analysis area as there are no additional area definition apertures before the input lens of the VersaProbe's analyzer [86]. For UPS characterizations a cathode capillary discharge lamp operated with helium is installed. Depending on the operating conditions two excitation energies can be achieved: For higher pressures and moderate currents the He line of the neutral atom (He I) at an energy of 21.22 eV dominates. By increasing the current and at the same time reducing the pressure the emission of singly charged ions (He II) increases giving photons with an energy of 40.8 eV.

Analyzer

The emitted photoelectrons are separated according to their energy using a concentric hemispherical analyzer. It consists of two concentric half spheres with radii R_1 and R_2 , on which a potential ΔV is applied. Electrons that enter the analyzer are deflected by this

potential and forced on a circular path. If their energy is equal to the pass energy E_{pass} they travel through the analyzer on the equipotential surface. The pass energy is determined by the analyzer radii and the applied potential

$$E_{\text{pass}} = \frac{e\Delta V}{\left(\frac{R_2}{R_1} - \frac{R_1}{R_2}\right)}. \quad (3.3)$$

To achieve data acquisition with constant relative resolution a complex lens system is usually inserted between sample and analyzer which selects and focuses the electrons as well as retards them to a constant potential. This operation mode is called constant analyzer energy (CAE) mode and the relative resolution (R) is then given by:

$$R = \frac{\Delta E_d}{E_{\text{pass}}} = \frac{W}{2R_0} + \frac{\alpha^2}{4}, \quad (3.4)$$

with

ΔE_d	FWHM (full width at half maximum), i.e. absolute resolution
E_{pass}	pass energy (in CAE mode)
W	width of the entry slit
R_0	radius of equipotential surface
α	acceptance angle of the analyzer.

Detector

For the detection of the electrons multi channel detectors are used both at SoLiAS as well as at the Clustertool. The respective detectors are based on channeltrons which have the task of enhancing the individual electron signal through a cascade process. The advantage of multi channel detectors is that not only the electrons exactly at the pass energy can be detected but also those with slightly higher or lower energy (schematically included in Figure 3.9). Thus, the count rate is increased and the measurement time is decreased.

3.3.3 Data Evaluation

Prior to any data evaluation, the binding energy is calibrated with respect to a silver standard. In XPS the data is given in binding energy with the values of measured kinetic

energy already transformed to a binding energy scale using a measurement software inherent spectrometer work function. Calibration is then achieved by shifting the binding energy values according to the measured shift in Fermi level (for low binding energy orbitals such as valence levels) and Ag3d level (for higher binding energy levels such as core levels). As these shifts depend on the pass energy and measurement conditions, the calibration measurements include the same spectrometer operation modes as chosen for data acquisition, that is XPS (at $E_{\text{pass}} = 11.875$ eV), He I (at $E_{\text{pass}} = 2.95$ eV) and He II (at $E_{\text{pass}} = 5.85$ eV) as well as He I under bias conditions (at $E_{\text{pass}} = 0.585$ eV and -2.5 V sample bias) for determining the secondary electron cutoff (SE cutoff).

At BESSY all raw data are given in kinetic energy scale. Therefore, the calibration can be done simultaneously with converting kinetic energy to binding energy. At every excitation energy the position of the Ag Fermi edge is determined in kinetic energy. This value is inserted in equation 3.2 thus converting the energy scale with respect to the actual Fermi level position.

Core Level

The core level peaks provide valuable information: From the binding energy and the relative intensities the chemical species can be identified and their relative concentration can be determined. The binding energies in general are characteristic for the different atoms. From the line shape the type of orbital can be determined because p, d, and f-orbitals are split into doublets due to a final state effect caused by the interaction of the spin of the remaining unpaired electron (s) with the orbit spin (l). The resulting overall spin (j) is obtained through vectorial addition of s and l :

$$j = l \pm s, \quad (3.5)$$

$$\text{with } l = \dots - 2, -1, 0, 1, 2, \dots \quad \text{and} \quad s = \pm \frac{1}{2}.$$

For s-orbitals l equals 0 therefore no splitting is observed. Due to the degeneracy of the different states given by $2j + 1$ the intensity ratio of the doublet peaks is characteristic for each subshell. Thus every measured emission can be identified unambiguously. This

includes all elements at concentrations above approximately 0.1 atomic % except hydrogen and helium [84]. The nomenclature of photoemission lines is given by Xnl_j with X being the elemental symbol, n being the principal quantum number, l being the orbital quantum number and j being the total angular momentum quantum number. Auger lines are labeled according to the X-ray notation (compare to Figure 3.7).

The energetic position of the photoemission lines is sensitive to changes in the surrounding potential. It can be an overall potential as an applied external potential or a potential change due to charge transfer doping. This will lead to a general shift of all peaks in the same direction and with the same magnitude. But also local potential changes influence the peak position. Changes in the outer electronic shells, i.e. when atoms take part in a chemical bond, affect the core level position resulting in a so called chemical shift. Thus, from the exact binding energy local bonding sites of different atoms of the same element can be distinguished. However, these shifts are relatively small for many elements involved in organic materials and individual components resulting from different bonding sites may overlap for the measured peak widths. Therefore, the obtained complex envelope of a core level emission can only be decomposed into the constituting peaks by fitting routines. To achieve consistent and feasible results, this process requires knowledge about line and background shapes.

Before starting the fitting routine a background correction is applied. In most cases a Shirley background function [87] can be applied giving physically reasonable results. This background function is based on the assumption that the background intensity for a specific binding energy is proportional to the intensity of elastically scattered electrons (i.e. the peak area above the background) at lower binding energies. In some cases a Tougaard background [88] might be applicable but also straight line backgrounds as well as polynomial functions have their justification in certain cases. If not specified differently a Shirley background has been used in the course of this work. The line shape is governed by the different excitation and detection processes. As in all radiative decay processes the line shape of the aluminum $K\alpha$ line is Lorentzian. The broadening due to the spectrometer is Gaussian and the natural core level line shape again is essentially Lorentzian. For metallic samples an asymmetric tailing towards higher binding energies is observed. In any case, the core level line shape is a complex convolution of Gauss and Lorentz shapes. Therefore, all lines are fitted with Voigt profiles which are implemented in the software package IGOR-pro4 (used in this work). In XPSPeak 4.1 (free ware) these are approximated by pseudo

Voigt functions ($V_{\text{pseudo}}(E)$, Gauss Lorentz sum functions) with tunable Gauss Lorentz ratio based on the following expression:

$$V_{\text{pseudo}}(E) = h \left(\underbrace{m \cdot \exp[-4 \ln(2) \cdot x^2]}_{\text{Gauss}} + (1 - m) \cdot \underbrace{\frac{1}{(1 + 4x^2)}}_{\text{Lorentz}} \right), \quad (3.6)$$

$$\text{with } x = \frac{(E - E_0)}{w}.$$

$V_{\text{pseudo}}(E)$	intensity at energy E
h	peak height
E_0	peak center
w	peak width
m	mixing ratio (1 = pure Gaussian, 0 = pure Lorentzian)

The Gauss Lorentz ratio is largely determined by instrumental parameters but during the fitting routines might be calculated to unreasonable values to compensate for wrongly chosen intensities. Therefore, this ratio is usually fixed within a physically plausible range of Gauss:Lorentz > 70% [85]. Additionally, certain guidelines or if necessary constraints were applied to achieve consistent and both chemically as well as physically acceptable fitting results. For instance the number of peaks and their relative intensities were chosen according to the chemical structure of the molecule or polymer repeat unit. The assignment of the different species on the binding energy scale, i.e. which component has the highest/lowest binding energy was estimated by considering electronegativity (EN) differences. This first approach to classify the different molecular components is relatively crude but with respect to the achieved resolution in photoelectron spectroscopy it is quite useful and allows for consistent and reproducible peak assignment. It needs to be noted, that this approach is based on initial state effects only and does not consider final state effects. Additionally, starting values for chemical shifts, i.e. the energy difference between the individual components, are taken from literature [85, 89]. If any of the fitting parameters obtained a value outside physically reasonable limits the respective value was fixed to a more reasonable value.

Additional core level features are so called shake-up and shake-off satellites. The shake-up contribution originates from the excitation of valence electrons into excited bound states. This results in defined energy losses thus giving rise to distinct intensity maxima on the high binding energy site. In the shake-off process a valence electron is excited into an

unbound state above the vacuum level. Since the involved states there are continuous no discrete features are observed but rather a step-like intensity increase on the high binding energy side of the main emission. The total energy range in which shake structures are observed is usually up to around 15 eV to 20 eV [81]. This in turn can make their interpretation rather difficult because in the same range inelastic scattering leads to a broad and extended intensity increase and sometimes the shakes coincide with components with a high chemical shift. However, the first shake-up satellite in organic materials stems from the $\pi \rightarrow \pi^*$ transition which is a measure for the HOMO-LUMO gap in the material [81].

By comparing the relative intensities (i.e. peak areas after background subtraction) of the different elemental contributions the composition of the sample can be calculated (with an accuracy of $<\pm 10\%$) [84, 90]. The intensity of a photoemission line depends on several parameters:

- (i) the concentration of the respective element in the probed volume element (n_i)
- (ii) the mean escape depth of the photoelectron ($\lambda(E)$)
- (iii) the photoionisation cross section of the probed orbital ($\sigma(E)$)
- (iv) the primary photon intensity
- (v) geometry factors such as the angular dependence of the photoelectron emission
- (vi) spectrometer parameters such as transmission function and detection efficiency.

For XPS experiments performed with the PHI VersaProbe system, the relative concentrations can be readily determined with the help of tabulated atomic sensitivity factors (ASF) [89] which already include the ionization cross section, the detection efficiency, and the transmission function. For the relative concentration of element A (n_A) in a homogeneous sample follows:

$$n_A = \frac{\frac{I_A}{ASF_A}}{\sum_i \frac{I_i}{ASF_i}}. \quad (3.7)$$

For synchrotron measurements the determination of relative concentrations is more complicated as the photoionization cross section is asymmetrically distorted for linearly polarized light. YEH and LINDAU calculated the photoionization cross sections including an energy dependent asymmetry parameter $\beta_{nl}(E)$ [91]. Following the detailed derivation

from [92], the cross sections applicable to measurements at the SoLiAS can be obtained from:

$$\sigma'_{nl}(E) = \sigma_{nl}(E) \cdot e^{\left[\frac{1}{32} \left(2 + \left[\frac{1}{2} + \frac{3}{\pi}\right] \beta_{nl}(E)\right)\right]}. \quad (3.8)$$

Since only relative intensities of peaks obtained in the same setup are compared, the parameters (iv) - (vi) can be neglected as they effect the measurements in the same way. The mean escape depths of the emitted electrons at a certain kinetic energy are be calculated with the NIST ELECTRON INELASTIC-MEAN-FREE-PATH DATABASE [93] where the calculation algorithm TPP-2M [94] is implemented. Thus, the relative concentration of element A (n_A) for synchrotron measurements is calculated according to:

$$n_A = \frac{\frac{I_A}{\sigma'_A(E) \cdot \lambda_A(E)}}{\sum_i \frac{I_i}{\sigma'_i(E) \cdot \lambda_i(E)}}. \quad (3.9)$$

As Lambert Beer's law also applies on the damping of a substrate emission line through an adsorbate layer this layer thickness can be determined from the substrate peak intensity decrease. This technique is applied to calculate deposition rates in evaporation experiments where no quartz micro balances were available to estimate film thicknesses for ultra-thin films. For the substrate intensity ratio before (I_{sub}^0) and after the deposition step (I_{sub}) follows

$$\frac{I_{sub}}{I_{sub}^0} = \exp\left(-\frac{d}{\lambda(E) \cdot \sin(\alpha)}\right), \quad (3.10)$$

where $\lambda(E)$ is the mean free path of the electron at the core level specific energy E and α is the angle between the sample surface and the analyzer.

Vice versa it is possible to obtain the same information about layer thicknesses by considering the adsorbate intensity increase:

$$\frac{I_{ads}}{I_{ads}^\infty} = 1 - \exp\left(-\frac{d}{\lambda(E) \cdot \sin(\alpha)}\right). \quad (3.11)$$

In this case I_{ads} is the integral intensity of the adsorbate at a certain thickness and I_{ads}^{∞} is the intensity at complete coverage. Both calculations only work for thin films where substrate emissions are still visible, which means that in the case of evaporation experiments larger film thicknesses are extrapolated by using the determined deposition rates. Additionally, only nominal layer thicknesses are obtained as these equations are based on the assumption of homogeneous substrate coverage which is not always the case.

Valence Level

The valence levels provide important information about electronic properties. The electrons with the highest kinetic energy originate from the highest occupied states. For metals this is the Fermi level, for semiconductors it is the valence band maximum and in the case of organic semiconductors it is the highest occupied molecular orbital. The valence spectra more or less image the density of states of bound electrons superimposed by a background caused by secondary electrons. At a kinetic energy of 0 eV (which corresponds to the maximum measured binding energy that in turn is governed by the incident photon energy) the secondary electron spectrum caves in since these electrons have no energy left to overcome the sample work function. Therefore, from the difference of this so called secondary electron cutoff (SE cutoff) to the excitation energy the work function of the sample can be directly deduced from equation 3.12:

$$E_{\text{kin}} = 0 \quad \Rightarrow \quad \phi_{\text{sample}} = h\nu - E_{\text{bind}}(\text{SE cutoff}). \quad (3.12)$$

The relation between the energy levels in the sample and the energy distribution of the photoelectrons for UPS for a Silver sample is schematically represented in Figure 3.10 a.

The evaluation of UPS data as conducted in the course of this work is exemplified in Figure 3.10 b and c for a PCBM sample. The work function is determined by approximating the SE cutoff by a straight line and taking the intersection of this line with the x-axis as the $E_{\text{bind}}(\text{SE cutoff})$. This process is implemented in the IGORpro software. The $\text{HOMO}_{\text{onset}}$ position is determined by a linear fit of the leading edge of the spectrum.

Since the $\text{HOMO}_{\text{onset}}$ position is taken as a measure for the highest occupied states and for the determination of the ionization potential as well as the photoemission gap (see

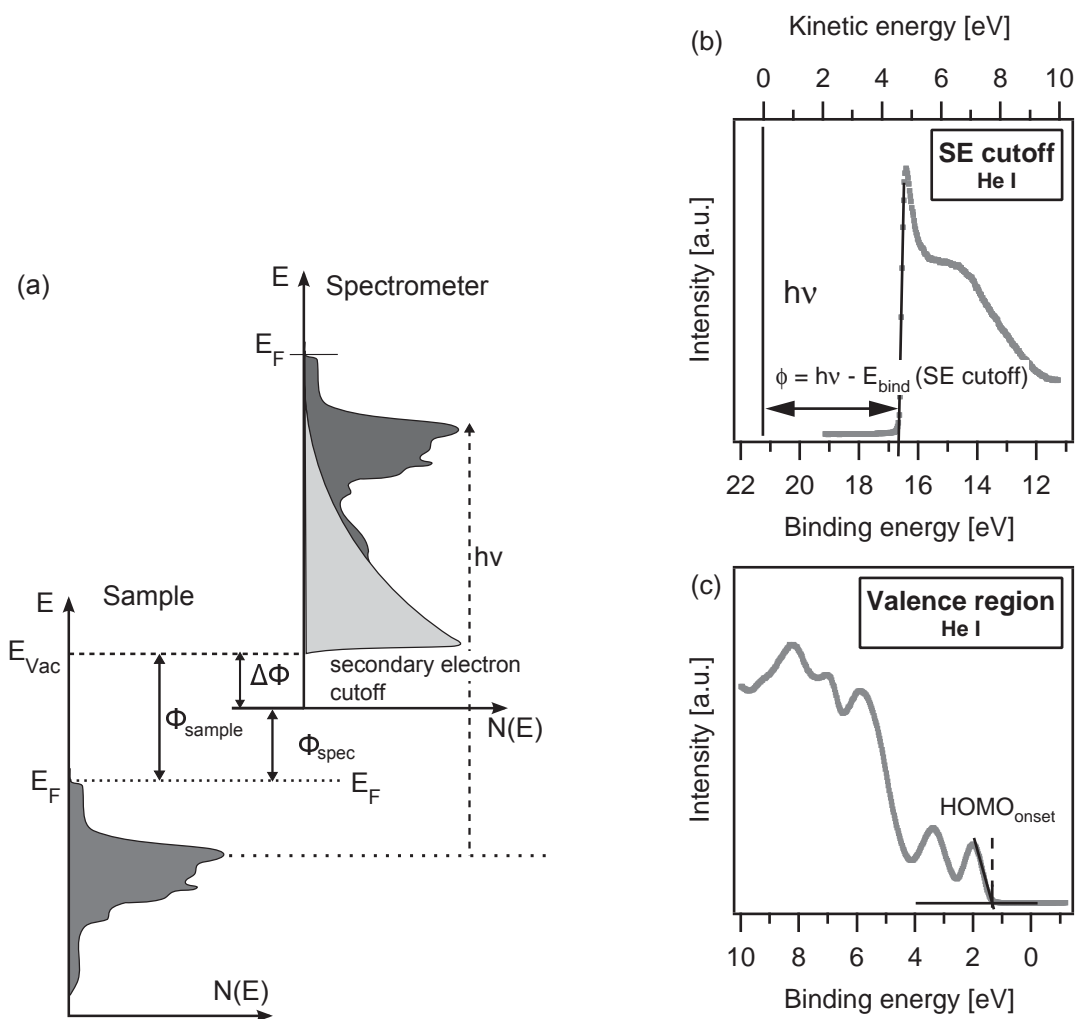


Figure 3.10: (a) Schematic representation of the energy levels within the sample and the photoelectron energy distribution in the spectrometer for UPS for a silver sample. The evaluation of the obtained valence level is shown in (b) for the secondary electron cutoff and in (c) for the HOMO_{onset} position. In case of the SE cutoff (b) the kinetic energy scale is included at the top for direct comparison.

Chapter 2) instrumental effects need to be discussed as the instrumental broadening could affect the accuracy of determining the position of the HOMO_{onset}. A measure for this broadening is the width of the Fermi edge of a freshly cleaned metal sample. Just due to thermal broadening the inherent width of the Fermi edge corresponds to about $4k_B T$. This gives a value of 100 meV at room temperature. The width of the Fermi edge of a sputter cleaned Ag sample at the VersaProbe system under He I conditions is in the range of 140 to 150 meV. This value corresponds to the width of a Gauss profile which is convoluted to the Fermi function during the fitting routine. A measured Silver Fermi edge

for He I excitation including a fit is shown in Figure 3.11. The determined $\text{HOMO}_{\text{onset}}$ position is influenced by half the difference between the instrumental and the thermal broadening (i.e. 20 to 25 meV). However, the absolute precision and reproducibility with which this value can be determined is about ± 50 meV which is well above possible effects of instrumental broadening on the measured position.

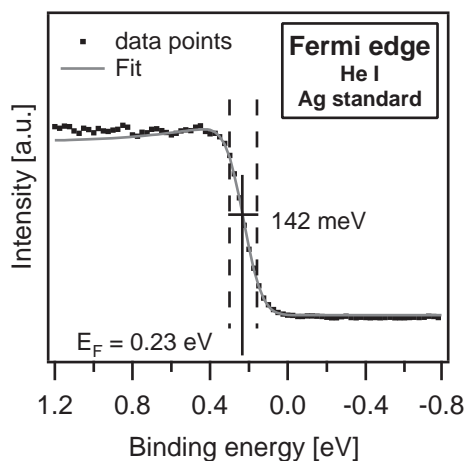


Figure 3.11: Silver Fermi edge as measured under He I conditions (dotted line) and the corresponding fit (solid gray line).

Additionally to He I also the He II line can be used to determine valence features. Besides possible effects on photoionization cross sections, an advantage is the lower secondary electron background but the generally much lower intensity also requires increased measurement time. Furthermore, for He II the satellite emissions of the β and γ lines are much more pronounced than in the case of He I. Therefore these are subtracted before the evaluation of the He II spectra is conducted. For the difference spectra only the first satellite line (He II β) is considered which leads to a signal shifted by 7.56 eV at an intensity of about 10% of the original spectrum.

3.4 Further Characterization Methods

3.4.1 Contact Angle Measurements

Theory

If a liquid drop hits a smooth solid surface, this is not an equilibrium situation. In principle, two limiting cases can be observed: The droplet will spread until it reaches a finite contact angle in the case of partial wetting or until ideally a monomolecular film is formed in the case of complete wetting. The extreme case of partial wetting is perfect non-wetting.

These three wetting situations with the characteristic contact angles is shown in Figure 3.12 [95].

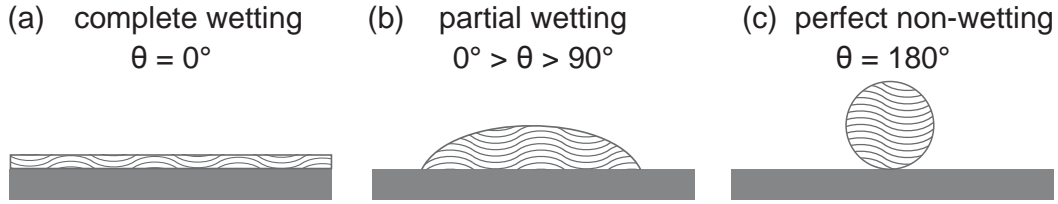


Figure 3.12: (a) Complete wetting, i.e. film formation. (b) Partial wetting. (c) Perfect non-wetting.

The degree of wetting is determined by the interplay between adhesive and cohesive forces. The adhesive forces between the liquid and the solid lead to a spreading of the liquid. The cohesive forces within the liquid cause the droplet to reduce its interface with the solid by taking a more spherical shape. A measure for the wetting ability is the contact angle θ (Figure 3.13).

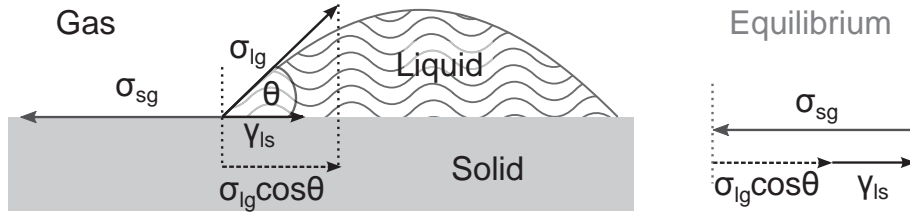


Figure 3.13: Schematic representation of the three phase contact of a liquid droplet on a solid surface. The contact angle θ results from the interplay of the surface tension between the solid and the gas phase σ_{sg} , the surface tension of the liquid at the liquid/gas surface σ_{lg} and the interface tension at the solid/liquid interface γ_{ls} .

The smaller the contact angle is, the better is the wetting. The contact angle is the result of the effects of three vectors describing the specific surface respectively interface tensions [95]:

$\vec{\sigma}_{sg}$: vector of the surface tension of the solid surface at the solid/gas surface

$\vec{\sigma}_{lg}$: vector of the surface tension of the liquid at the liquid/gas surface

$\vec{\gamma}_{ls}$: vector of the interface tension at the solid/liquid interface

According to the parallelogram of forces (see Figure 3.13 right) follows the Young equation 3.13:

$$\sigma_{sg} = \gamma_{sl} + \sigma_{lg} \cos \theta . \quad (3.13)$$

According to Owens, Wendt, Rabel, and Kaelble (OWRK), the total surface tension can be written as the sum of polar interactions (σ^P) and unpolar or dispersive interactions (σ^D) [96]:

$$\sigma = \sigma^D + \sigma^P. \quad (3.14)$$

The polar and dispersive components of the surface tension can now be used to describe the adhesion energy (β), which is gained when the interface between two phases A and B is formed using the geometric mean:

$$\begin{aligned} \gamma_{A,B} &= \sigma_A + \sigma_B - \beta, \\ \gamma_{A,B} &= \sigma_A + \sigma_B - 2 \left(\sqrt{\sigma_A^D \cdot \sigma_B^D} + \sqrt{\sigma_A^P \cdot \sigma_B^P} \right). \end{aligned} \quad (3.15)$$

Considering that the surface tension of the liquid phase as well as the solid phase can be divided into a dispersive and polar component, one obtains

$$\gamma_{sl} = \sigma_s + \sigma_l - 2 \left(\sqrt{\sigma_s^D \cdot \sigma_l^D} + \sqrt{\sigma_s^P \cdot \sigma_l^P} \right), \quad (3.16)$$

which then can be combined with the Young equation (3.13) eliminating γ_{sl} :

$$\sigma_s - \sigma_l \cos \theta = \sigma_s + \sigma_l - 2 \left(\sqrt{\sigma_s^D \cdot \sigma_l^D} + \sqrt{\sigma_s^P \cdot \sigma_l^P} \right). \quad (3.17)$$

This can be written in the form of a universal linear equation $y = m \cdot x + b$ resulting in:

$$\underbrace{\frac{(1 + \cos \theta) \cdot \sigma_l}{2\sqrt{\sigma_l^D}}}_y = \underbrace{\sqrt{\sigma_s^P}}_m \cdot \underbrace{\sqrt{\frac{\sigma_l^P}{\sigma_l^D}}}_x + \underbrace{\sqrt{\sigma_s^D}}_b. \quad (3.18)$$

Now, the surface energy of a solid can be deduced from the linear regression from contact angle data of multiple liquids (with known polar and dispersive surface energy components). The polar component of the surface energy of the solid can be deduced from the

slope m while the dispersive component is obtained by squaring the ordinate intercept b [96]. The total surface energy of the solid can then be determined according to equation 3.14.

To determine the surface energy of a liquid, a tensiometer can be used. In the plate method the liquid which is to be characterized is raised in a special sample container until contact between the surface with the plate is registered. From the force which is exerted on the wetted length of the plate the surface tension can be calculated according to equation 3.19 [96]:

$$\sigma = \frac{F}{L \cdot \cos \theta}, \quad (3.19)$$

with

- σ surface tension
- F force acting on the balance
- θ contact angle.

Wetting Envelope

The wetting envelope is a special representation of the relation between contact angle and the polar and dispersive contributions of the surface tension of a solid. It allows to predict if a certain liquid with known polar and dispersive surface energy components can wet the respective solid completely.

To calculate the wetting envelope the above described method to determine the surface energy of a solid is reversed. The polar and dispersive surface energy contributions from the solid need to be known either from literature or from measurements. It is then calculated for which polar/dispersive surface energy ratio $\cos \theta$ equals one (which describes complete wetting). From the plot of the value pairs of the polar and dispersive part of the surface energy giving $\cos \theta = 1$ a curve which originates at $(0,y)$, exhibits a maximum and ends on the x-axis again is described. The area enclosed by this curve is the wetting envelope meaning that all liquids whose surface energy data lies within the area wet the respective solid [96].

Instrumentation

The contact angle measurements have been performed in the course of the diploma work of C. Scichocki. The data was obtained using a Krüss DSA 100 setup followed by data evaluation according to the presented method of OWRK.

The method is based on a static droplet. The droplet is generated before the measurement and does not change in volume during the measuring time. However, this does not mean that the contact angle is constant, since time-dependent changes due to evaporation, migration of the droplet, chemical reactions or dissolving processes might take place. An advantage of this method is, that the droplet is not in contact with the deposition needle any more allowing a better angle determination as the complete droplet shape can be considered.

The characterization of the surface tension of the solvent and the solutions were performed with a Krüss tensiometer K100C-MK2. For the plate method, a Teflon substrate, which only has a dispersive surface tension component of 19 mN m^{-1} [97] was used.

3.4.2 Infrared Spectroscopy

Infrared (IR) spectroscopy probes molecular vibrations which are excited by the infrared part of the spectrum. A requirement for the IR activity of a vibrational mode is a change in the dipole moment during the vibration. Additionally, electronic transitions in molecules can be excited with IR photons.

The energy scale in IR spectra is usually given in wave numbers $\tilde{\nu}$, which gives the number of waves of the IR radiation per centimeter. The unit is therefore cm^{-1} . The advantage of this convention is that the wave number $\tilde{\nu}$ is proportional to the frequency (ν) and thus the energy (E) of the absorbed light:

$$\Delta E = h \cdot \nu = \frac{h \cdot c}{\lambda} = h \cdot c \cdot \tilde{\nu}, \quad (3.20)$$

with h as the Planck constant, c as the speed of light, and λ as the wave length.

Wave numbers translate to electronvolt by: $1000 \text{ cm}^{-1} \approx 124 \text{ meV}$.

Instrumentation

The IR experiments performed in this work were all acquired using Fourier-Transform-IR (FT-IR) spectroscopy run by the Surface Science and Infrared Spectroscopy group of Prof. A. Pucci (Kirchhoff-Institut für Physik, Universität Heidelberg). This is an interference technique and the spectrum is obtained via an interferogram. The basic experimental setup follows the Michelson interferometer. The complete spectrum of the radiation source is directed onto a beam splitter. Half of the radiation is reflected onto a fixed mirror while the other half passes through and gets reflected on a movable mirror. The two beams interfere at the beam splitter and subsequently pass through the sample to the detector. The detailed description for the specific spectrometer Vertex 80v (Bruker) can be found in [82]. The transformation from the interferogram to the IR spectrum is achieved via a Fourier transformation.

The advantage of the FT-IR technique is the improved signal-to-noise ratio since all intensity of the light source is used simultaneously while in the conventional grid spectrometer only small sections of the spectrum are used at a time. In general, FT-IR spectroscopy features high sensitivity, fast data acquisition and high wave number precision [98].

Spectral Features

The IR data is usually plotted as transmission (T) over wave number. Since the spectrum is largely influenced by external parameters such as the radiation source, the detector, and the optical components as well as contaminations in the optical path, a reference spectrum (T_{ref}) is measured prior to the sample spectrum (T_{sample}). The reference can either be without any sample in the light path or with the bare substrate materials. Taking the relative spectrum (T_{rel})

$$T_{\text{rel}} = \frac{T_{\text{sample}}}{T_{\text{ref}}}, \quad (3.21)$$

the external influences on the spectrum can be eliminated.

The number of possible vibrations of a complex molecule can be estimated from the number of degrees of freedom. Each of the N atoms of a molecule can move along the three independent space coordinates. Hence, the total number of vibration modes is $3 \cdot N$ minus three degrees of freedom for translational movement of the whole molecule along the x , y

and z directions as well as the three degrees of freedom for the rotation. In case of linear molecules the rotation has only two degrees of freedom. For a linear molecule follows $n = 3 \cdot N - 5$ and for a non-linear molecule $n = 3 \cdot N - 6$.

In principle, two different vibration modes can be distinguished: In a valance mode ν , the bond length changes while in a deformation modes the binding angle changes. The latter can be further divided into in plane (δ) and out of plane (γ) as well as torsion (τ) vibrations. The absorptions at higher energies (wave numbers approx. larger than 1000 cm^{-1}) are attributed to the individual functional groups of the molecule. Absorptions in the low energy region are typically vibrations of the molecular structure or larger groups (i.e. fingerprint region). The different absorption regions are schematically shown in Figure 3.14.

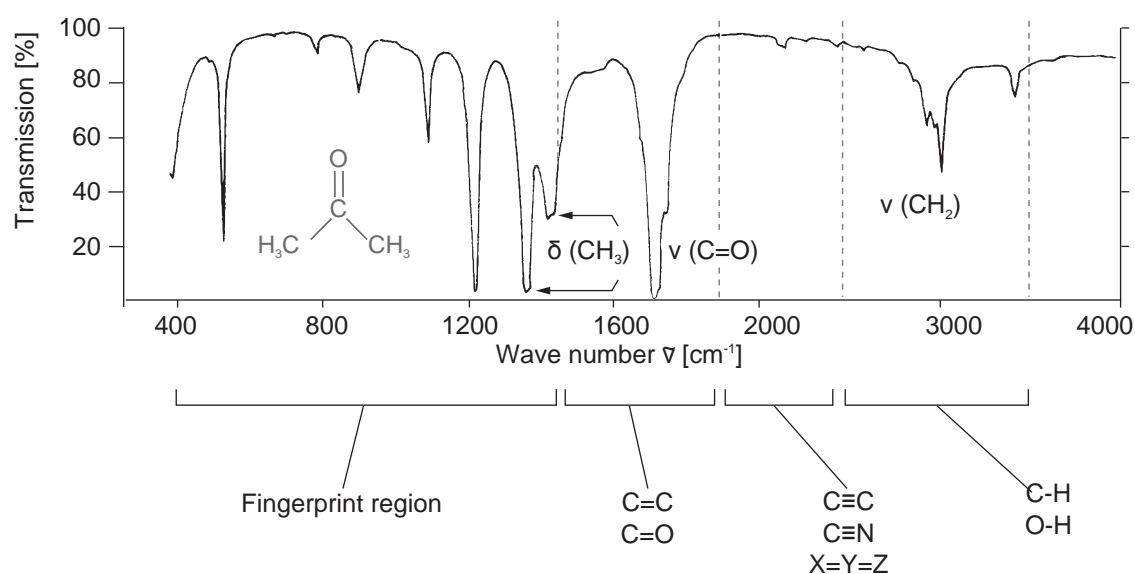


Figure 3.14: IR absorption regions schematically shown for the example of an acetone spectrum. The molecular structure of acetone is shown in the inset. Adapted from [98].

The energy of a vibrational mode depends on the binding strength of the respective bond, e.g. $\nu(\text{C}\equiv\text{C}) \approx 2200 \text{ cm}^{-1} > \nu(\text{C}=\text{C}) \approx 1640 \text{ cm}^{-1} > \nu(\text{C}-\text{C}) \approx 1000 \text{ cm}^{-1}$ [98]. These can be estimated using the anharmonic oscillator model. The intensities of the respective vibration bands hold information about bond polarity (strongly polar bonds lead to intense IR signals) as well the number of equal structure elements. In this work the assignment of the individual vibrational modes was supported by quantum mechanical calculations based on density functional theory (DFT).

3.4.3 Chemical Analysis

The following characterization techniques are routinely applied in synthetic organic chemistry for material characterization. The experimental techniques are available at Organisch-Chemisches Institut (Universität Heidelberg) and the analysis have been performed by T. Adermann (Bunz Group).

Thermogravimetric Analysis

With thermogravimetric analysis (TGA) the mass change of a sample as a function of temperature and time is measured. A TGA setup usually consists of a temperature regulated oven in which the sample is placed in a crucible which is coupled to a micro-balance. To prevent reactions with the crucible it is made from an inert material and the oven is usually kept in inert, i.e. oxygen-free, atmosphere. In this work, the material was placed in Al_2O_3 crucibles and the experiments were performed under nitrogen flow. A thermocouple is used to monitor the sample temperature during the heating process. Therefore, mass changes and temperature are registered for a given heating rate. The heating rate as well as overall times at certain temperatures can be set in advance. The mass changes can have various origins. Mass loss can be due to physical processes like evaporation or sublimation or a decomposition reaction in which volatile reaction products occur. Mass gain can be observed if for instance an oxidation takes place.

In differential scanning calorimetry (DSC) the amount of heat taken in or released by a sample during heating or cooling is recorded as a function of temperature with respect to a reference. With this technique phase transitions temperatures and the nature of these processes (i.e. endothermic or exothermic) can be characterized and quantified.

In this work, a TGA/DSC-instrument which combines both TGA and DSC features, was used to investigate the thermal behavior of PCBM simulating evaporation conditions. The setup used is a Mettler-Toledo TGA/DSC1 instrument. It is equipped with a TGA/DSC-Sensor 1100 and a Mettler-Toledo MX1 balance as well as a gas control box GC100 providing the nitrogen supply.

Ultra Performance Liquid Chromatography

Ultra Performance Liquid Chromatography (UPLC) is a chemical analysis method. It is used to separate and identify the components of a mixture or detect impurities. The underlying principle of this technique is the interaction of the dissolved sample material with a stationary phase in a separation column. This stationary phase usually consists of granular material with particle sizes in the range of $1.7\ \mu\text{m}$ [99]. The sample is provided in solution. After injection into the high-pressure chromatography system, it is diluted over the separation column using defined and fine-tuned solvent mixtures. The time the different sample components need to pass the separation column depends on the adsorption strength to the stationary phase. By adding a mass spectrometer at the end of the column the weight of the different molecular species can be determined. Thus, a chemical identification is possible.

The solvent as well as any other weakly interacting sample components or contaminations such as silicon oils will not be detected since they all will be included in the first (almost immediate) mass signal.

The experiments in this work were performed with a Waters ACQUITY H-class UPLC setup with a SQD2 single quadrupole mass detector. The ionization was performed using an atmospheric pressure chemical ionization (APCI⁻). To perform the separation of the fullerene species the chromatography conditions were based on a solvent mixture of acetonitrile and isopropanol with a linear increase of the isopropanol fraction from 40 % to 95 % in 10 min followed by a washing sequence of 3 min with a solvent flow of $0.5\ \text{ml}\ \text{min}^{-1}$. As a separation column a Waters ACQUITY UPLC BEH-C18 $1.7\ \mu\text{m}$ $2.1 \times 50\ \text{mm}$ was utilized. To achieve the successive negative ionization a source temperature of $550\ ^\circ\text{C}$, a corona voltage of $-1.5\ \text{kV}$ and a cone voltage of $50\ \text{V}$ were applied. For sample preparation, ortho-dichlorobenzene (o-DBC, puriss, p.a.) and tetrahydrofuran (THF, UPLC grade) as diluting agent were used. The injection volumes did not exceed $1\ \mu\text{l}$ for all samples containing o-dichlorobenzene.



Part I

Breaking it Down

From P3HT/PCBM to the Small
Molecular Model System DH6T/PCBM



4 Characterizing a PCBM:P3HT Bulk Heterojunction Layer

In this chapter, results of the characterization of a bulk heterojunction layer consisting of the archetypical donor:acceptor combination P3HT:PCBM are presented. First, the photoelectron spectroscopic features of the pristine materials are presented as a reference to the following experiments on blend and bilayer systems. Then, different approaches to characterize the interface of the intermixed active layer of a P3HT:PCBM bulk heterojunction solar cell are described. The chosen starting system is widely studied both electrically and electronically [19, 20] and also exemplifies the challenges one has to overcome when applying photoelectron spectroscopy on solution-processed organic semiconductors as well as mixed systems thereof. Therefore, these experiments are the starting point and motivation for the experiments in the later chapters.

4.1 PCBM

A layer of the electron acceptor Phenyl-(C61)-butyric acid methyl ester (PCBM) was prepared via spin-coating using a 20 mg ml^{-1} solution in chlorobenzene. As substrate material solvent-cleaned and ozone-treated ITO was used. The spin-coating process was performed in a nitrogen glovebox directly attached to the UHV Clustertool in Heidelberg (see Figure 3.4). The spin-coating parameters were 800 rpm for 60 s. The layer was annealed at 120°C for 5 min as this is a common process step in bulk heterojunction fabrication [100, 101]. The layer thickness is approximately 20 nm determined by a Dektak profilometer.

In the survey spectrum in Figure 4.1 a only carbon and oxygen features are visible as expected from the molecular structure (Figure 4.1 b). The absence of any substrate emission, e.g. the In3d at around 450 eV, shows that the prepared film is indeed in the order of 20 nm in thickness and at least within the measured spot size pinhole-free.

In the detail spectra a relative intensity scale is given to allow intensity comparison. In the O1s spectrum (Figure 4.1 c) a double structure is observed. To separate the individual

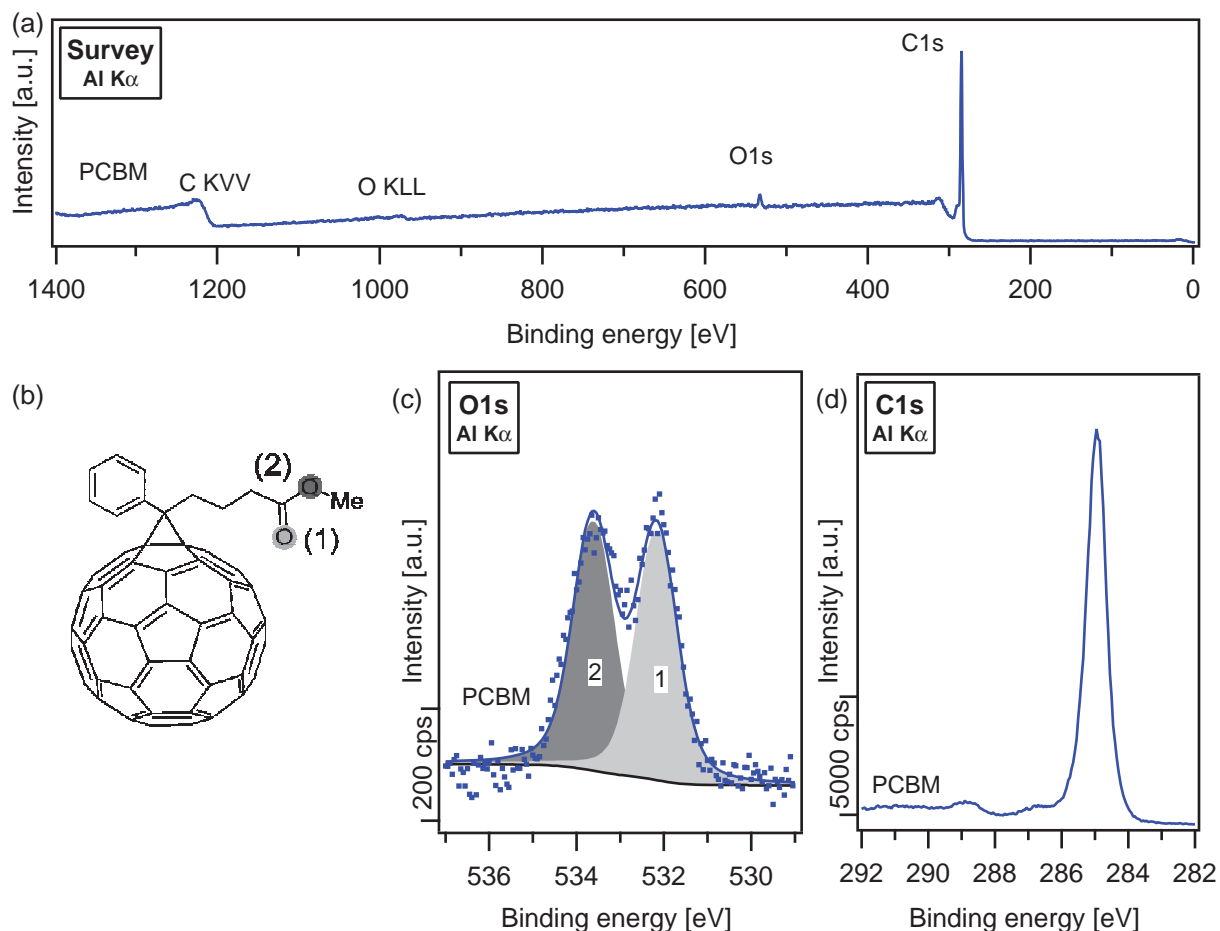


Figure 4.1: (a) survey spectrum. (b) molecular structure. (c) O1s spectrum. The original data is represented as blue dots while the fitted curve is given as a solid blue line. The constituting components are shaded in grey. (d) C1s spectrum.

emissions curve fitting using Voigt profiles was applied. In the case of the O1s emission, this results in two components of equal intensity. These can be attributed to the two oxygen bonding sites within the molecule as indicated in Figure 4.1 b. The lower binding energy component (1) at 532.2 eV is assigned the oxygen in the carbonyl group. The second component (2) at 533.7 eV originates from the oxygen in the methoxy group [24, 102]. The C1s emission is dominated by one main peak centered at 285 eV. On the high binding energy side a substructure is visible with two distinct maxima at 287 eV and 289 eV. These structures could have two possible origins: The emissions could be due to shake-up satellites or could arise from the C-O and C=O bound carbon as these are expected in this energy region [102].

Of course, also a mixture of both effects could be responsible for the increased intensity in the range of 286 eV to 290 eV. In section 5.1 a detailed assignment is attempted as differently prepared PCBM films and a C₆₀ film are compared.

From the molecular structure as shown in Figure 4.1 b a stoichiometric ratio of 1 to 36 is expected for the oxygen to carbon intensities. The obtained intensity ratio is 1:32.4 showing an overestimation of the oxygen component and/or an underestimation of the carbon signal. However, this value is still within the experimental error (about 10 % according to Ref. [90]) for quantifications in XPS. In any case, deviations could be explained by the extension of the shake-up and shake-off structure of the C1s in fullerenes. According to LEIRO ET AL. the satellite structure can extend several tens of electronvolt on the high binding energy side [103]. In the measurements presented here, only a range of up to 10 eV on the high binding energy side was recorded. The satellite structure observed in this range was of course included in the intensity calculations but the further shifted features were not. Thus, some of the C1s intensity was most likely not considered. In addition, the choice of background function is also a possible origin for the intensity deviations. In order to include as much of the satellite structure, a Tougaard background was applied on the C1s emission (according to ref. [103]).

The valence region spectra probed with UV light at $h\nu = 21.22$ eV are shown in Figure 4.2. The valence spectrum shows two distinct maxima centered at around 2 eV and 3.5 eV, respectively, and further maxima at 5.8 eV, 7 eV and 8.2 eV (Figure 4.2 b). The first emission is attributed to the HOMO and the HOMO_{onset} of PCBM is located at 1.4 eV. Together with a work function of 4.6 eV as obtained from the SE cutoff ((Figure 4.2 a) an ionization potential of 6 eV is obtained. This is in agreement to literature values (e.g. 5.96 eV in [104], 5.8 eV in [24]).

While in C₆₀ the first peak observed in UPS stems from the fivefold degenerate HOMO, in PCBM this feature stems also from five molecular orbitals but they are not degenerate any more due to the reduced symmetry of PCBM compared to C₆₀ [104]. A direct assignment is possible through the comparison with a calculated UP spectrum. This is obtained from the calculated eigenvalues of the different molecular orbitals (for a single molecule in the gas phase). The density functional theory (DFT) calculations (DFT/B97-D/TZVP) were performed by Christian Krekeler¹. The eigenvalues were shifted and scaled to fit the binding energy scale and convoluted with a Gaussian function with a width of 0.2 eV. The

¹ Institut für Hochfrequenztechnik, Technische Universität Braunschweig

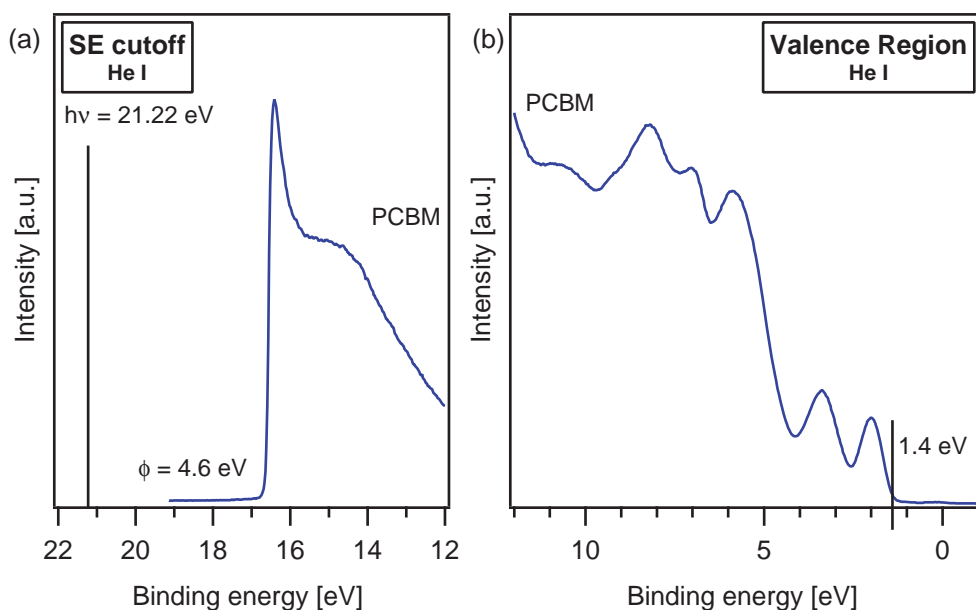
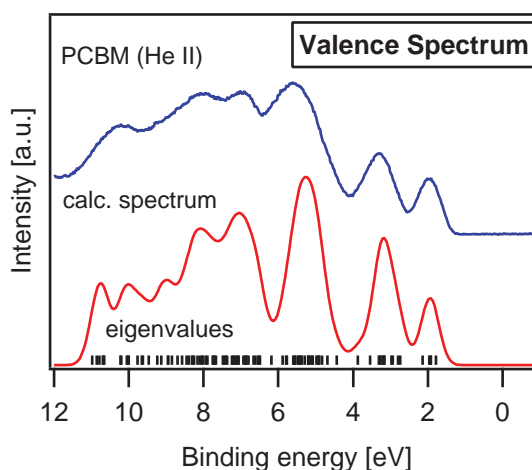


Figure 4.2: (a) Secondary electron cutoff and (b) valence region spectrum of PCBM on ITO measured at He I.

Gaussian width was chosen as a guide to the eye but also close to the measured broadening of a silver Fermi edge at He II excitation (about 150 meV). The result is compared to a He II UP spectrum (excitation energy = 40.8 eV) as this is less influenced by inelastically scattered electrons in the low binding energy region (see Figure 4.3).

Figure 4.3: The calculated valence spectrum of PCBM (red) from the DFT eigenvalues (black ticks) of the molecular orbitals is shown in comparison to a measured valence spectrum of PCBM (blue) at He II excitation. To obtain the valence spectrum, the eigenvalues were convoluted with a Gaussian function with a width of 0.2 eV and shifted and scaled to fit the UPS binding energy scale.



The general agreement between the calculated and the measured spectrum is striking. Small deviations can arise from the fact that the eigenvalues are calculated for a single molecule in the gas phase. Therefore, bulk polarization effects are not considered. Fur-

thermore, the different molecular orbitals might have different cross sections at He II excitations which can cause intensity deviations. The plotted eigenvalues again show the reduced degeneracy of the molecular orbitals responsible for the first maximum in the UP spectrum centered at 2 eV supporting the choice of the spectral onset as a measure for the HOMO.

4.2 P3HT

The P3HT layer was prepared via spin-coating on an ultrasonically cleaned ITO substrate. The concentration of the chlorobenzene solution was 10 mg ml⁻¹. The rotation speed of the spin coater was set to 800 rpm. According to bulk heterojunction fabrication procedures the film was annealed at 120 °C for 5 min [100, 101]. As no substrate emission line (e.g. the In3d at 450 eV) was visible in the XP spectra the layer thickness was determined with a Dektak profilometer to be around 50 nm.

The survey spectrum is given in Figure 4.4 a. All P3HT characteristic emissions are indicated and besides the expected carbon and sulphur components (compare molecular structure in Figure 4.4 b) no other emissions could be detected indicating contamination-free sample preparation within the detection limits of XPS. Detail spectra of the C1s as well as the S2p core level emission are given in Figure 4.4 c and d.

The C1s emission clearly shows an asymmetric structure with a shoulder on the low binding energy side which indicates several chemically different carbon bonding sites in P3HT. To separate the individual emissions according to their chemical state in the monomer unit, curve fitting was applied. However, the assignment was not straight forward and the assumptions made are briefly summarized in a working hypotheses developed in the course of this work. The following assignments will be based on this model.

4.2.1 Working Hypotheses for Peak Assignment

The aim of the model is to use the basic concepts of electronegativity and mesomeric as well as inductive effects to consistently and comprehensively assign peak components in organics in general and in particular in thiophenes. In a first step it is helpful to consider the different hybridization states of the carbon atoms as there is a dependency of the electronegativity (EN) on hybridization state. The general trend is $EN(sp^3) < EN(sp^2) <$

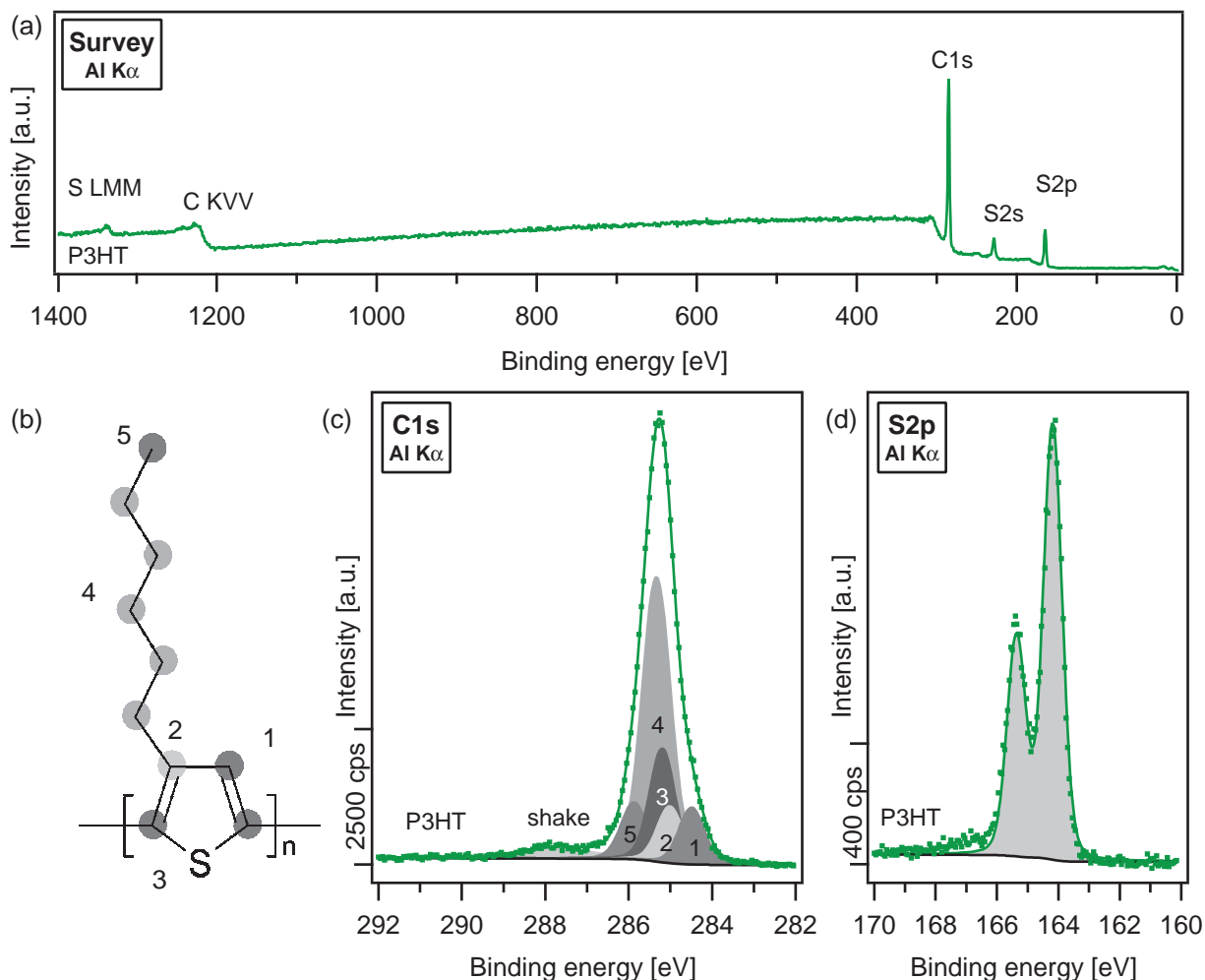


Figure 4.4: (a) Survey spectrum of a P3HT layer deposited via spin coating. All P3HT features are indicated. (b) Molecular structure of P3HT with the different carbon bonding sites emphasized by differently shaded circles. (c) C1s emission. The individual components are obtained through peak fitting. At the high binding energy side a weak and rather diffuse shake-up satellite is observed. (d) S2p emission. The doublet structure is clearly resolved.

$EN(sp)$. Values for different EN scales and calculation approaches can be found in [33]. In the course of this work values based on the bond polarity scale will be used together with the Pauling electronegativity scale. It is noteworthy, that also other elements involved in the aromatic systems, e.g. sulphur in the case of the thiophenes, can have different electronegativities than the tabulated values. Due to the lack of these specific values the Pauling values are used. Furthermore, mesomeric and inductive effects are considered as they influence the overall electron density in π -electron systems which has a similar effect as an external potential. In principle, we therefore consider the electron distribution in

conjugated systems on three levels: The EN differences are taken as a measure for bond polarity. Hence, one can estimate which of the atomic cores involved in the σ -bond attracts the electrons more and therefore has the higher electron density. In heterosystems, e.g. thiophenes, the mesomeric effect influences the π -electron distribution for all atoms contributing to the conjugated system. The inductive effect, which describes the electrostatic charge redistribution exerted by a functional group, is assumed to have a rather localized effect on the specific atom, where the inductively active side group is attached to. These steps are illustrated in scheme 4.5 for a thiophene unit. Especially in the case of thiophenes these considerations might oversimplify reality as the Sulphur d-orbitals might also be involved in the electronic system.

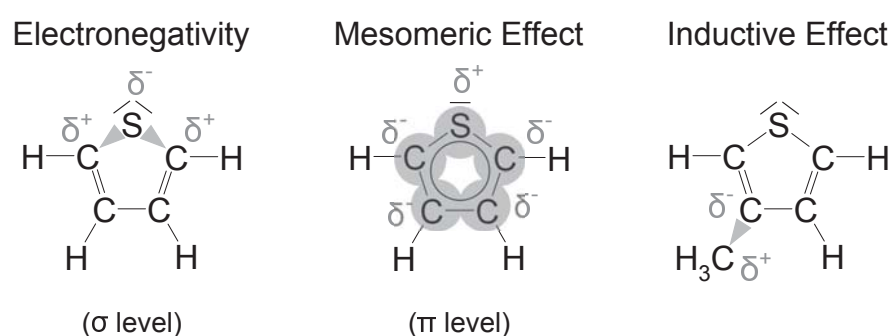


Figure 4.5: Evaluation of the different effects influencing peak assignment. (left) As sulphur has the higher electronegativity than sp^2 carbon, the σ bond is slightly polarized with increased electron density at the sulphur atom. (middle) One of the free electron pairs of sulphur takes part in the aromatic system giving a total number of six electrons in the π -orbitals. Assuming that these electrons are equally distributed among all five cores, the carbon atoms have negative partial charge while the sulphur is partially positively charged. (right) The inductive effect of the alkyl group increases the electron density at the carbon atom at which the side chain is bound to.

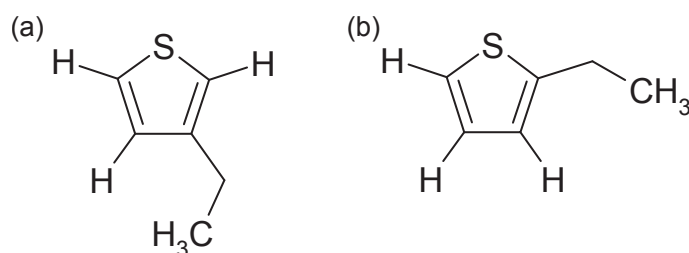
As a consequence of the described effects, the alkyl carbon atoms would have the lowest electron density and thus would be assigned at the highest binding energy in the PES spectrum, followed by the carbon atoms bound to sulphur. The C-C bound carbon atoms from the ring would have the lowest binding energy.

Computation

In order to substantiate the peak assignment following the working hypothesis Hartree-Fock (HF) and density functional theory (DFT) calculations have been performed by

Christian Krekeler² and Christian Lennartz³ for alkylated thiophene model systems such as depicted in Figure 4.6. While the HF calculations describe the order of the C-C/C-H and C-S bonds within the thiophene ring in agreement to literature and the above presented assignment, the calculated positions of the contributions from the alkyl chain do not fit to the experimental data. GW calculations (based on Green's function and the screened coulomb interaction W) on the other hand result in orbital energies in the order $C-H_3 > C-H_2 > C-H/C-C_{thio} > C-S$. Thus, the position of the alkyl carbons is represented according to the experimental fit results but the order of the C-C and C-S components is reversed. In general, deviations between experiment and calculation could originate from the size differences of the systems under consideration. The calculations have been performed on small model molecules compared to the thiophene materials P3HT and DH6T to reduce the calculation time. Additionally, only single molecules in the gas phase have been considered. In the photoelectron spectroscopy experiments, thin films of molecules are investigated, therefore also multi-electron interactions such as $\pi-\pi$ stacking and solid state screening effects can influence the peak position. Current theoretical approaches are not able to describe these effects.

Figure 4.6: Small thiophene building blocks as model systems for DFT calculations of the C1s binding energies. (a) "P3HT" model system. (b) "DH6T" model system.



Following the presented working hypothesis, a physically and chemically reasonable fitting result was obtained by decomposing the peak into five distinct carbon bonding sites. The components within a monomer unit of P3HT are assigned as follows: The C-H bound carbon within the thiophene unit (1) has the lowest binding energy of 284.5 eV as it has a higher electron density due to the π -system. The effect on the carbon atom 2 is reduced as it is also bound to the hexyl chain. This emission is located at 285 eV. The carbon atoms directly bound to sulphur (3) have a higher binding energy (285.2 eV) compared to the other thiophene carbon atoms as sulphur itself attracts electrons on the σ level. This assignment is also consistent both in absolute position as well as in energy difference with previously reported binding energies in carbon-sulphur compounds [85, 105]. The fourth

² Institut für Hochfrequenztechnik, Technische Universität Braunschweig

³ BASF SE

component at 285.3 eV is assigned to the C-H₂ bound carbon atoms within the hexyl-chain (4). The carbon atom in the terminal methyl group (5) has the highest binding energy (285.9 eV) as it exerts the strongest inductive effect on the neighboring carbon atoms. The intensity ratio of the five components is roughly 1:1:2:5:1 which is consistent with the number of carbon atoms per specific bonding configuration. These are also indicated in Figure 4.4 b. Additionally, a shake-up contribution on the high binding energy side is included in the fit in Figure 4.4 c.

The origin of the shake-up around 287.7 eV could be due to the defined energy loss of a HOMO-LUMO excitation. The energy difference between the shake-up satellite and the main C1s emission should then correspond to the photoelectron spectroscopy band gap. This value was determined in Ref. [24] to be 2.5 eV which is in accordance to the observed peak-shake-up binding energy difference of 2.4 eV. The S2p detail spectrum (Figure 4.4 c) clearly shows the expected doublet structure of the 2p orbital. The spin orbit splitting of 1.18 eV for sulphur [89] as well as the intensity ratio of 0.5 were fixed during the fitting routine. The low binding energy component belongs to the S2p_{3/2} and is located at a binding energy of 164.2 eV.

The valence features of P3HT are investigated using He I excitation in UPS. The resulting spectra are shown in Figure 4.7. The valence region spectrum shows two distinct features in the energy range of 0 to 5 eV (Figure 4.7 b). The peak centered at about 4 eV is attributed to localized π -states whereas delocalized π -states contribute to the rather flat feature from 1 to 3 eV [26, 106]. The same assignment can be concluded from measurements by FUJIMOTO ET AL. [107], who investigated the valence features of thiophene molecules in dependence of the number of monomer units showing a clear influence of the conjugation length but also of localized states around 4 eV on the measured valence region. From the delocalized frontier orbital states the HOMO_{onset} is determined at 1 eV while the work function ϕ derived from the secondary electron cutoff equals 3.5 eV. Adding those two values an ionization potential of 4.5 eV is obtained. This is slightly lower than the reported values in literature (4.6 eV in [26] and 4.65 eV in [24]) but still comparable including the experimental error of about 0.1 eV for determining the work function.

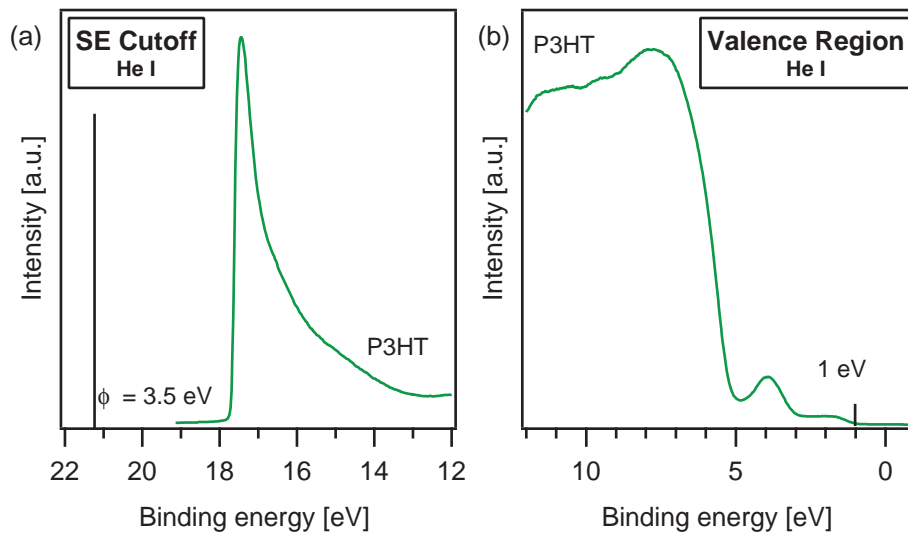


Figure 4.7: P3HT valence region. (a) SE cutoff and derived work function. (b) Valence levels with $\text{HOMO}_{\text{onset}}$ indicated.

4.2.2 Influences on Spectral Features

The presented results are intended to exemplify a typical P3HT layer investigated by photoelectron spectroscopy. However, certain influence factors have been observed in the course of this work. As both the results from SALANECK ET AL. [106] and FUJIMOTO ET AL. [107] imply that the electronic properties of P3HT are affected by morphology because this in turn influences the conjugation length, the effects of annealing on the electronic properties of P3HT have been investigated. Additionally, the influence of the deposition technique and resulting lateral film inhomogeneities have been studied. These results are analyzed and discussed in great detail in ref. [108]. Therefore only the key results will be given here:

Annealing By both thermal and vapor phase annealing the crystallinity of P3HT could be increased. This results in a decrease of the ionization potential and the HOMO level is shifted to higher binding energies. The core level emissions showed no changes due to annealing. A possible explanation could be that the frontier π -states are delocalized over several monomer units and thus are more susceptible to morphology changes than the localized core electrons.

Preparation techniques Drop-casting as well as spin-coating produced samples with a certain degree of lateral changes in electronic properties although the effect was

much more pronounced in drop-cast films. These inhomogeneities could be caused by variations in film thickness as well as crystallinity although to a certain extent also radiation induced changes of 0.2 eV [109] have to be taken into account.

4.3 Characterizing a Bulk Heterojunction Layer

In this section the active layer of a BHJ solar cell is investigated in comparison to its constituting components P3HT and PCBM. All layers were deposited via spin-coating in the glovebox at the Clustertool at the InnovationLab in Heidelberg. The layer thickness of the BHJ layer was adjusted to PES requirements to prevent charging. Using a profilometer, the layer thickness is determined to be 40 nm. The mass ratio of P3HT and PCBM was 1:1 and the overall concentration of the active materials in the chlorobenzene solution was around 15 mg ml⁻¹. The details for these experiments can be found in [108].

The survey spectra of the bulk heterojunction layer together with the spectra of the single materials are shown in Figure 4.8 a. Besides the expected contributions of carbon, oxygen (in the case of PCBM), and Sulphur (in the case of P3HT and the BHJ layer) no other features could be observed. The absence of substrate emission lines such as the In3d component indicates a layer thickness above the probing depth of XPS. The striking agreement between the BHJ and the P3HT spectrum implies a P3HT dominated surface of the mixed film. Also in the core level spectra shown in Figure 4.8 b) to d) the strong influence of P3HT on the emissions is obvious.

In the O1s spectrum of the BHJ layer no clearly defined emission stemming from PCBM could be observed due to the rather low overall O1s intensity even in pure PCBM. A slight intensity increase in the binding energy range from 531 eV to 534 eV could be attributed to PCBM but a detailed and reliable evaluation was not attempted due to the poor signal-to-noise ratio. The C1s and S2p signals of P3HT and the BHJ layer show remarkable similarity. The C1s spectrum of the BHJ has the same asymmetric shape with a shoulder on the high binding energy side as pure P3HT. Any shake-up and/or C-O bond-related structure at higher binding energies such as observed in the PCBM C1s spectrum at around 287 eV and 289 eV is absent. The doublet structure of the S2p doublet in the BHJ layer is as clearly resolved as in the P3HT layer. The C1s and S2p emission lines are further evaluated to track down possible influences of PCBM in the BHJ surface layer investigated in these

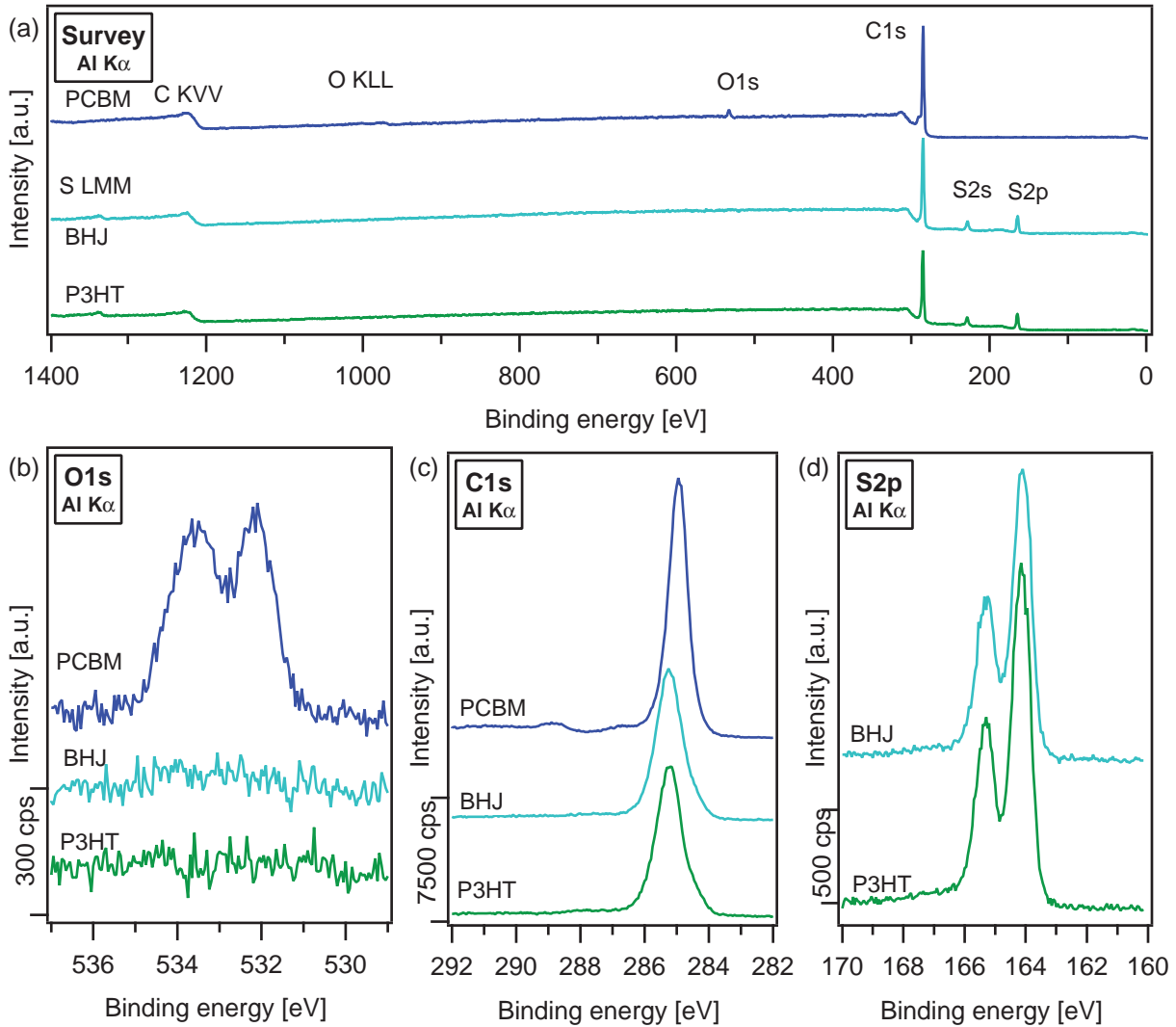


Figure 4.8: (a) Survey spectrum of a BHJ active layer (middle) in comparison to P3HT(bottom) and PCBM (top). (b) O1s detail spectrum. (c) C1s detail spectrum. (d) S2p detail spectrum. The spectra of the BHJ layer show remarkable similarity to the pristine P3HT spectrum. A clearly defined O1s emission stemming from PCBM cannot be observed. However, in the S2p component a slight intensity decrease possibly due to a reduced P3HT content compared to the pure material is observed.

experiments. Therefore the spectra are background corrected using a Shirley background function and plotted without any offset in the intensity scale (Figure 4.9).

In the C1s and S2p spectra no difference can be observed either in the line-shape or in the position on the binding energy scale. While the intensity of the C1s emission remains almost unchanged a decrease of the S2p emission is observed. The intensity of the S2p emission in a film depends on the volume fraction of P3HT in the film. If

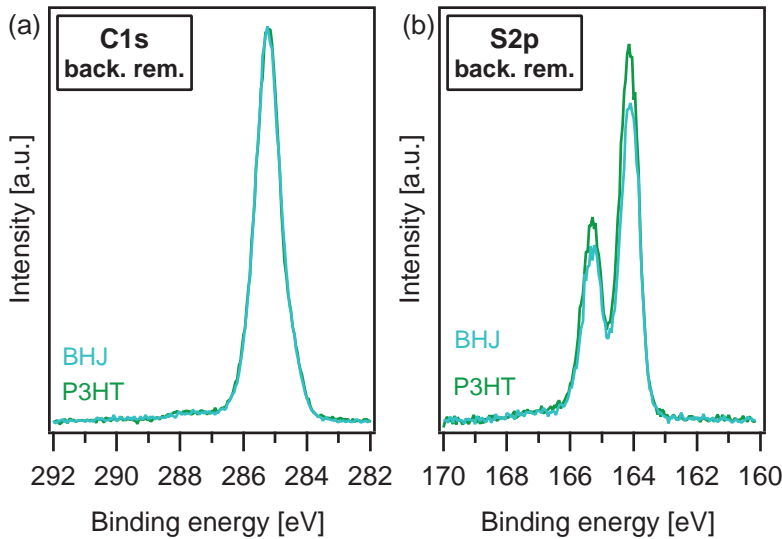


Figure 4.9: Background corrected spectra of C1s (a) and S2p (b) emissions of pristine P3HT (green) and the bulk heterojunction layer (turquoise).

the intensity in pristine P3HT is $I(S2p)_{P3HT}$ and in the BHJ $I(S2p)_{BHJ}$, then the quotient $I(S2p)_{BHJ}/I(S2p)_{P3HT}$ gives a measure for the volume fraction of P3HT in the BHJ layer. Thus, if this change in S2p intensity was attributed to a reduced P3HT content in the probed volume due to the mixing with PCBM, a blend surface ratio of 86 % P3HT and 14 % PCBM would be obtained. However, taking this ratio, an additional carbon emission from PCBM should be clearly observed. As this is not the case, the above described calculation provides only a rough estimation and should rather be interpreted as an additional indication of P3HT enrichment at the BHJ layer surface. This tendency of P3HT enrichment at the surface has been described in literature e.g. by XU ET AL., CAMPOY-QUILES ET AL., and YAO ET AL. [21, 110, 111] and is partially attributed to the lower surface energy of P3HT as compared to PCBM.

The UP spectra of the secondary electron cutoff and the valence levels are shown in Figure 4.10. Considering the shape of the measured valence spectrum of the BHJ layer, a clear correlation to the P3HT spectrum can be made. Distinct PCBM features as shown in the top spectrum of Figure 4.10 b are not observed.

Although the shape of the valence level spectrum of the BHJ is also controlled by P3HT, the influence of the mixing with PCBM becomes obvious in the strongly shifted energy levels. Both the work function as well as the $HOMO_{onset}$ are shifted by about 0.4 eV compared to pristine P3HT.

The possible origins for the differences in the electronic shifts in the core level emissions compared to the valence features are discussed at length in [108]. According to ref. [108],

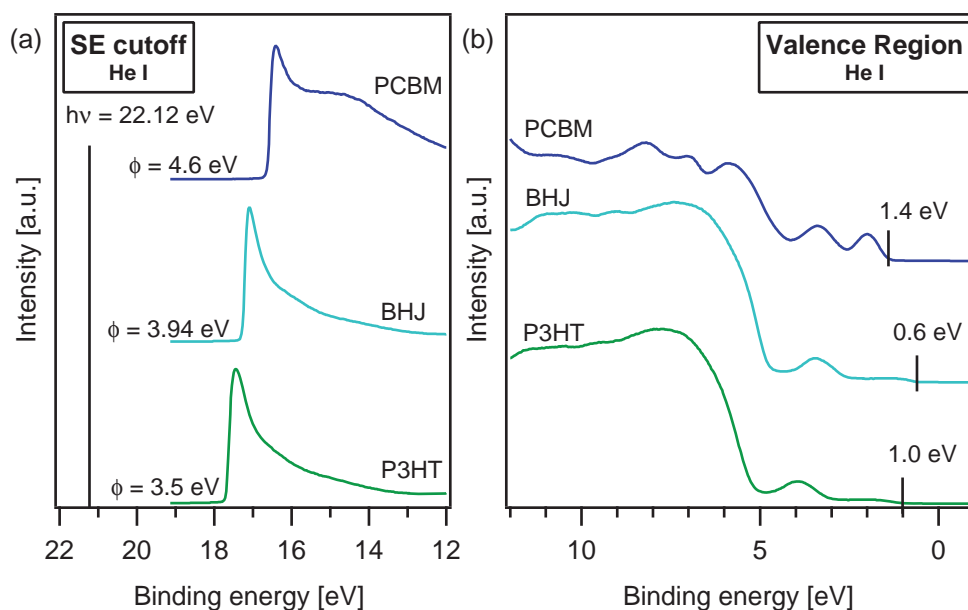


Figure 4.10: SE cutoff (a) and valence region spectra (b) of a BHJ layer (middle) in comparison to P3HT (bottom) and PCBM (top).

it could be possible, that in the case of polymers the valence levels are more susceptible to charge transfer due to their large delocalization. Additionally, the conjugation length itself influences the HOMO position [107, 108]. The determination of the PCBM HOMO_{onset} position in the BHJ spectrum is not possible. Therefore the energy level diagram of the BHJ film or better said the P3HT component in the BHJ is compared to the Andersson line-up of the pristine materials is shown in Figure 4.11.

The ionization potentials of P3HT and the P3HT component in the BHJ layer are almost unchanged (4.5 eV for P3HT and 4.54 eV for P3HT in the BHJ). However, the position of the Fermi level is shifted downward in the gap upon mixing P3HT with PCBM. This indicates an electron transfer from the P3HT to the PCBM. From the representation in Figure 4.11, the question arises, how the transition from the pristine material levels to those in the intermixed structure occurs. A first attempt to find an answer is given in the following section.

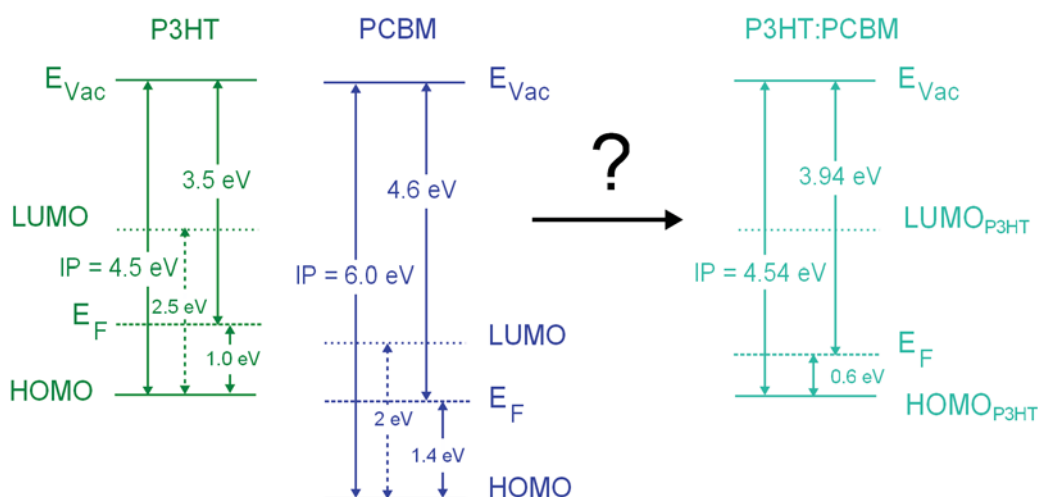


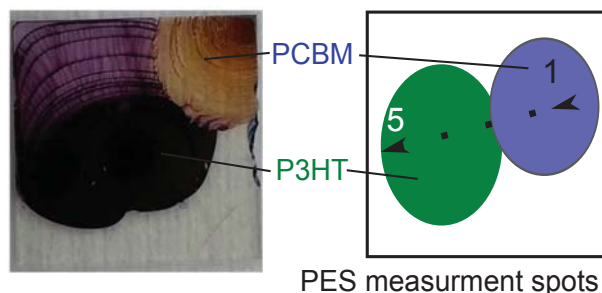
Figure 4.11: Energy levels of pristine P3HT and PCBM as determined from thin films on ITO for vacuum level alignment (left) compared to the measured energy level positions of P3HT in a bulk heterojunction layer (right). Energy gap values are taken from literature [24].

4.4 Approaching the Interface

At least within the probing depth of XPS, the surface of a P3HT:PCBM BHJ layer is dominated by P3HT as could be shown in the previous experiments. Both materials are processed from solution from the same solvent. Thus, successive deposition of one materials on top of the other is not directly possible or at least accompanied by significant intermixing. Therefore, different techniques to create a defined interface between P3HT and PCBM have been investigated. Two approaches are evaluated in detail by M. SCHWARZE [108]. In one case, both solutions were drop-cast right next to each other to create a vertical interface while in the second case, PCBM was spin-coated on an already dry P3HT layer also produced via spin-coating. In principle, it turned out that both experiments produced a composition gradient between the donor and the acceptor yielding very similar results. Therefore, in the following, only the vertical interface created by drop-casting will be discussed in detail.

A P3HT droplet was deposited onto an ITO substrate at a substrate temperature of approx. 35 °C in the top left corner. The sample was then annealed at 120 °C and at this elevated temperature the PCBM droplet was deposited right next to the P3HT. The elevated temperature was necessary to speed up the solvent evaporation to reduce the possibility of material mixing. Both materials were deposited from chlorobenzene solu-

Figure 4.12: (left) Photograph of the sample with P3HT and PCBM drop-cast right next to each other. (right) Schematic representation of the sample geometry with the materials represented in the previously introduced color coding (P3HT = green, PCBM = blue).



tions at 2.8 mg ml^{-1} and 3.8 mg ml^{-1} for P3HT and PCBM, respectively. In Figure 4.12 a photograph and a sketch of the sample is given.

In the photograph, two different regions can be clearly distinguished by color. P3HT usually forms purple layers in the dry state as can be seen in the left corner of the image. In the right corner, PCBM dominates, visible from the brownish color. Where the two materials meet, diffuse structures can be observed indicating mixing of the materials and thus the lack of a clearly defined interface. In addition, inhomogeneities with respect to layer thickness are clearly observed from the step-like changes in brightness. The PES characterizations have been performed from the PCBM-rich sample side to the P3HT-rich sample edge as indicated in Figure 4.12 at five different positions. The resulting XP spectra are shown in Figure 4.13.

Already from the survey spectra it can be seen that the upper right sample corner does not only consist of PCBM as could be anticipated from the optical impression since not only the PCBM characteristic carbon and oxygen signals are observed but also the P3HT specific sulphur emissions. This means that even though the P3HT film was already completely dry and annealed and the PCBM droplet drying was accelerated, some mixing of P3HT and PCBM cannot be avoided during PCBM deposition. No other emissions such as the In3d from the ITO substrate could be detected. This shows a rather large layer thickness in all cases, although the rise in the diffuse background in spectra 2, 3, and 4 between 600 eV to 1100 eV indicates a reduced layer thickness compared to the other two positions as this feature arises due to inelastically scattered In3d electrons. Taking a closer look at the core level emission lines the transition from PCBM-rich to P3HT-rich sample region can be investigated in more detail. The O1s peaks of the spectra 1 and 2 depicted in Figure 4.13 b coincide in shape and in energetic position. Compared to the previously reported results of spin-coated PCBM on ITO, the binding energies of the two oxygen components are reduced by 200 meV to 532 eV and 533.5 eV. However, independent of the P3HT content, no shift in binding energy is observed. This indicates a constant Fermi level in the PCBM component.

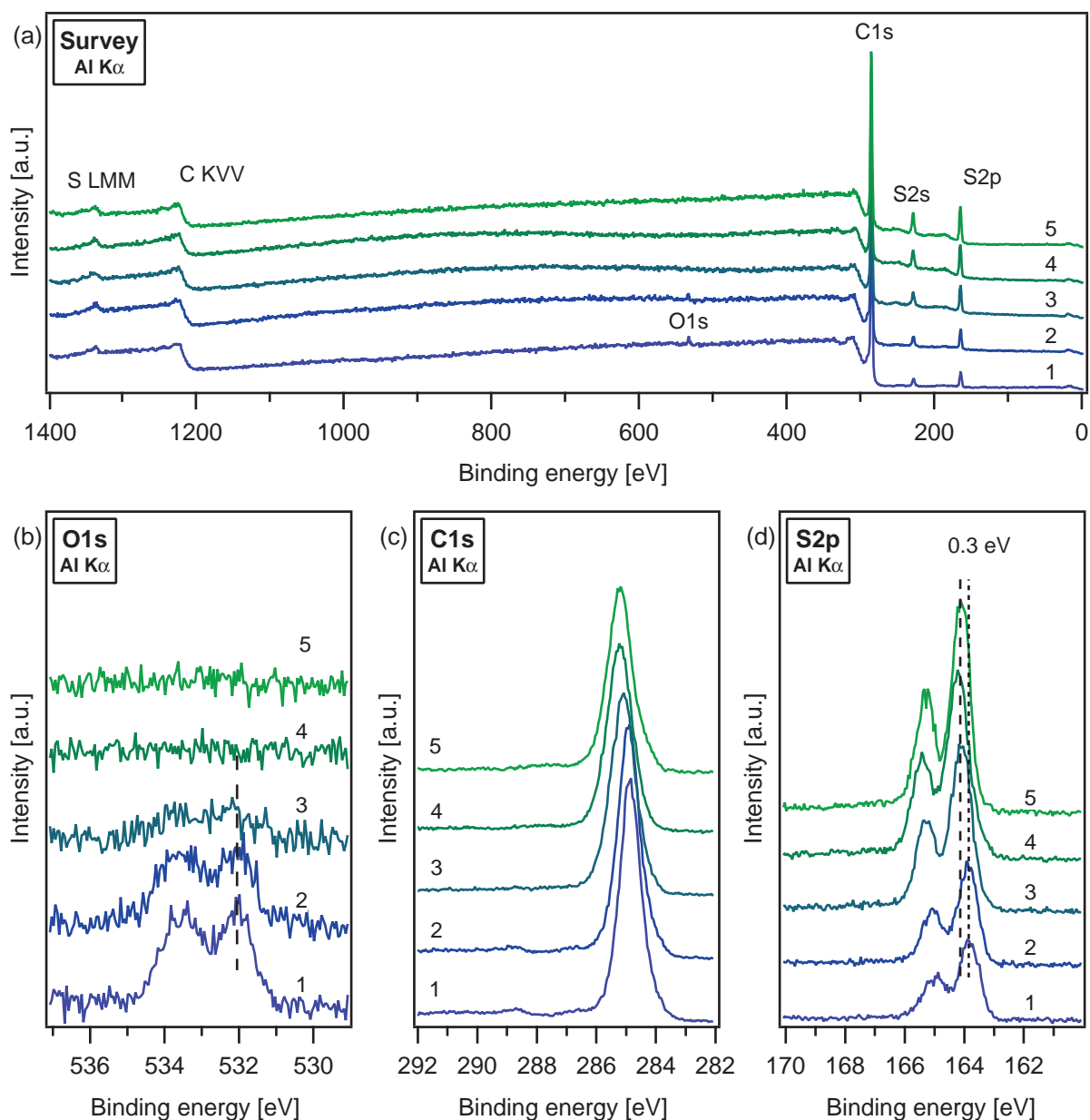


Figure 4.13: (a) Survey spectra of PCBM drop-cast next to P3HT to create a vertical interface. (b) O1s emission. (c) C1s emission. (d) S2p emission. The spectra are displayed in the order of increasing P3HT content. Spectrum 1 corresponds to the PCBM-rich right sample corner while spectrum 5 represents the P3HT-rich left sample area.

In spectrum 3 a slight increase in the O1s intensity is observed but a detailed evaluation is not possible due to the poor signal to noise ratio. In spectrum 4 and 5 no oxygen emission is visible. The C1s emission shows a rather gradual transition from the PCBM features with a maximum intensity at 284.8 eV and the two features at higher binding energies with maxima at around 286.6 eV and 288.7 eV to the asymmetric P3HT C1s peak with an

intensity maximum at 285.2 eV. The S2p emission rises in intensity from spectrum 1 to spectrum 5 and shifts by about 0.3 eV to higher binding energies, which hints towards a change in Fermi level position in P3HT with increasing distance to the PCBM/P3HT lateral interface.

The UP spectra are clearly dominated by P3HT as can be seen in Figure 4.14. PCBM related features are not observed, however a broadening e.g. in the encircled area indicate a certain degree of PCBM contribution to the valence spectra at position 1 and 2. The HOMO_{onset} of P3HT can be determined for all positions and shifts by 0.8 eV to higher binding energies. Also, the work function shifts by 0.8 eV from 4.4 eV to 3.6 eV. The work function in position 1 roughly corresponds to the previously determined work function of PCBM in section 4.1. Due to the lack of any clearly defined PCBM features in the valence region, assigning this value to PCBM seems questionable. Although the surface seems to be dominated by P3HT, the secondary electron cutoffs measured at position 3 and 4 show a double structure. The origin of this is yet undetermined. Even if a mixture of PCBM and P3HT was present at the surface, it would be expected to measure only the lower work function. The double structure could also hint towards two different P3HT phases at the surface. In general, the lack of PCBM features even for position 1 and 2 in the UP spectra can be explained by the higher surface sensitivity compared to XPS. Additionally, small compositional inhomogeneities might be easier to detect in XPS as the measurement spot and thus the sample area from which the signal is integrated is smaller.

In an effort to create a more defined interface, PCBM was spin-coated on top of an already annealed P3HT layer. The resulting sample geometry is shown in Figure 4.15 together with a schematic representation. In the center, PCBM seems to have replaced the P3HT, visible from the light brownish color. PES characterization was again performed from the PCBM-rich phase to the P3HT-rich phase with decreased intervals at the transition between the two regimes as indicated in Figure 4.15.

In total 11 measurement spots have been characterized giving in principle the same results in XPS as the lateral interface, namely a constant Fermi level in PCBM and a downward shift of the Fermi level in the band gap of P3HT with increasing distance from the PCBM/P3HT interface.

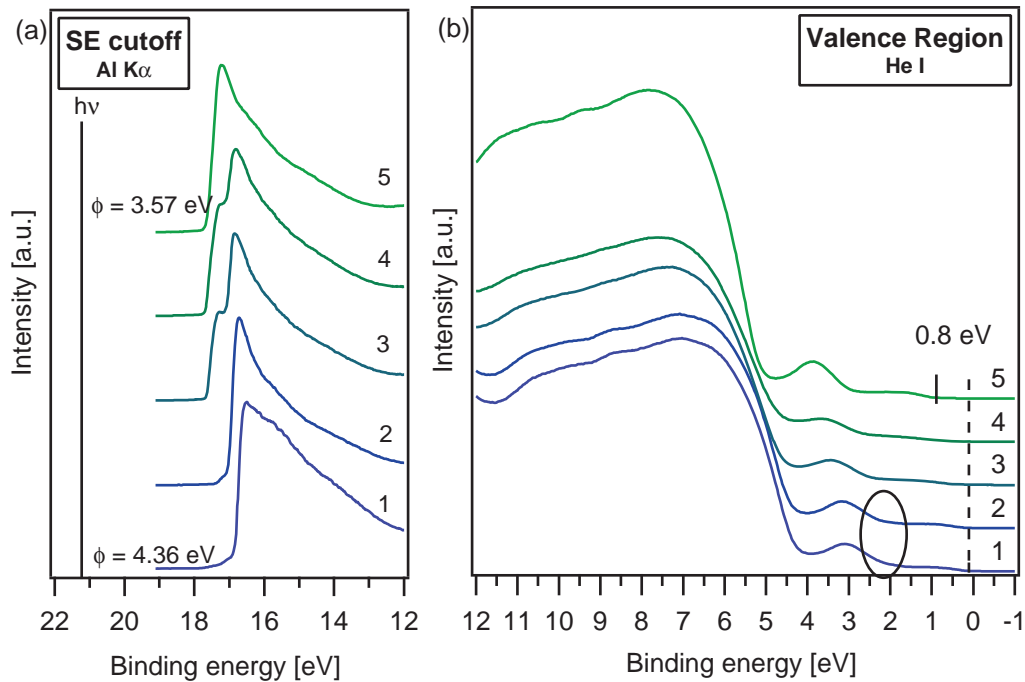


Figure 4.14: (a) Secondary electron cutoff and (b) valence region spectra in the order of increasing P3HT content as determined from XPS for the drop-cast P3HT/PCBM interface.

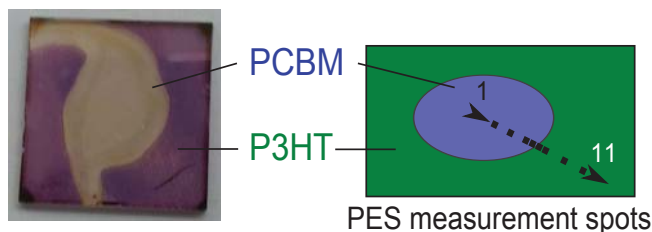


Figure 4.15: Photograph of the sample and schematic representation of the sample in the previously used color coding. Additionally, the positions of the individual measurement spots are indicated.

While in the SE cutoff spectra the same double structure possible arising from both materials is also visible, in the valence region spectra PCBM features can be clearly observed for this sample (see Figure 4.16).

The valence region spectra show a gradual transition from PCBM to P3HT features. The $\text{HOMO}_{\text{onset}}$ of PCBM can be clearly determined in this experiment and stays constant in energy at 1.65 eV independent of the composition at the measurement spot. This is in accordance to the observed constant binding energy of the O1s emissions. The P3HT $\text{HOMO}_{\text{onset}}$ again shifts to higher binding energies with increasing P3HT content from 0.15 eV to 1 eV. Also as in the previous experiments, a change in the work function of roughly the same magnitude as the P3HT $\text{HOMO}_{\text{onset}}$ shift is observed. Since the secondary electron cutoff spectra again show a double structure, an undisputed assignment of the work functions to one of the materials is not possible.

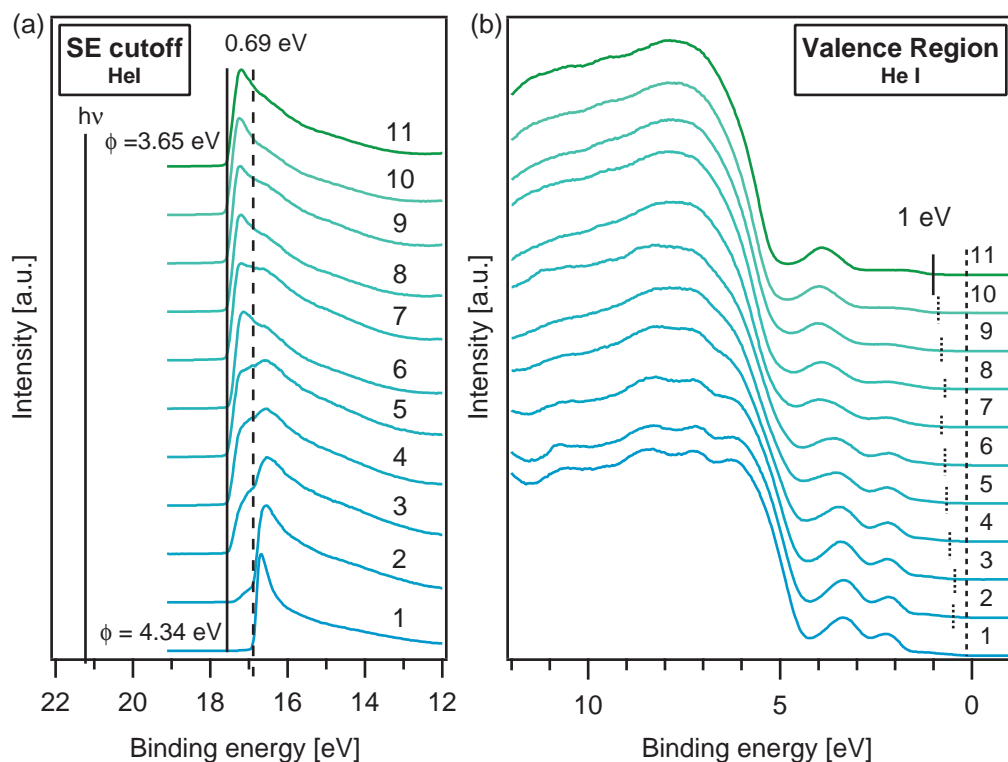


Figure 4.16: (a) Secondary electron cutoff and (b) valence region spectra in the order of increasing P3HT contribution for the sequentially spin-coated P3HT/PCBM interface. A decrease in work function by about 0.7 eV is observed while the P3HT HOMO_{onset} shift by about 0.9 eV to higher binding energies. For the positions 1 to 7 PCBM features are clearly observed.

From the above presented experiments, a model cross sectional structure for each of the samples is proposed. Despite the efforts of preventing a donor cap layer, P3HT still seems to dominate the sample surface even on the PCBM rich sample parts. This makes the unequivocal assignment of level positions and the determination of a possible interface dipole for this specific donor:acceptor couple difficult if not impossible at the current stage. Therefore, the shown model cross sections together with the energy level positions of the sequentially spin-coated sample in Figure 4.17 represent our interpretation of the data and were not directly obtained through a step-by-step interface experiment. The trend of increasing P3HT HOMO_{onset} binding energy as indicated by the dashed lines hints towards band bending in P3HT. The direction of the band bending would then be in such a way that it is disadvantageous for device performance as it would promote hole accumulation at the interface and thus increases the charge carrier recombination probability. However, the exact transition from the pristine material Andersson line up to the obtained values

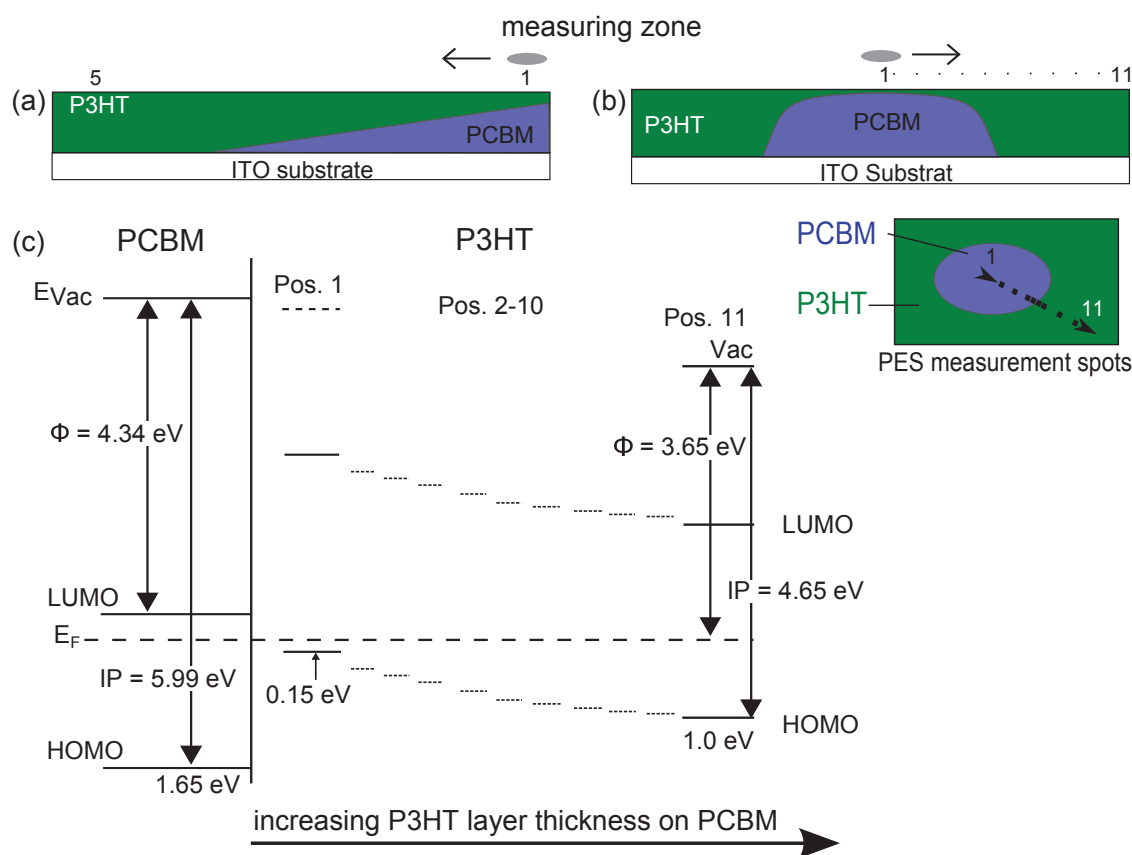


Figure 4.17: (a) Model cross section of the sequentially drop-cast sample. (b) Model cross section of the sequentially spin-coated sample. (c) Energy level diagram derived from the UPS data of the sequentially spin-coated sample. As the donor capping layer prevents unequivocal assignment of level positions especially in case of the work function, the P3HT $\text{HOMO}_{\text{onset}}$ positions (as indicated by the dashed lines) relies on our interpretation of the data and was not directly obtained via a step-by-step interface experiment. However, the observed trend in the $\text{HOMO}_{\text{onset}}$ positions implies band bending in the P3HT.

in the BHJ layer (see section above) or these lateral gradients could not be completely resolved up to now. For a more throughout discussion, the reader is kindly referred to Ref. [108].

4.5 Motivating the Next Steps

The above presented results are promising and show the possible capability of photoelectron spectroscopy for characterizing organic solution-processable semiconductors for OPV applications. However, the aim of directly analyzing the energy level alignment at the P3HT-PCBM donor-acceptor interface has not yet been fully accomplished. Thus, there is clearly a need for further experiments in order to fully understand the electronic interplay

at the P3HT:PCBM interface(s) in bulk heterojunction structures. Further experimental approaches such as using different solvents for P3HT and PCBM and lamination techniques are currently evaluated within the Surface Science group and at the InnovationLab in Heidelberg.

In this work, the following sections of this part will focus on a set of experiments in which the polymeric donor was replaced by a small molecular thiophene DH6T in order to achieve higher diversity in terms of preparation techniques. DH6T can be deposited from solution as well as through thermal evaporation in UHV. Therefore classical step-by-step interface experiments are possible. Also, the possibilities to deposit PCBM via thermal evaporation are explored. The second part of this work will deal with developing and exploring a method to perform sequential depositions and subsequent characterization of organic molecules from solutions.

5 Processing Possibilities of PCBM and DH6T

This chapter focusses on the comparison of different preparation techniques for thin films of PCBM and DH6T. Both materials are deposited via solution-based techniques as well as thermal evaporation as a mean for step-by-step deposition. For DH6T, there are results in literature, where both techniques are successfully applied [75, 105, 112]. Therefore, the focus lies on the investigation of the influence of the preparation techniques on the electronic properties of DH6T. For PCBM, however, contradicting reports on the feasibility of thermal evaporation for this material exist in literature [104, 113, 114]. In order to clarify whether or not this deposition technique can be applied to PCBM, the evaporation was attempted. Since degradation effects were observed during thermal evaporation, additional chemical and structural characterization techniques are applied to understand the possible decomposition mechanisms and evaluate their effect on the electronic properties. The latter techniques were performed in close collaboration by Torben Adermann¹ (chemical analysis) and Tobias Glaser², Sebastian Beck², and David Gerbert² (IR spectroscopy).

5.1 Thermal Evaporation of PCBM

In order to achieve a stepwise deposition of PCBM, thermal evaporation was explored for this material. There are a few publications in which PCBM is evaporated [104, 113, 115], which were used as guidance for determining evaporation parameters. The evaporation was performed at the Clustertool in Heidelberg on polished silicon wafers with a natural oxide as this is a suitable substrate material for both PES and FT-IR characterization. To eliminate possible synthesis effects all experiments have been performed with material from a single batch (American Dye Source, Lot. 12K018E1). The base pressure in the evaporation chamber was held in the 10^{-7} mbar regime during evaporation although pressure

¹ Organisch-Chemisches Institut, Ruprecht-Karls-Universität Heidelberg

² Kirchoff-Institut für Physik, Ruprecht-Karls-Universität Heidelberg

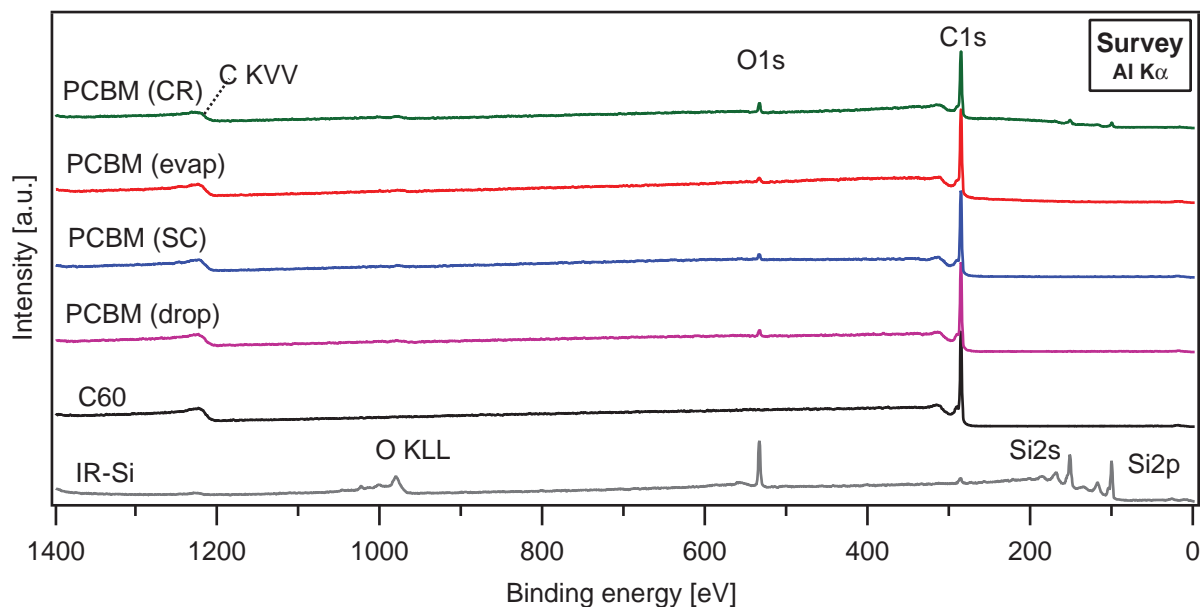


Figure 5.1: Survey spectra of the silicon substrate, C_{60} , drop-cast PCBM (drop), spin-coated PCBM (SC), evaporated PCBM (evap) and the PCBM crucible residues (CR) (from bottom to top).

bursts of up to 10^{-6} mbar were observed. These occurred since the material melts prior to evaporation and eventually boils in the crucible. In order to achieve a considerable layer thickness the substrate was placed over the crucible as soon as PCBM melted and the first pressure bursts occurred. The crucible temperature ranged from $240\text{ }^{\circ}\text{C}$ at the beginning of the deposition to finally $280\text{ }^{\circ}\text{C}$. The temperature was monitored by a thermocouple placed outside the crucible. The total deposition time added up to 75 min.

To trace changes in the film composition, the photoemission spectrum of evaporated PCBM is plotted in comparison to drop-cast and spin-coated PCBM (see Figure 5.1). The spin-coating deposition was performed in the glovebox at 1000 rpm for 50 s using a 10 mg ml^{-1} solution in chlorobenzene. The same solution was used to perform a drop-casting experiment in the glass cell to compare these two techniques and to exclude effects of the glovebox environment or the deposition process. Additionally, PES was performed on C_{60} and a film produced from the remains in the crucible after the evaporation. C_{60} was evaporated at $450\text{ }^{\circ}\text{C}$ for 20 min at a base pressure of 10^{-8} mbar to 10^{-7} mbar. Thus, in total four films of PCBM and one layer of C_{60} were prepared. The survey spectra of all films together with the survey spectrum of a solvent cleaned silicon substrate are shown in Figure 5.1.

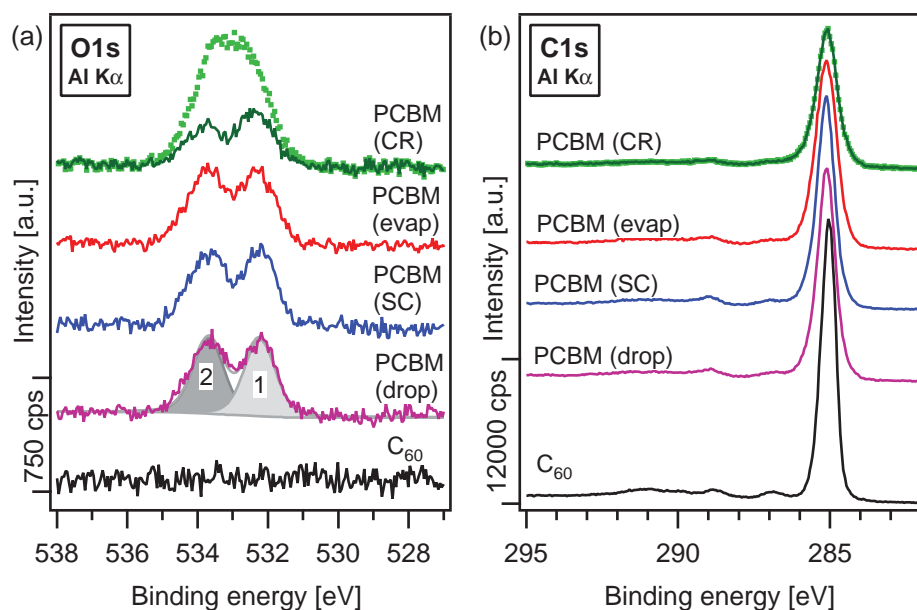


Figure 5.2: (a) O1s detail spectra and (b) C1s detail spectra of C₆₀, drop-cast PCBM (purple), spin-coated PCBM (blue), evaporated PCBM (red), and the PCBM crucible residues (green) (from bottom to top). In case of the PCBM crucible residues, the original data is plotted as dotted line while the difference spectra after the subtraction of the substrate C1s and O1s emission are shown as solid lines.

From the survey spectrum of the substrate can be seen that, also after the solvent cleaning, a minor carbon emission is still present. However, since in all organic spectra except the crucible residue spectrum no substrate emission lines (e.g. Si2p at 100 eV) are visible, these most likely do not have a significant contribution to the measured C1s emission lines. In case of C₆₀, only carbon related emissions could be detected as expected. In all PCBM derived samples, both carbon and oxygen signals could be detected. The core level spectra are shown in Figure 5.2. Using spin-coating, a layer of 30 nm thickness was deposited while the evaporation of PCBM yielded a film of approximately 15 nm thickness. The C₆₀ film was 45 nm thick according to the Dektak measurement.

In case of C₆₀ no oxygen signal was detected as expected (Figure 5.2 a at the bottom). The O1s spectra of drop-cast, spin-coated, and evaporated PCBM samples show two distinct oxygen species which correspond to the two different oxygen binding sites in PCBM. Independent of the preparation technique, the binding energy position as well as the intensity is very similar. Exemplified for the drop-cast sample, Voigt profiles were applied for curve fitting. The two resulting components have equal intensity as expected from the molecular structure. The component (1) at 532.2 eV is attributed to the oxygen in the carbonyl group

while the signal at 533.7 eV (2) is generated by the oxygen in the methoxy group (compare section 4.1). The presence of substrate emissions in case of the crucible residues indicates a poor film quality as initially the same concentration as for pristine PCBM was used to drop-cast the film. Therefore, the oxygen signal of the crucible residues is superimposed by the oxygen signal from the underlying SiO_x . Difference spectra have been calculated to eliminate the substrate signal. First, the difference spectrum of the Si2p emission was calculated in such a way that the emission was completely removed (see Figure A.1 in the appendix). The obtained scaling and shifting parameters were then used to calculate the O1s and C1s difference spectra (see Figure A.2 and A.3 in the appendix) to achieve consistent results. In the resulting O1s difference spectrum, also two maxima at about the same positions as for the other PCBM samples are observed. However, the intensity ratio is different from 1:1. This could indicate a change in the PCBM molecular structure due to the temperature exposure in the crucible. Yet, from chemical analysis it becomes evident that no processes involving the loss of one of the oxygen containing groups occurs during temperature treatment (see section 5.1.1). Although the difference spectra were calculated consistently as described above, the peak shape is very sensitive to this process. Therefore, the change in the intensity ratio might be an artifact introduced from the difference spectrum calculation.

At a first glance all PCBM C1s spectra show a remarkable similarity to each other and to C_{60} . In all cases the major component is located around 285 eV followed by a satellite structure at higher binding energies. The main C1s emission is broadened in the PCBM spectra compared to C_{60} . This could be due to the reduced symmetry of the molecule and the reduced crystallinity of the PCBM films. While in the C_{60} spectrum, the satellite structure is solely due to shake-up and shake-off processes as described below, the assignment is more complicated in the case of PCBM. In the same binding energy region, in which the shake-up satellites are observed, also contributions from the C-O bonds of the side chain and possibly of the phenyl ring could be expected [102]. In literature two partly contradicting assignments of the high binding energy emissions in the PCBM C1s spectra have been found. On the one hand, FELICISSIMO ET AL. assign the major C1s emission at 285.2 eV to the C-C bonds in the C_{60} core and attribute the features at 286.9 eV and 289.8 eV to the C-O bond and the C(O)O bond. In addition, the emissions at 289 eV and 291.2 eV are referenced to two shake-up satellites [116]. On the other hand, RICHTER ET AL. have located the main C1s emission from the conjugated carbon atoms in C_{60} core at 285.3 eV and a component from not further specified C-C bonds at 286.1 eV. The emission from the C-O

bond is assigned to the feature at 287.2 eV and the C=O contribution at 289.3 eV. Finally, a broad shake up satellite is included in their fitting result at 291.2 eV [117]. While FELICISSIMO ET AL. and RICHTER ET AL. agree on the general position of the the carbon species bound to oxygen which are also in agreement to previously reported results [85, 102], the two publications differ in the number and position of the shake-up satellites.

From the intensity ratio of the carbon and oxygen 1s emissions of the PCBM layers the molecular composition is estimated. For the crucible residues, the intensities after subtracting the substrate emissions are used. The results are summarized in Table 5.1. For all PCBM samples, the carbon intensity is again underestimated as the expected atomic ratio of 36:1 is not achieved (compare section 4.1). Between the drop-cast, the spin-coated, and the evaporated PCBM layer, almost no difference in the composition is observed. For the crucible residues however, it seems that the amount of oxygen is reduced. This could possibly indicate decomposition or fragmentation of PCBM in the crucible during evaporation.

Table 5.1: C-to-O ratio of the PCBM samples in dependence of the deposition technique. The stoichiometric ratio as derived from the molecular structure is given in the bottom row.

Deposition Technique	C-to-O ratio
drop-casting	30.9:1
spin-coating	30.6:1
evaporation	30.4:1
crucible residues	34.5:1
molecule	36:1

In order to pinpoint any changes in the molecular structure due to the different preparation methods from the C1s spectra, a closer look is taken at the comparison to C₆₀. In a first step, the C1s spectrum of C₆₀ is discussed in detail. The spectrum is shown in Figure 5.3. Besides the major emission of the conjugated carbon atoms in the C₆₀ cage at 285.05 eV a characteristic satellite structure at the high binding energy side is observed. This structure is represented enlarged in the inset in Figure 5.3. All emissions were fitted using Voigt profiles after a Tougaard background has been subtracted. ENKVIST ET AL. [118] calculated the absorption spectrum of the core ionized C₆₀ molecule, thus the individual features can be assigned to specific electron excitations. The first satellite at 1.8 eV higher binding energy corresponds to the energy loss due to the excitation of a HOMO-LUMO transition in the ionized molecule [118]. The fitting result obtained for the measured C₆₀ C1s spectrum

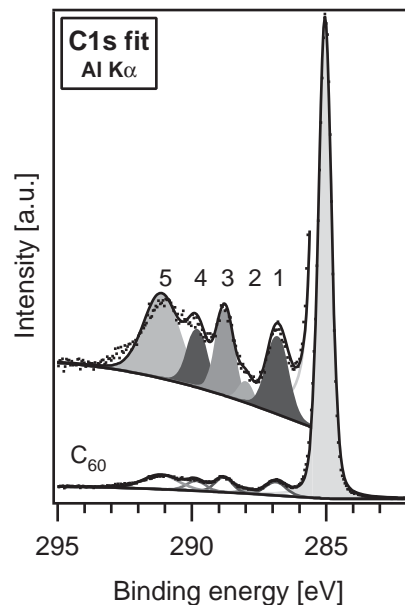


Figure 5.3: C1s spectra of C_{60} . Voigt profiles are used to fit the major C1s emission as well as the shake-up satellites on the high binding energy side.

Table 5.2: Binding energies of the measured C1s spectrum in comparison to the calculated shake-up satellite positions

Emission	E_{bind} [eV]	$\Delta E_{\text{measured}}$ [eV]	ΔE_{calc}^a [eV]
C-C (C_{60})	285.05	-	-
1	286.87	1.82	1.8
2	288.05	3	2.9
3	288.82	3.77	3.7
4	289.84	4.79	4.8
5	291.16	6.11	5.9

^a Values from ENKVIST ET AL. [118]

is indeed in very good agreement to the calculated and measured shake-up satellites given in ref. [118]. The values are given in Table 5.2 for comparison.

In the second step, the C_{60} spectrum is now directly compared to the spectra of the differently prepared PCBM films. These spectra are shown in Figure 5.4. Assuming that the $\pi - \pi^*$ excitations responsible for the shake-up structure in C_{60} remain almost unchanged in the course of adding the side chains to form PCBM, any changes in the high binding energy substructure can be attributed to the additional carbon bonding states in PCBM.

From the plot of the intensity normalized C1s spectra deviations of the PCBM spectra compared to the C_{60} spectrum are observed at around 286 eV to 287 eV and 289 eV as encircled and enlarged as an inset in Figure 5.4 a. The rather broad shake feature between 290 eV to 292 eV is rather similar for all samples. As in this region no direct contributions

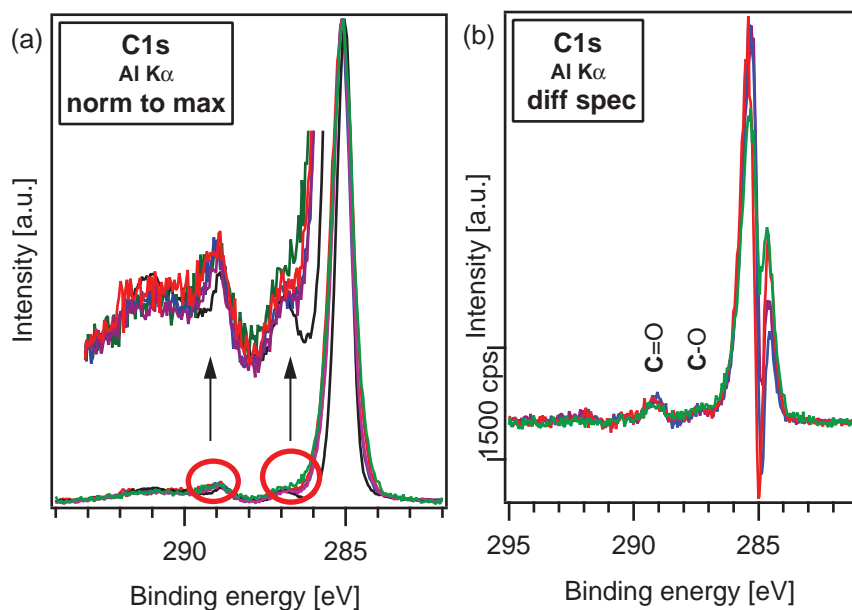


Figure 5.4: (a) C1s spectra of C₆₀ (black), drop-cast PCBM (purple), spin-coated PCBM (blue), evaporated PCBM (red), and the crucible residues (green) normalized to the maximum intensity. The high binding energy region is displayed enlarged in the inset to make the intensity changes more clear. (b) Difference spectra of the C1s emissions of drop-cast PCBM (purple), spin-coated PCBM (blue), evaporated PCBM (red), and the crucible residues (green), where the C1s signal of C₆₀ has been subtracted in such a way to eliminate the shake-up feature at 291 eV.

from chemically shifted C1s components are expected, it is used as a reference to calculate difference spectra as shown in Figure 5.4 b. These spectra were calculated in such a way that the emission between 290 eV to 292 eV was removed for the PCBM samples. Although the relative remaining emissions in the PCBM difference spectra vary in intensity, they all show a very similar structure. After the subtraction of the C₆₀ core signal, some intensity remains at around 284.6 eV and 286 eV. This corresponds to the before described observed broadening of the main C1s emission and could be due to the reduced molecular symmetry but also to additional contributions from the phenyl-group and the butyl side chain as suggested by synchrotron photoelectron spectroscopy results of RICHTER ET AL. [117]. The calculation of the difference spectra produced some negative intensity where the main C1s emission of C₆₀ is located. This could indicate, that the satellite structure for the PCBM samples is reduced in intensity as compared to the unfunctionalized fullerene. Remarkably, the difference spectra also show perfect agreement in the remaining satellite structure at the expected positions of the C-O and C=O bonds at 287 eV and 289 eV, respectively. Therefore, these remaining emissions are now attributed to the two carbon atoms bound

to oxygen in the PCBM side chain. In total, the PCBM C1s spectrum on the high binding energy side therefore is assumed to consist of a superposition of the C1s shake structure as observed in C₆₀ and chemically shifted carbon species.

Considering the stoichiometry of PCBM the signal intensity of the C-O and C=O peaks can be estimated. Taking $\frac{1}{70}$ of the main C1s emission, which should correspond to the intensity of each C-O peak, an intensity of around 200 cps would be expected. This corresponds fairly well to the obtained remaining intensity at 287 eV and 289 eV after the subtraction of the C₆₀ signal in the C1s spectrum.

The valence level of the differently prepared PCBM samples together with the C₆₀ spectra are shown in Figure 5.5 a and b. The valence features of C₆₀ and PCBM show a general accordance in peak position and relative intensity. From the He I spectra the electronic properties are derived. For C₆₀ a HOMO_{onset} position of 1.84 eV and an ionization potential of 6.4 eV is obtained. For the two solution-processed PCBM samples, the agreement between the individual values of HOMO_{onset} (1.82 eV and 1.87 eV) and work function (4.25 eV and 4.21 eV) is almost perfect and the films have identical ionization potentials of 6.1 eV. Thus, the two preparation techniques yield very comparable results concerning the electronic properties of the film. The evaporated PCBM film still shows the same ionization potential of 6.1 eV but the HOMO_{onset} and work function are shifted by about 100 meV compared to the solution-processed PCBM samples. This could be caused by a different Fermi level position induced by the substrate due to a lower film thickness or by unintentional doping which occurred during the evaporation. From the crucible residues only a thin and rather inhomogeneous film could be deposited via drop casting. The resulting valence features are slightly broadened compared to the other PCBM samples and the ionization potential is reduced by about 100 meV compared to the PCBM films. These effects could be due to the film morphology but they could also imply changes in the molecular structure or composition due to the thermal stress during evaporation.

To determine possible changes in the valence structure the He II spectra are background corrected and compared to C₆₀ to firstly identify the molecular orbitals which are influenced by the addition of the side chain and to secondly find out if any of the MOs are changed during the different deposition steps. Therefore, also the calculated UP spectra from the DFT eigenvalues³ are compared. The measured and background subtracted HeII spectra as well as the calculated spectra are shown in Figure 5.6.

³ calculated by C. Krekeler, TU Braunschweig, see also section 4.1

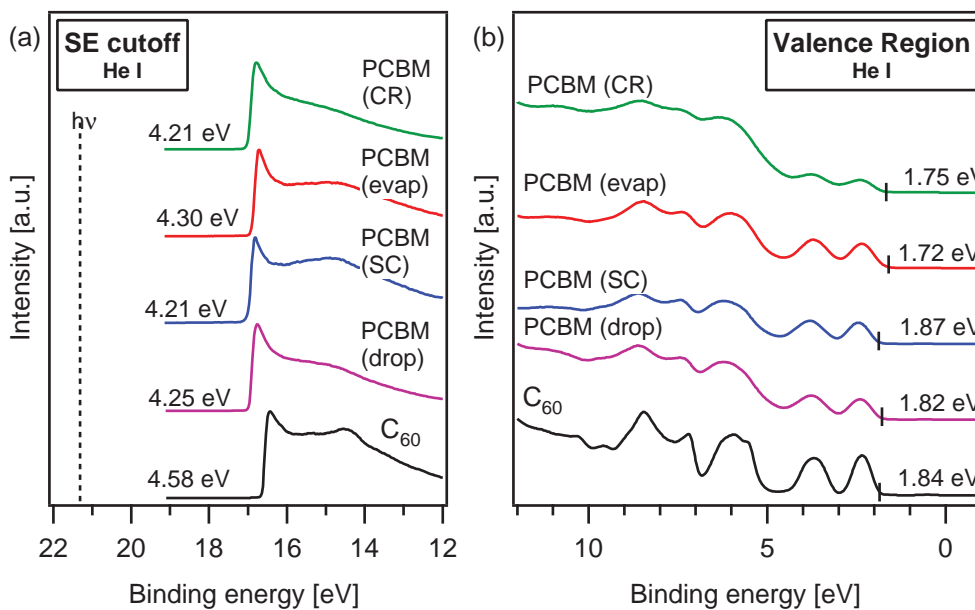


Figure 5.5: (a) Secondary electron cutoff and (b) valence region spectra of C₆₀, drop-cast PCBM, spin-coated PCBM, evaporated PCBM, and the PCBM crucible residues (from bottom to top).

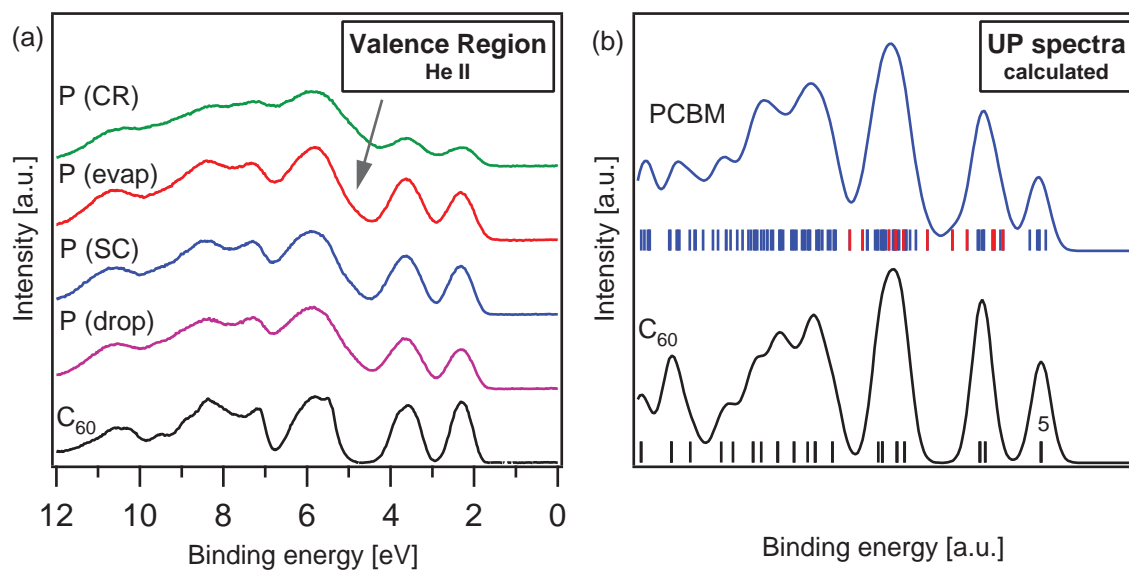


Figure 5.6: (a) He II spectra of C₆₀, drop-cast PCBM, spin-coated PCBM, evaporated PCBM, and the crucible residues. A Shirley background has been removed for all spectra. (b) Calculated valence spectra from DFT eigenvalues. The individual eigenvalues (marked as ticks in the plot) of the gas phase molecules have been convoluted by a Gaussian function with a width of 0.2 eV. The energy axis has been shifted and scaled to fit the measured spectra.

Also in the He II spectra no distinct changes or transitions towards pristine C₆₀ in the PCBM spectra due to the deposition process are observed. The great similarity to the C₆₀ valence spectrum is still preserved. Comparing the calculated spectra, this agreement between the PCBM valence spectrum and the C₆₀ valence spectrum can be explained since many of the frontier orbitals in PCBM arise from electrons located (mainly) on the C₆₀ cage. The molecular orbitals which could be identified to arise from the side chain or the bridging atom are marked as red ticks. Due to the achievable resolution, changes in the spectral features at the energies corresponding to these specific MOs could not clearly be observed. Only in the case of the evaporated film compared to the two solution-processed films (drop and SC) a minor intensity decrease in the binding energy region of around 5 eV is evident. As in this region mainly side chain specific molecular orbitals are located, this could indicate a decomposition involving a change in or loss of the side chain. In the case of the calculated C₆₀ spectrum (Figure 5.6 b) the overall number of MOs seems to be reduced. However, the applied DFT calculations simply exploit the high molecular symmetry, thus for some degenerate MOs only one value (one tick in the plot) is given. For instance, the C₆₀ HOMO is fivefold degenerate as indicated.

The comparison of the different preparation techniques show no significant changes either in chemical composition or in electronic properties. Only from the crucible residues a molecular decomposition of PCBM under high thermal stress is indicated from the changed atomic ratio. The comparison with a neat C₆₀ film shows that the electronic structure of the occupied states is mainly dominated by the molecular orbitals located on the C₆₀ core. In the energy range where contributions from MOs of the side chain were expected as deduced from the calculated eigenvalues, no clear changes in the photoelectron signal were observed. However, this might also be due to the great number of molecular orbitals forming the valence states and the limited experimental resolution. To verify or contradict the observations made from XPS and UPS IR spectroscopy as well as detailed chemical analysis of the material before and after the different preparation techniques are performed.

5.1.1 Chemical Analysis

As discussed already, photoelectron spectroscopy is a surface sensitive technique and relies on the already deposited material. In order to understand the chemical processes which

might be involved during the evaporation process, thermal analysis in combination with chemical analysis was performed.

TGA/DSC

In order to determine the temperature dependant phase-behavior of PCBM a TGA/DSC analysis was performed. The characterization of the pristine PCBM material was realized using 10 mg PCBM in a $70\mu\text{l}$ aluminum oxide crucible with a lid which has a pinhole. The temperature range was chosen according to the UHV evaporation experiments, thus a final temperature of $300\text{ }^\circ\text{C}$ was chosen. The DSC traces of the pristine material is shown in Figure 5.7.

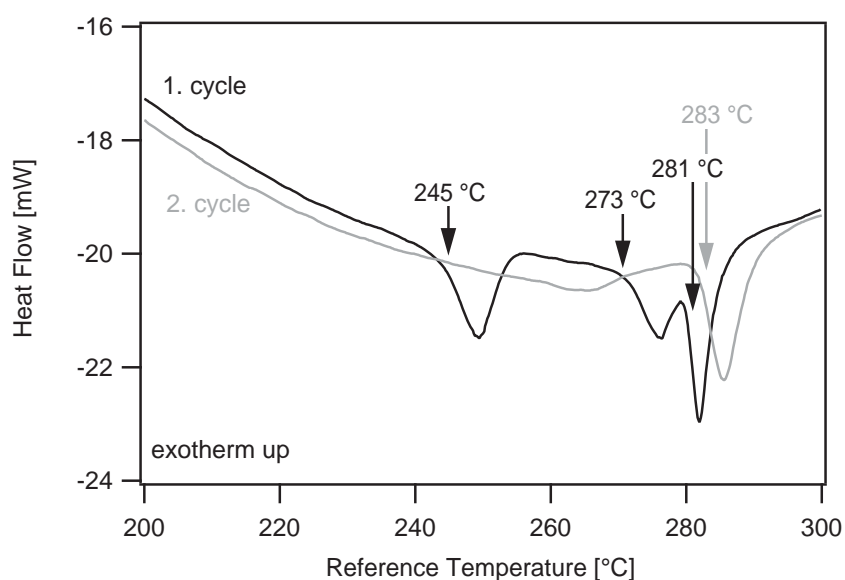


Figure 5.7: DSC trace of a pristine PCBM sample. The first heating cycle is depicted in black, the second in grey. The phase transitions are marked with their onset temperatures.

In the first heating cycle in total three transitions are observed: The first transition occurs at $245\text{ }^\circ\text{C}$, the second transition at $273\text{ }^\circ\text{C}$, and the final transition at $281\text{ }^\circ\text{C}$. The latter is most likely to be the melting point. The first transition at $245\text{ }^\circ\text{C}$ has been observed in literature before by TRINH TUNG ET AL. [119] and is attributed to the evaporation of solvent residues as a mass loss of about 1% was simultaneously detected. In case of the experiments presented here a weight loss of only 0.05% is observed. The detected integral heat flow, however, is in the same order as for the succeeding melting process. Therefore, it is very likely that a major phase transition takes place at $245\text{ }^\circ\text{C}$ accompanied by simultaneous

release of minor solvent residues. Further mass reduction has not been detected which supports the interpretation of the DSC signals to account for phase transitions only. The DSC trace of the second heating cycle shows just one phase transition at 283 °C which is in agreement to ref. [119].

These experiments confirm the observed melting of PCBM in the crucible of the evaporation source under UHV conditions. However, no evaporation or any other mass loss due to decomposition was observed in this temperature range. This can have two possible origins: During the evaporation experiments, PCBM was heated under high vacuum conditions whereas the TGA/DSC experiment was performed under atmospheric pressure. The reduced surrounding pressure influences the vapor pressure of PCBM and facilitates evaporation. Additionally, the temperature was measured by a thermocouple placed outside the evaporation crucible. Thus, the true material temperature might differ from the measured values of 240 °C to 280 °C. A different set of experiments was therefore carried out trying to simulate the thermal stress on PCBM during the UHV evaporation. To achieve this, TGA was applied in a preparative manner. Different temperature profiles were chosen according to a device production process, the phase transitions observed in TGA/DSC, and the evaporation experiments. These are summarized in Table 5.3.

Table 5.3: Thermal treatment steps of PCBM to simulate evaporation conditions

Sample	Temperature [°C]	Time [min]	Comment
1	130	5	BHJ annealing conditions
2	240	60	just before first phase transition
3	275	60	just before second phase transition
4	300	60	PCBM melt
5	350	60	molten PCBM with additional thermal stress

The samples used to simulate the thermal stress in the evaporation source crucible were also placed in 70 μ l Al₂O₃ crucibles. This crucible material was deliberately chosen to be as similar as possible to the evaporation conditions where the same crucible material is used. Hence, possible reactions with the crucible material would also be reproduced in the preparative thermal treatment performed with TGA. To prevent oxidation, the processes were conducted under nitrogen flow. After the thermal treatments, some of the samples were already recovered in a different morphological state. While sample 1 (130 °C, 5 min) and sample 2 (240 °C, 60 min) were still available as black powders after the temperature treatments, sample 3 (275 °C, 60 min) showed a calcination-like shrinkage and was

recovered as a shiny brittle solid. Samples 4 and 5 were treated above the previously determined melting point (283 °C) and were therefore retrieved as thin films covering the crucible bottom which could be transformed into black powdered samples by mechanically scraping the crucibles. The samples were then chemically characterized using UPLC-MS and the results will be discussed in the next paragraph.

UPLC-MS

Ultra performance liquid chromatography (UPLC) combined with mass spectrometry (MS) was used to separate and identify the different components present in the differently prepared PCBM samples for thin film analysis as well as in the thermally treated samples. The powdery samples of the pristine PCBM as well as the temperature treated PCBM samples were dissolved in 100 μl o-dichlorobenzene (o-DCB) and further diluted with 600 μl tetrahydrofuran (THF). To perform UPLC-MS characterization of the already deposited material, the coated wafers were washed. This was done by placing the wafers in a glass vial and adding 1 ml of o-DCB and shaking for three minutes. The resulting solution was separated and evaporated to dryness using a rotary evaporator under reduced pressure to achieve a dry and solid residue. These were then redissolved in 20 μl o-DCB and this solution was again thinned by adding 60 μl THF.

The UPLC-MS characterization of the pristine material (not shown) confirmed the high purity as only one signal with the expected mass of $m/z = 910.2$ was detected. The same holds true for the spin-coated sample. In the UPLC chromatogram of the wafer extract after the evaporation multiple signals could be detected. The two chromatograms plotting the absorbance at 255 nm over the retention time are shown in comparison in Figure 5.8.

In the chromatogram of the wafer extract after spin-coating only one signal at a retention time of 5 min could be detected. From the mass spectrometer trace, this signal could be identified as PCBM ($m/z = 910.2$). The same signal with the corresponding PCBM mass is observed in the case of the wafer extract after evaporation at a similar retention time ($t_r \approx 5.1$ min). However, additional signals at $t_r \approx 4.2$ min, at $t_r \approx 6.1$ min, and at $t_r \approx 10$ min are observed. These signals clearly show the presence of additional chemical species in the evaporated film. While the first signal corresponds to an undefined side-product, the signal at $t_r \approx 6.1$ min has the same mass as PCBM. A probable reaction scheme to produce this species would be an isomerization of PCBM to the [5,6]-cage-

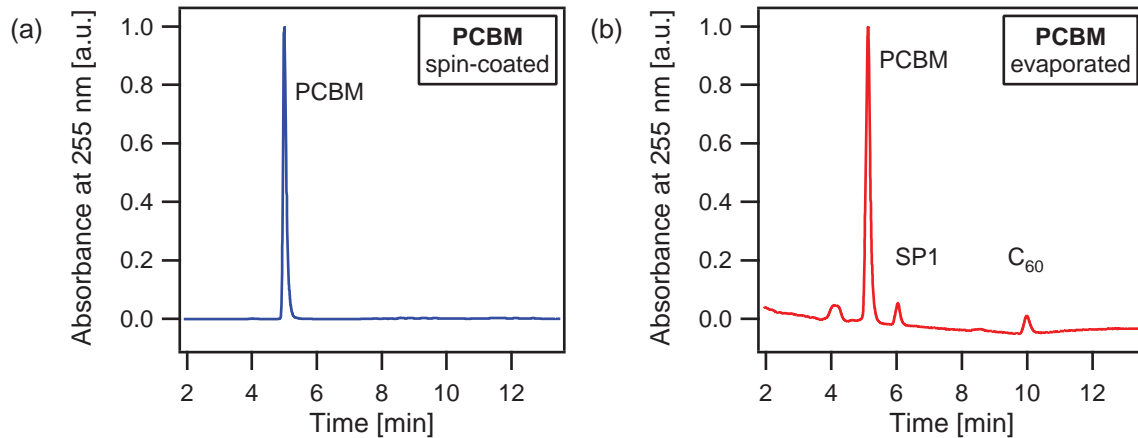


Figure 5.8: (a) Chromatogram of the wafer extract of the spin coated film. (b) Chromatogram of the wafer extract after thermal evaporation. While in the spin-coated film only one signal from PCBM could be detected, in the chromatogram of the evaporated film multiple signals indicate molecular degradation.

opened fulleroid [80]. The signal corresponding to this side product is marked as SP1 in Figure 5.8 b. The signal at $t_r \approx 10$ min showed a mass of $m/z = 720$ which corresponds to C_{60} . Thus, for some molecules the complete side chain was eliminated during the evaporation process. From the integral absorbance intensities the relative concentrations of the individual side products can be calculated. From this follows that the evaporated PCBM film has a reduced PCBM content of approx. 77 % as compared to the PCBM content in the pristine materials (99.8 %). The detailed intensity evaluation is summarized in Table 5.4.

Table 5.4: Intensity evaluation of the chromatogram of the wafer extract after evaporation

t_r [min]	Integral Intensity	Fraction [%]
4.1	784525	6.32
4.2	347849	2.8
5.13^a	9594312	77.34
6.04 ^b	765935	6.17
8.54	111643	0.90
9.98 ^c	801775	6.46

^a corresponds to PCBM

^b corresponds to SP1

^c corresponds to C_{60}

The chemical analysis confirms the decomposition of PCBM during thermal evaporation as was already indicated from the PES results presented above. Interestingly, the detected

side products all have masses that allow the conclusion, that the C_{60} cage remains intact. For some of the molecules, the side chain was completely eliminated but no mass signal corresponding to this phenyl-butyric acid methyl ester group could be detected. This could be either due to the fact, that the side chain is not removed in one step or that the remaining molecular parts only weakly interact with the chromatography column and are therefore flushed out directly with the solvent.

The chemical composition of the thermally treated PCBM samples (Tab. 5.3) in addition to crucible residues recovered from the UHV evaporation source was also analyzed using UPLC-MS. The resulting chromatograms are depicted in Figure 5.9.

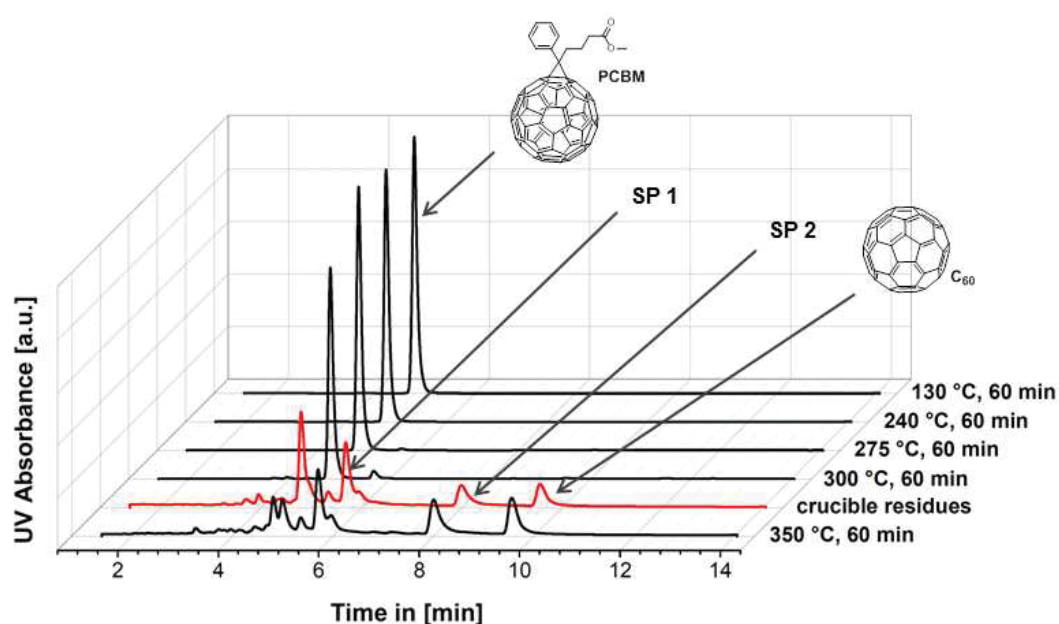


Figure 5.9: UPLC chromatograms of the differently thermally treated PCBM samples in comparison to the crucible residues. The chromatograms are displayed in the order of decreasing PCBM content. The appearances of the side products SP1, SP2, and C_{60} are indicated.

The chromatograms show that during the commonly used temperature treatment for annealing bulk heterojunction layers and even elevated temperatures up to $240\text{ }^{\circ}\text{C}$, no molecular changes should be expected. However, as soon as the solid PCBM has undergone the first phase transition at $245\text{ }^{\circ}\text{C}$, first decomposition products could be detected (see chromatogram of sample 3 at $t_r = 5.7\text{ min}$). This signal corresponds to the before mentioned side product 1 (SP 1), which does not differ from PCBM by mass and thus could be a [5,6]-cage-opened fulleroid. The overall purity of the PCBM sample treated at $275\text{ }^{\circ}\text{C}$ is reduced from 99.8% to 98.6%, although so far only a solid state phase transition oc-

curred according to the TGA/DSC experiments. Once PCBM melts and is kept in the melt at 300 °C for 60 min the purity is further reduced below 90 % and traces of two additional side products, namely SP 2 and C₆₀, are detected. Further stressing PCBM in the melt at 350 °C for 60 min reduced the PCBM content below 10 % while a C₆₀ content of about 15 % was observed. The chromatogram of the crucible residue obtained after the evaporation experiment shows a PCBM content of about 32 % and the decomposition pattern closely resembles the one obtained for sample 5 (350 °C, 60 min). This is somewhat surprising as the temperature measured during the evaporation experiment ranged from 240 °C to 280 °C. Yet, the temperature was monitored with a thermocouple placed outside the crucible and provides therefore only a rough measure for the actual temperature stress on PCBM inside the crucible. The comparison of the UPLC-MS results suggests that the real temperature inside the crucible was in the range of 320 °C to 340 °C giving considerable material degradation.

From the mass analysis of the UPLC separated molecular species can be seen that the decomposition products have predominantly masses between $m/z = 904$ and $m/z = 913$. Since the molecular mass of PCBM is $m/z = 910$, this shows that no C-C or C-O bonds are involved in most of the decomposition reactions. The exemption is the side product at a retention time of 9.6 min which could be identified as C₆₀ ($m/z = 720$) formed through the complete elimination of the side chain. The side product at $r_t = 8$ min (labelled as SP2) has a mass of $m/z = 904$. This corresponds to the formal elimination of six hydrogen atoms. As this specie is only formed at temperatures above 300 °C, a large variety of reactions are possible and many different structures thinkable.

Although the exact chemical structure could not be determined, the elimination of hydrogen would likely occur through the thermal elimination of protons in the side chain (SP A) or via radical loss of hydrogen and addition to the fullerene core (SP B) or a combination of both. The structures of these possible candidates involved in the decomposition of PCBM are shown in Figure 5.10 together with PCBM and C₆₀.

5.1.2 IR Spectroscopy

Using IR spectroscopy the vibrational modes of PCBM were probed. If changes e.g. in the side chain configuration or defragmentation involving the complete side chain occur, they should be traceable with IR spectroscopy, as the vibrational modes are specific to the

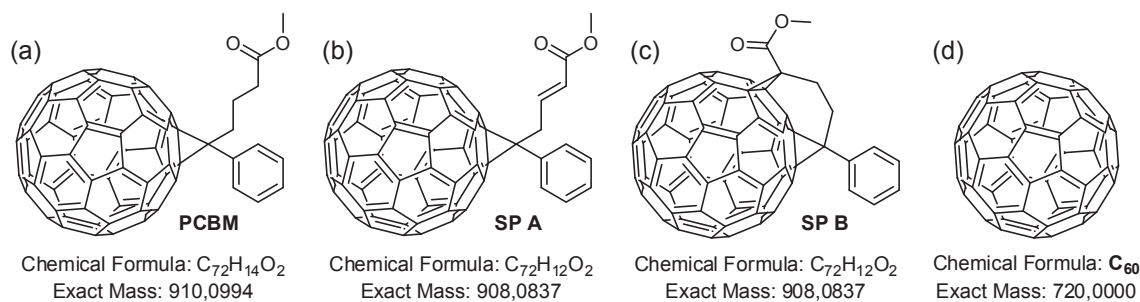


Figure 5.10: Structures of (a) PCBM, possible side products (b,c) and (d) C_{60} . SP A is a proposed structure for a side product formed through thermal elimination of two protons (b) and SP B gives the proposed structure for a side product formed by radical loss of hydrogen and addition to the fullerene core (c).

bonding configuration. The experiments were performed on the exact same samples as prepared for the PES experiments. After the PES characterization, the samples were taken out of the UHV system and were installed in the spectrometer together with a freshly cleaned Si wafer substrate as a reference. The evaporated PCBM film is compared to the spin-coated film. The layers obtained via drop-casting generally yield rather inhomogeneous films concerning layer thickness which is obstructive in FT-IR data evaluation. Therefore, only one solution-processed layer (i.e. the spin-coated sample) was taken for comparison. The spectra were measured in transmission geometry with a resolution of 4 cm^{-1} . The resulting IR spectra are shown in Figure 5.11 together with a DFT calculated spectrum.

The assignment of the different vibrational modes is assisted by DFT calculations⁴ (based on the BP86 functional) of the IR active vibrations shown in blue at the top in Figure 5.11. For better comparison of the calculated spectra with the experimental spectra, the DFT-calculated absorption lines were broadened using Gaussian profiles with a full width at half maximum of 10 cm^{-1} . The agreement between the calculated and measured spectra is sufficient for unambiguous mode assignment for most of the absorption bands of the spin-coated PCBM spectrum. Compared to this spectrum changes in spectrum of the evaporated PCBM are observed. As a guide to the eye, these are encircled in Figure 5.11. Additional bands appear at 1510 cm^{-1} , 1540 cm^{-1} , and in the range of 1630 cm^{-1} to 1690 cm^{-1} . As these absorption bands are not occurring in the DFT calculated spectra, they are a clear indication for chemical changes due to the evaporation process. The additional bands in the case of the evaporated film in the range of 1630 cm^{-1} to 1690 cm^{-1} potentially

⁴ provided by A. Fuchs, formerly BASF SE, now SAP

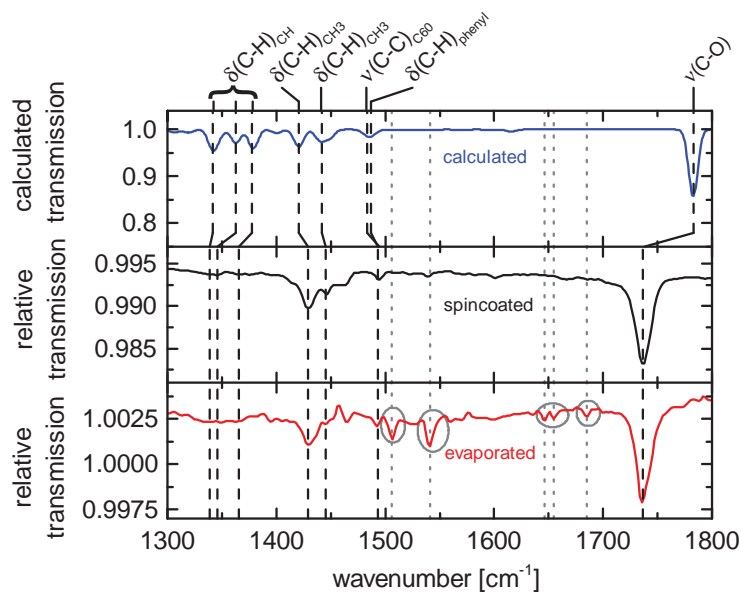


Figure 5.11: IR spectra of spin-coated (black) and evaporated PCBM (red). The DFT calculated vibration spectrum used for vibration mode assignment is shown at the top (blue).

correlate to the proposed reaction products (see section 5.1.1) in which a carbon-to-carbon double bond is formed as these bonds are typically observed in this wave number range [98]. This would also correlate to the proposed change in side chain structure derived from UPLC-MS as depicted in Figure 5.10 b. However, a clear assignment would require additional calculations which were not performed since the exact structure of the side products emerging during the evaporation are yet unknown. Therefore, the changes in the vibrational modes should only be considered as a clear indication of a change in the molecular structure of PCBM during evaporation.

5.1.3 Summary

Through the combination of photoelectron spectroscopy, chemical analysis, and IR spectroscopy the effects of the thermal stress during evaporation of PCBM in contrast to solution processing were thoroughly investigated. The chemical analysis confirmed the decomposition of PCBM during evaporation and in the crucible as indicated from the PES measurements. From the UPS results, no significant changes in the electronic properties of PCBM in dependence of the different preparation techniques could be deduced. As most of the frontier molecular orbitals in the valence region arise from the π -electron system of the C_{60} cage, this is not surprising, assuming that the C_{60} structure remains unaltered during

the decomposition reactions. This could also be confirmed by the UPLC-MS experiments as mostly proton elimination reactions are responsible for the observed mass changes. In addition, C₆₀ could be identified as one of the side products. The decomposition of PCBM already starts when the first internal phase transition occurs and increases significantly beyond the melting point temperature of 283 °C. Changes in the molecular structure could be confirmed by FT-IR measurements but the exact structure of the side products could not be determined as many reaction paths are possible and the assignment of the new modes due to the decomposition is not reliable without a suitable theoretical model based on the anticipated structure.

The presented set of experiments show that thermal evaporation of PCBM is very inefficient, strongly influenced by the evaporation conditions, and the material deposited as a thin film but also remaining in the crucible contains a significant amount of other fullerene-derived impurities. In the crucible residues, the PCBM content is so low that the material should be discarded after the deposition and not used for repeated depositions. Therefore, the thin film deposition of PCBM via thermal evaporation was not further pursued in the following experiments.

5.2 Comparison of Drop-cast and Evaporated DH6T

The following section deals with synchrotron experiments performed on films of DH6T prepared via both thermal evaporation in UHV and drop-casting in the glass cell at the SoLiAs end station at BESSY II. The spectra were recorded during two different synchrotron operation modes. The spectra of the drop-cast film were obtained during standard multi bunch hybrid mode with individual bunch currents of up to 0.9 mA giving a total ring current of about 300 mA. The evaporated film, however, was characterized during a beam time slot in which the synchrotron was operated in low- α multi bunch hybrid mode. This mode is designed to offer possibilities to perform time-resolved experiments in the hybrid mode [120]. Although this option is not exploited in our measurements the reduced bunch current of 0.1 mA per bunch affects the total measured intensity. Therefore, the following spectra are all normalized in intensity to allow comparison of the films.

From the survey spectra shown in Figure 5.12 a all appearing emissions, namely C1s, S2p, and S2s can be identified as expected from the molecular formula. A spectrum of the ITO substrate is included as the film thickness of the drop-cast layer is low, therefore some substrate lines especially at low binding energy (and thus high kinetic energy) are still visible (e.g. In4d at 17 eV). In the drop-cast film one additional feature is observed at roughly 70 eV. This could be identified as Bromine 3d. The origin and possible influences will be discussed in a separate section (see sec. 5.2.1). The core level emissions at $E_{\text{excit}} = 600$ eV of carbon and sulphur for both films are shown in Figure 5.12 c and d.

The asymmetric shape of the C1s core level line indicates the presence of different carbon bonding states within the molecule comparable to P3HT (see chapter 4.2). In total three different bonding sites as marked in the chemical structure in Figure 5.12 b are identified. The component at the lowest binding energy is attributed to the C-C_{thio} bond (1) within the thiophene units at 284.6 eV for the evaporated film and at 284.4 eV for the drop-cast film measured at 600 eV. The emission stemming from the C-S_{thio} bond (2) are located at approximately 0.7 eV to higher binding energies. In order to take the equal number of these bonding states into account their intensity ratio was fixed to 1:1 during the fitting routine. The remaining third component at 285.7 eV and 285.4 eV for the evaporated and drop-cast films, respectively, are assigned to the C-C bonds within the hexyl chains. This peak assignment follows the working hypotheses presented in section 4.2.1. According to the chemical structure, for all three components the same intensity is expected. However,

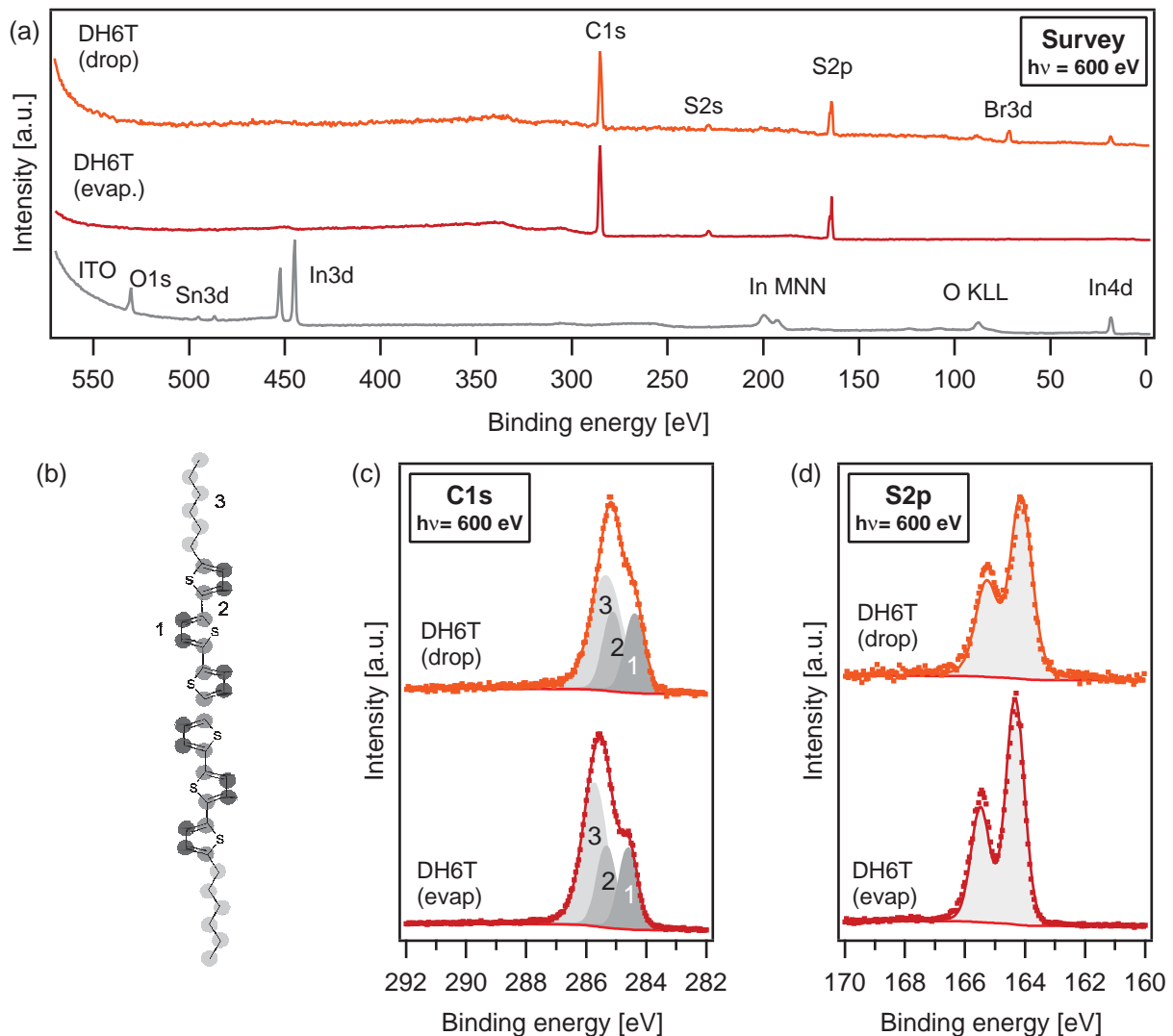


Figure 5.12: (a) Survey spectra of ITO, evaporated DH6T and drop-cast DH6T (from bottom to top). (b) Molecular structure of DH6T. (c) C1s core level emission and (d) S2p core level emission of evaporated (bottom) and drop-cast DH6T (top) at $h\nu = 600$ eV. The C1s emission line is fitted according to the three different carbon bonding sites as indicated in (b).

the data does not meet this expectation but rather shows an intensity increase of emission (3) by a factor of roughly 2. A possible reason for this enhanced intensity could be an upright orientation of the rather rod-like molecules as described in literature [75, 112, 121]. This behavior will be further investigated by a variation of excitation energy to probe a different depth of the film surface (see section 5.2.2). The S2p core level depicted in Figure 5.12 clearly shows the expected doublet structure. The absolute binding energy

of the drop cast DH6T S2p component is at 164.1 eV and therefore 200 meV shifted to lower binding energies compared to the evaporated DH6T film.

The stoichiometry can be calculated using the original intensity ratio of the C1s emission to the S2p emission. Since these spectra were obtained at a synchrotron light source with polarized light, tabulated asymmetry factors [91] as well as the inelastic mean free paths for the different kinetic energies [93] have to be considered (see appendix B). These calculations are described in 3.3.3 and in detail in ref. [92]. The results are 6:1.01 in the case of the evaporated film and 6:1.19 in the case of the drop-cast film. These values are in good agreement with the actual atomic C-to-S ratio of 6:1. Therefore it can be concluded that both deposition routes allow for DH6T film preparation without decomposition.

Minor variations in broadening and a consistent shift to lower binding energies is observed for the films deposited from solution compared to the evaporated film. A similar effect has been observed in literature and is attributed to changes in morphology due to the different preparation techniques [105]. Additionally, the spectra of the evaporated and the drop-cast films were obtained during two separate beam times with different synchrotron operation modes (high- α in the case of the evaporated film and low- α in the case of the drop-cast film). Therefore, the films might have suffered differently from the radiation exposure.

5.2.1 Bromine Content

As DH6T was used as received without any further purification some reaction products from the material synthesis could still be present. One reaction or side product component could be identified, namely bromine which is used in the oligomerization process [75]. According to the reaction scheme Br is introduced from N-bromosuccinimide and is attached to a bithiophene unit after a monobromination reaction. The Br3d core level emission at 150 eV is shown in Figure 5.13.

The doublet structure of the d-orbital is clearly resolved at the expected intensity ratio of 3 to 2. The Br3d_{5/2} emission is centered at 70.1 eV as observed for Br-organic compounds [85]. Including the integrated intensity of the Br3d emission measured at 600 eV into the composition calculation a relative Br content of up to 3 % is found. A bromine contribution was detected in almost all solution-processed layers. In some cases even the evaporated layers showed a small Br intensity at the same binding energy position. However, the

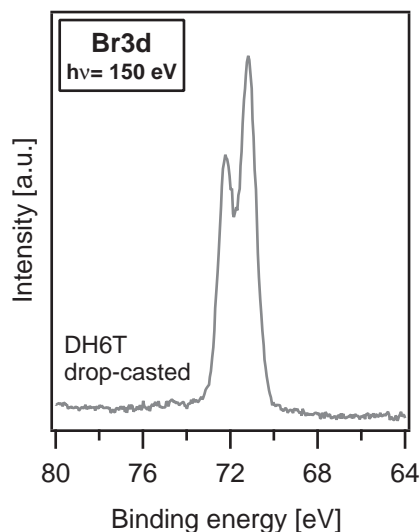


Figure 5.13: Br3d emission at 150 eV of a drop-cast layer of DH6T showing possible residues of synthesis reaction products.

evaporation process itself can be viewed as a cleaning process as the smaller bithiophene units are most likely more volatile. In fact, a pressure increase at temperatures well below the actual evaporation temperature was observed when heating up a freshly filled DH6T crucible. In any case, Br-related impurities cannot be excluded for any DH6T film since a concentrations around or below the detection limit of 0.1 atom% to 1 atom% will not give rise to a distinct PES signal.

The increased bromine content could also be a source for the previously observed core level shifts comparing evaporated and drop-cast DH6T, as it might lead to unintentional doping and thus different Fermi level positions.

5.2.2 SXPS Observed Orientation of DH6T

To a certain extent depth profiling can be achieved at a synchrotron light source through the variation of excitation energy. In the case of DH6T this technique was applied on an evaporated film to further support the assumption of molecular orientation based on the observed intensity discrepancies in section 5.2. To track the evolution of the C1s components a series of spectra from highest surface sensitivity achieved at 320 eV to rather bulk-representing spectra at 600 eV are recorded. The result is shown in Figure 5.14.

It can be clearly seen from Figure 5.14 that the absolute positions of the previously obtained three components remain unchanged with the variation of excitation energy. However, the absolute intensity and the relative intensity ratio changes. The decrease in absolute intensity is caused by the interplay of cross

section and photon flux. The cross section of the C1s decreases from roughly 0.8 Mb at 320 eV to 0.17 Mb at 600 eV photon energy [91]. The flux changes in the same photon energy range from 2×10^{12} Photons / (s · 100 mA · 0.1 %BW) to 3.5×10^{12} Photons / (s · 100 mA · 0.1 %BW) [122]. As the measured intensity I is proportional to the product of cross section σ and flux J_0 in a first approximation, the measured C1s intensity decreases with increasing excitation energy in the considered photon energy range. Nonetheless, the relative intensity changes of the three components attributed to the different carbon bonding sites within DH6T cannot be caused by this change in cross section and flux.

To investigate the intensity ratios of the individual components more closely, for three different excitation energies, namely 400 eV, 500 eV, and 600 eV, the carbon contributions are separated with the help of a fitting routine (see Figure 5.14 b-d). Consistent results were obtained using three individual Voigt profiles. The fits give two components with almost equal intensity at 284.3 eV (1) and 285 eV (2) and one component at 285.6 eV (3) with higher intensity than the first two components. The agreement of the fits to the measured data seems reasonable in all presented cases as can be seen from the five times magnified error curve in Figure 5.14 b to d at the bottom. Despite the overall intensity decreases with increasing excitation energy, the intensity of the two lower binding energy components (1 & 2) increases slightly with increasing excitation energy indicating a damping of these two emission by the aliphatic carbon atoms (3) for highest surface sensitivity. The emission (3) at 285.6 eV strongly decreases in relative intensity from 320 eV excitation energy to 600 eV excitation energy. Thus, at the sample surface probed with the lowest excitation energy the component attributed to the hexyl chain shows the highest intensity and is increased compared to the other two thiophene-core associated components by a factor of roughly 6. The larger the probing depth gets with increased excitation energy the more the intensities of the three components equalize until for $h\nu = 600$ eV a ratio of 1:1:1.7 is reached. These observations support the assumed upright orientation of the molecule and agrees to the reported orientation of DH6T determined by x-ray diffraction [75, 112].

To exclude possible radiation influences a series of spectra of the S2p emission line for the same kinetic electron energies were taken from 200 to 480 eV excitation energy. The spectra are given in Figure 5.15.

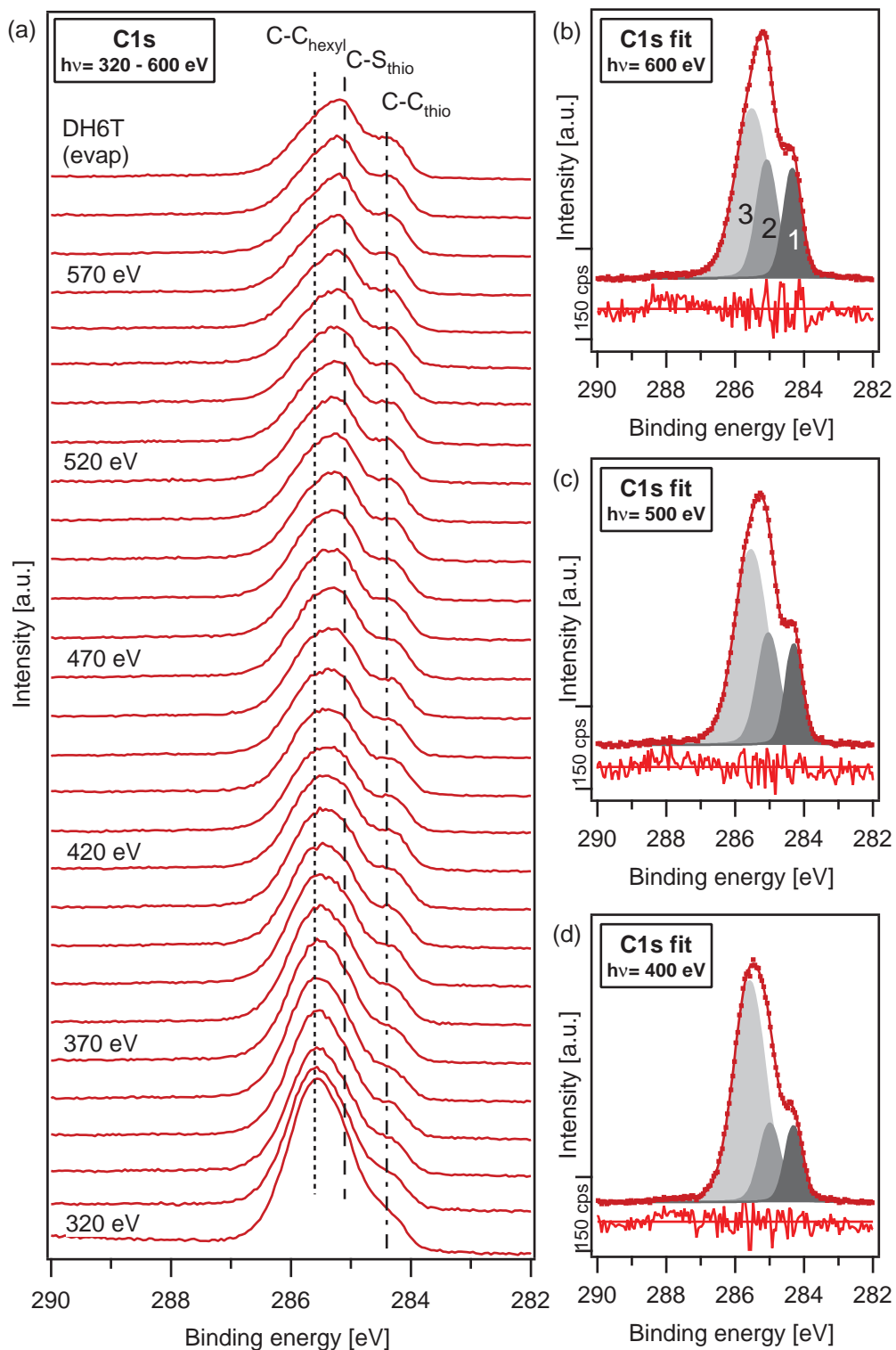


Figure 5.14: (a) C1s core level evolution from 320 eV to 600 eV excitation energy. On the right, detailed line fits following the assignment as presented in Figure 5.12 including a five times magnified error curve are shown for (b) 600 eV, (c) 500 eV, and (d) 400 eV (from top to bottom).

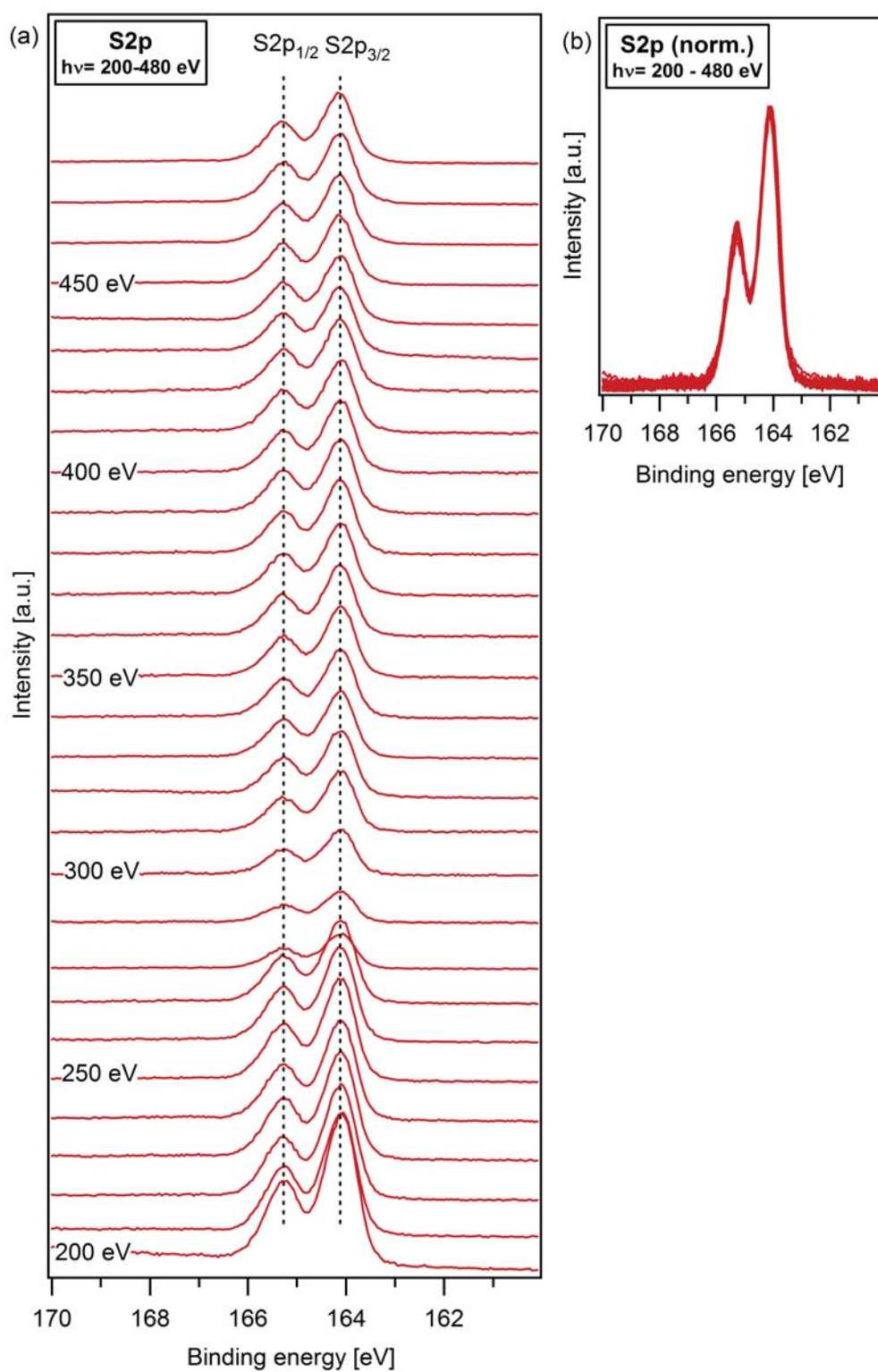


Figure 5.15: (a) S2p core level evolution from 200 eV to 600 eV excitation energy. (b) All S2p spectra normalized in intensity showing no variation in position or line shape.

Independent of the excitation energy, the S2p binding energy position stays constant as indicated by the two dashed lines. Furthermore, the doublet structure is clearly resolved in all cases and the expected intensity ratio for p-orbitals of 2:1 is preserved. The intensity drop for photon energies in the range of 280 to 300 eV is due to the beam line inherent absorption due to carbon contaminations. Therefore all spectra are additionally represented background corrected and normalized to their maximum intensity in Figure 5.15 b. From this representation the equivalence of all spectra concerning line shape and position is even more pronounced as the individual traces perfectly lie on top of each other. Thus, from the sulphur peaks at the different kinetic energies no indications towards decomposition or extensive radiation induced changes can be drawn.

As a final remark it should be noted that PES is inherently no method to examine molecular orientations. Therefore these measurements can only support the assumption of a molecular orientation (almost) perpendicular to the sample surface. To confirm this other techniques such as x-ray diffraction (XRD) or near edge x-ray absorption fine structure (NEXAFS) measurements need to be applied.

5.2.3 Electronic Properties

The electronic structure of the filled states of DH6T is determined from SXP spectra measured at 90 eV. The resulting valence level spectrum as well as the secondary electron cutoff spectrum are shown in Figure 5.16.

The valence fingerprint region of DH6T is characterized by two rather low intensity features centered at 1.5 eV and 2.6 eV followed by a third maximum at 3.5 eV. According to density DFT calculation results presented by DUHM ET AL., these features in the low binding energy range are derived from delocalized π -orbitals and narrowly spaced localized π -states of the conjugated sexithiophene backbone [112]. The first emission is attributed to the DH6T HOMO. Between 5 eV and 8 eV binding energy a broad high intensity feature is observed followed by two further maxima at 10.7 eV and 14 eV, respectively. These features are dominated by localized σ -states mainly located on the hexyl chains of DH6T [112]. The HOMO_{onset} positions are determined to be 0.98 eV and 1.01 eV for the evaporated and drop-cast DH6T, respectively. From the SE cutoff spectra work functions of 4.12 eV and 4.09 eV were determined for the evaporated and drop-cast layer, respectively. Thus both films exhibit the same ionization potential of 5.1 eV. This value is in good agree-

ment to the published values of 5.06 eV [123] and 4.7 eV–5.0 eV [124] of DH6T on gold. Besides the same electronic properties derived from the IP the fingerprint valence structure of both films shows perfect agreement irrespective of the chosen preparation route. Furthermore, the measured structure coincides remarkably with reported spectra from literature [124] both in shape as well as HOMO_{onset} position. However, it needs to be noted that in a recent publication, OPITZ ET AL. [109] determined the frontier orbital onset of unsubstituted sexithiophene at 0.4 eV. According to their findings higher onset values are caused by radiation exposure and consequent molecule degradation. Therefore the values determined in this work could already hint towards synchrotron radiation induced shifts.

In order to draw a complete energy level diagram, information about the LUMO position is needed. In the case of DH6T no inverse photoemission data was available. However, for the unfunctionalized analogue sexithiophene (6T) IPES measurements have been performed [125]. This HOMO LUMO gap from combined UPS and IPES measurements coincides with the DH6T HOMO LUMO gap determined by cyclic voltammetry [126]. Therefore, a band gap of 2.3 eV is assumed for DH6T. The resulting line-up is represented in Figure 5.17 and is valid for both, the solution-processed as well as the evaporated DH6T layer.

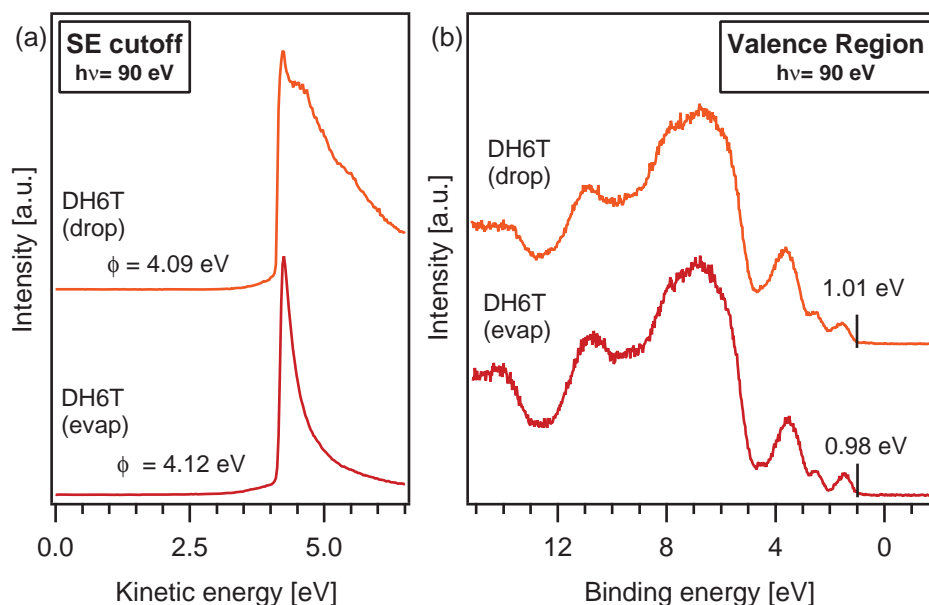


Figure 5.16: (a) Secondary electron cutoff and (b) valence region spectra of an evaporated (bottom) and a drop-cast (top) film of DH6T.

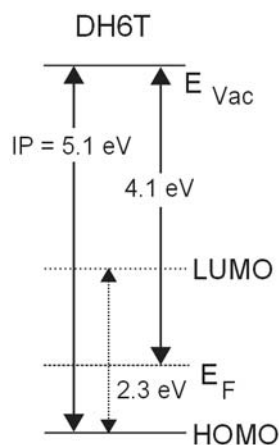


Figure 5.17: Energy level diagram of DH6T. As the measured electronic properties were identical, independent of the preparation technique, it is valid for both solution- as well as vacuum-processed DH6T. The energy gap value is taken from literature [125, 126].

5.2.4 Summary

The equivalence in producing thin DH6T films with the same electronic properties via the two different preparation approaches based on thermal evaporation and solution processing, respectively, could be clearly shown with the above presented results. Deviations are possible, since the molecular orientation influences the measured spectra. In drop-casting experiments, the overall molecular orientation is usually reduced compared to evaporated films. Nonetheless, in both cases a rather upright standing orientation of the DH6T molecules on the substrate was deduced from the C1s relative intensity changes of the individual bonding site contributions in the SXPS measurements. This is in agreement with previously determined DH6T orientations using x-ray diffraction [75, 112]. In addition, it should be noted that drop-cast layers are more susceptible for layer inhomogeneities such as pinholes or pronounced thickness gradients. Furthermore, the detected bromine content, which is possibly due to syntheses remains in the source material, could be a cause of unintentional doping. However, effects on the electronic levels have not been observed as the evaporated and drop-cast layers showed different bromine contents but the same energy level positions.

The presented experiments prove that DH6T is a very valuable material in characterizing donor:acceptor interfaces as it enables a versatile sample preparation. For the following experiments, DH6T will therefore be utilized as a P3HT substitute as it can be deposited via thermal evaporation allowing defined interface preparation as well as by solution-based techniques such as drop-casting allowing bulk heterojunction formation.



6 Deciphering the Band Energy Diagram of a PCBM:DH6T BHJ

As the previous results show that DH6T can indeed be deposited via both thermal evaporation and from solution, this diversity in processing conditions is utilized to gain a deeper insight into the electronic interface structure of PCBM and DH6T. The results of a classical UHV step-by-step interface experiment are presented followed by the results obtained from solution-processed blend films. Finally, the findings of both approaches are combined to derive a model which describes the electronic interface properties across the bulk heterojunction and into the donor cap layer. The experiments were all performed at the SoLIAS endstation at BESSY II.

6.1 Interface Experiment

To characterize the electronic interface properties of the PCBM/DH6T heterostructure a classical in-situ UHV interface experiment was performed using stepwise deposition of the donor DH6T onto a drop-cast PCBM film. PCBM was deposited in the glass cell from a 2 mmol l^{-1} chlorobenzene solution on argon sputter-cleaned ITO. The evaporation of DH6T was performed with a homemade effusion cell. The base pressure of the deposition chamber during evaporation was held in the 10^{-8} mbar regime. The Al_2O_3 crucible temperature was around 170°C . To calculate the film thicknesses and the mean evaporation rate the intensity increase of the S2p emission of DH6T was used. For these calculations, the inelastic mean free path of the emitted photoelectrons in the DH6T layer is needed. It was calculated using the NIST database and the tabulated values for the respective electron energies can be found in the appendix (see section B). An evaporation rate of approximately 6 \AA min^{-1} was obtained. The obtained survey spectra are shown in Figure 6.1 with drop-cast PCBM as the substrate at the bottom followed by the individual DH6T deposition steps.

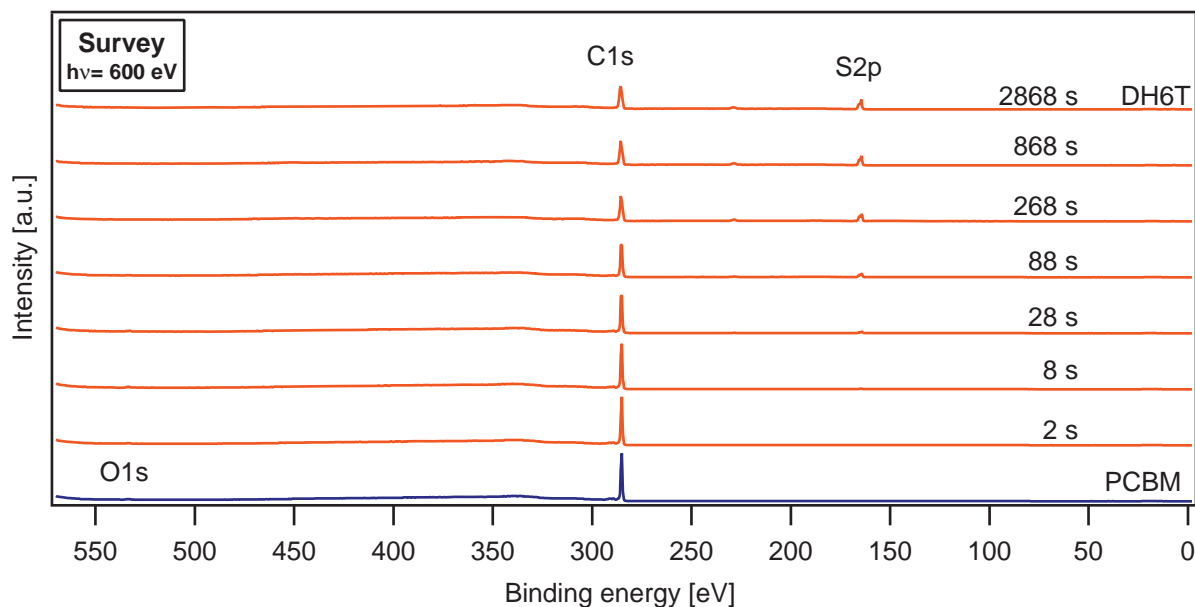


Figure 6.1: Survey spectra of PCBM and DH6T deposited via stepwise evaporation. The overall deposition time of each spectrum is indicated.

The survey spectrum of PCBM is dominated by the high intensity C1s signal at 285 eV. The O1s signal of PCBM is also present but hardly visible in the survey spectrum representation due to the low signal intensity. With increasing DH6T deposition the evolution of the S2p (and S2s) signal is clearly observed and the C1s signal shape changes. No other elemental features are observed indicating clean and homogeneous sample preparation. For a more detailed analysis the core level spectra are shown in Figure 6.2.

In the O1s spectrum of PCBM (Figure 6.2 a at the bottom) two oxygen components are clearly discerned and fitted using two Voigt profiles of equal intensity. The emission at 532.5 eV stems from the carbonyl group (1) while the component at 533.9 eV is attributed to the methoxy group (2). As only PCBM contains oxygen these emissions originate solely from this molecule also in the spectra where DH6T is already adsorbed. The binding energy of these two components stays constant with increasing DH6T coverage and the intensity decreases rather abruptly between the overall deposition times of 88 s and 268 s. In the C1s spectrum of PCBM the expected peak shape of one central, high intensity feature at 285 eV is observed followed by a satellite structure with maxima at 287 eV and 289 eV to which also the C-O bonds possibly contribute. The main PCBM emission is indicated by the shaded fit. With increasing DH6T deposition time the peak shape changes until from around 268 s the DH6T characteristic asymmetric peak shape is observed. For the thickest

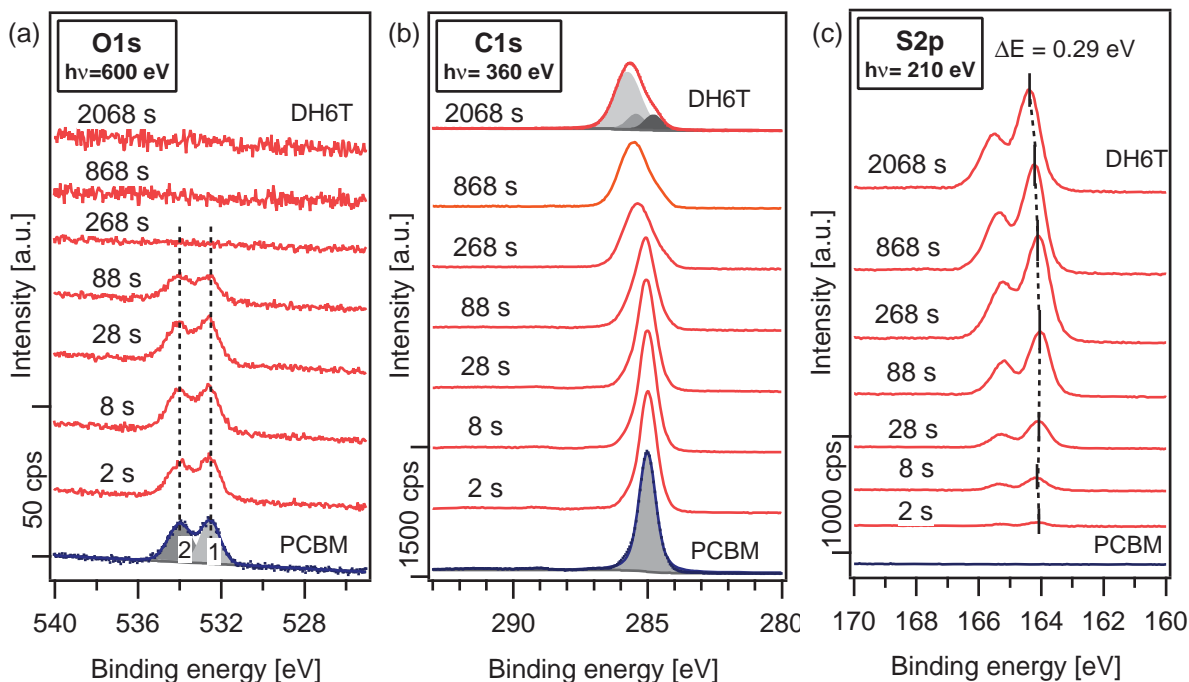


Figure 6.2: (a) O1s spectra, (b) C1s spectra, and (c) S2p spectra of PCBM as substrate and DH6T deposited stepwise via thermal evaporation. All spectra are recorded at highest surface sensitivity. The PCBM O1s emission stays constant in energy while the DH6T S2p emission shifts by 0.3 eV to higher binding energies. Adapted from [127].

DH6T film after a total deposition time of 2068 s (which corresponds to a film thickness of about 25 nm) the three C1s components are indicated by fits using Voigt profiles following the analysis presented in chapter 5.2. Already for the very first deposition step a S2p signal is observed with the maximum of the S2p_{3/2} at around 164.1 eV. Its intensity significantly increases up to a deposition time of 268 s. During the DH6T deposition, the S2p signal shifts by 0.3 eV to higher binding energies. Since the DH6T signal in the C1s is not as readily spotted as the S2p signal due to the high intensity of the PCBM C1s, difference spectra have been calculated for the first deposition steps. These are shown in Figure 6.3 together with the unchanged C1s emissions for the higher coverages.

The difference spectra were calculated in such a way as to eliminate the fullerene-derived high energy shake structure. From the difference spectra the presence of the DH6T C1s signal also from the first deposition steps can be seen. Additionally, also in these core level lines a shift of the intensity maximum to higher binding energies is observed. Due to the uncertainties introduced by the calculation of the difference spectra, the magnitude of the shift is not evaluated.

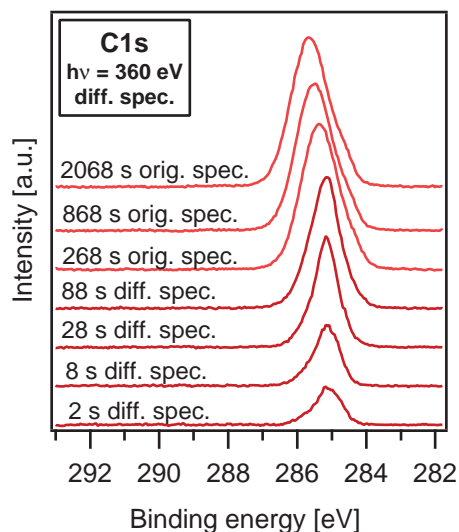


Figure 6.3: C1s difference spectra for the low DH6T coverages together with the original DH6T C1s spectra for total deposition times of 268 s to 2068 s.

As the DH6T molecular structure is rather rod like, different orientations of the molecules in thin films have been observed [121]. The steady increase of S2p intensity but sudden decrease of substrate emission (e.g. the O1s signal) hints to variations in growth mode and could indicate that DH6T initially (up to 28 s) is penetrating the PCBM layer and then starts to overgrow PCBM. Also a change from initially parallel to the surface orientate DH6T to more or less upright standing molecules may be considered. On the one hand, the constant energy of the O1s emission of PCBM indicates constant Fermi level in the substrate independent of the DH6T coverage. The shifts in the DH6T core level, on the other hand, indicate band bending in this material.

The secondary electron cutoff and the valence region spectra of the interface experiment are shown in Figure 6.4 a and b, respectively. The secondary electron cutoff changes gradually with increasing DH6T coverage to lower kinetic energies. Thus, the work function changes from initially 4.37 eV for PCBM to 3.81 eV for DH6T after the last deposition step. Up to around 88 s of DH6T deposition the valence spectra are dominated by the PCBM features. After that the shape of the fingerprint valence region resembles more closely that of DH6T. The DH6T HOMO, however, is already visible after the first deposition step allowing the determination of the onset value. The $\text{HOMO}_{\text{onset}}$ values of PCBM (1.67 eV) and the stepwise deposited DH6T (0.83 eV to 1.13 eV) are indicated in Figure 6.4 b. From the work function and $\text{HOMO}_{\text{onset}}$ values of PCBM and DH6T after the last deposition step, the ionization potentials are derived. These are 6 eV in the case of PCBM and 4.9 eV in the case of DH6T which are both in agreement to the previously determined values (see sections 4.1 and 5.2).

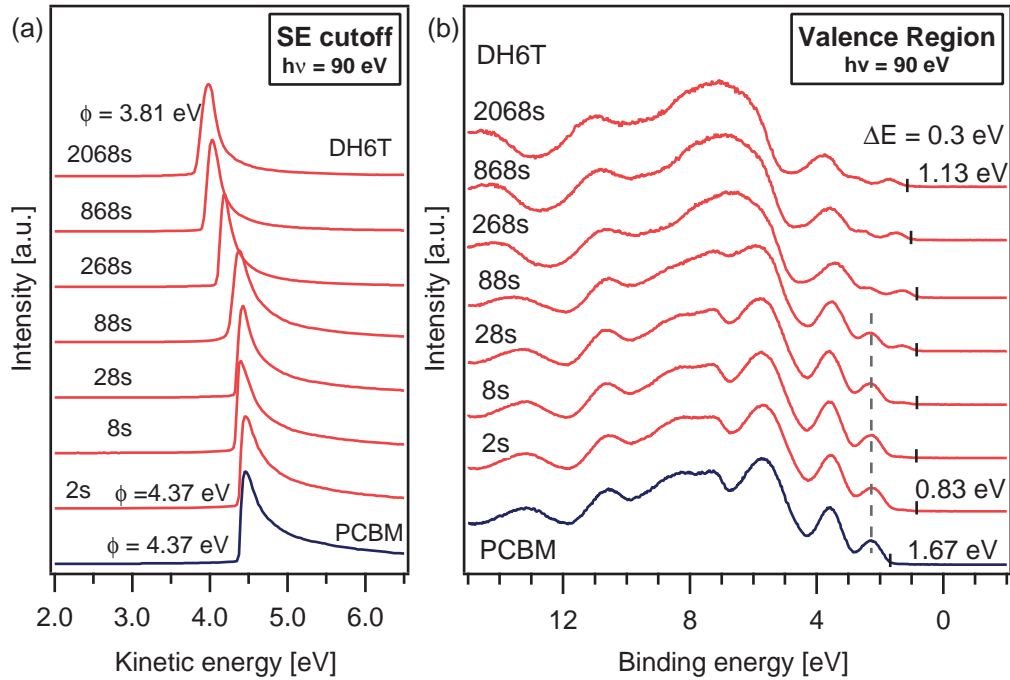


Figure 6.4: (a) Secondary electron cutoff and (b) valence band spectra in the course of DH6T evaporation onto drop-cast PCBM. Adapted from [127].

The HOMO of PCBM stays constant in energy as indicated by the dashed line in Figure 6.4 b. This is in agreement to the above observed constant O1s binding energy in PCBM. The HOMO_{onset} of DH6T shifts from 0.83 eV after the first evaporation step to 1.13 eV after the last deposition step. Thus, in total a shift of 0.3 eV is observed which corresponds to the S2p binding energy shift. Since the work function shifts by 0.56 eV the difference between this shift and the DH6T level shift is attributed to the formation of an interface dipole δ of 0.26 eV at the PCBM/DH6T interface.

Plotting the work function shift and the shift in the DH6T S2p and HOMO versus deposition time provides further information about layer formation and growth processes. This is shown in Figure 6.5. From this representation three different regimes may be distinguished. At first, only minor changes in the work function are observed. This is tentatively interpreted as DH6T interdiffusion. In the second regime the work function decreases significantly while the DH6T S2p and HOMO level only slightly shift towards lower binding energies. This is explained by the formation of an interface dipole by an adsorbed monolayer. Additionally, this step could be accompanied by a change in molecular orientation as indicated by the core level intensity changes described above. The extension of regime (II) goes up to a deposition time of roughly 250 s or a layer thickness of about

3 nm which nicely fits to the obtained monolayer thickness of upright oriented but tilted DH6T molecules which is 35 Å according to GARNIER ET AL. [75]. In regime (III), the S2p and HOMO level shift in parallel to the work function which indicates band bending in the order of 0.3 eV in the DH6T layer. The difference between the total work function shift and the total binding energy shift is the interface dipole of 0.26 eV as indicated by the arrow in Figure 6.5. The final layer thickness after the overall deposition time of roughly 35 min is about 25 nm as calculated from the deposition rate.

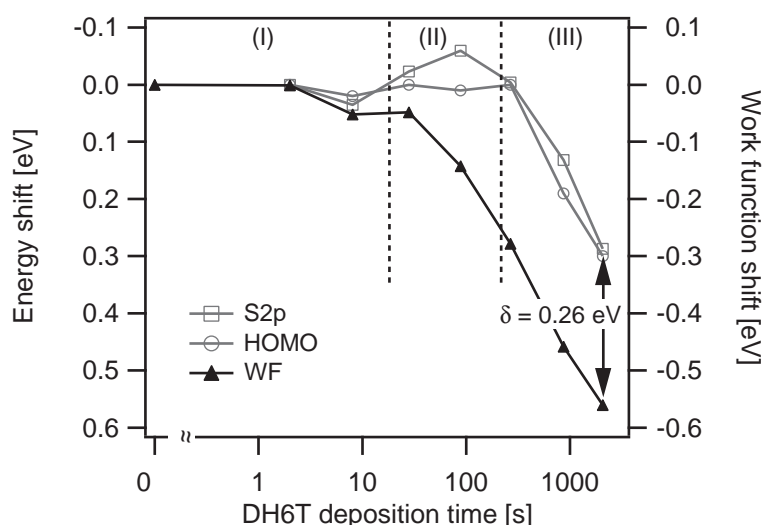


Figure 6.5: DH6T S2p (empty square) and HOMO (empty circle) shift together with the work function shift (solid triangle) over deposition time. Three different regimes are indicated by the dashed vertical lines: (I) Initially small changes in the work function are observed attributed to DH6T interdiffusion. (II) Decrease of work function anti-parallel to slight DH6T emission shift to lower binding energy indicating dipole formation by DH6T monolayer formation. (III) Work function and DH6T emission shift in parallel indicating band bending in the growing DH6T multilayer. Adapted from [127].

From the electronic information obtained from the interface experiment an energy level diagram can be deduced including constant Fermi level in PCBM, interface dipole, and band bending in DH6T. Compared to the pristine materials referenced to common vacuum level, this is depicted in Figure 6.6.

From the Anderson line up (Figure 6.6 a) of the pristine materials follows a work function difference between PCBM and DH6T of 0.56 eV. This energy difference is taken up by an interface dipole of 0.26 eV and band bending of 0.3 eV in the PCBM/DH6T bilayer system. The induced band bending in DH6T directs the majority charge carriers (i.e. holes in DH6T)

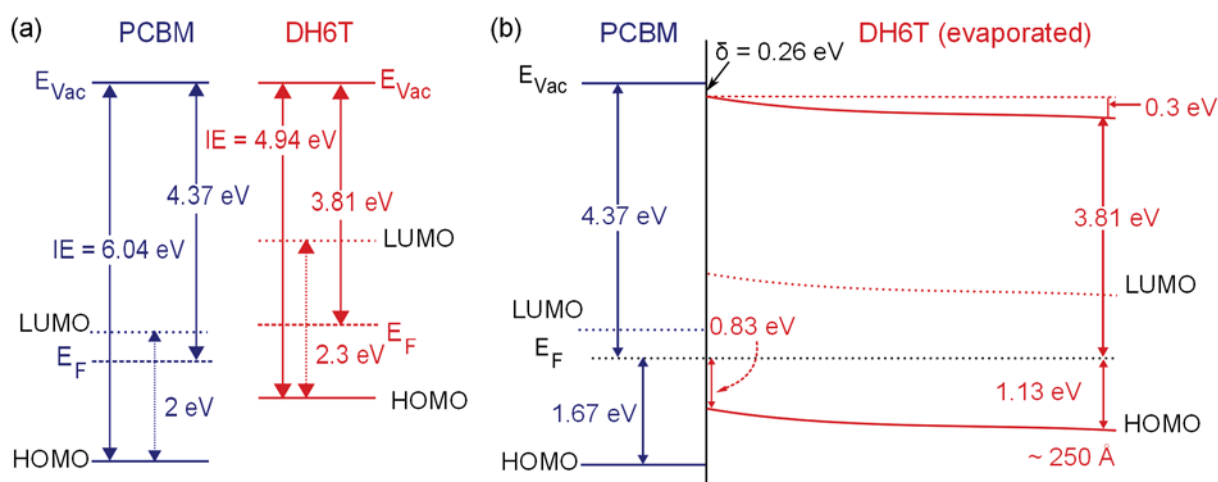


Figure 6.6: (a) Anderson line up of PCBM (left) and DH6T (right). (b) Band energy diagram of DH6T deposited via step-by-step via thermal evaporation on drop-cast PCBM. LUMO values were taken from literature [22, 24, 126]. Adapted from [127].

towards the interface. This could promote charge carrier recombination with the electrons which have been transferred to acceptor in the process of exciton splitting [15].

While the PCBM energy level diagram agrees with the previously obtained values, deviations of around 200 meV in the DH6T energy level positions are observed when compared to e.g. section 5.2. These are tentatively attributed to different Fermi level positions due to unintentional doping.

Summarizing, the interface formation of DH6T evaporated on PCBM was characterized showing three distinct regimes of work function and DH6T binding energy shifts. These regimes were assigned to morphology variations in the deposited DH6T: Initially DH6T interdiffuses into the PCBM layer as only very little changes in the work function and the DH6T orbital binding energies are observed. With increasing deposition time, a DH6T monolayer forms and presumably the molecular orientation changes during this phase, indicated by decreasing work function (to the value of DH6T) although the binding energy of the DH6T levels also decreases slightly. Finally, the work function decreases and the DH6T levels shift to higher binding energies, which both can be correlated to a growing DH6T multilayer structure with band bending.

6.2 Blends

As in a the photovoltaic device donor and acceptor are used in a bulk heterojunction rather than a bilayer structure, the two materials PCBM (in the following abbreviated by "P") and DH6T (in the following abbreviated by "D") were mixed together in solutions at three different concentration ratios to deposit blend layers for the second approach to investigate solution-processed interfaces. This way BHJ-like and interface-rich films were created to study the effect on the electronic properties. The molar ratios in solution as calculated from the individual sample weights were P70:D30, P50:D50, and P:30:D70. The drop-casting experiments were performed in a glass cell purged with clean Ar (5.0) at atmospheric pressure. The molecules were dissolved in chlorobenzene at overall concentrations of 2 mmol l^{-1} . The survey spectra of the different drop-cast blend films are shown together with spectra of the drop-cast pristine materials in Figure 6.7.

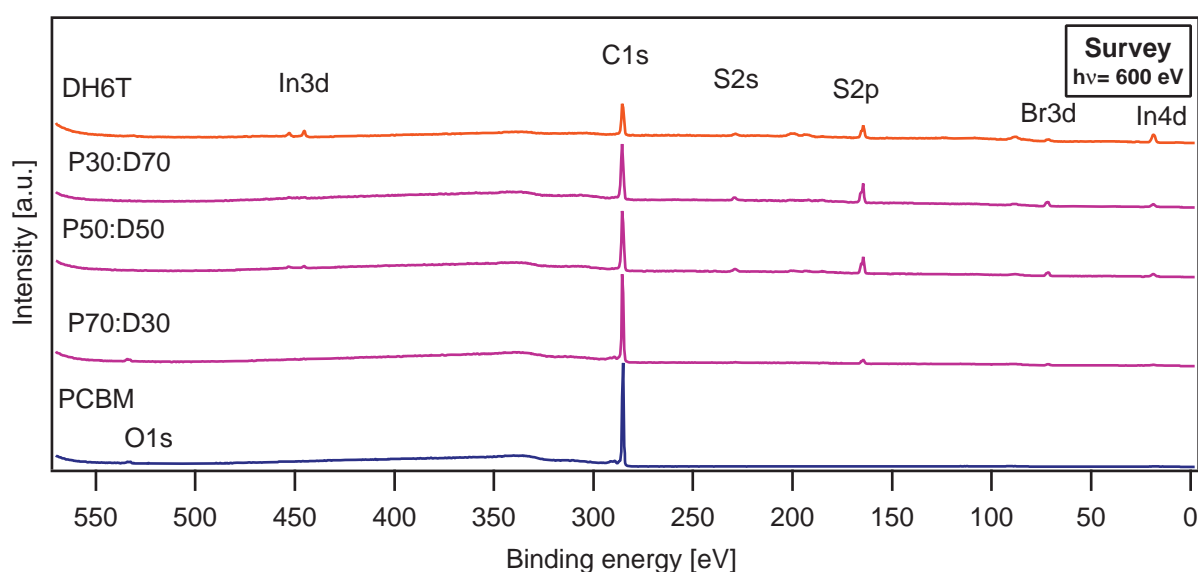


Figure 6.7: Survey spectra of PCBM, the PCBM:DH6T blends in the order of increasing DH6T content, and pristine DH6T (from bottom to top).

The survey spectrum of PCBM shows only carbon and oxygen features as expected. In the blends, already for the lowest DH6T concentration, the S2p emission from the thiophene is present. In the spectra of the blend layers and of the pristine DH6T also emissions from the underlying ITO substrate are present (In3d, In4d, but also oxygen and indium Auger emissions at around 100 eV and 190 eV, respectively). Additionally, a Br3d signal at around 72 eV is detected. Its origin is described in detail in section 5.2.1.

In Figure 6.8 the O1s, C1s, and S2p core level emissions from PCBM and DH6T are shown for highest surface sensitivity. In the PCBM O1s spectrum the two oxygen bonding sites are clearly resolved. These can also be clearly identified for the P70:D30 blend. However, for the P50:D50 and P30:D70 blend, these emissions are only weakly visible and superimposed by an additional low intensity feature which is also present in the case of pristine DH6T. As this molecule does not contain any oxygen species and since the binding energy position of 531 eV coincides with the O1s emission of the underlying ITO (see e.g. Figure 8.2 b), this emission is attributed to the ITO O1s. The presence of this signal indicates film inhomogeneities such as pinholes [128]. The binding energy of the PCBM O1s emission does not change with the initial blend concentration ratio. In the C1s spectra (Figure 6.8 b) a transition in peak shape from pristine PCBM to pristine DH6T can be observed for the different blend compositions. The major C1s emission in PCBM is located at 285 eV and stays constant in energy independent of the donor:acceptor ratio. The three components of the DH6T C1s emission increase in intensity with increasing DH6T content and shift towards higher binding energies. The individual molecular components are separated using Voigt profile fits as indicated in Figure 6.8 b. From the intensity ratio of the C1s components from the two molecules within the blend films, an estimate of the surface blend composition is calculated. In case of the P70:D30 blend a PCBM-to-DH6T ratio of 26 to 74 was obtained. The surface composition of the P50:D50 and P30:D70 blends is rather similar as PCBM-to-DH6T ratios of 10 to 90 and 9 to 91, respectively, were obtained from the C1s intensities. The obvious discrepancies to the ratio in the solutions clearly indicate a DH6T cap layer formation. This corresponds to the previous observations of P3HT surface enrichment in chapter 4 and has been reported in literature for both P3HT:PCBM bulk heterojunction layers [21, 110, 111] as well as for the DH6T:PCBM system [128]. In the S2p spectra (Figure 6.8 c) no emission is detected for PCBM as expected but for all blend layers a very strong S2p signal is observed. The intensity increases from the P70:D30 blend to the P50:D50 blend and stays rather constant between the latter and the P30:D70 blend. The binding energy position of the S2p emission changes by 0.17 eV to higher values from the blend with the lowest DH6T concentration to pristine DH6T. From the observed intensity development in dependence of the donor concentration in solution, it can be reasoned that the thickness of the capping layer increases with increasing DH6T concentration rather than the DH6T fraction in the intermixed bulk. Additionally, the observed changes in DH6T binding energy indicate the formation of a space charge layer in the DH6T cap as will be discussed later on in more detail.

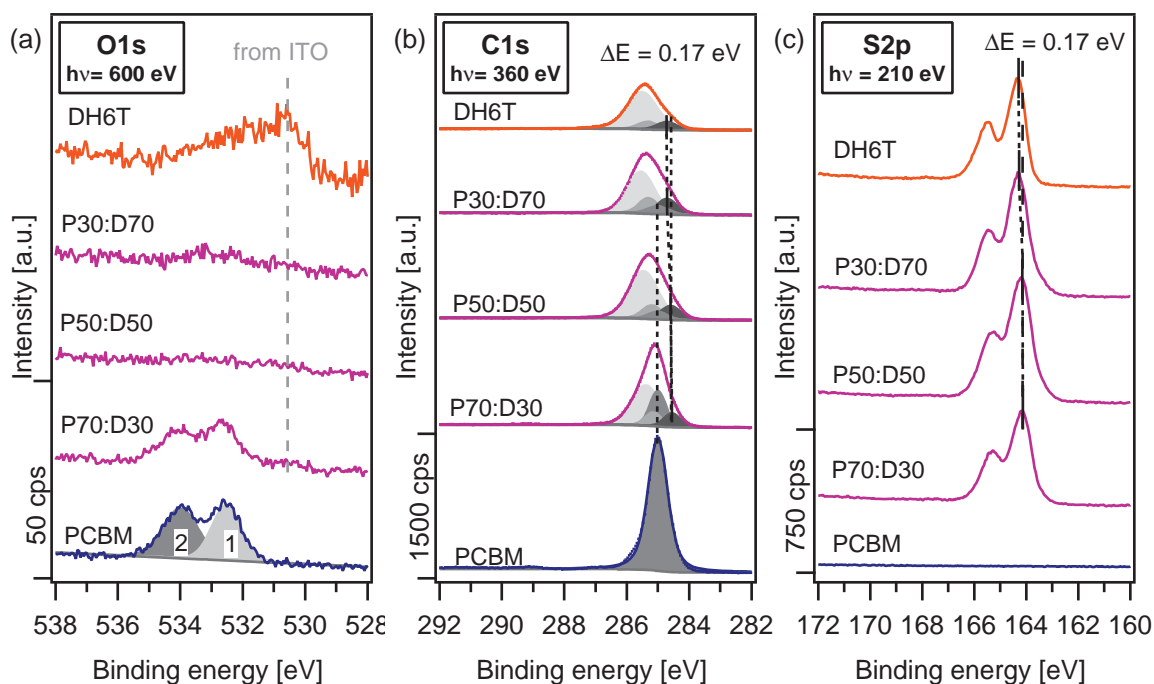


Figure 6.8: (a) O1s spectra, (b) C1s spectra, and (c) S2p spectra of PCBM, the PCBM:DH6T blends in the order of increasing DH6T content, and pristine DH6T. The disproportionate decrease of PCBM emissions and increase of DH6T emissions clearly indicate the formation of DH6T capping layers. In the O1s spectra in addition to the two PCBM features, an emission at around 531 eV is observed which can be assigned to the ITO substrate pointing towards inhomogeneities in the blends and pristine DH6T layers [127].

The valence region spectra are shown together with the secondary electron cutoff for the pristine materials and the different blend layers in Figure 6.9. The work function, the valence fingerprint region, and the corresponding $\text{HOMO}_{\text{onset}}$ of PCBM agree nicely with the expected positions (see e.g. section 4.1). The work functions of all blends are very similar to the work function of the pure DH6T film and show a slight decrease with increasing DH6T content. In the case of the P70:D30 blend, the overall valence structure resembles the one observed for pristine PCBM. For the other two blend films, the general valence structure is similar to that of pure DH6T. This is in accordance to the above described intensity behavior of the core level emissions. As far as the PCBM HOMO can be observed in the blend layers, its position does not vary with increasing DH6T content and the $\text{HOMO}_{\text{onset}}$ is determined at 1.67 eV for pristine PCBM. For all blend layers and the pristine DH6T layer, the DH6T HOMO can be discerned and the $\text{HOMO}_{\text{onset}}$ is indicated. It shifts towards higher binding energies by 220 meV from 0.93 eV for the P70:D30 blend to 1.15 eV for pure drop-cast DH6T. As the shift in work function is roughly in parallel to

this DH6T HOMO binding energy shift, the blend work functions are therefore attributed to a DH6T capping layer.

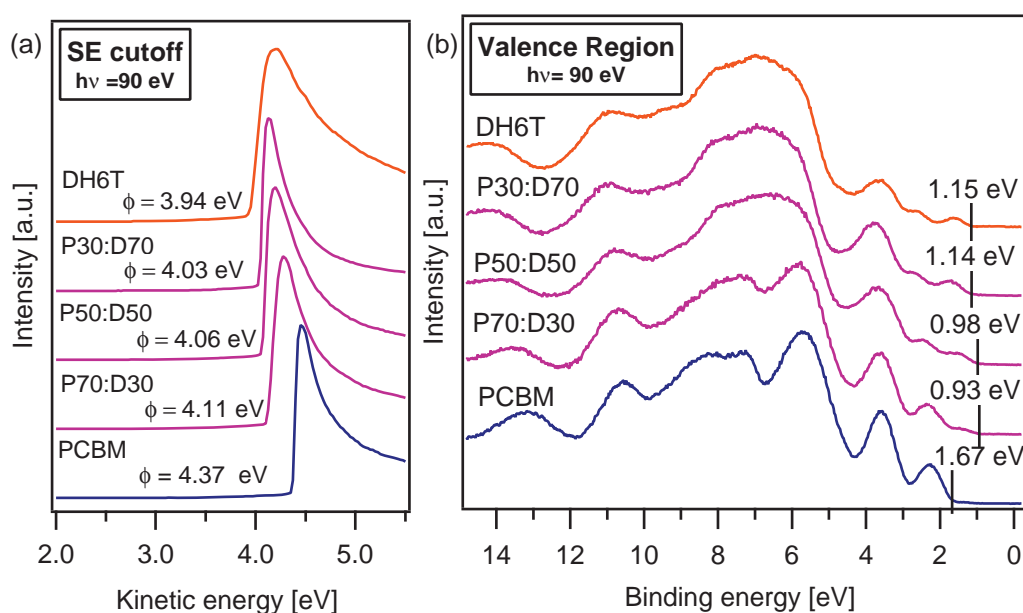


Figure 6.9: Secondary electron cutoff and valence level spectra of PCBM, P70:D30, P50:D50, P30:D70, and DH6T (from bottom to top). The work function and HOMO_{onset} values are indicated. The work functions of the blends are dominated by DH6T corroborating donor surface enrichment [127].

To investigate the valence structures more closely, difference spectra were calculated as depicted in Figure 6.10. The PCBM difference spectra obtained from the blends showed strongest similarity with the spectrum of pristine PCBM, when the subtracted pristine DH6T spectrum was shifted to lower binding energies. The obtained PCBM difference spectra show no shift versus the spectrum of pristine PCBM. Vice versa, the DH6T difference spectra showed strongest similarity to the spectrum of pristine DH6T, when the binding energy of the subtracted pristine PCBM spectrum was not shifted at all [128]. This again agrees to the above observed core level shifts in DH6T and the constant Fermi level in PCBM. Summarizing, the valence difference spectra also confirm a constant PCBM HOMO position independent of the PCBM:DH6T ratio in solution and a shift in the DH6T HOMO to higher binding energies with increasing DH6T content.

The derived energy level alignment for the blends in comparison to the pristine acceptor and donor is shown in Figure 6.11 for Fermi level alignment. With increasing DH6T content in the blend, the HOMO energy difference reduces from 0.74 eV to 0.53 eV. Since

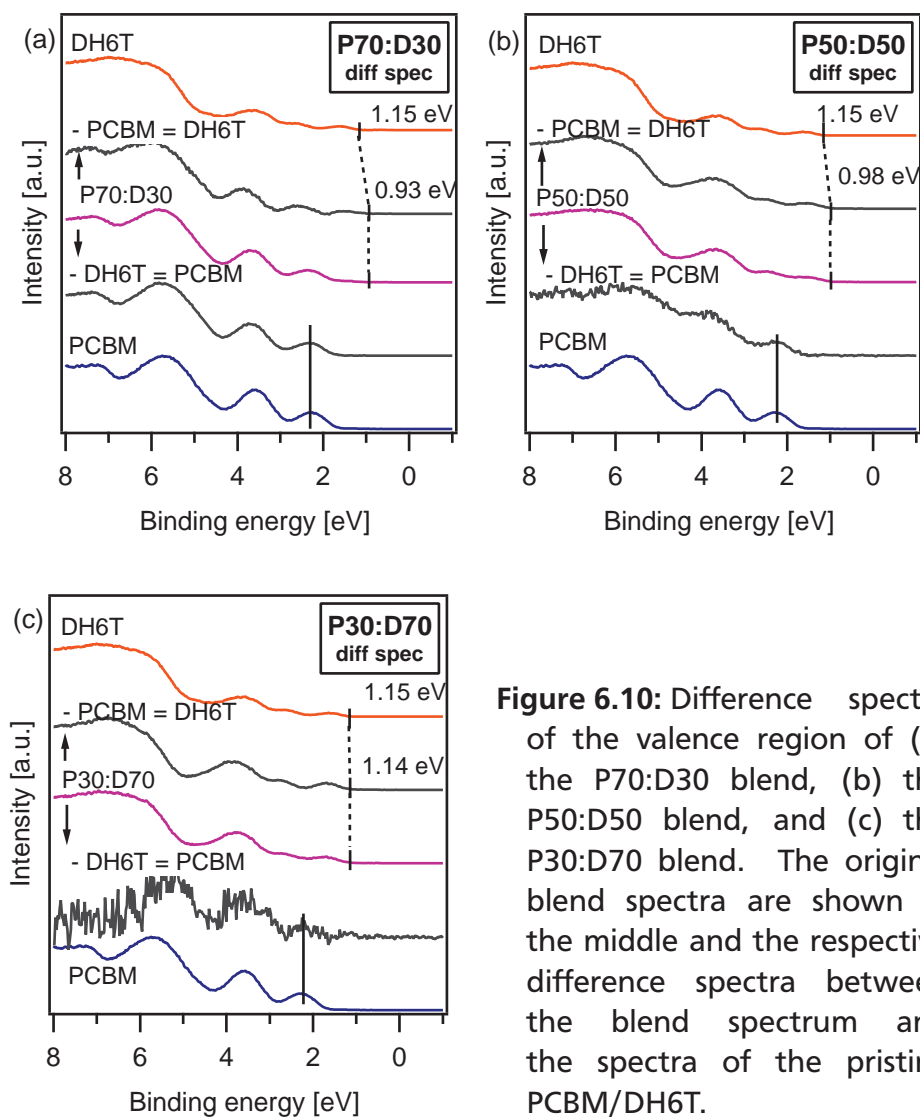


Figure 6.10: Difference spectra of the valence region of (a) the P70:D30 blend, (b) the P50:D50 blend, and (c) the P30:D70 blend. The original blend spectra are shown in the middle and the respective difference spectra between the blend spectrum and the spectra of the pristine PCBM/DH6T.

these values are all smaller than the determined ionization potential difference of pristine PCBM and DH6T, which is 0.94 eV, the formation of a dipole potential at the internal interfaces of the bulk heterojunctions is indicated.

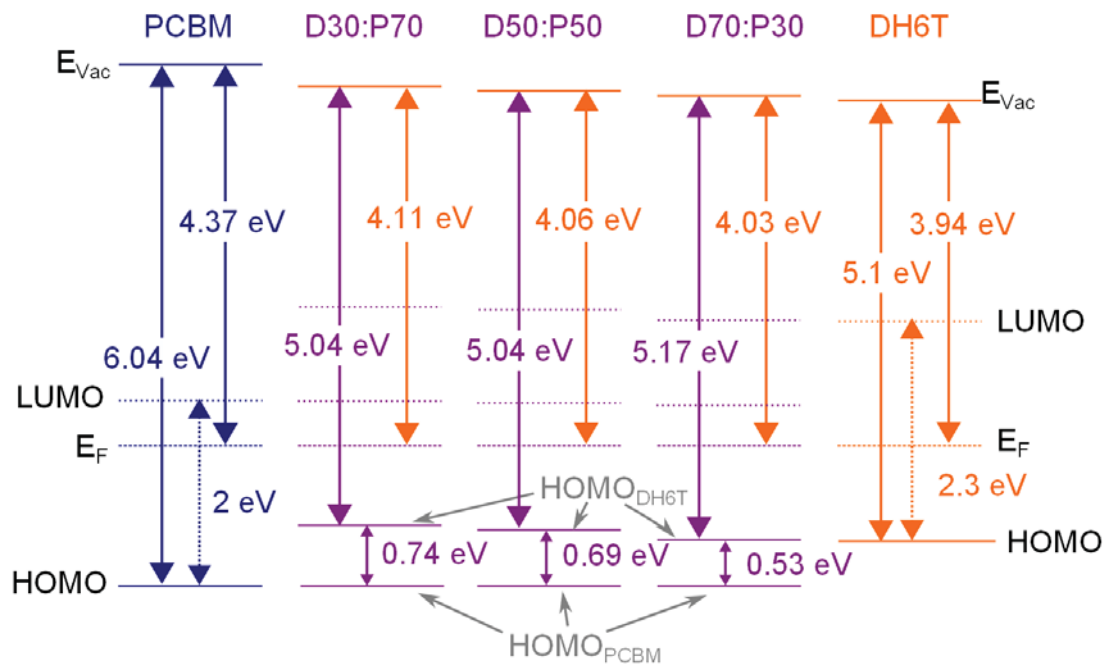


Figure 6.11: Energy level line up with common Fermi level for the pristine materials PCBM (left) and DH6T (right) and the blends from solutions with increasing DH6T content (from left to right). The almost constant ionization energy of DH6T confirms the donor capping layer formation. Therefore, the measured work functions of the blends are attributed to DH6T [127]. Energy gap values are taken from literature [22, 24, 126].

6.3 Derived Model

Combining the results of the bilayer and blend structures, a model for the electronic and geometric structure in the bulk heterojunction blends is derived. In both cases constant Fermi level in PCBM was observed. In DH6T, however, a change in binding energy in the core and valence levels was observed upon contact to PCBM, independent whether the contact was formed in a bilayer structure or in an intermixed system. Due to the formation of a DH6T capping layer for the solution-processed blends, the obtained energy level positions for the three different blends are added to the DH6T band diagram of the evaporated DH6T layer in Figure 6.12, which represents the summarizing model. In Figure 6.12, a schematic illustrating the bilayer development during the interface experiment is included above the interface band diagram and a schematic illustrating the blend layer configurations is given below.

The DH6T binding energy positions on the bulk heterojunction films formed from mixed PCBM-DH6T solutions with increasing DH6T content perfectly fit to DH6T binding en-

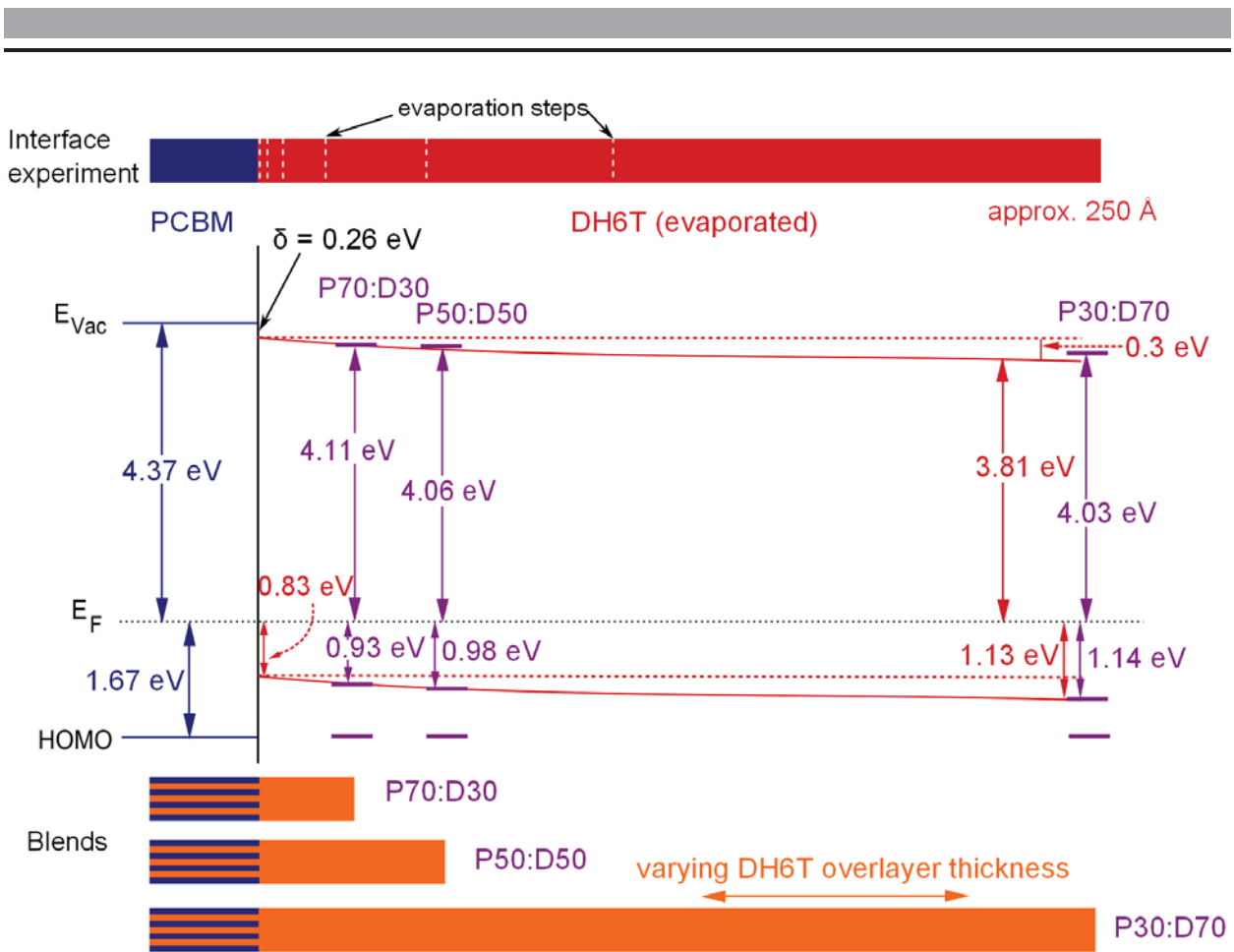


Figure 6.12: Interface band diagram for the PCBM/DH6T bilayer (see section 6.1) and PCBM:DH6T bulk heterojunction films with DH6T cap layer formed from mixed PCBM:DH6T solutions of increasing DH6T content (see section 6.2). The binding energy positions on the cap layers follow the band bending in the PCBM/DH6T bilayer formed by DH6T evaporation onto PCBM, indicating increasing capping layer thickness with increasing DH6T content in the mixed PCBM-DH6T solution [127].

ergy positions measured on PCBM/DH6T bilayers. This supports the above postulated formation of capping layers of increasing thickness with increasing DH6T concentration in the mixed solutions and band bending in the cap layer. Due to the increasing overlayer thickness with increasing DH6T concentration in the blends, the measured energy level positions of DH6T are closer to the thermodynamic equilibrium of the orbital energy position at the surface of pristine DH6T.

Thus, the interface band diagram is valid for both, the bilayer formed by evaporation of DH6T onto drop-cast PCBM and heterojunction films with increasing cap layer deposited from mixed DH6T:PCBM solutions. In addition, the presented model is suitable to explain the variation in the HOMO-HOMO distance for the differently composed blends and thus

provides valuable insights for the actual donor/acceptor interfaces in intermixed systems which are otherwise not directly accessible.

In literature, similar blend experiments have been performed on P3HT:PCBM by XU ET AL. [20]. In that case, the authors have also observed a downward shift in the donor energy levels with increasing P3HT content. However, the shift was interpreted to be due to the varying blend composition and assumed varied energy level alignment at the substrate contact, in accordance to the integer charge transfer (ICT) model [46]. The above presented bilayer interface experiment contradicts this interpretation as it clearly shows that the change in energy level position in the donor is induced by the formation of a space charge layer in DH6T at the PCBM/DH6T interface as the ITO/PCBM contact is not varied at all.

6.4 Conclusion

Using a combination of different sample preparation techniques and approaches to the interface, valuable information about the electronic contact formation of solution-processed donor:acceptor systems was obtained. The comparison of DH6T binding energy positions measured on the BHJ cap layers to the PCBM/DH6T bilayer indicates band bending in the cap layer as measured in the evaporated bilayer. Thus, the otherwise not directly accessible donor:acceptor interface prepared from solution can be described with the presented model. The experiments show the formation of an interface dipole of 0.26 eV at the DH6T/PCBM bilayer interface and bulk heterojunction interfaces. Band bending of up to 0.3 eV in DH6T in the bilayer has been measured and was deduced for the bulk heterojunction cap layer.

The direction of the band bending is obstructive for device performance, as it drives holes in the donor towards the interface, which would promote recombination with electrons transferred in the exciton splitting reaction to the LUMO of the acceptor. Band bending in a photovoltaically unfavorable direction is a general phenomenon for intrinsic donor acceptor interfaces and can be cured by n-doping of the acceptor and/or p-doping of the donor as shown by C. HEIN [15, 38].

Summarizing, by comparison of PES data from in-situ stepwise grown bilayers and ex-situ drop-cast bulk heterojunction layers, the interface band diagram of donor acceptor BHJ

structures including Fermi level pinning in the PCBM acceptor, interface dipole, and band bending in the DH6T donor cap layer could be deduced.

7 Evaluation of the Model Experiments

The presented experiments show that photoelectron spectroscopy is a very suitable tool in characterizing the electronic properties of organic semiconductors processed from solution. Different liquid-based deposition techniques were applied such as spin-coating and drop-casting and if clean and contamination-free process conditions are maintained, PES provides reliable and reproducible information about thin film surface compositions and energy level positions. The suitability of the glass cell setup for in-depth studies of the electronic properties of organic semiconductors using PES could be shown e.g. by the direct comparison of solution- and vacuum-deposited DH6T. However, only by means of drop-casting and spin-coating, a direct interface characterization of two solution-processed organic semiconductors was not achieved. In the case of P3HT:PCBM bulk heterojunctions for example, this was hindered by the surface accumulation of P3HT shielding the interface. Potentially, orthogonal (or close to orthogonal) solvents will help to circumvent problems of redissolving the previously deposited layer and minimize intermixing. This approach based on chlorobenzene as a solvent for P3HT and dichloromethane as solvent for PCBM (following ref. [129]) is currently investigated by C. Scichocki within his master thesis project in the Surface Science group.

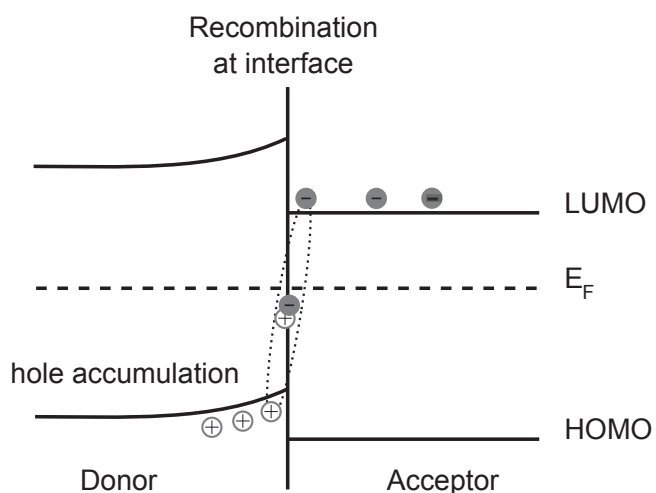
To achieve defined interfaces, thermal evaporation under UHV was applied. The influence of this deposition technique on PCBM and DH6T as a small molecular thiophene model molecule was investigated in detail. In the case of PCBM, it could be shown that the molecule is not suitable for thermal evaporation as changes in the molecular structure occur. For DH6T, however, both solution-based deposition as well as thermal evaporation yield thin films with identical chemical and electronic properties. This interchangeability of processing conditions enabled further experimental means to investigate the donor:acceptor interface in bulk heterojunction systems.

Using a combined approach using both vacuum- and solution-based deposition techniques for DH6T and PCBM, respectively, the band energy level alignment was determined for this donor:acceptor model system. From the results follows an interface dipole of 0.26 eV at the internal DH6T/PCBM interface and band bending in the DH6T capping layer. Although the

direct determination of these electronic interface properties was not yet achieved for the prototypical donor:acceptor system P3HT:PCBM, the results are of general importance as they show a band bending in the donor capping layer. Additionally, these direct DH6T:PCBM results correlate to the implicit results on P3HT:PCBM interface obtained in chapter 4, namely constant Fermi level in PCBM and upward shift of the Fermi level in P3HT.

The significance of the observed band bending becomes clear, if the charge carrier transport directions in an organic solar cell are considered. It turns out that the band bending forms in such a way that it promotes hole accumulation at the donor:acceptor interface. This in turn might increase the recombination with electrons transferred to the acceptor LUMO and would thus negatively influence solar cell device performance. The recombination process due to hole accumulation is schematically depicted in Figure 7.1.

Figure 7.1: Schematic representation of charge carrier recombination at the donor:acceptor interface due to hole accumulation caused by band bending in the donor.



For intrinsic organic semiconductors, this PV performance obstructive band bending has been observed previously [15] and a possible cure could be p-doping of the donor and/or n-doping of the acceptor. Although controlled doping in solution might be challenging, in literature both p- and n-doping of organic semiconductors in solution are described. For instance QI ET AL. [130] have used air-stable n-dopants based on Ru- and Rh-organometallic complexes to change the Fermi level position in TIPS-Pentacene (6,13-bis(tri-(isopropyl)silylethynyl)pentacene). The p-doping efficiency of the all-organic dopant F_4 TCNQ (7,7,8,8-tetracyano-2,3,5,6-tetra-fluoro-quinodimethane) in P3HT in solution has been characterized by DUON ET AL. [131]. Solution-based doping has also been applied to various polymeric solar cell configurations e.g in ref. [132–134] to improve device efficiencies. The improvements are mostly attributed to better charge transport prop-

erties such as enhanced mobility as well as increased absorption and efficient collection of photo-generated charges. Nonetheless, a direct correlation to electronic donor:acceptor interface properties has not yet been drawn for solution-processed organic solar cells.

Concluding, the presented experiments provide valuable insight into the electronic donor:acceptor interface formation in bulk heterojunction systems. This could be achieved by combining ultra-clean deposition of organic semiconductors and their mixtures from solution at atmospheric pressure and deposition via thermal evaporation in UHV. The step-by-step contact formation experiment was crucial in determining the band energy diagram of the DH6T:PCBM bulk heterojunction. Therefore, the results also demonstrate the necessity to directly access the interface, which can only be revealed by building-up the contact in a deposition of one semiconductor on top of the other also for solution-processed systems. Therefore, the second part of this work will deal with the development of a step-by-step deposition method from solution.



Part II

Building it Up

**Developing Methods to Perform
Interface Experiments from Solution**



8 Developing the Nebulizer Deposition Method

In this chapter the development steps of the nebulizer method are reviewed. Considerations concerning the droplet deposition are presented, as they might affect the resulting film and its properties. Furthermore, a closer look is taken at the substrate and solvent materials as in this part of this work, the aim is to create ultra thin layers from solution. The effect of UHV in combination with the argon environment present in the buffer chamber on ozone-treated ITO was characterized. Additionally, the bare solvent, i.e. chlorobenzene, was deposited through various techniques in order to identify its possible contributions to the obtained data.

8.1 Development Steps

The core piece of the nebulizer deposition method is an ultrasonic nebulizing unit from TDK (NB-59S-09S type) (see Figure 8.1 a). This piezoelectric device is originally designed for air humidifying purposes. A detailed description of this application and the associated features can be found on the product data sheet and on the manufactures homepage [135]. The most efficient mist output is created, if a liquid column of 35 mm is maintained on top of the nebulizer unit. However, these operating conditions are not applicable for ultra thin film deposition of organic semiconducting materials at least in this early testing stage as the amount of available material is limited and mainly highly volatile and toxic solvents are used. Therefore, it was mounted on a KF 59 flange to be incorporated into the glass cell setup (see Figure 8.1 b). Through the design of a nebulae steering unit and by adding a nozzle structure, individual deposition steps are possible with only about 0.1 ml to 1 ml of the respective solution. It needs to be noted that prolonged operation of the nebulizer unit without any liquid can permanently damage the transducer. Although the nebulizer unit is originally intended to be used with an AC power supply the nebulizer deposition was performed using a DC power supply tuning the input power via the voltage. Typically, 40 V to 45 V were applied and the current ranged from 0.4 A to 0.6 A.

To avoid larger droplets and generate a homogeneous deposition, a chimney-like structure with a gas inlet (see Figure 8.1 c and d) was applied which directed the nebulae towards the sample surface. But only through the addition of a nozzle at the top of this structure (see Figure 8.1 e) a fine mist output was created that allowed material deposition on the substrate. A positive side effect of this steering unit is that larger droplets, which are created when the nebulization process is started, are kept away from the sample. Additionally, the distance between the sample and the nozzle was increased to achieve a more homogeneous and wider deposition field. An anticipated advantage of this change in distance was also to have some if not all solvent evaporate prior to the droplet reaching the surface. However, this was not observed. A summary of the complete development process is depicted in Figure 8.1.

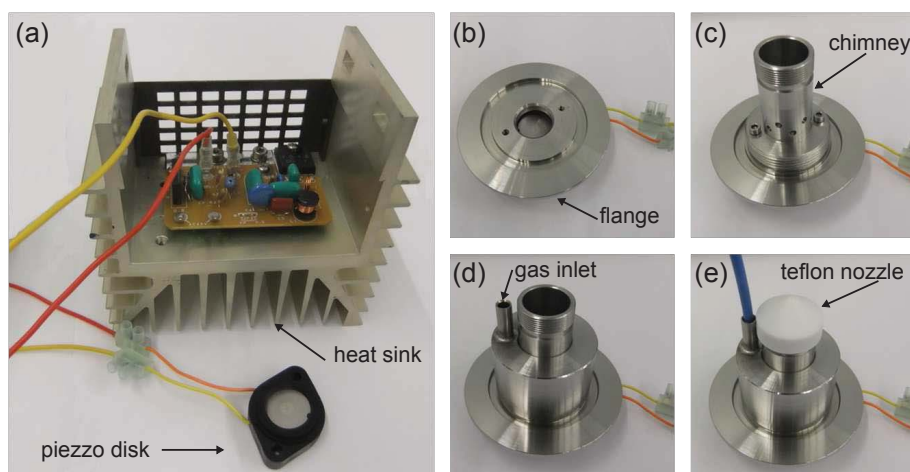


Figure 8.1: (a) The complete nebulizer unit with the driving electronics mounted on a heat sink. (b) The piezo nebulizer attached to a KF 50 stainless steel flange to connect the unit to the glass cell. The solution which will then be deposited is placed on the piezo disk in the cavity of the flange. (c) First nebulae steering stage with gas inlet holes mounted on nebulizer flange. (d) Gas distribution cap screwed on the first steering stage. (e) Complete nebulizer and steering setup with Teflon nozzle and gas inlet tube.

8.2 Method Related Considerations

The developed deposition technique relies on the formation of small liquid droplets which are then steered towards the substrate. Ideally, the solvent would have evaporated on its way from the nebulizer to the substrate to achieve an almost dry meaning solvent-free, evaporation-like molecular deposition. As this could not be achieved, the sticking, wetting and drying of the droplets on the substrate surface are of importance.

Upon the impact of a liquid drop on a solid and in this case hard surface, several phenomena might occur, which will influence the film forming properties. These include drop spreading, splashing, receding, and even rebounding. The cause and occurrence of these phenomena is given in a comprehensive review by A.L. YARIN [136]. In principal, the result of the drop impact depends on the velocity of the droplet upon impact (V_0), its direction with respect to the surface, and the droplet size (D) and is characterized e.g. by the dimensionless Weber (We) and Reynolds (Re) numbers:

$$We = \frac{\rho D V_0^2}{\sigma} \quad Re = \frac{\rho D V_0}{\mu} . \quad (8.1)$$

The Weber number describes the droplet deformation due to the deforming inertia caused by the flow counteracted by the droplets surface tension (σ) while the Reynolds number gives the ratio of inertial forces to viscous forces. Thus, liquid inherent properties such as density (ρ) and viscosity (μ) play a key role. Additionally, the roughness and wettability of the solid substrate need to be considered. As many of these influence factors are very complex and reach well beyond the scope of this work, only the surface tension and wettability will be investigated to ensure the principle possibility of film formation.

As the aim of the nebulizer method is to create a thin solid film, the formation of a liquid lamella resulting from actual drop deposition is a precondition. The shape of this liquid lamella is governed by the drop impact characteristics. The drying of the film then involves non-isothermal effects such as solvent evaporation and solidification. Since only individual droplets have been observed so far, the drying parameters have been left out in the further considerations as it is not possible to form homogeneous layers simply by optimizing the drying process if a homogeneous layer is not present in the liquid phase.

The wetting depends on the interplay of the surface energies of the involved species. Therefore, the surface energies of solvent-cleaned and ozone-treated ITO were determined. The wetting envelope for ozone-treated ITO was calculated from surface energy measurements. The results show that this substrate should be wetted by the solvent chlorobenzene. Therefore other possibilities for the poor film formation during the nebulizer deposition have to be discussed. The droplet size should not influence the sticking behavior as the surface tension is only for very small droplets (diameter smaller than $1 \mu\text{m}$)

dependent on the droplet radius [137]. However, concentration gradients might influence the deposition results and are therefore considered.

The surface tension can be a function of the droplet composition as described by hydrodynamics. The Marangoni effect describes the mass transfer along an interface between two fluids due to a surface tension gradient [138]. The gradient can be caused by temperature, compositional differences, and electric potential differences. Since the deposited droplets are not pure solvent but solutions of small molecules, the concentration gradient effect might influence the sticking and wetting properties.

8.3 Substrate and Solvent Characteristics

8.3.1 Ozone-Treated ITO

The ITO substrates were solvent-cleaned in acetone and isopropyl alcohol with ultrasonic agitation. The ozone treatment was then performed in a PR-100 UV-Ozone Photoreactor™ (UVP) for 15 min. For this last step, the substrates were already mounted on the sample holder so that the samples could be directly introduced to the UHV load lock to minimize the possible re-formation of surface contaminations. However, the ozone cleaning activates the surface and changes its termination. The possible effects are thoroughly characterized by Y. GASSENBAUER [71]. In the case of ozone-treated ITO the formation of a surface phase possible involving peroxides is discussed which strongly influences the surface dipole.

The spectra of the ozone-treated ITO substrate before and after argon exposure are shown together with an untreated ITO in Figure 8.2. In the survey spectra all emissions can be assigned to the ITO components. Only in the case of the solvent-cleaned ITO a small carbon emission is visible in the survey. Through the ozone treatment, this surface contamination was removed or at least reduced to a level below the detection limit of XPS as can be seen in the absence of any carbon signal (see also Figure 8.2 d). Due to the ozone treatment the signal intensity in both the O1s (Figure 8.2 b) and In3d (Figure 8.2 c) increase as the contaminations are removed, which before led to a damping of the substrate signal. Also for both the In3d and O1s lines, an asymmetry is observed. While in the latter, these are most likely due to different oxygen compounds, in the In3d this high binding energy tail can be related to different In binding states and/or plasmonic loss processes [71].

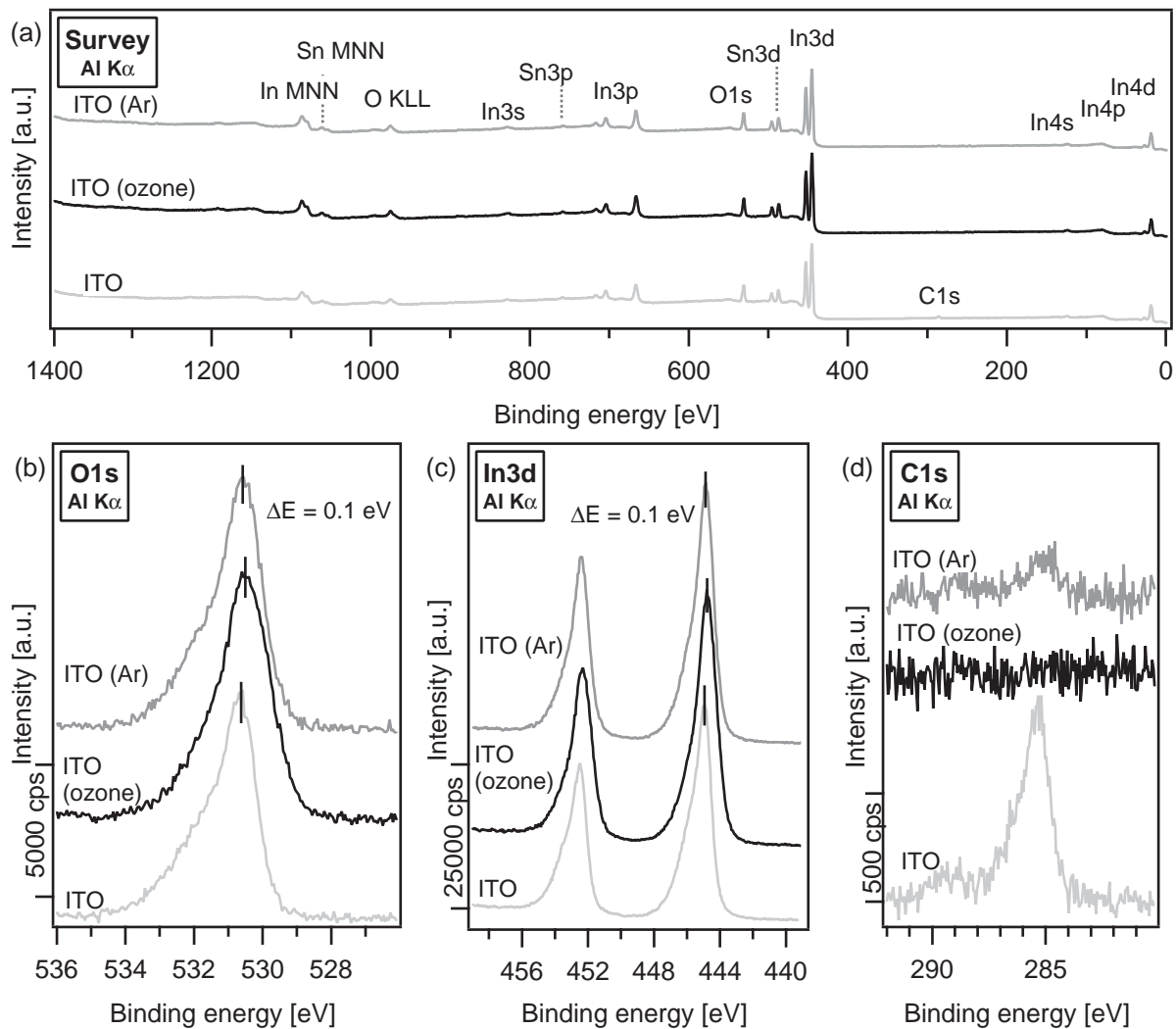


Figure 8.2: (a) Survey spectrum and (b) O1s, (c) In3d, and (d) C1s detail core level spectra of differently treated ITO substrates. The bottom spectra correspond to a solvent-cleaned ITO, the middle spectra are obtained for a freshly ozone-treated ITO (ozone), and the top spectrum shows the ITO emissions after argon exposure (Ar).

Additionally, a small shift (about 100 meV) to lower binding energies is observed which can be attributed to an oxidation due to the ozone exposure. This shift partially disappears again after the exposure of the sample to argon in the buffer chamber. Argon but also UHV act as reducing environments. Simply because of the transfer in the UHV system at a base pressure of 10^{-8} mbar and the exposure to argon 6.0 for 10 min a small carbon signal is observed in the C1s detail spectrum. Although the intensity of this emission is rather small, it is nonetheless noteworthy that the processes in and around the glass cell are not entirely contamination-free as the experiments in the following sections aim at depositing and detecting very low quantities of organic and thus carbon based materials.

The changes of the ITO surface due to the ozone treatment and the argon exposure are even more pronounced when looking at the valence level, especially the work function (see Figure 8.3).

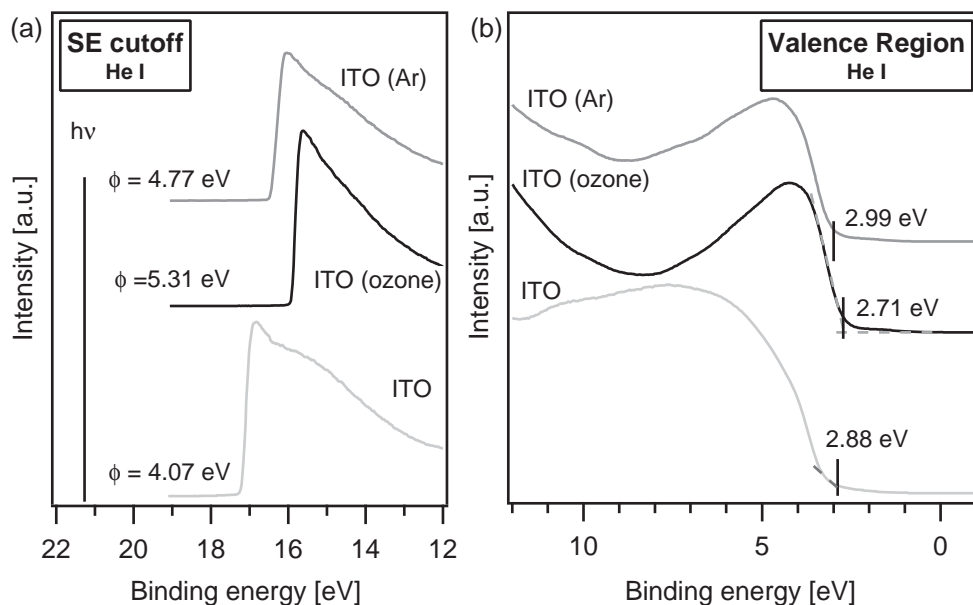


Figure 8.3: SE cutoff and valence region spectra of the differently treated ITO substrates: Solvent-cleaned ITO (bottom), ozone-treated ITO (middle), argon exposed ITO (top). The ozone treatment drastically increases the work function of ITO by about 1 eV. This effect is partially reversed by exposing the ozone-treated substrate to UHV and Argon.

From the shifts of the secondary electron cutoffs the drastic effect on the work function of the ozone treatment is visible: The work function changes by more than 1 eV from 4.07 eV for the solvent-cleaned ITO to 5.31 eV for the ozone-treated ITO. The change in the valence band onset is not as pronounced confirming the findings in literature [71, 139] that the ozone treatment mainly changes the surface dipole. The change in work function is decreased by about 0.6 eV after the sample was transferred in UHV to the buffer chamber and exposed to argon for 10 min. We attribute these changes to absorption of C_xH_y contaminants.

The shape of the valence spectra also shows the removal of surface contaminations as the rather round shape in the case of only solvent-cleaned ITO indicates the presence of carbohydrates (see also Figure 8.6 b where the ITO surface was deliberately contaminated). These contaminations superimpose the ITO valence band maximum located at around 2.88 eV. For the ozone-treated as well as the Ar-exposed ITO the valence band structure is much more defined. The onset values for these two samples are 2.71 eV and 2.99 eV,

respectively. Thus, the shifts observed in the valence band maxima correspond to the core level shifts of the differently treated ITO samples. The general positions of the valence band maxima also correlate to results published e.g. in [71] where onset values of 3.1 eV for solvent-cleaned and 3.0 eV for ozone-treated ITO were reported for commercial ITO samples. Comparing the shape of the valence spectra of ozone-treated and argon exposed ITO in more detail, an intensity increase in the range of 6 eV to 10 eV is observed in the case of argon exposed ITO which can be correlated to the increase of C1s intensity after the sample has been left in the Ar-vented buffer chamber (see Figure 8.2). In all cases, a tailing of the occupied states from the observed valence band maxima into the energy gap is observed. A similar tailing is assumed for the conduction band resulting in the high conductivity of the material.

Summarizing, the cleaning procedure based on ozone-treating the ITO surfaces provides substrates without any detectable carbon contamination. However, due to the ozone treatment the surface is activated and the effect wears off quickly in UHV and due to argon exposure. Furthermore, the surface energy is increased from around 43 mN m^{-1} for untreated ITO to around 70 mN m^{-1} after the ozone treatment as measured by contact angle measurements (see section 8.4).

8.3.2 Chlorobenzene

In order to examine possible contributions of the solvent chlorobenzene, since it is rather aggressive towards any kind of rubber or sealing material, it was deposited on ozone-treated ITO through different preparation routes. The pristine solvent was simply nebulized (denoted by the add-on nebu), it was drop-cast in the glass cell (drop) and additionally the solvent was contaminated on purpose by repeatedly putting it in contact with the nebulizer sealing material (denoted by the add-on contaminated). The survey and detail core level spectra are shown in Figure 8.4 in the order of increasing carbon signal.

In all survey spectra the ITO substrate features (In3d at 444 eV, Sn3d at 485 eV, and O1s at 530 eV) are clearly visible. After the chlorobenzene deposition a C1s emission emerges at around 285 eV. Both In3d (Figure 8.4 c) and O1s (Figure 8.4 b) show an asymmetric peak shape as observed in the previous section 8.3.1. The additional shoulder on the high binding energy side of the O1s emission in Figure 8.4 b (marked by the arrow) after the deposition of the solvent possibly corresponds to adsorbed water, OH groups or

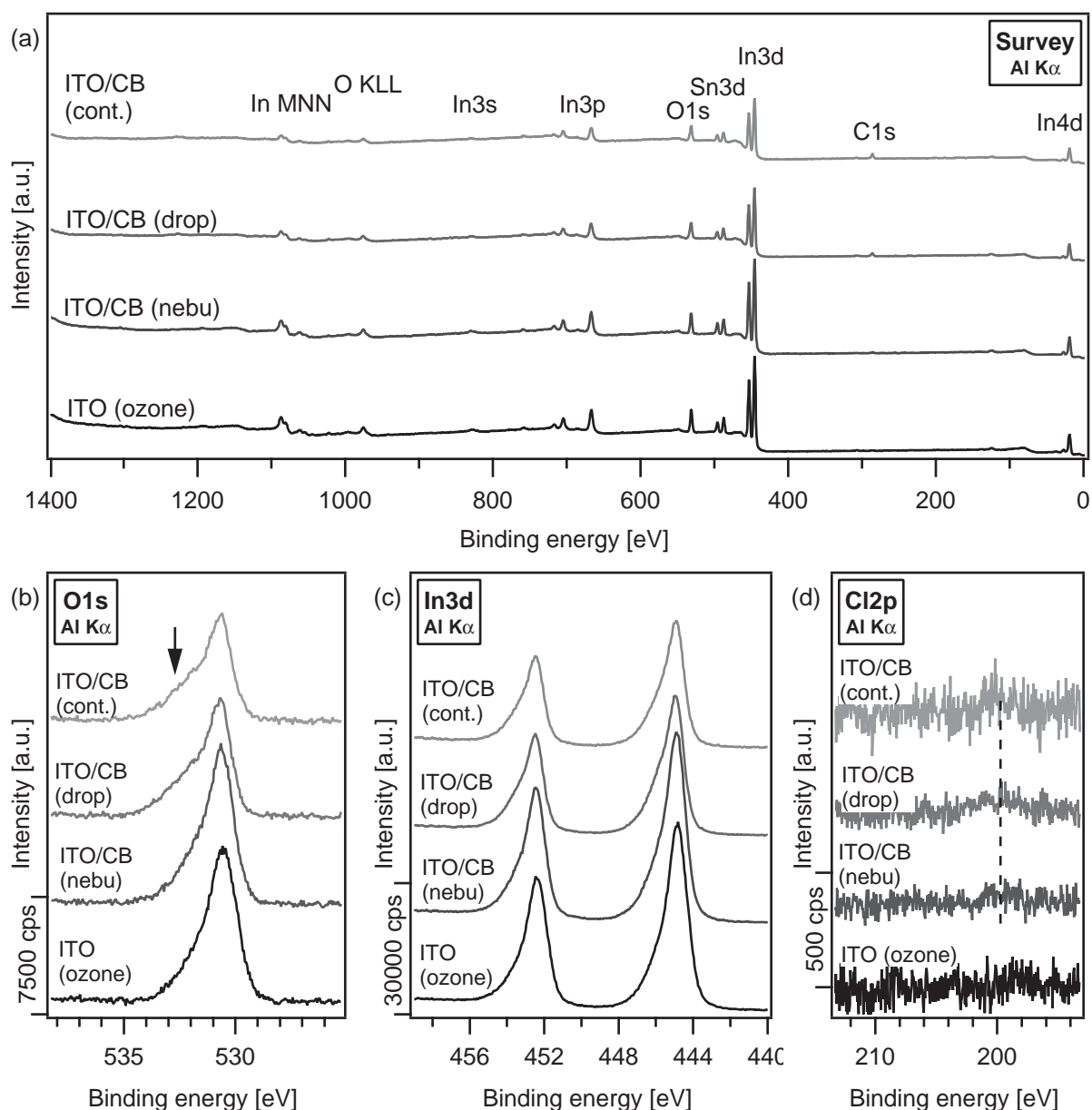


Figure 8.4: (a) Survey spectra and detail (b) O1s, (c) In3d, and (d) Cl2p core level spectra of chlorobenzene on ITO. From bottom to top: Solvent- and ozone-cleaned ITO, chlorobenzene on ITO via nebulization (nebu), chlorobenzene on ITO via drop-casting (drop), and deliberately contaminated chlorobenzene on ITO (cont.).

other hydroxyl-containing contaminations (see e.g. p. 146 ff in ref. [71]). In general, only very little material is deposited by simply exposing the substrates to the solvent via the different preparation routes as expected. This becomes obvious when looking at the substrate In3d emission intensities in Figure 8.4 c which undergo almost no attenuation due to the chlorobenzene exposure, especially after the nebulizer deposition. Also, there

is barely any Cl2p signal present (Figure 8.4 d). The dotted line is intended as a guide to the eye where the Cl2p_{3/2} emission should be expected. The detail spectra of the C1s emission line are shown in Figure 8.5.

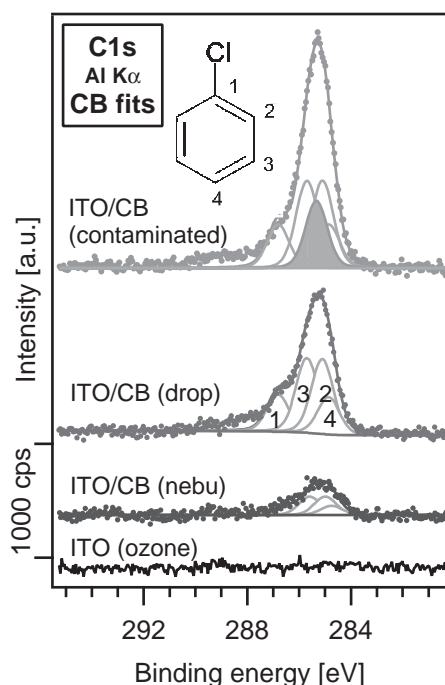


Figure 8.5: C1s emission of solvent- and ozone-cleaned ITO, chlorobenzene on ITO via nebulization (nebu), chlorobenzene on ITO via drop-casting (drop), and deliberately contaminated chlorobenzene on ITO (cont.). The cleaning procedure left no detectable carbon contamination on the ITO substrate as confirmed previously. For the C1s features emerging after the chlorobenzene exposure fits were performed to discern possible additional carbon contaminations from adsorbed solvent. Inset: Molecular structure of chlorobenzene with the different C1s binding sites indicated.

In the case of chlorobenzene being deposited via the nebulization technique as well as via drop casting the measured C1s emission can be described by four components at 284.9 eV, 285.1 eV, 285.7 eV, and at 286.8 eV, which can be attributed to the carbon binding sites within chlorobenzene according to the inset in Figure 8.5. The emission at the highest binding energy corresponds to the carbon bound to the chlorine atom. All components were assigned according to their relative binding energy shifts taken from ref. [140] and their expected relative intensities. In the case of the deliberately contaminated chlorobenzene, an additional carbon emission around 285.3 eV is needed to describe the C1s emission completely. Since all the previously assigned carbon species are still present and unchanged in intensity or energy position, this additional component is attributed to

contaminations brought into the solvent by repeatedly exposing it to the rubber sealing material of the nebulizer unit.

The influence of the solvent exposure through the various deposition techniques on the work function and the valence features is shown in the UP spectra in Figure 8.6. Both the secondary electron cutoff as well as the valence band spectra are influenced by the chlorobenzene deposition. Features emerging in the valence region spectra (Figure 8.6 b) in the range of 7 eV to 10 eV are attributed to diffuse carbon contaminations. These go along with a significant decrease in work function (Figure 8.6 a). In fact, the spectra obtained for the intentionally contaminated chlorobenzene resemble those obtained for the only solvent-cleaned ITO in Figure 8.3. The work function change induced by the nebulization of chlorobenzene is comparable to the change also observed by exposing the ozone-treated ITO to argon atmosphere (see Figure 8.3). This is understandable since only very little material was deposited, so the major effect could also just be due to the reducing UHV and argon atmosphere.

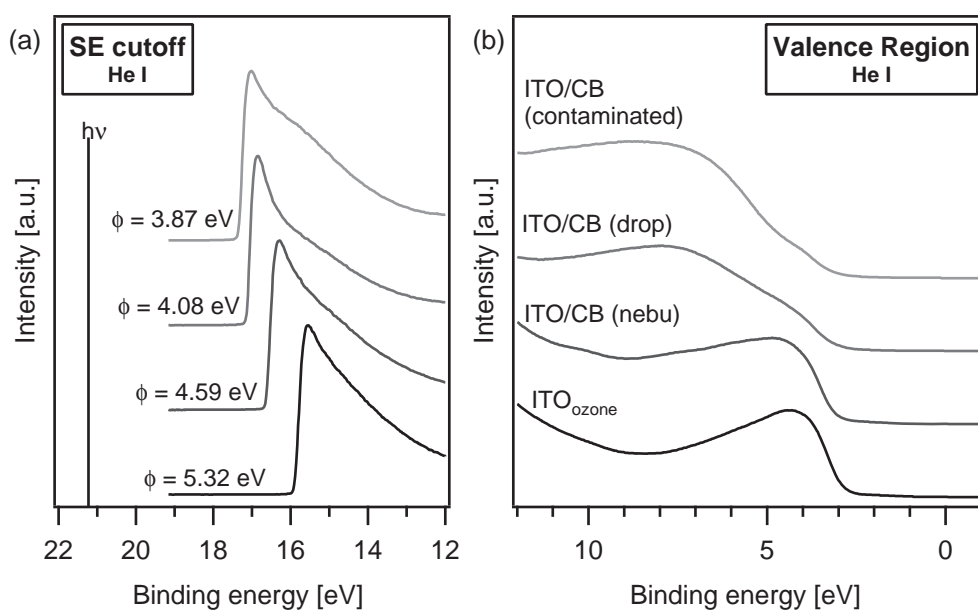


Figure 8.6: Secondary electron cutoff and valence region spectra of solvent- and ozone-cleaned ITO (ITO), chlorobenzene on ITO via nebulization (ITO/CB (nebu)), chlorobenzene on ITO via drop-casting (ITO/CB (drop)), and deliberately contaminated chlorobenzene on ITO (ITO/CB (cont.)) (from bottom to top).

8.4 Wetting of Ozone-Treated ITO by Chlorobenzene

The combination of ozone-treated ITO as a substrate material and chlorobenzene as a solvent is the basis for the further deposition experiments of DH6T and PCBM. Therefore the wetting of ITO by chlorobenzene was investigated. As stated above, the ozone treatment increases the surface energy of ITO. With the help of the contact angle measurements performed with the Krüss DSA 100 setup, the polar σ_s^D and dispersive σ_s^D portion of the surface energy are determined and then included in the wetting envelope calculations. The result of the contact angle measurements with the liquids diiodomethane, ethylene glycol, and water are shown in Figure 8.7.

The contact angles of the three different solutions on ITO together with their tabulated surface energy and the individual dispersive and polar contributions are summarized in Table 8.1.

Using these values, the polar and dispersive contributions to the surface energy of ozone-treated ITO can be calculated from the linear fit to the data according to equation 3.18 and

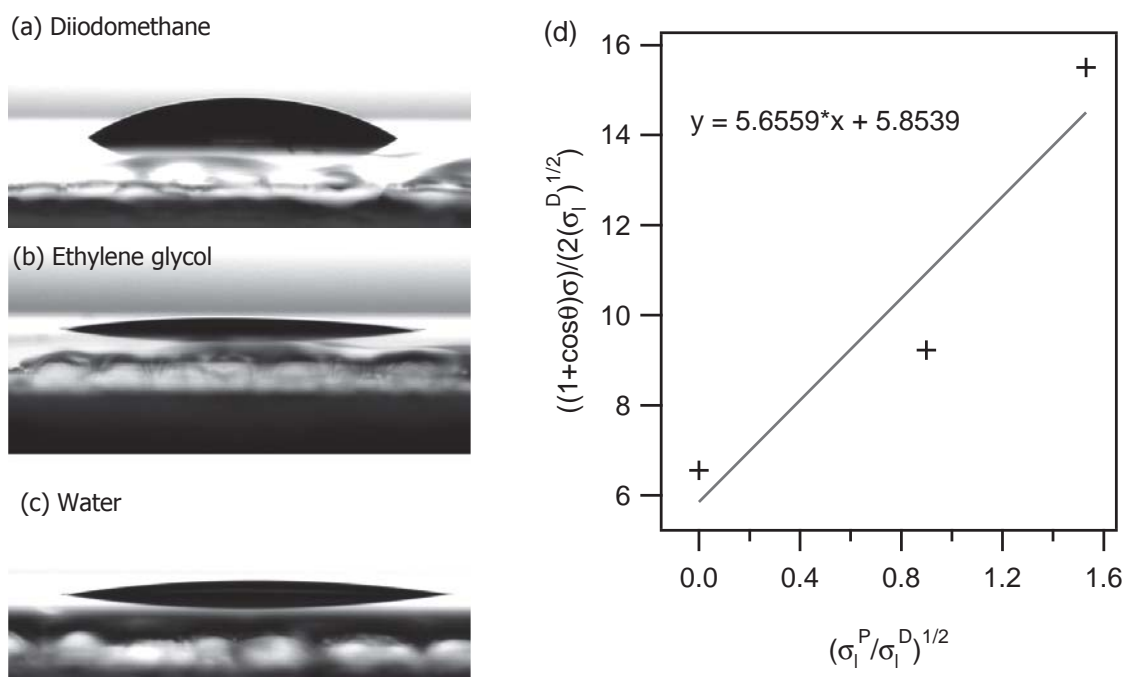


Figure 8.7: Image of contact angle measurements of diiodomethane (a), ethylene glycol (b), and water (c) on ITO, that has been treated in the ozonizer for 15 min. (d) Plot of the contact angle evaluation according to OWRK (see section 3.4.1).

Table 8.1: Measured contact angles of the different liquids on ozone-treated ITO. The values for the surface tension (σ_l) and the dispersive (σ_l^D) and polar (σ_l^P) components are taken from the Krüss software.

Liquid	contact angle [°]	σ_l	σ_l^D	σ_l^P
Diiodomethane	32,8 ± 3,01	50,8	50,8	0
Ethylene glycol	9,1 ± 3,2	47,7	26,4	21,3
Deionized water	8,4 ± 0,77	72,8	21,8	51

as shown in Figure 8.7 d. The polar contribution of the surface tension equals 32 mN m⁻¹ while the dispersive contribution is 34.3 mN m⁻¹. Thus, the total surface energy σ of 15 min ozone-treated ITO is 66.3 mN m⁻¹ (according to equation 3.14).

To determine the surface energy of chlorobenzene, a tensiometer (Krüss K100C-MK2) applying the plate method (see section 3.4.1) was used together with Teflon substrates. The obtained surface energy is 33.12 mN m⁻¹. Since the polar and dispersive contribution to the surface energy are known for the Teflon ($\sigma^D = 18\text{--}20$ mN m⁻¹, $\sigma^P = 0\text{--}2$ mN m⁻¹) substrates [141, 142], these contributions can also be calculated for chlorobenzene. Thus the values of σ^P (0–2 mN m⁻¹) and σ^D (31–33 mN m⁻¹) can be compared to the calculated wetting envelope for ozone-treated ITO. The result is graphically represented in Figure 8.8 and clearly shows the wettability of ozone-treated ITO by chlorobenzene as the value couple lies within the wetting envelope.

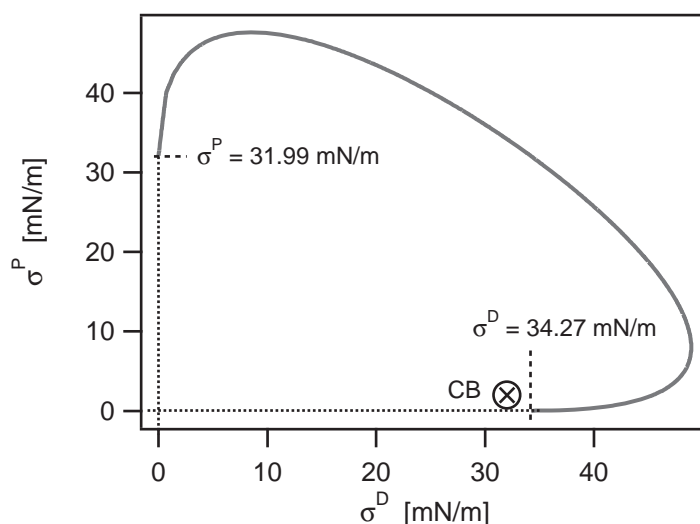


Figure 8.8: Wetting envelope of ozone-treated ITO. The value pair of the polar and dispersive part of the surface energy of chlorobenzene (CB) is included and lies within the wetting envelope. This indicates wettability of the ITO substrate by chlorobenzene.

8.5 Summary

By engineering the nebulizer setup, the requirements for deposition of organic semiconductors from solution through ultrasonic mist production was enabled. To achieve this deposition also from sub-ml quantities the piezo disk of the nebulizer unit was incorporated into a specially designed steering unit which transports the ultrasonically produced nebulae with the help of an argon flow to the substrate. The complete setup was successfully incorporated into the glass cell deposition chamber to enable clean sample preparation suitable for PES characterization.

Summarizing the substrate and solvent experiments, it was shown that ozone-treated ITO seems to be a suitable substrate for the nebulizer experiments as it provides a reproducible method to obtain carbon contamination free substrates (with respect to XPS) which will allow the tracing of any carbon emission stemming from the deposited organic materials. Special care needs to be taken when applying aggressive solvents such as chlorobenzene because prolonged exposure of the solvent to the sealing material of the nebulizer unit will lead to contaminations in this otherwise very clean deposition procedure. However, during the intended duration of the nebulization process only a very small fraction of carbon on the ITO surface could be detected which was attributed to adsorbed solvent molecules rather than contaminations. The surface tension evaluation of both ozone-treated ITO and chlorobenzene showed that in principle this solvent should wet the substrate completely. Therefore, this material combination should not be the limiting factor concerning layer deposition with the nebulizer method.



9 Nebulization of DH6T

In this chapter the first results of the nebulizer deposition of DH6T are presented. The distinguished property to deposit this material both via thermal evaporation and via solution-based techniques offers the possibility to characterize the glass cell setup at the Clustertool at the InnovationLab as well as the nebulizer method in comparison to evaporated films. Besides the electronic properties of the differently prepared DH6T films, also the chemical composition and in particular the molecular integrity after the nebulization through ultrasonic agitation are investigated. The film formation is characterized using optical microscopy.

9.1 Chemical and Electronic Structure of Differently Prepared DH6T

The evaporated and drop-cast DH6T films were prepared on solvent-cleaned ITO. For the nebulizer deposition, ozone-treated ITO was used, as only very little material deposition was expected and with ozone-cleaned ITO, the tracking of any arising carbon emission is facilitated. Therefore, the spectra of both solvent-cleaned ITO and ozone-treated ITO are shown together with the DH6T data to enable the direct retracing of substrate influences on the organic layers. The two solution-based deposition techniques were performed using the same solution at a concentration of 5 mmol l^{-1} of DH6T in chlorobenzene. For the drop-casting experiment roughly 5 droplets from a glass pipette of the DH6T solution were deposited onto the substrate. For the nebulizer deposition, 0.2 ml of the solution were ultrasonically nebulized at an input voltage of 40 V and the deposition time was 10 s. During the nebulization of DH6T the formation and drying of individual droplets was observed. To perform the PES characterization, the measuring spot was centered on one of these droplets. The evaporation was performed for 35 min using a home-built evaporation source. The evaporation temperature was 180°C to 190°C and the base pressure in the deposition chamber was in the low 10^{-7} mbar regime. The obtained survey and core level spectra are shown in Figure 9.1.

The intensity of the solvent-cleaned ITO survey spectrum was decreased by a factor of five to facilitate comparative representation of the spectra. All major emission lines are identified and annotated in the graph. In the case of the solution-processed films, the substrate emission lines are still visible after the DH6T deposition. This indicates either thinner layers compared to the evaporated film or a poorer film quality. Especially in the spectrum of the nebulized film the low film thickness or poor coverage shows a broad intensity increase in the range of 400 to 1000 eV due to inelastically scattered electrons stemming from the ITO. This agrees to the above mentioned observation of individual droplets rather than a closed layer during the nebulizer deposition. In addition to the expected carbon and sulphur signal also bromine could be detected in the DH6T films most likely stemming from the DH6T synthesis (compare to section 5.2.1). The Br concentration in the evaporated film is lower than in the solution-processed films. This is understandable as the evaporation process acts as a purification step. These observations are in accordance to the previously reported results and their discussion (see section 5.2).

The Indium 3d emissions of the solvent-cleaned and ozone-treated ITO in Figure 9.1 b are reduced in intensity by a factor 5 for clear representation. From the original intensity ratios of the bare and covered substrate the formal layer thickness of DH6T was calculated to 62 Å and 92 Å for the nebulized and drop-cast film, respectively. The inelastic mean free path was calculated using the NIST data base [93] and is 27 Å for the kinetic energy of the In3d photoelectrons (see Table B.2 in the appendix B). The layer thickness of the evaporated DH6T sample is around 40 nm and was obtained from a profilometer scan.

The DH6T characteristic C1s and S2p core level emissions are shown in Figures 9.1 c and d. In all three cases the asymmetric shape of the C1s emission is visible and the S2p doublet is clearly resolved. The peaks observed for the evaporated film are slightly more defined than for the two solution-processed DH6T layers. This could be due to morphology differences [105]. Taking the tabulated atomic sensitivity parameters [89], the atomic ratio can be calculated from the respective C1s to S2p intensity ratios. From the molecular structure a carbon to sulphur ratio of 6 to 1 is expected and this could be nicely reproduced in all cases as the obtained ratios are 6:1.1, 6:1.2, and 6:1.12 for the nebulized, the drop-cast, and the evaporated DH6T films, respectively. This confirms the intact deposition of the DH6T molecules by all presented techniques.

The C1s emission is further evaluated by fitting the complex envelope using Voigt profiles (Figure 9.2). A consistent fitting result is achieved using three Voigt profiles which repre-

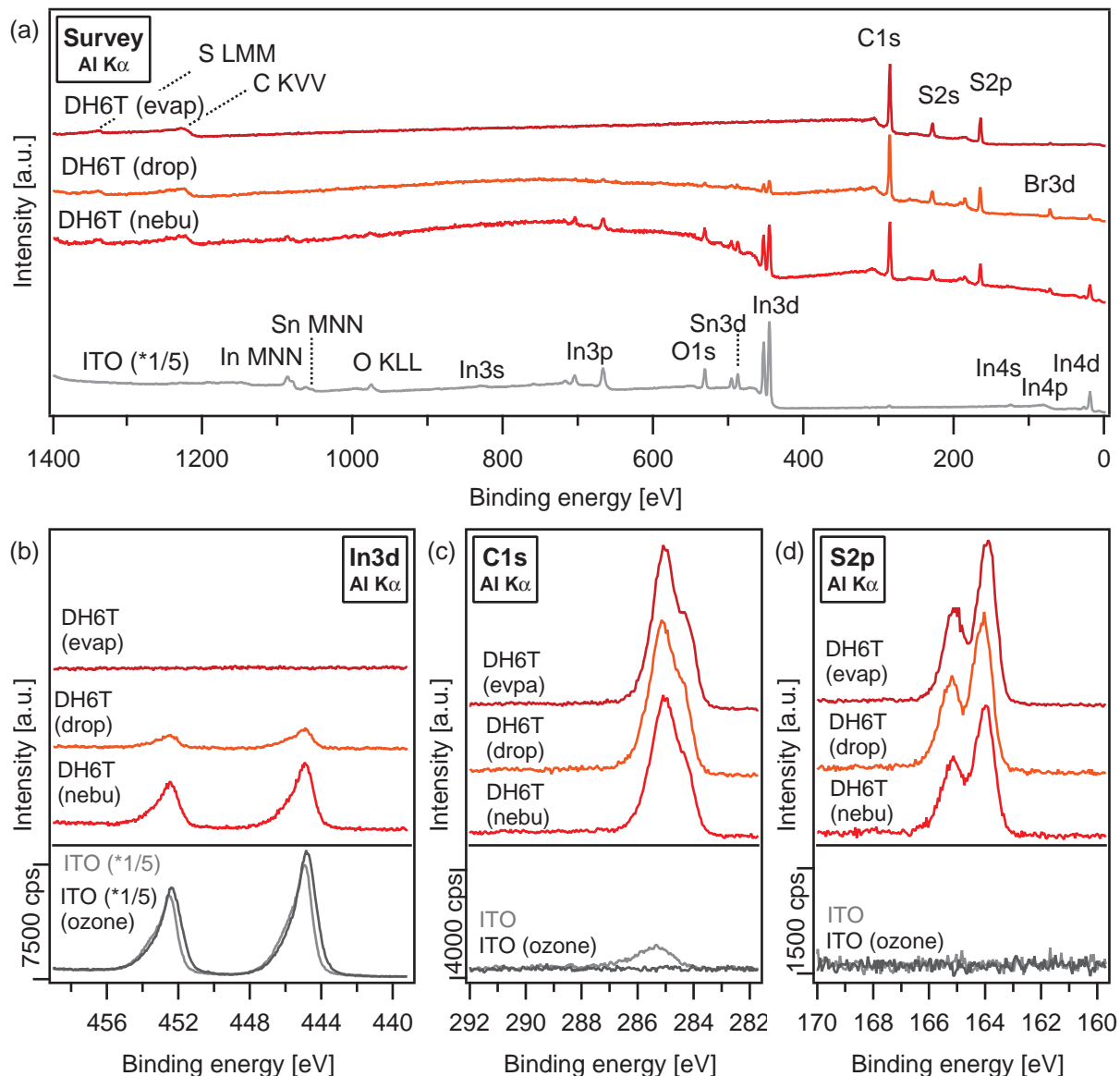


Figure 9.1: (a) Survey spectra of ITO (intensity decreased by a factor of 5) and the three differently prepared DH6T layers. In case of the nebulized and the drop-cast film the layer thickness or coverage is rather low so that the substrate emission lines are still visible. In addition, bromide could be detected for the solution-derived films while it could not be detected in the evaporated film (compare to section 5.2). (b) In3d core level spectrum, (c) C1s core level spectrum, and (d) S2p core level spectrum of solvent- and ozone-treated ITO, nebulized DH6T, drop-cast DH6T, and evaporated DH6T (from bottom to top).

sent the three different carbon binding sites according to the molecular structure (Figure 9.2 a). The fitting parameters are given in Table 9.1. The lowest binding energy component (1) is attributed to the carbon atoms which are only bound to carbon and hydrogen within the thiophene unites followed by the emission of the sulphur bound carbon atoms

(2). The third component (3) at highest binding energy corresponds to the terminal hexyl groups. This assignment follows the working hypothesis developed in section 4.2 and is consistent to the previously presented results on DH6T (see chapter 5.2). The intensity ratios of the different C1s components are listed in Table 9.1 and roughly correspond to their expected number in the molecule (1:1:1). Furthermore, these ratios nicely correlate to the ratio of 1:1:1.7 determined for the most bulk-like SXPS measurements at 600 eV in section 5.2. The component of the hexyl group (3) is slightly broadened with respect to the other two components. This can be understood due to the higher flexibility of these side chains and thus less order but also due to slight potential differences caused by the inductive effects along the chain. Strong orientation effects as observed for the synchrotron measurements in chapter 5.2 are not expected as the probing depth in XPS ($3\lambda \approx 90 \text{ \AA}$) is much higher than the size of the oriented molecules (which is around 35 \AA according to ref. [75]).

In general, the core level emission lines of the differently prepared DH6T films show very good agreement concerning line shape and energetic positions verifying that the nebulizer method is capable of depositing low quantities of an organic soluble material without changing the molecules chemical composition or structure.

The influence of the preparation technique on the electronic levels can be extracted from the valence spectra shown in Figure 9.3 together with the secondary electron cutoff spectra. In the valence fingerprint regions of all DH6T films (Figure 9.3 b) the same spectral features are observed. Only in the case of the nebulized sample, these features appear slightly broadened compared to the other two films. This might be caused by the very low quantity of deposited material giving a lower signal strength. Also, impurities e.g. from the nebulizer rubber seal dissolved in the chlorobenzene (as observed in section 8.3.2) might be involved giving rise to a rather diffuse background. Additionally, ordering effects could play a role. Due to the very small droplet size the drying is increased significantly compared to the drop-cast film. Therefore, the time for molecular arrangements is also limited, which might result in a less ordered film. This in turn could cause an additional intrinsic broadening. As described above, a similar effect was observed in the core level spectra.

Due to the ozone treatment of the ITO substrate for the nebulizer deposition this substrate has a much higher work function (i.e. 5.33 eV) than the solvent-cleaned ITO (4.07 eV). This effect of the treatment seems to be passed partly on to the DH6T deposited via the

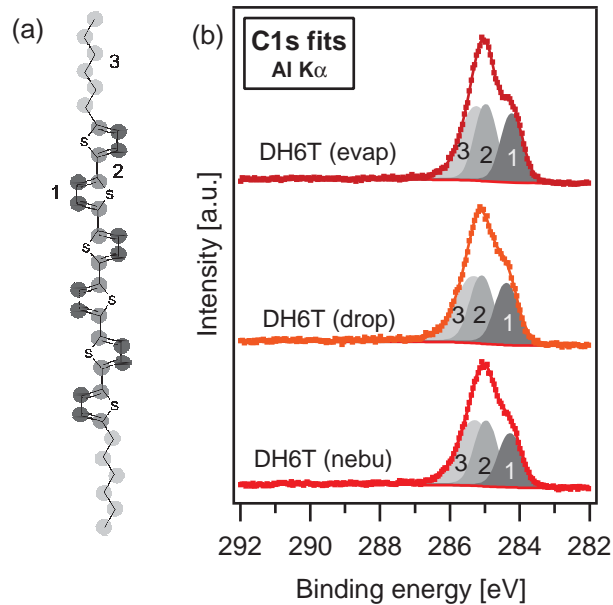


Figure 9.2: (a) Molecular structure of DH6T with the three different carbon binding sites indicated by the differently shaded circles. (b) Fits of the C1s emission line to separate the three components according to the molecular structure. The original data sets are represented as dotted lines.

Table 9.1: Fitting parameters for the C1s emission of the differently prepared DH6T samples as depicted in Figure 9.2.

	$E_{\text{bind}} (1)$ [eV]	$E_{\text{bind}} (2)$ [eV]	$E_{\text{bind}} (3)$ [eV]	w_{Gauss} (1 & 2) [eV]	w_{Gauss} (3) [eV]	Intensity ratio I(1):I(2):I(3)
DH6T (evap)	284.2	284.9	285.2	0.66	0.9	1:1.1:1.7
DH6T (drop)	284.4	285.1	285.4	0.7	1.1	1:1.1:1.8
DH6T (nebu)	284.3	285.0	285.3	0.7	1.0	1:1.2:1.9

nebulizer method as all valence level are shifted by 0.2 eV to 0.3 eV to lower binding energies compared to the other two layers. For all three films, the $\text{HOMO}_{\text{onset}}$ values were determined through a linear fit to the spectral onset (Figure 9.3 b) and the work functions were obtained through linear fits to the secondary electron cutoffs (Figure 9.3 a). The values are summarized in Table 9.2 together with the calculated ionization potentials. To further discuss the origin of the energetic shift in the nebulized film, the layer thickness are included.

Although the spectral onset and cutoff values differ by about 0.3 eV, both solution-processed DH6T samples show the same ionization potential (5.05 eV and 5.06 eV), which perfectly agrees to the before determined value of 5.1 eV in section 5.2. Therefore, the

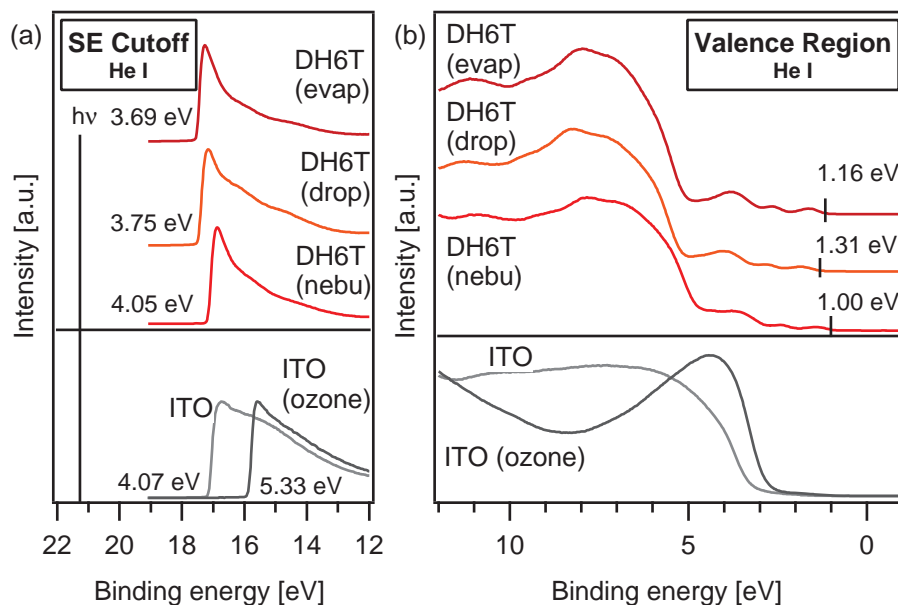


Figure 9.3: (a) SE cutoff and (b) valence region of ITO (both only solvent-cleaned as well as ozone-treated), nebulized DH6T, drop-cast DH6T, and evaporated DH6T (from bottom to top).

Table 9.2: HOMO_{onset} and work function values for the differently prepared DH6T samples including the calculated ionization potentials (IP) and layer thicknesses.

Preparation technique	HOMO _{onset} [eV]	ϕ [eV]	IP [eV]	d [\AA]
evaporation	1.16	3.69	4.85	400
drop-casting	1.31	3.75	5.06	92
nebulization	1.0	4.05	5.05	62

relative shift of the electronic levels could be explained by a different Fermi level position. Possibly, this could be induced by the substrate as in the case of the nebulization experiment, ozone-treated ITO was used which has significantly different electronic properties compared to solvent-cleaned ITO (see section 8.3.1) and could thus induce an interface dipole. Furthermore, a thickness dependence of the Fermi level position, i.e. band bending, could also contribute to this relative shift as the differently prepared DH6T layers have different thicknesses as indicated in Table 9.2. The ionization potential of the evaporated film, however, differs by ca. 0.2 eV from the value obtained for the solution-processed films. This could be due to the preparation technique as the evaporated film is less contaminated through solvent exposure and possible syntheses residues and therefore has a different level of unintentional doping. It could also be caused by radiation exposure as thiophenes are reported to be radiation sensitive. OPITZ ET AL. report on a work function

decrease of up to 0.2 eV during 20 min of UV light exposure (at He I emission). This shift is accompanied by a parallel shift of the valence and core levels and is attributed to UV induced charged traps and/or a change in the molecular density of states caused by radiation induced damage to the molecules [109]. It is also reported that no additional changes in the spectral features like broadening are observed. This contradicts the assumption of radiation damage in the sense of changing the molecular chemistry but could hint towards UV induced energetic changes e.g. in the interface dipole which could also contribute to the often observed light soaking effect in OPV devices [143–145]. Although all samples were measured in the same setup, exposure times might have differently changed the degree of possible radiation damage. Furthermore, it is noteworthy that ionization potential values from 4.7 eV [124] to 5.06 eV [123] have been reported which includes both obtained values from this set of experiments. Additionally, DUHM ET AL. [124] showed an orientation dependence of the electronic properties of DH6T and by evaporation, typically, highly ordered films are obtained. This can affect or lead to the formation of a surface dipole which also alters the measured work function.

To compare the general valence structure in more detail, the spectra are normalized to the maximum HOMO intensity and shifted so that maxima are aligned. The result is shown in Figure 9.4. The dotted lines are meant as a guide to the eye indicating that the most pronounced features nicely correspond in energetic distance. This again is taken as a proof that the molecular structure remains unchanged during the nebulizer deposition.

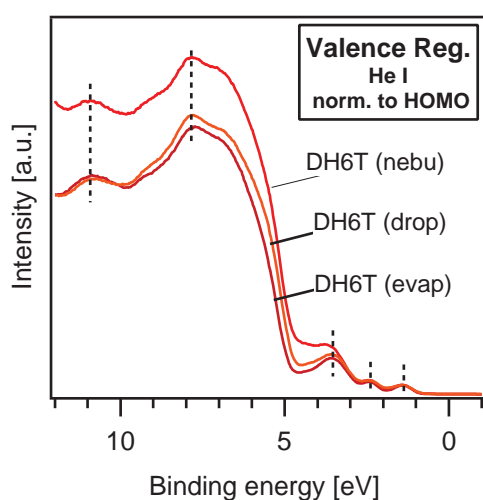


Figure 9.4: Detail valence region normalized in intensity to the HOMO and aligned showing perfect agreement in maxima position and overall shape of the valence spectra.

9.2 Optical Microscopy

To characterize the nebulized film concerning the layer structure optical microscopy is applied. Already from the observations during the deposition and the appearance in the spectrometer during PES analysis, no complete layer is expected but rather individual droplets. Optical microscopy images were taken at two different sample positions using an Olympus BX41 microscope in bright field mode. Two exemplary images are shown in Figure 9.5.

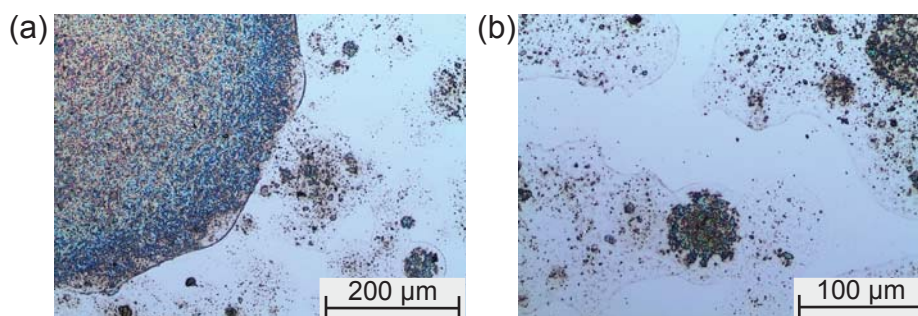


Figure 9.5: Optical microscopy images of nebulized DH6T. (a) Sample position 1 at 100x magnification. (b) Sample position 2 at 200x magnification.

The optical microscopy confirmed the presence of individual droplets after the nebulizer deposition of DH6T. In Figure 9.5 a large droplet with a diameter of several hundreds of μm can be seen in the upper left corner. Although no direct correlation to the measurement positions in PES is possible, a feature of such dimensions will most certainly allow both XPS and UPS analysis. However, the probed area in the used VersaProbe PES system is defined by the spot size of the excitation source. This could lead to a deviation in signal strength comparing XPS and UPS. On the one hand, a focussed x-ray source with a spot diameter in the order of $200\mu\text{m}$ was used for the XPS analysis, which could be placed centrally on one of the observed droplets. On the other hand, the gas discharge lamp for the UV excitation creates a light spot significantly larger in diameter. Since in PES the integral signal of the excited sample surface and volume is detected, the fraction of the signal stemming from deposited material could be reduced in UPS as compared to XPS.

In addition to this spatially extended feature, smaller droplets are observed. The darker and rather edgy features within the droplets possibly indicate crystallite formation. Especially in Figure 9.5 b in between these crystallite agglomerations a film is visible. This

could possibly be related to a thin DH6T film with some material agglomeration at the contact line of the formerly liquid droplet (comparable to the coffee stain effect [146]).

9.3 Summary

The presented experiments demonstrate the suitability of the newly developed nebulizer method for the deposition of organic semiconducting materials as the obtained spectra and the resultant chemical and electronic properties are equivalent to those obtained via drop-casting. On the example of DH6T, it could be shown, that a small quantity of an organic donor material could be deposited from solution on an inert substrate. Molecular integrity irrespective of the preparation techniques was confirmed by the striking agreement in both the core level spectra and the valence spectra for evaporated, drop-cast and nebulized DH6T. The determination of the electronic properties was possible, although no continuous film but rather individual droplets could be deposited via the nebulizer method (as confirmed by optical microscopy).

While in chapter 5.2 perfect agreement between evaporated and drop-cast DH6T was found considering both chemical as well as electronic properties, this could not be reproduced in this chapter. The two sets of experiments were performed at different setups using different excitation sources, i.e. synchrotron radiation and laboratory x-ray and gas discharge sources, respectively. Thus, one explanation could be the different intensities of the excitation sources together with potentially different exposure times. Since the obtained electronic properties of the solution-processed films correlate nicely to the previously obtained SPXS results, also the evaporation conditions might be crucial. Especially considering the purification effect during material heating in UHV, the number and duration of evaporation depositions made from one crucible filling might have a strong influence on the impurity level of the organic thin film.

In addition to the DH6T specific results, the general suitability of the glass cell setup at the Clustertool for organic thin film preparation from solution could be established through the comparison to evaporated films.



10 Nebulization of PCBM

In this chapter the results of the first nebulizer depositions of PCBM are presented. To exclude reactions of PCBM with the activated ITO the deposition was also carried out on poly(3,4-ethylenedioxythiophene) : poly(styrene-sulfonate) (PEDOT:PSS), which also provides a high work function substrate. Since PCBM is used as the electron acceptor in OPV devices, Polyethylenimine (PEI) covered ITO was used as a third and low work function substrate. Both interfaces of PCBM to PEDOT:PSS and PEI are technologically relevant concerning their hole and electron selectivity, respectively. In all cases of nebulized PCBM, thickness-dependent electronic properties were observed.

10.1 Nebulizer Parameters

For the nebulizer experiments the depositions were run with about 0.2 ml of dilute PCBM solution for each step. The solution was deposited on the nebulizer unit with a glass Pasteur pipette. The concentration of PCBM in chlorobenzene was kept low around 3 mg ml^{-1} to 5 mg ml^{-1} since the aim was to produce ultra thin PCBM layers. For the drop-casting and spin-coating experiments the same solutions were used to be consistent concerning concentration and possible other external effects. The nebulizer input voltage was set to 42 V–45 V DC allowing for an input power of 20 W to 25 W.

To steer the formed mist, a conical nozzle with a single, centered hole was used. The argon flow through the nebulizer unit was set to be 0.1 mbar to 0.2 mbar. The time of each individual deposition varied between 10 s in the case of ITO and ITO/PEI as a substrate and 20 s to 30 s when PEDOT:PSS was used as a substrate material.

10.2 PCBM on ITO

As a first substrate material ozone-treated ITO was chosen for the nebulizer deposition as this surface treatment technique in combination with solvent cleaning provides substrates

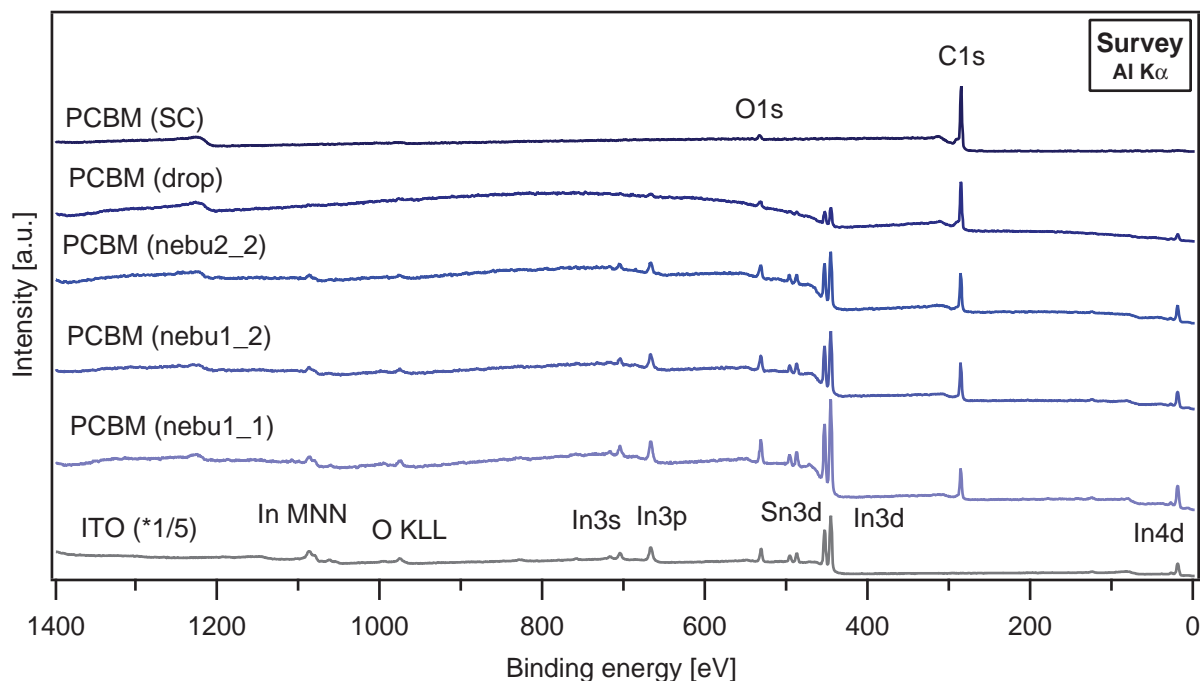


Figure 10.1: Survey spectra of PCBM deposited via the nebulizer method (denoted by nebu) on ozone-treated ITO (bottom) in comparison to drop-cast (drop) and spin-coated (SC) PCBM. The intensity of the ITO survey spectrum is decreased in intensity by a factor of 5 for clear data representation.

with no detectable carbon contamination (see section 8.3.1). Therefore, the deposited material can be directly traced by the increase in C1s intensity. Additionally, the ozone-treated ITO has a suitable surface energy to allow wetting by PCBM dissolved in chlorobenzene (see section 8.4). The nebulizer process was repeatedly performed on the same substrate taking spectra after each individual deposition step and at different sample positions as the drying of individual droplets was observed (comparable to chapter 9). The resulting survey and core level spectra are shown in Figure 10.1 and Figure 10.2, respectively. In addition to the data from the nebulizer deposition, the substrate spectra as well as the spectra of a drop-cast and a spin-coated PCBM sample are included. The drop-casting experiment was performed in the glass cell while the spin-coating was performed ex-situ but the sample was placed in the load lock while still warm to prevent excessive surface contamination and water adsorption.

The intensity of the ITO survey spectrum as well as the ITO O1s spectrum (in Figure 10.2) are reduced in intensity by a factor of 5 for the sake of clear data arrangement. In the survey spectrum of the ozone-treated ITO all major emissions of the constituting elements

indium, tin and oxygen are present but no carbon emission could be detected. Already after the first nebulizer deposition (position 1: nebu1_1 and position 2: nebu1_2) a clear carbon signal is visible. Besides this, no other additional signals could be detected in XPS. The detailed evaluation of the signal intensities follows for the core level spectra.

Although the O1s spectrum of PCBM for all nebulized films as well as for the drop-cast layer is superimposed by the ITO oxygen signal, the two PCBM characteristic oxygen peaks at 532.1 eV and 533.6 eV as indicated in the inset molecular structure and marked by the arrows can be identified in Figure 10.2 a. In the In3d signal (Figure 10.2 b) an intensity decrease can be observed going from position 1 after the first nebulizer deposition (nebu1_1) to position 2 after the first deposition (nebu1_2) to the same position after the second deposition step (nebu2_2). This intensity decrease in the In3d corresponds to the intensity increase of the C1s emission in Figure 10.2 c. From the damping of the substrate signal a formal layer thickness could be calculated for the different nebulization positions and steps as well as for the drop-cast sample. The results are summarized in Table 10.1. In general, the formal layer thickness is in the range of several tens of Ångström for the nebulized samples and the layer obtained for the drop-cast sample is almost twice as thick. Especially noteworthy is the increase in formal layer thickness between nebu1_2 and nebu2_2 as these correspond to the same measurement spot but after repeated nebulae exposure. This shows that successive material deposition via the nebulizer method is in principle possible without (completely) removing the previously deposited material. Since the layer of the spin-coated PCBM sample was so thick that no substrate signal could be detected any more (see survey spectrum), no detail spectrum of the In3d was acquired. From Dektak measurements the thickness is determined in the range of 20 nm.

Table 10.1: Calculated layer thickness of the different PCBM samples prepared via the nebulization technique as well as drop-casting. The layer thickness of the spin-coated sample was determined from a profilometer scan.

Sample	Layer thickness [Å]
PCBM (nebu1_1)	30.3
PCBM (nebu1_2)	40.7
PCBM (nebu2_2)	46.1
PCBM (drop)	76.6
PCBM (SC)	200

The secondary electron cutoff and the valence level spectra corresponding to these XPS measurements are shown in Figure 10.3. In the secondary electron cutoff spectra a drastic

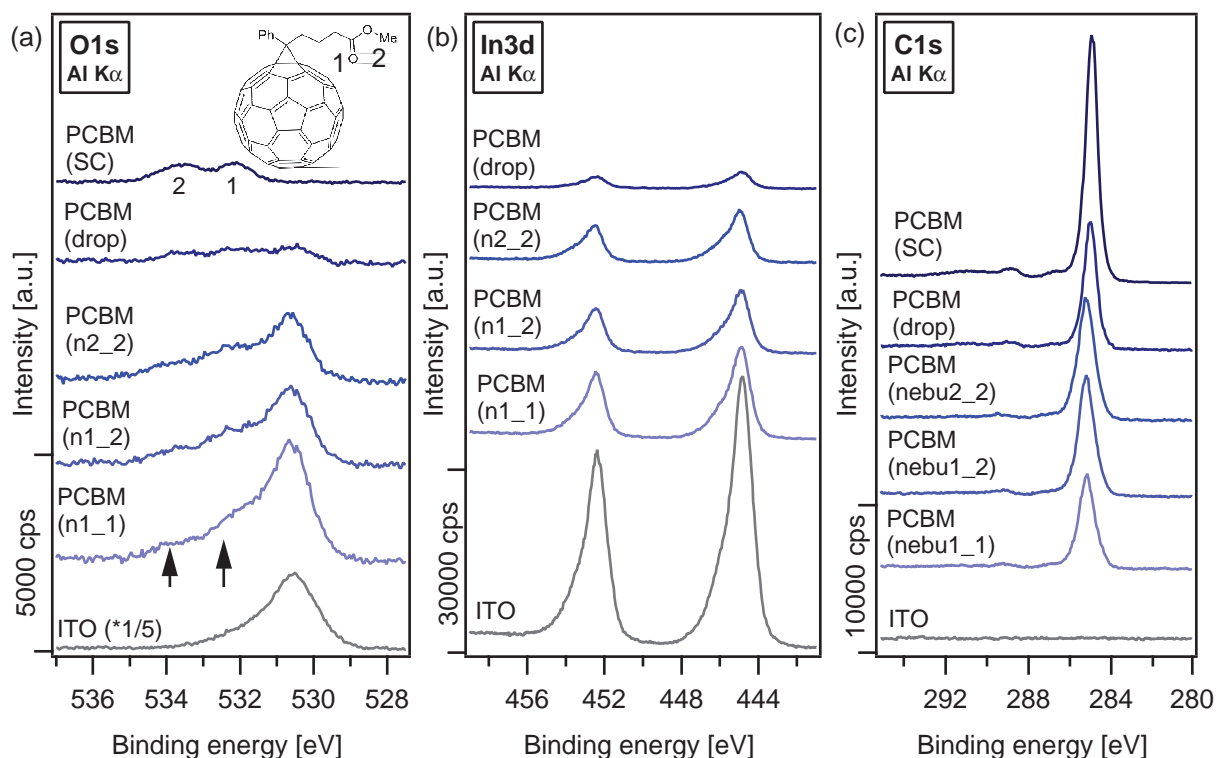


Figure 10.2: (a) O1s core level emission, (b) In3d core level emission (without spin-coated spectrum as no substrate emission is visible), and (c) C1s core level emission for PCBM deposited via the nebulizer method (denoted by nebu or n) on ozone-treated ITO (bottom) in comparison to drop-cast (drop) and spin-coated (SC) PCBM. The intensity of the ITO O1s spectrum is decreased in intensity by a factor of 5 for clear data representation.

change in work function from the bare ozone-treated ITO to the nebulized PCBM samples is observed. As previously described (see chapter 8.3.1), part of this work function reduction could be caused simply by the exposure to a reducing atmosphere. However, the here observed change of about 1 eV exceeds the Ar induced change of 0.6 eV and is thus attributed to the deposited PCBM (or a combination of both). For the thicker PCBM layers deposited via drop-casting in the glass cell or spin-coating, the work function actually increases again to values of 4.46 eV and 4.6 eV. In the valence region spectra the PCBM signal strength in the case of the nebulizer depositions is weak compared to the drop-cast and spin-coated PCBM. This could be due to the ultra low thickness of the film deposited via the nebulizer method and probably the small droplet size.

Despite the low intensity of the features in the energy range of 1.5 eV to 4 eV concerning the nebulized samples the $\text{HOMO}_{\text{onset}}$ positions can be determined for all PCBM samples. With increasing layer thickness the $\text{HOMO}_{\text{onset}}$ shifts from 1.93 eV for the first nebulization

deposition to 1.56 eV and 1.4 eV for the drop-cast and spin-coated PCBM film, respectively. Although the $\text{HOMO}_{\text{onset}}$ can be readily determined for all nebulized PCBM samples, the general shape of the valence structure differs from the fingerprint region observed for drop- or spin-cast PCBM films on the same substrate material (see Figure 10.3 b). Especially in the region of 5 eV to 11 eV, an intensity increase is observed. This rather plateau-like feature exhibits a weak sub-structure although no clear correlation to the maxima observed in PCBM (drop) and PCBM (SC) in this energy region can be observed. A detailed discussion of the valence features follows in section 10.6.

Combining the work function values with the $\text{HOMO}_{\text{onset}}$ positions an ionization potential of around 6 eV was measured for all PCBM samples. Summarizing the obtained data and ordering them according to their PCBM layer thickness on ITO a preliminary energy level diagram can be drawn such as in Figure 10.4.

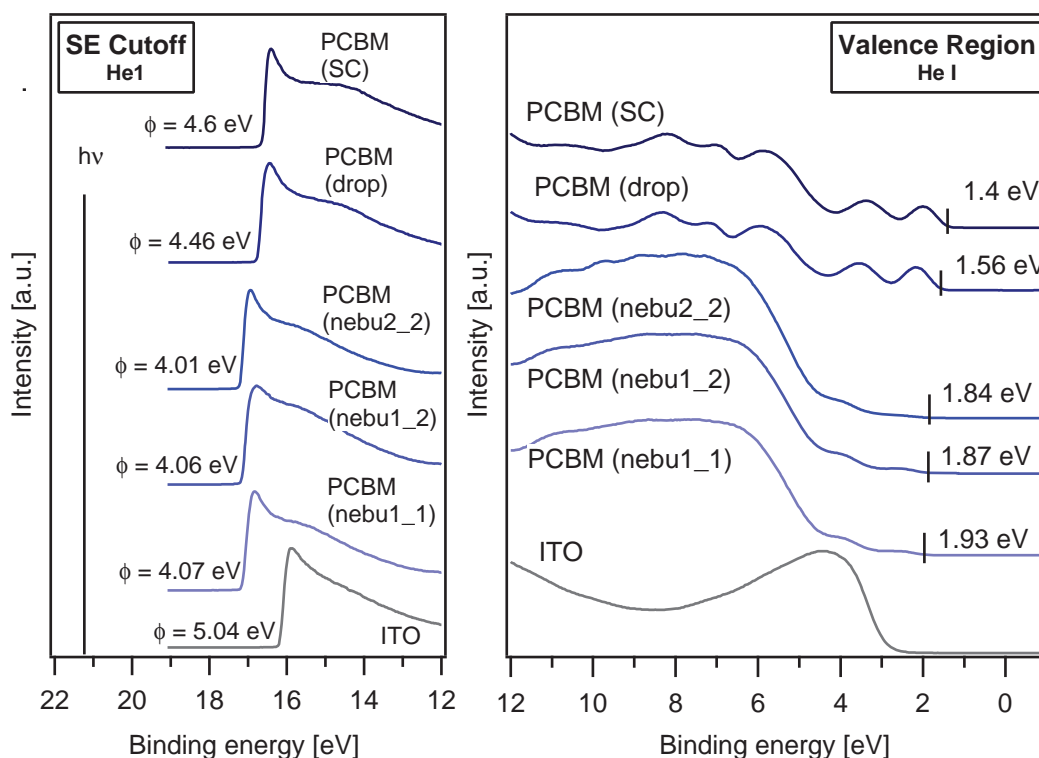
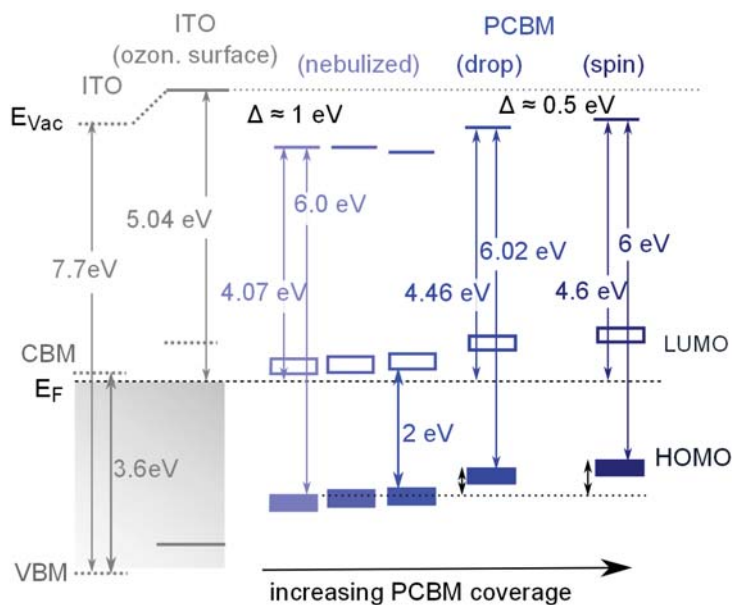


Figure 10.3: (a) Secondary electron cutoff. (b) Valence region spectra. From bottom to top: ITO substrate, PCBM after the first nebulization at position 1, PCBM after the first nebulization at position 2, PCBM after the second nebulization at position 2, drop-cast PCBM, and spin-coated PCBM. The latter two are meant as a reference for thick, solution-processed layers.

Figure 10.4: Energy level diagram of the different nebulization steps of PCBM on ozone-treated ITO in comparison to drop-cast and spin-coated PCBM. The $\text{HOMO}_{\text{onset}}$ shifts with increasing PCBM coverage to lower binding energy values. This hints towards an electron transfer from the ITO to the PCBM. The energy gap values of PCBM and ITO are taken from ref. [24, 71].



The PCBM $\text{HOMO}_{\text{onset}}$ shifts by 0.37 eV from the first nebulizer deposition compared to the drop-cast layer towards lower binding energy values. Compared to the even thicker spin-coated film the shift in the $\text{HOMO}_{\text{onset}}$ is 0.53 eV. This change in $\text{HOMO}_{\text{onset}}$ binding energy with increasing PCBM coverage indicates a charge transfer from the ozone-treated ITO to PCBM. In addition, a vacuum level offset Δ of 1 eV for the nebulized films and 0.5 eV for the drop-cast and spin-coated samples, respectively, is observed. This potential drop could be due to an interface dipole and/or band bending as different layer thicknesses for PCBM were achieved. However, morphology differences due to the different preparation techniques or possibly a reaction between PCBM and the activated ITO surface also need to be considered as possible reasons for this observed change. A further evaluation of this energy level alignment follows in section 10.5.

To provide some information as to whether or not a reaction between the ozonized ITO and PCBM might take place during the nebulizer deposition, which could be responsible for the change in valence shape and/or the possible charge transfer, PCBM was also deposited on different polymeric substrates via the nebulization method.

10.3 PCBM on PEDOT:PSS

PEDOT:PSS is a polymer mixture of poly(3,4-ethylenedioxythiophene) and poly(styrene-sulfonate) (see Figure 10.5). The one component is sodium polystyrene sulfonate which is a sulfonated polystyrene salt. The sulfonyl groups are partly deprotonated and thus carry a

negative charge. The other component is a polythiophene-based conjugated polymer and carries positive charges. The so formed macromolecular salt is dissolved in water to form a spin-coating solution. The PEDOT:PSS grade used in this work was Clevios PVPAl 4083 (Heraeus).

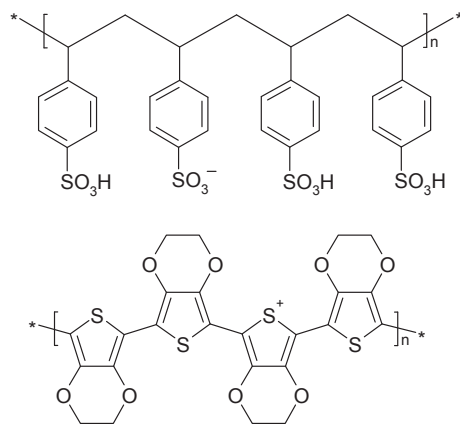


Figure 10.5: Molecular structure of Poly(3,4-ethylenedioxythiophene) (PEDOT) and Polystyrene-sulfonate (PSS).

In all cases, PEDOT:PSS was spin-coated on solvent-cleaned and ozone-treated ITO (15 min). Prior to the deposition of the suspension, PEDOT:PSS was filtered using a $0.45\ \mu\text{m}$ PTFE filter. Spin-coating was performed at 2000 rpm and 2500 rpm/s acceleration for 30 s resulting in films of approx. 40 nm in thickness. The films were then dried on a hot plate at $120\ ^\circ\text{C}$ for 60 min. To minimize possible contaminations, the substrates were screwed on the sample holder while still hot and directly placed in the UHV load lock for characterization and the following PCBM deposition.

PCBM was deposited via the nebulizer method in the glass cell. Since the produced film was rather inhomogeneous with respect to layer thickness and substrate coverage, spectra were taken at three different positions denoted by PCBM (nebu1), PCBM (nebu2) and PCBM (nebu3) in the order of increasing PCBM layer thickness. The drop-casting experiment was also performed in the glass cell but on a different PEDOT:PSS substrate using a PCBM solution of $5\ \text{mmol l}^{-1}$. The coverage of PEDOT:PSS with the drop-cast PCBM was rather inhomogeneous but a sufficiently large area for the PES measurements could be located. The resulting spectra are labeled PCBM (drop). In the case of the spin-coated PCBM layer (PCBM (SC)), the PEDOT:PSS substrate was covered with PCBM ex-situ directly after the PEDOT:PSS annealing. A subsequent heating step to around $120\ ^\circ\text{C}$ was again used to anneal the film and potentially reduce water and any other volatile adsorbates before introducing the sample into the PES setup.

All PEDOT:PSS spectra, which were measured before any PCBM deposition showed remarkable reproducibility both in chemical composition and electronic properties. Therefore, in the following discussion of the PCBM films only the PEDOT:PSS substrate emission of the nebulizer experiments will be shown as a reference. Since the focus is on the deposition of PCBM via different techniques, the evaluation of PEDOT:PSS as a substrate material is deliberately kept short and mainly follows the work of GRECZYNSKI ET AL. [147]. The survey spectra are shown in Figure 10.6.

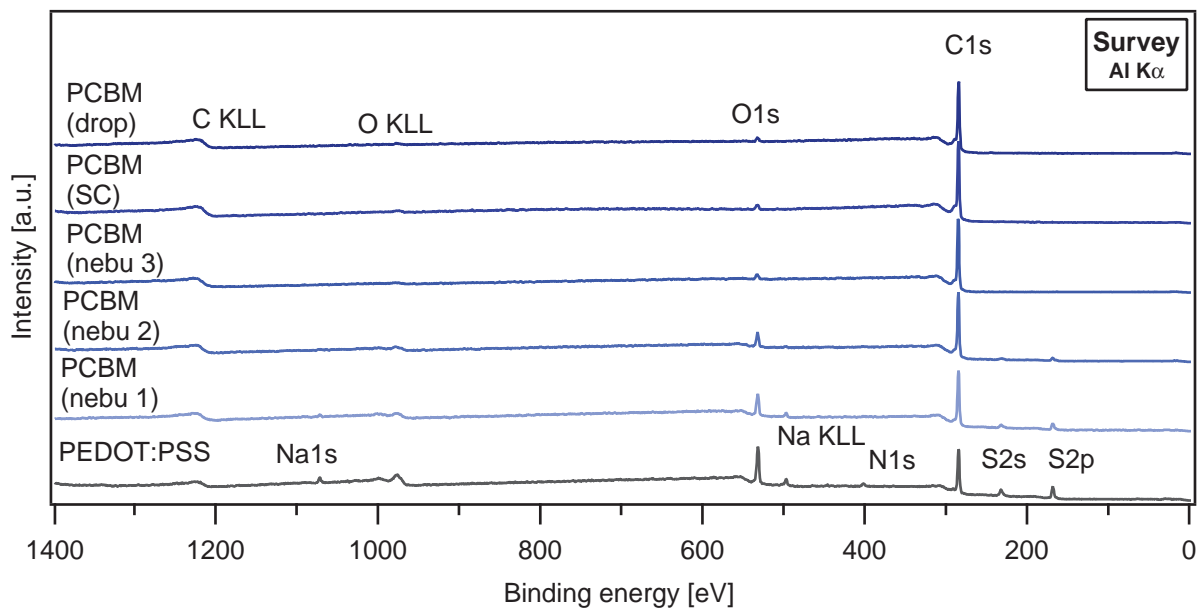


Figure 10.6: Survey spectra of PEDOT:PSS, PCBM (nebu1), PCBM (nebu2), PCBM (nebu3), PCBM (SC), and PCBM (drop) in the order of (anticipated) increasing PCBM coverage. The observed emission lines are indicated. PCBM (nebu1) to PCBM (nebu3) refer to different measurement spots on the same sample after the nebulizer deposition.

In the PEDOT:PSS survey spectrum the C1s, O1s, and S2p emission lines are observed as expected from the structure formula. The sodium contribution stems from the counter ion of the PSS-Na. Additionally, a contribution from $\text{Na}_2\text{S}_2\text{O}_8$ could be possible as this substance is used as an oxidizing agent during polymerization of PEDOT [148]. The N1s signal most likely originates from impurities introduced to the film during processing or adsorbates as the preparation took place in ambient air. The absence of any ITO related emissions (e.g In3d at 445 eV) indicates a pin-hole free PEDOT:PSS layer with a thickness larger than the probing depth of XPS. Already from the survey spectra, it can be seen that the S2p emission decreases in intensity for the individual PCBM depositions until for the samples PCBM (nebu3), PCBM (drop), and PCBM (SC) only the PCBM characteristic C1s

and O1s emissions are detected. To characterize the individual PCBM depositions in more detail, the O1s, C1s, and S2p emission lines are further evaluated (see Figure 10.7).

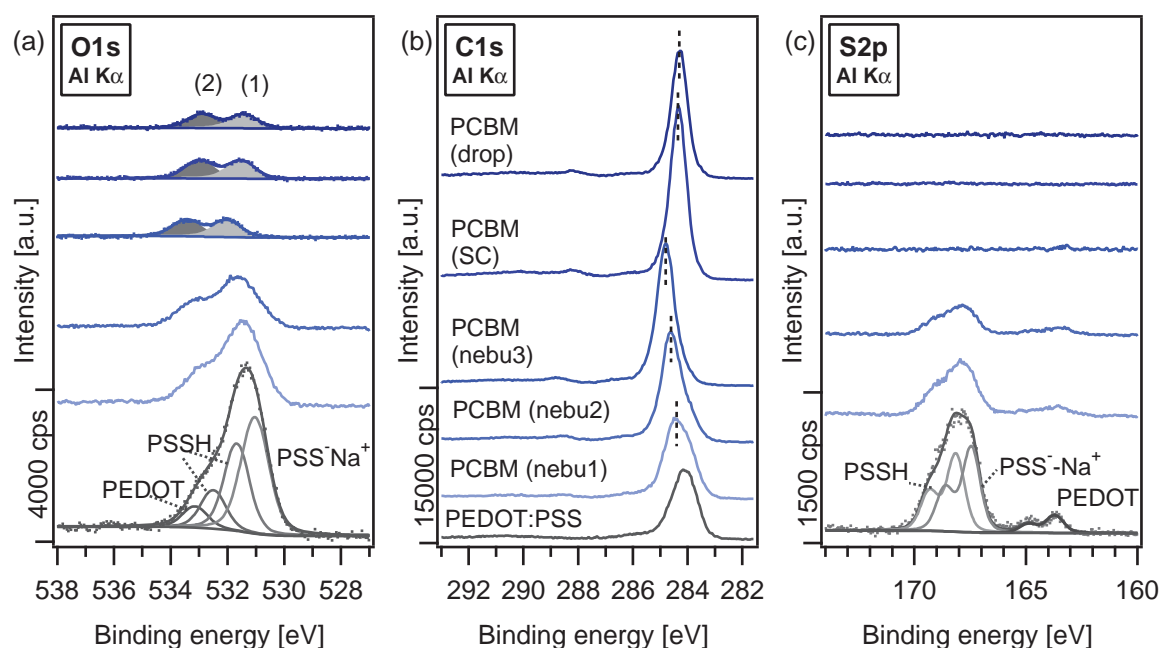


Figure 10.7: (a) O1s detail spectrum (numbers indicate the different oxygen bonding states), (b) C1s detail spectrum, (c) S2p detail spectrum of PEDOT:PSS, PCBM (nebu1), PCBM (nebu2), PCBM (nebu3), PCBM (SC) and PCBM (drop) (from bottom to top).

The S2p and O1s core level emissions of PEDOT:PSS were decomposed into three respective four different components following the assignment of GRECZYNSKI ET AL. as indicated in Figure 10.7 a and c. The energetic distances between the individual components correspond to the reported values and the intensity ratio of the PSS-Na and PSS-H components (1.2:1) is also nicely reproduced. The ratio between PSS and PEDOT in our experiments agrees with the value of a HWANG ET AL. [149] as a ratio of PSS/PEDOT of roughly 8 was obtained while in ref. [147] a ratio of PSS/PEDOT between 2.6 and 3.5 was obtained. The initial PSS-to-PEDOT ratios in the aqueous suspension were similar (i.e. 6:1 by weight according to Heraeus [150]). This could indicate a higher degree of surface accumulation of PSS in our experiments.

Both the O1s and S2p emissions of the PEDOT:PSS substrate remain unchanged in binding energy with increasing PCBM coverage. From the intensity decrease of the S2p emission (Figure 10.7 c) the thickness of PCBM for the measurement positions 1 and 2 after the nebulizer deposition can be estimated. For PCBM (nebu1) a formal layer thickness of approx.

30 Å and for PCBM (nebu2) a value of 50 Å was obtained. As for the third measurement position of the nebulized film and for the drop-cast as well as the spin-coated sample, no S2p signal could be detected, this estimation of layer thickness from the substrate emission damping was not possible.

Considering the PCBM deposition in the O1s (Figure 10.7 a) and the C1s (Figure 10.7 b) spectra a transition from the PEDOT:PSS spectral features to the PCBM spectral features is observed with increasing PCBM thickness. In the O1s spectra this is evident in the rising of the two characteristic emissions at around 531.5 eV to 532 eV and 533 eV to 533.5 eV attributed to the oxygen in the carbonyl group (1) and the methoxy group (2), respectively. These could be clearly identified through a fitting routine as indicated in Figure 10.7 a. In the C1s emission this transition can be seen from the rise of the high intensity C1s signal at around 285 eV and the PCBM characteristic substructure on the high binding energy side. The energetic positions of the characteristic PCBM core level vary in dependence of the preparation technique. While the emissions of the drop-cast layer are shifted by only 0.1 eV towards lower binding energies as compared to the spin-coated layer, the emissions of PCBM (nebu3) are shifted to higher binding energies by 500 meV compared to spin-coated PCBM. Additionally, the C1s level the nebulized PCBM shifts by approximately 0.4 eV from the lowest to the highest PCBM coverage. A similar shift in the O1s emissions is rather hard to discern due to the high intensity O1s signal of the underlying PEDOT:PSS. From the intensity ratio of the C1s to O1s emissions of PCBM (nebu3), PCBM (SC), and PCBM (drop) the carbon-to-oxygen ratio is calculated to be 31:1, 32:1, and 31:1, respectively. These values differ from the expected ratio of 36:1 according to the chemical structure but are still within experimental error for quantifications using XPS and agree with the previously determined ratios for PCBM on ITO (see section 4.1). Therefore, these ratios together with the measured binding energy positions and observed characteristic peak shapes are interpreted as a confirmation for the successful deposition of intact PCBM molecules on PEDOT:PSS with the nebulization technique.

The valence spectra of the different PCBM depositions on PEDOT:PSS are shown in Figure 10.8. The valence spectrum of PEDOT:PSS shows three distinct features with maxima at around 3 eV, 6 eV, and 9 eV (see Figure 10.8 b). This valence spectrum mainly stems from PSS and is in accordance to the observed PSS surface layer in the XPS measurements as well as reported spectra in literature [147, 149]. A value for the HOMO_{onset} is not given as in principle, the density of filled states extends up to the Fermi level (not shown)

attributed to the strongly p-doped PEDOT [147, 149]. The work function of PEDOT:PSS is 5.5 eV, which is slightly higher than the reported values of around 5.2 eV [149, 151, 152] but makes PEDOT:PSS a suitable, high work function electrode in OPV devices. For PCBM, already at the measurement spot of the nebulized film with the lowest formal layer thickness, the frontier orbital features of PCBM can be located with maxima at around 2 eV and 3.5 eV. The $\text{HOMO}_{\text{onset}}$ changes from PCBM (nebu1) to PCBM (nebu3) by 0.2 eV from 1.45 eV to 1.64 eV. For the two solution-processed PCBM films (PCBM (drop) and PCBM (SC)) the $\text{HOMO}_{\text{onset}}$ is located at 0.91 eV and 0.93 eV, respectively. Besides this drastic downward shift in $\text{HOMO}_{\text{onset}}$, also the general structure of the valence fingerprint region differs between the nebulized films and the drop-cast and spin-coated PCBM layers. While the latter shows the characteristic PCBM-like structure as observed and calculated (in section 4.1), the structure observed for PCBM deposited via the nebulizer method on PEDOT:PSS resembles the structure of PCBM nebulized on ozone-treated ITO. The first two features are clearly resolved but than a rather broad intensity plateau with a weak substructure arises. The trend of increasing binding energy of the $\text{HOMO}_{\text{onset}}$ with increasing layer thickness of the nebulized sample is not followed by the thick drop-cast and spin-coated PCBM layers on PEDOT:PSS. However, the observed shifts in the drop-cast and spin-coated PCBM in the valence spectra agree with the obtained shifts determined from the core level detail spectra.

The work function of originally 5.5 eV for PEDOT:PSS is dramatically reduced upon PCBM deposition via the nebulizer unit to 4.5 eV and decreases even further to 4.4 eV and 4.2 eV for increasing coverage with PCBM (see Figure 10.8 a). The drop-cast and spin-coated PCBM films on PEDOT:PSS again show a higher work function of around 5.1 eV. In all cases, the PCBM ionization potential remains almost unchanged around 6 eV. A schematic figure representing the electronic levels with increasing PCBM thickness is shown in Figure 10.9.

According to the measured work functions of PEDOT:PSS and the nebulized PCBM, an overall potential drop Δ , which could include an interface dipole as well as band bending, of around 1 eV forms at the interface between the two materials followed by a further decrease in energy levels for the thicker nebulized PCBM. In contrast to this, for the spin-coated and drop-cast PCBM films, a work function change of only 0.5 eV is observed from PEDOT:PSS to PCBM and the $\text{HOMO}_{\text{onset}}$ energies are decreased. A comparison to the energy level diagram of PCBM on ITO and a further discussion follows in section 10.5.

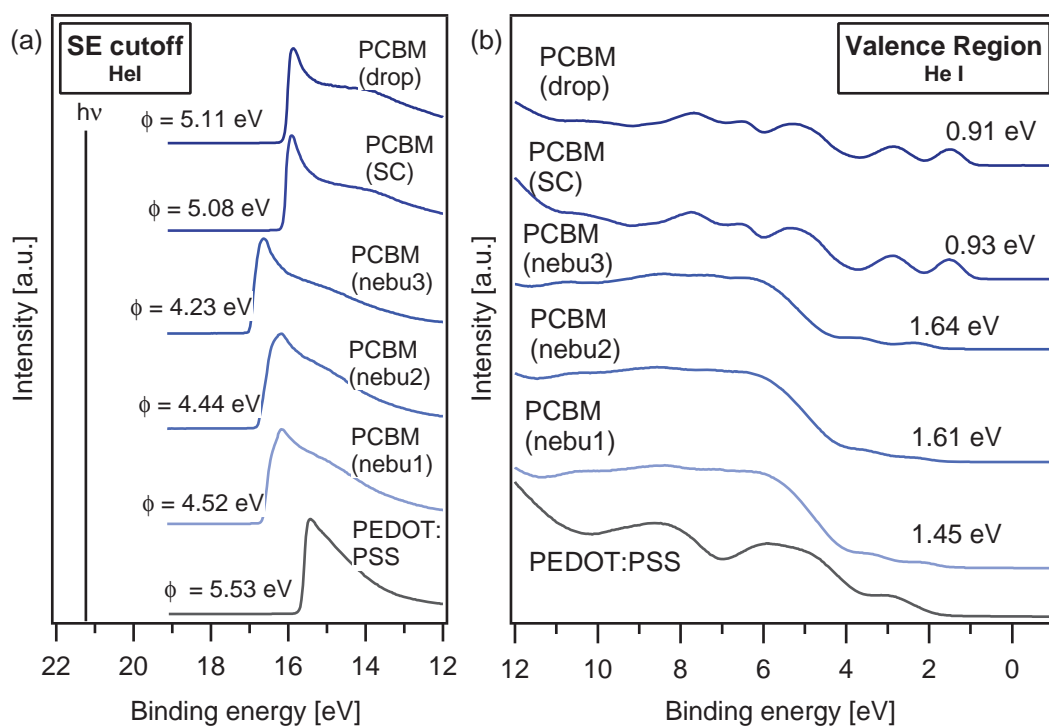


Figure 10.8: (a) Secondary electron cutoff and (b) valence region spectra of PEDOT:PSS, PCBM (nebu1), PCBM (nebu2), PCBM (nebu3), PCBM (SC), and PCBM (drop). The spectra of the nebulizer deposition are arranged in the order of increasing PCBM coverage and compared to the two other solution-processed PCBM films.

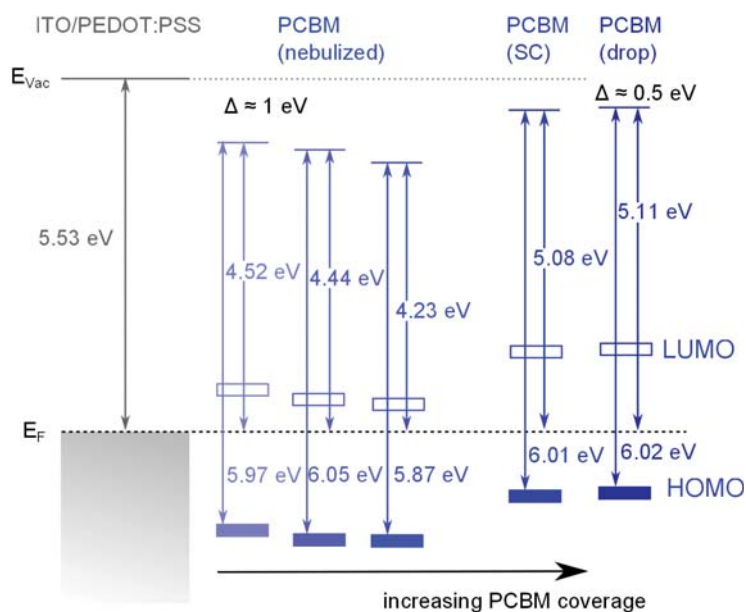


Figure 10.9: Schematic representation of the energy levels at the PEDOT:PSS/PCBM interface as measured with the nebulizer method. The values for spin-coated and drop-cast PCBM on PEDOT:PSS are included.

10.4 PCBM on PEI

Polyethylenimine (PEI) is used for surface modifications of well known contact materials to produce electron-selective electrodes for organic electronic devices. By the functionalization with this polymer material the work function is significantly reduced, yielding a low work function electrode suitable of efficient electron transport out of the solar cell [73]. Therefore, the interface of PCBM on PEI-covered ITO is of technological interest as electrons need to be transferred from the PCBM LUMO to the anode. Branched PEI was obtained from Sigma Aldrich with an average molecular weight of $25\,000\text{ g mol}^{-1}$. The molecular structure is shown in Figure 10.10. Following ZHOU ET AL. the material was dissolved in 2-methoxyethanol at a concentration of 0.4 weight% and stirred for 15 min [73]. This solution was then used to spin-coat a thin film on ozone-treated ITO at 5000 rpm for 60 s to prepare an air-stable low work function substrate. The coated substrates were heated at $120\text{ }^{\circ}\text{C}$ for 10 min. As for PEDOT:PSS the substrates were then directly placed in the UHV load lock while they were still warm to prevent excessive surface contaminations. The layer thickness of the PEI was estimated from the In3d damping of the PEI-covered ITO compared to a freshly ozone-treated ITO to be around 1.5 nm which is in the expected thickness range [73].

PCBM was again deposited via three different solution-based deposition techniques. As during the nebulization deposition only very little material was deposited and to eliminate effects from different substrates, the drop-casting experiment was performed in one corner of the same ITO/PEI sample as the nebulizer deposition. The survey spectra of the PEI-covered ITO (ITO/PEI), nebulized PCBM (nebu), drop-cast PCBM (drop), and spin-coated PCBM (SC) are shown in Figure 10.11.

In the survey spectrum of the PEI-modified ITO the core level emissions characteristic of ITO (namely In3d, Sn3d, O1s ect.) and PEI (namely C1s and N1s) are detected. The strong intensities of the ITO lines show the low PEI layer thickness. The ITO and PEI lines are

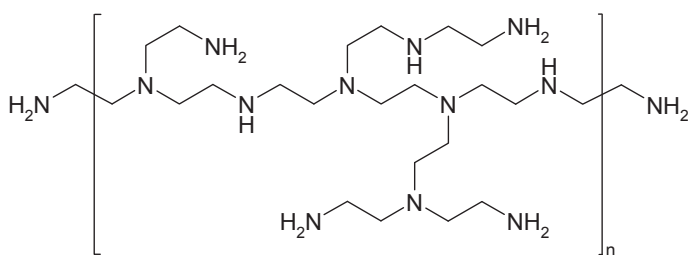


Figure 10.10: Molecular structure of Polyethylenimine (PEI).

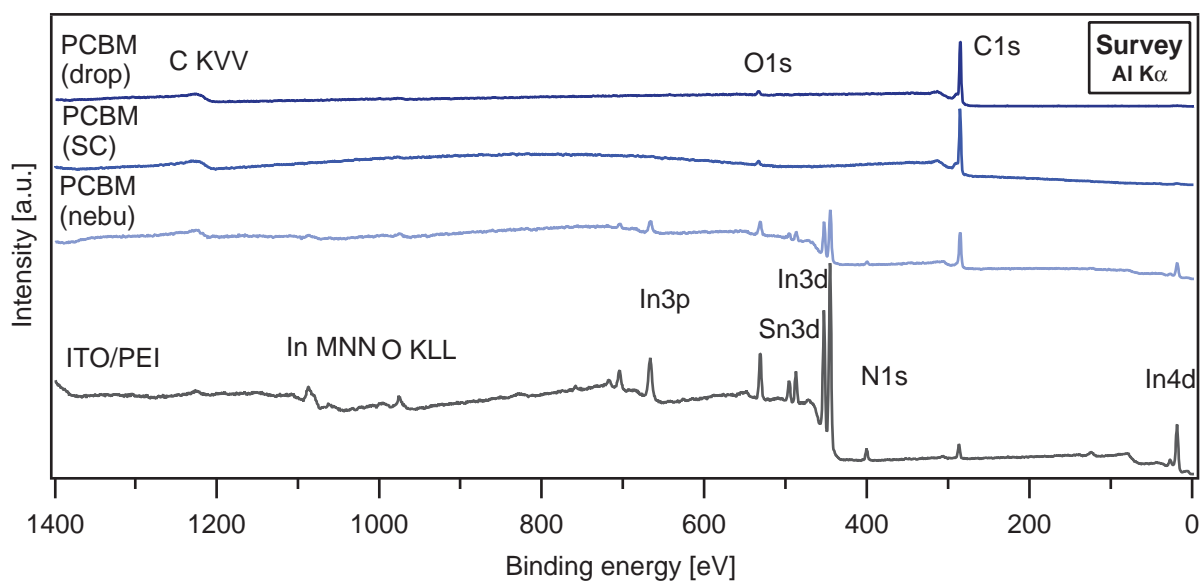


Figure 10.11: Survey spectra of the substrate PEI-modified ITO and the differently prepared PCBM films in order of increasing layer thickness: nebulized PCBM, spin-coated PCBM, and drop-cast PCBM.

also still visible after the deposition of PCBM via the nebulizer method. In the spectrum of the spin-coated PCBM on ITO/PEI no distinct ITO or PEI lines are detected but the broad intensity increase in the range of 700 eV to 1100 eV indicates a rather low film thickness as this broad feature is caused by inelastically scattered In3d photoelectrons. The PCBM core level emissions from C1s and O1s are clearly observed. The same trend results for the drop-cast PCBM. The absence of the broad intensity increase in the range of 700 eV to 1100 eV shows the increased layer thickness compared to the spin-coated sample although it needs to be noted that drop-casting usually produces films of rather inhomogeneous thickness.

To gain further information about layer thicknesses, the substrate core levels need to be considered. The In3d and N1s detail spectra are shown in Figure 10.12 a and b. The individual peaks of the In3d doublet show an asymmetric peak shape with a tail on the high binding energy side as observed during the substrate characterization in section 8.3.1. As this peak shape is preserved even after PEI deposition only physisorption between ITO and PEI is indicated as described in ref. [73]. The N1s signal of PEI consists of one single, slightly asymmetric peak centered at 400.4 eV which corresponds to the binding energy range of nitrogen in organic matrices [89]. All nitrogen atoms in PEI are singly bound to three atoms, either carbon or hydrogen. Thus, their individual binding configurations

vary only slightly explaining the little variation in binding energy as observed. The strong In3d signal from the underlying ITO as well as the N1s signal from the PEI are attenuated because of the nebulizer deposition of PCBM. In the case of the spin-coated and drop-cast PCBM, the two emissions are not present anymore indicating a layer thickness above 3λ (i.e. above 9 nm, see Table B.3). The formal layer thickness of the nebulized PCBM film was calculated using the intensity decrease of the In3d from the underlying ITO and from the N1s signal stemming from PEI. Both calculations lead to a value of around 40 \AA .

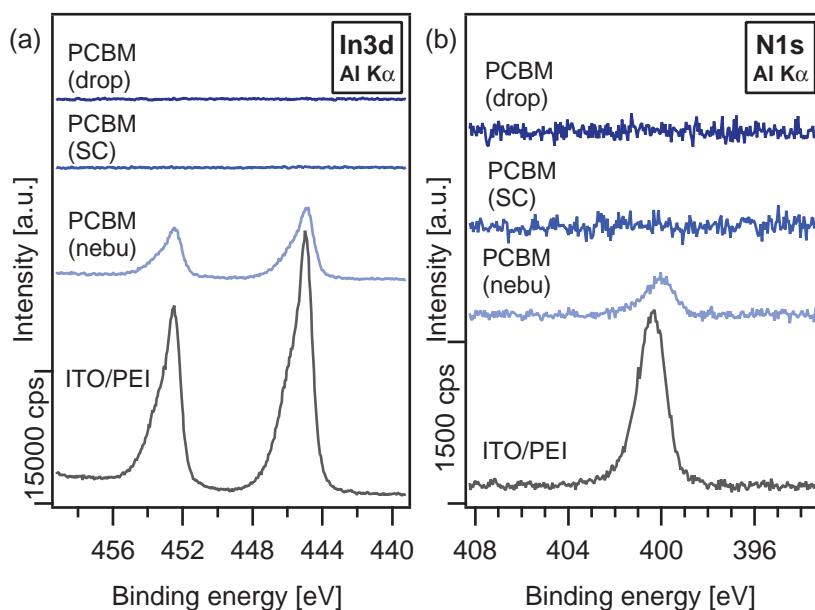


Figure 10.12: (a) In3d and (b) N1s emission of PEI on ITO, nebulized PCBM, spin-coated PCBM, and drop-cast PCBM.

The O1s and C1s core levels are shown in Figure 10.13. In the case of PEI on ITO, the O1s signal in Figure 10.13 solely stems from the underlying oxide as PEI does not contain any oxygen species (see chemical structure in Figure 10.10). However, oxygen containing adsorbates might also contribute as the PEI film was prepared at ambient air. For clear data presentation the substrate O1s signal is reduced in intensity by a factor of 5. In the O1s spectrum of the nebulized PCBM, the O1s signal is still dominated by the ITO oxygen emission. However, on the high binding energy side the emissions of the two oxygen atoms in PCBM arise at about 532 eV and 533.5 eV. For the spin-coated and drop-cast O1s spectra, only contributions of the PCBM oxygen species are detected. The emissions were fitted using two Voigt profiles. The resulting components have equal intensity as expected from the PCBM structural formula. Component (1) at 532 eV is attributed to the oxygen

from the carbonyl group and component (2) is attributed to the oxygen from the methoxy group. Hence, the resulting components perfectly agree to the previous obtained results (see e.g. sections 4.1 and 10.2) in both energy position and intensity ratio. Independent of the preparation technique and resulting PCBM layer thickness the O1s binding energies only slightly vary (by about 50 meV) and are thus considered constant. In the C1s spectrum of PEI a broad feature centered around 287 eV is observed. This corresponds to the binding energy range in which the C-N and neighboring C-C bonds are expected [89, 153]. After the deposition of PCBM with the nebulization technique, the PCBM carbon 1s signal rises at around 285 eV but the underlying carbon from the PEI is still visible in the high binding energy tail. In the case of the spin-coated and drop-cast PCBM layer, a single high intensity peak at 285.1 eV is followed by the PCBM-characteristic sub-structure at the high binding energy side with two distinct maxima at 287 eV and 289 eV. Again, no significant shift in binding energy of the PCBM C1s emission depending on the deposition technique is observed.

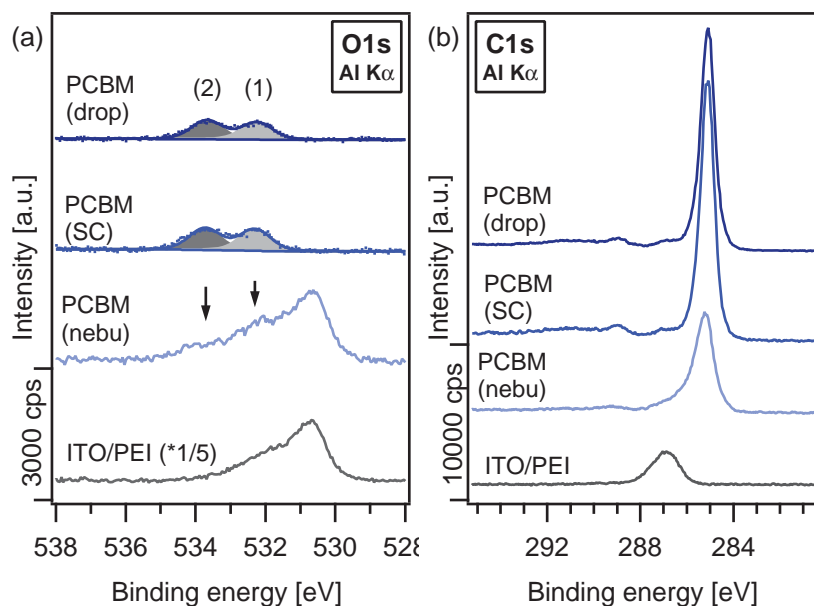


Figure 10.13: (a) O1s detail spectrum (numbers indicate the different oxygen bonding states) and (b) C1s detail spectrum of PEI on ITO and the differently prepared PCBM films in order of increasing PCBM content. The intensity of the ITO/PEI oxygen signal is reduced in intensity by a factor of 5 for clearer representation of the PCBM O1s signal.

From the intensity ratio of the C1s and O1s signal of the spin-coated and drop-cast sample, the approximate atomic ratio of carbon to oxygen is determined using tabulated ASFs [89]. For the spin-coated sample a C-to-O ratio of 33:1 was obtained while for the spin-coated

sample a ratio of 34:1 was calculated. Both values follow the previously observed trend of underestimation of the C1s intensity, as the expected ratio of 36:1 is not reached. This is possibly due to the underestimation of the extension of the C1s shake-up structure (see section 4.1 and Ref. [103]). A similar evaluation was not attempted for the nebulized film as both the C1s and O1s signal are still significantly influenced by the underlying ITO/PEI substrate. In any case, the emergence of the PCBM related features show the successful deposition of PCBM with the nebulizing technique also on PEI-modified ITO.

The valence spectra of PCBM deposited on ITO/PEI are shown in Figure 10.14. From the secondary electron cutoff spectra the work function values of the different samples are obtained. The ITO/PEI substrate has a work function of 3.22 eV. Compared to freshly ozone-treated ITO ($\phi=5.3$ eV, see section 8.3.1), this implies a reduction of the work function by about 2 eV. In the case of the nebulized PCBM the secondary electron cutoff shows a double structure. The work function obtained from the cutoff at around 18 eV binding energy is 3.48 eV. Estimating a work function from the possible second cutoff as indicated by the dotted lines at 17.2 eV gives a work function of around 4 eV. The double structure could be a side effect of the deposition technique as only small individual droplets are deposited as a result of the nebulization. Therefore, it could be possible that the two secondary electron cutoffs are caused by the substrate and the dried PCBM droplet. Then, the lower work function of 3.48 eV would be attributed to the PEI-modified ITO substrate and the higher work function of 4 eV would be attributed to PCBM. This seems to be reasonable as for the spin-coated and the drop-cast PCBM on ITO/PEI work functions of 4.12 eV and 4.23 eV, respectively, are measured. In the valence region spectrum of ITO/PEI two maxima are observed at around 4.5 eV and 8.5 eV. From the first maximum a tail of occupied states extends up to the Fermi level. After the nebulization deposition the shape of the valence spectrum changes giving rise to two maxima in the energy range of 2.5 eV and 4 eV followed by a plateau like intensity increase in the range of 5 eV to 12 eV as observed previously for nebulized PCBM (see sections 10.2 and 10.3). From the first maximum, which is attributed to the PCBM HOMO an onset value of 1.82 eV is obtained. For spin-coated and drop-cast PCBM on ITO/PEI the fingerprint valence feature of PCBM (see e.g. section 4.1) are nicely reproduced. Additionally, the obtained HOMO_{onset} values of the spin-coated and drop-cast PCBM are 1.84 eV and 1.73 eV, respectively, and thus differ by only 0.1 eV which corresponds to the minimal shifts observed in the binding energies of the PCBM core levels.

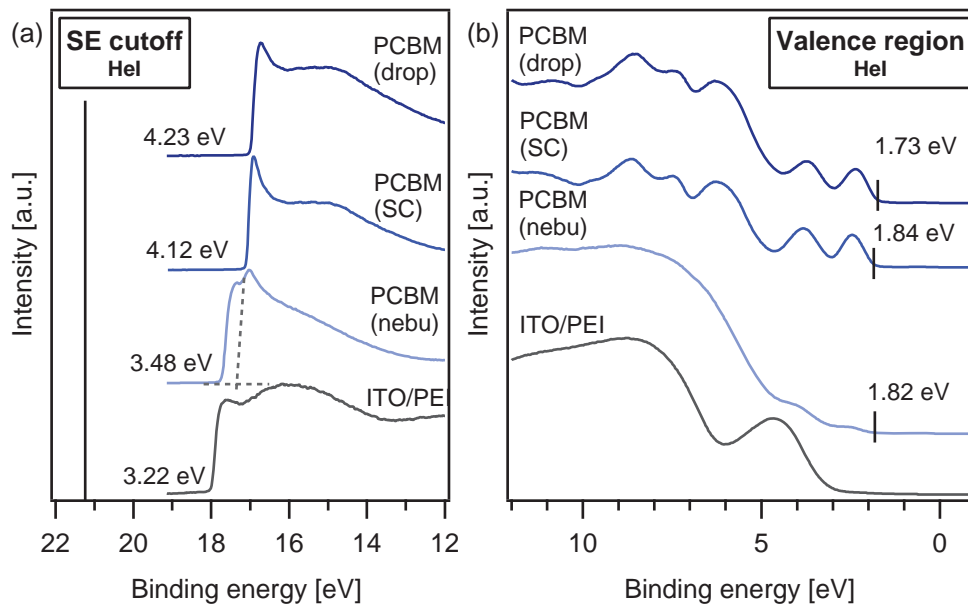


Figure 10.14: (a) Secondary electron cutoff and (b) valence region spectra of PEI-modified ITO, nebulized PCBM (nebu), spin-coated PCBM (SC), and drop-cast PCBM (drop).

The electronic levels of PCBM deposited on PEI-modified ITO are summarized in an energy level diagram in Figure 10.15 in the order of increasing PCBM thickness. The ionization potentials of the spin-coated and drop-cast PCBM are 6 eV in both cases. Assuming that the double structure in the secondary electron cutoff indeed corresponds to the two different work functions of substrate and PCBM, the ionization potential of PCBM deposited via the nebulizer method is 5.8 eV which is comparable to the obtained value for the two other deposition techniques. Therefore, the shown energy level representation is based on this interpretation of the secondary electron cutoff spectra, but the value of the work function of the first SE cutoff is indicated by the dotted line for completeness.

From the depicted energy level alignment a potential step Δ of roughly 1 eV forms at the interface between ITO/PEI and PCBM. The energies of the PCBM levels are almost constant with increasing PCBM thickness. This indicates that the potential step between PEI and PCBM is due to an interface dipole and not to band bending. In the next section 10.5, this energy level diagram will be further discussed and compared to the ITO/PCBM and PEDOT:PSS/PCBM interfaces.

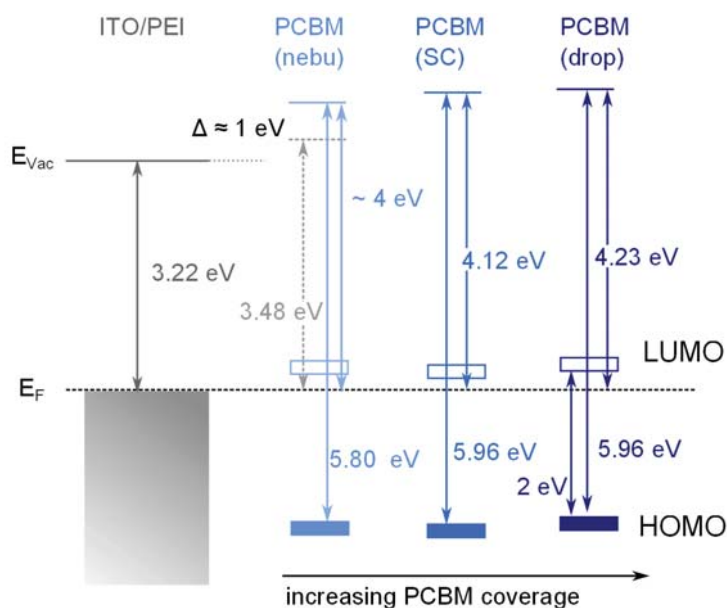


Figure 10.15: Schematic representation of the energy level diagram of PCBM on PEI-modified ITO. The energy gap value of PCBM was taken from literature [24].

10.5 Comparison and Evaluation of the Different Energy Level Alignments

Enabled by the nebulizer method, different thickness-dependent electronic contact behaviors of PCBM with ITO, PEDOT:PSS and PEI were observed. The obtained trends in energy level positions for the different contact materials are discussed in the following. In a first step the energy level positions closest to the respective interfaces as obtained from the nebulizer depositions are compared on Figure 10.16.

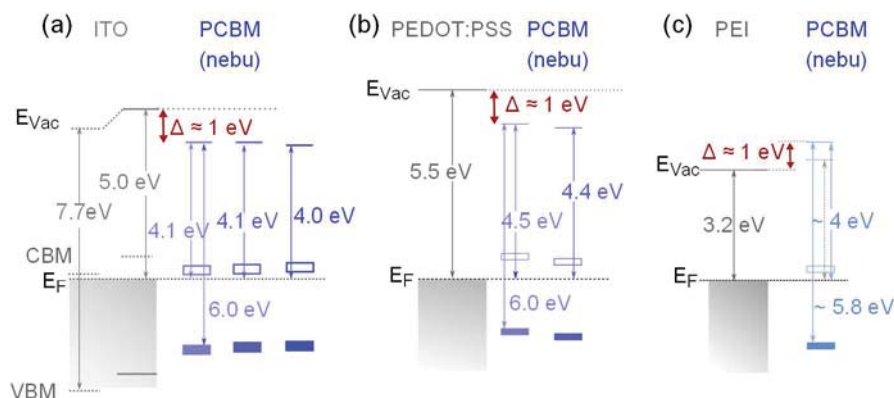


Figure 10.16: Comparison of the energy level diagrams of PCBM on ozone-treated ITO (a), PEDOT:PSS (b), and PEI (c) for the nebulizer deposition steps.

The energy level positions depicted in Figure 10.16 all stem from the measurements with nominal PCBM layer thicknesses in the range of 30 Å to 50 Å as calculated from the substrate emission damping. For all nebulized PCBM samples, an ionization potential of

around 6 eV is observed, which is comparable to the previously determined values (see e.g. section 4.1) and indicates molecular integrity after the nebulizer deposition. In the case of the high work function substrates, namely ozone-treated ITO and PEDOT:PSS, a potential drop of 1 eV is observed in the vacuum level. In the case of PCBM on ozone-treated ITO a trend of decreasing binding energy of the HOMO levels with increasing layer thickness is observed. This hints towards band bending due to an electron transfer from PCBM to ITO. The trend in energy level positions in the case of PCBM on PEDOT:PSS, however, is reversed as a slight increase in the HOMO_{onset} binding energy as well as a decrease in the work function is observed. Considering the contact between PEI and PCBM a vacuum level offset of 1 eV is observed, too, but it is oriented in the different direction as PCBM has a higher work function than PEI. The Fermi level position in PCBM on PEI is comparable to the Fermi level position in PCBM on ITO.

As the spin-coating results are equivalent to the drop casting results, only the latter will be considered in the evaluation of the substrate/PCBM levels for thicker PCBM layers. These are shown in Figure 10.17.

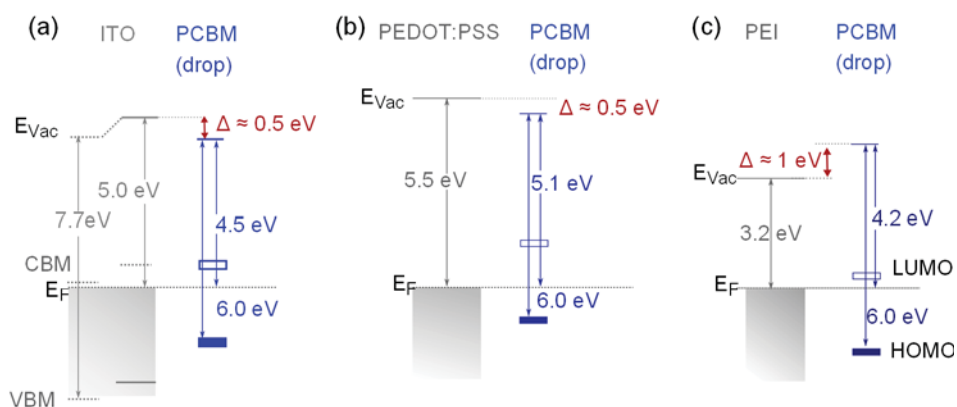


Figure 10.17: Comparison of the energy level diagrams of PCBM on ozone-treated ITO (a), PEDOT:PSS (b), and PEI (c) for the drop-cast films.

Also for the thicker PCBM layers, a constant ionization potentials of 6 eV is obtained independent of the substrate material. Comparing the two high work function contact materials ITO and PEDOT:PSS, as for the nebulizer samples a similar overall potential drop Δ of now 0.5 eV as compared to 1 eV (see Figure 10.16) is deduced from the measured work function differences in both cases. However, the position of the Fermi level in PCBM is different for PCBM on ITO and PCBM on PEDOT:PSS, respectively. In the case of PCBM on PEI the same rise in the vacuum level of 1 eV as for the thin, nebulized layer, is observed.

Combining now all deposition steps for the three substrate materials, the different trends in the energy level alignments are depicted in Figure 10.18.

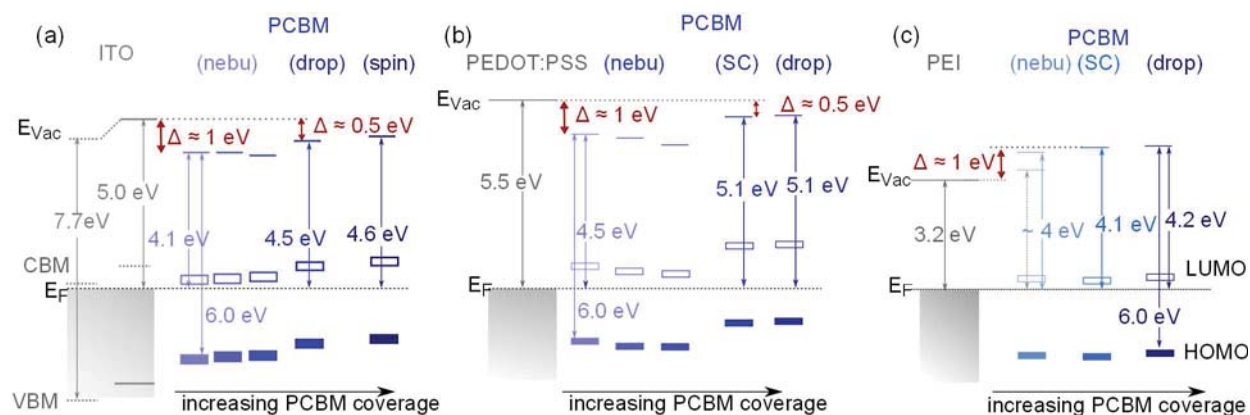


Figure 10.18: Comparison of the energy level diagrams of PCBM on ozone-treated ITO (a), PEDOT:PSS (b), and PEI (c) for the all deposition steps.

Qualitatively, the nebulized and drop-cast/spin-coated samples behave alike considering the occurrence and direction of potential steps at the interfaces but quantitatively, differences in the magnitude of these steps are observed. While the trends in PCBM energy levels in the case of the nebulizer steps on ITO and PEDOT:PSS are opposite, as the levels shift upward on ITO and downward on PEDOT:PSS, in both cases the PCBM levels are shifted upward with respect to the Fermi level for the thicker layers. Also the change in vacuum level offsets for the thin layers compared to the thicker, drop-cast or spin-coated layers is very similar. According to the integer charge transfer model [46], for high work function substrates, vacuum level alignment of PCBM and the contact material is predicted. XU ET AL. have determined the ICT- state of PCBM to be at 4.3 eV. Thus, when brought in contact with a material with a work function higher than this value no charge transfer should occur resulting in vacuum level alignment of PCBM and the substrate material [20]. However, vacuum level alignment was not observed and the trends in changing energy level positions also contradict the postulated absence of charge transfer. The exact origin of this discrepancy and also of the seemingly contradicting behavior of PCBM with increasing thickness when comparing the nebulizer experiments and the other solution-based techniques is yet undetermined. Since e.g. all investigated levels of PCBM spin-coated (drop-cast) on PEDOT:PSS are shifted in parallel by about 0.5 eV (0.6 eV) with respect to the thickest PCBM layer nebulized on PEDOT:PSS (compare to section 10.3), the shifts could be caused by a change of the Fermi level position possibly introduced through the nebulization pro-

cess. Maybe, the nebulizer method itself has an influence on the energy level alignment due to molecular or orientational changes. Even different levels of unintentional doping introduced during the nebulization cannot be excluded.

Considering the contact of PCBM on PEI a constant vacuum level offset of 1 eV and constant energy level positions are observed independent of the PCBM thickness. The latter indicates, that the potential step is due to an interface dipole and not caused by band bending. Compared to the ICT model, this result corresponds to the predicted Fermi level pinning at the ICT- state of PCBM at 4.3 eV [20], since the work function of the used substrate is below this value and PCBM exhibits a work function comparable to the predicted pinning level. The energy difference between the PCBM LUMO and the Fermi level in the PEI-modified ITO is about 0.1 eV which makes electron transfer from the organic LUMO to the electrode favorable although it needs to be noted that the LUMO position was not directly measured but taken from ref. [24].

10.6 Discussion of Valence Features

For all cases of PCBM being deposited via the nebulization technique, the same valence features were observed, that significantly differ from the otherwise measured and calculated valence fingerprint spectrum of PCBM (see e.g. Figure 4.3). Since this is independent of the underlying substrate material, i.e. ozone-treated ITO or polymeric materials, a reaction of PCBM with the substrate material is tentatively excluded. Also, excessive contaminations during the nebulizer deposition as a source for the different valence structure is unlikely, as in the case of DH6T (see chapter 9) perfect agreement in the valence spectra between drop-cast and nebulized films was observed using the same solvent, namely chlorobenzene. Additionally, the intensity increase in the range of 4 eV to 10 eV as detected for the different substrate/PCBM combinations which would then have its origin in contaminations introduced during nebulization is absent in the case of DH6T.

However, a similar valence structure was observed once for a spin-coated PCBM layer on a silicon substrate (with natural oxide layer). The He I valence spectra of this sample are shown in Figure 10.19 a together with one representative valence spectrum of nebulized PCBM on the different substrates in Figure 10.19 b.

In the spectra of PCBM spin-coated on Si, at the three different sample positions at which PES characterization was performed, different shapes of the valence spectra are observed.

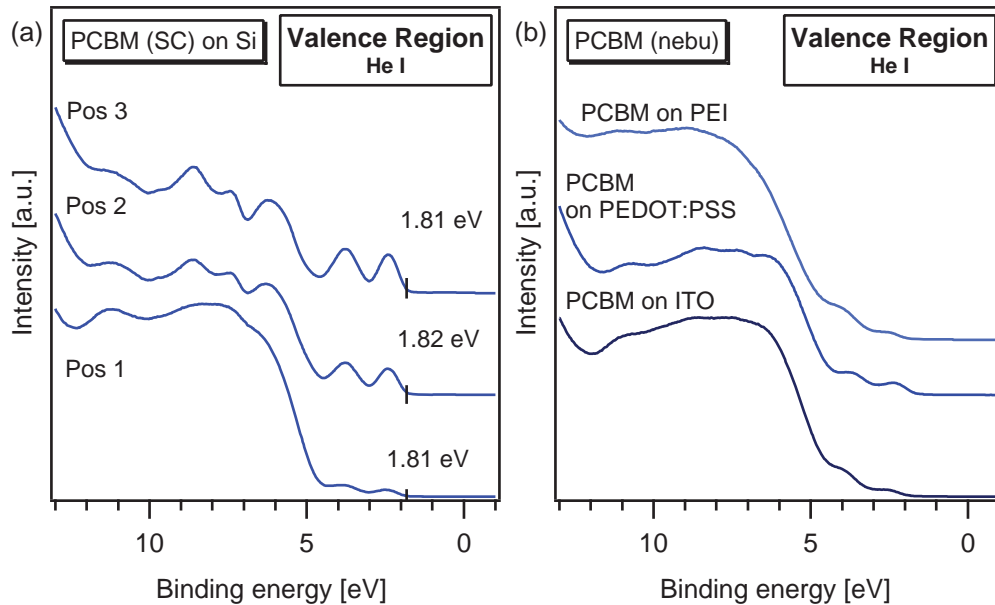


Figure 10.19: (a) Valence spectra of PCBM spin-coated on a Si-wafer with natural oxide at different sample positions. (b) Valence spectra of PCBM nebulized on ITO, PEDOT:PSS, and PEI.

While for the spectrum obtained at position 3 (top spectrum in Figure 10.19 a) the expected PCBM valence fingerprint structure was measured, the features are slightly broadened for position 2. The shape of the valence spectrum at position 1 closely resembles the spectra obtained for PCBM deposited via the nebulizer technique as shown in Figure 10.19 b. The position of the $\text{HOMO}_{\text{onset}}$ of spin-coated PCBM on Si as indicated in Figure 10.19 a does not change with respect to the sample position and only a minor increase in the work function of 0.25 eV going from position 1 to position 3 is observed (not shown).

To further investigate the origin of the observed changes in the general shape of the valence structure for the spin-coated sample, the corresponding core level emissions are evaluated. In Figure 10.20 the PCBM specific C1s and O1s emissions and the approximate location of the different measurement spots on the sample are shown.

In the O1s spectra the PCBM characteristic double peak is observed in all cases although the absolute intensity increases from position 3 to position 1. While the binding energy positions of sample position 2 and 3 only show minor deviations, the O1s emissions obtained from position 1 are shifted by about 400 meV to higher binding energies. All O1s spectra could be fitted using two Voigt profiles of nearly the same intensity, indicating the absence

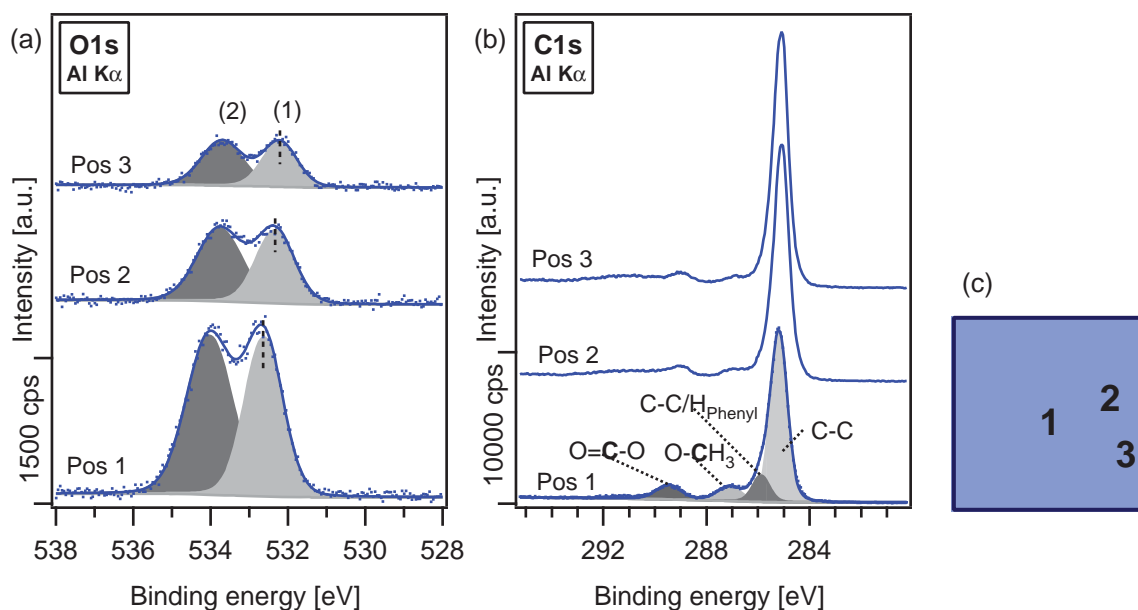


Figure 10.20: (a) O1s core level emission and (b) C1s core level emission of PCBM spin-coated on a Si-wafer at three different positions. The locations of the individual measurement spots on the sample are schematically shown in (c).

of any additional oxygen containing species. In the C1s emission, not only a change in intensity but also in peak shape is observed. While the C1s spectra of position 2 and 3 generally reproduce the previously observed PCBM C1s peak shape with one major component centered around 285 eV followed by a high binding energy sub-structure (see e.g. Figure 4.1 d), the peak shape observed at position 1 is slightly different. The maximum emission of position 1 is shifted by 0.1 eV to higher binding energies and the overall intensity is significantly reduced. However, the intensity maxima observed at 287 eV and 289.5 eV are more pronounced for measurement spot 1 than for spots 2 and 3. A fit of the C1s emission of position 1 using four individual Voigt profiles is shown in Figure 10.20 b. The two components at highest binding energies are of equal intensity and are therefore attributed to the carbon atoms bound to oxygen in the carbonyl group (O=C-O) and the methoxy group (O-CH₃). An additional component at around 285.9 eV is attributed tentatively to the C-C or C-H bound carbon atoms in the side chain and phenyl ring while the main emission is still assigned to the carbon atoms in the C₆₀ cage. Any contributions from shake-up satellites are not considered. This assignment is based on previously reported chemical shifts in literature [24, 81, 102] and follows the discussion of the C1s emissions of the differently prepared PCBM films in comparison to C₆₀ from section 5.1. Interestingly, the obtained fit results from the C1s emission of position 1 nicely correspond in energetic position to

expected PCBM intensity contributions derived from the C1s difference spectra in Figure 5.4 b.

The observed changes in core level shape and intensity indicate very pronounced inhomogeneities from the sample center to the sample edge. In the center, the carbon-to-oxygen ratio is dramatically decreased to 7:1 which is accompanied by the above described change in valence features. At position 2 the ratio is 18:1 correlating to the observed minor changes in the spectral shape. Towards the sample edge the carbon to oxygen ratio changes to the in this work generally observed ratio of approximately 34:1, which is within experimental error of the expected C-to-O ratio of 36:1. In all cases no Si2p substrate emission could be detected and Dektak measurements showed a rather homogeneous layer thickness in the range of 40 nm to 45 nm. Therefore, the layer thickness most likely has no influence on the measured sample composition and peak shapes. Additionally, no other chemical species or contaminations could be identified in XPS.

Due to the higher sensitivity of UPLC-MS, chemical analysis was performed to further investigate the sample composition. Therefore, the PCBM coated wafer was again washed off as was performed for the evaporated PCBM layer (see section 5.1.1) and compared to a wafer that was according to XPS analysis homogeneously covered with PCBM via spin-coating. This analysis proved that the layer, which showed the inhomogeneities in the C:O ratio has the same chemical composition as the spin-coated layer, where these inhomogeneities were not observed. Both results perfectly correspond to the PCBM standard, which was derived from the pristine powder prior to any deposition step (compare to section 5.1.1). It needs to be pointed out that the UPLC-MS analysis probes the overall composition. Therefore, it is not specific to surface contaminations and also solvent residues and contaminations with similar interaction forces cannot be detected in UPLC-MS.

As an additional reason that the observed change in valence structure in PCBM is not related to contaminations, the already mentioned striking similarity of the DH6T valence feature in chapter 9 can be considered. However, this does not exclude molecular changes of PCBM during the nebulization process although at least on PEDOT:PSS, where a thick PCBM layer was nebulized, the obtained carbon-to-oxygen ratio contradicts molecular decomposition. Additionally, a change in the side chain is doubtful as all O1s spectra (see Figure 10.20 a) of the spin-coated sample perfectly reproduced the expected two oxygen components of equal intensity.

A possibility to further investigate molecular changes in PCBM during the nebulizer method could be to deposit a rather thick film on a Si-substrate to perform IR spectroscopy. The drastic change in the valence structure could indicate an opening / rupture of the C₆₀ cage. Unless a significant number of carbon atoms is separated from the main part of the molecule, this would not influence the intensity ratio of C1s to O1s so much but should largely influence the valence structure as these spectral features mainly originate from the C₆₀ frame. Yet, rupture of the PCBM molecule or C₆₀ core seems unlikely during spin-coating after which a very similar valence structure was observed.

Combining these observations, the change in valence structure, the overestimation of the oxygen component and the change in C1s peak shape could possibly be due to orientation effects. PCBM generally tends to crystallize and if the solvent evaporates quickly as in the case of nebulized films (and the sample center in spin coating as this section usually dries first) it could crystallize in other orientations, e.g. a more upright orientation of the molecules with the side groups pointing towards the surface. This could explain both the over-pronunciation of the oxygen species in the spin-coating experiment as well as the different valence features in both the nebulizer and the spin-coating experiment. As could be shown in section 5.1 the valence level of PCBM are clearly dominated by the C₆₀ core. If the side groups are pointing upwards and maybe are less ordered, this could lead to an intensity increase of the side chain associated valence levels overshadowing the C₆₀ levels and broadening of the involved electron states.

10.7 Optical Microscopy

As all layers of PCBM produced via the nebulizer technique showed only individual droplets and/or a rather high degree of inhomogeneity, a first characterization of the films using an optical microscope (Nikon Eclipse 80i) was performed. The resulting images for two exemplifying positions taken at 200 times magnification are shown in Figure 10.21 for the different substrates. In the case of PCBM on ITO (Figure 10.21 a) the inhomogeneous coverage of the substrate through PCBM is visible. The underlying ITO appears grayish-blue in the microscopy image while the PCBM causes the brownish features. The observed features seem to be caused by coalescing individual droplets. The changing colors within the PCBM features arise most likely from different thicknesses. In general, in both images recorded at different sample positions, a substructure within the PCBM areas is visible.

The origin of this is yet unclear. In the case of PEDOT:PSS as a substrate (Figure 10.21 b) the substrate is visible in a darker shade of blue due to the blue color of PEDOT:PSS. In the top image the substrate is only inhomogeneously covered with PCBM (brownish structure). The structure is similar to that observed for PCBM on ITO and from a first impression looks like a wet film that has receded upon drying. In the bottom image, however the overall brownish color indicates a complete coverage with PCBM. This is in accordance to the observed different sample regimes in PES (compare to section 10.3). PCBM nebulized on PEI seems to form rather individual droplets as can be seen from the very spherical shapes in Figure 10.21 c. In contrast to PCBM on ITO and PEDOT:PSS, where some degree of interconnection between the individual, potentially coalescing droplets or structures is visible, this is absent in the case of PEI. This sharp interface (especially if considering the large droplet as visible in Figure 10.21 c at the bottom) supports the assumption of the two simultaneously measured work functions of the PEI substrate and PCBM adsorbate made in section 10.4. Generally, complete wetting of the substrate resulting in complete coverage was not observed in any case. This could either be due to surface energy mismatch or maybe is induced by the limited amount of liquid reaching the substrates during the nebulization process. At least in the case of PEDOT:PSS as a substrate material, a prolonged nebulae exposure led to a rather thick and closed layer at least on part of the substrate.

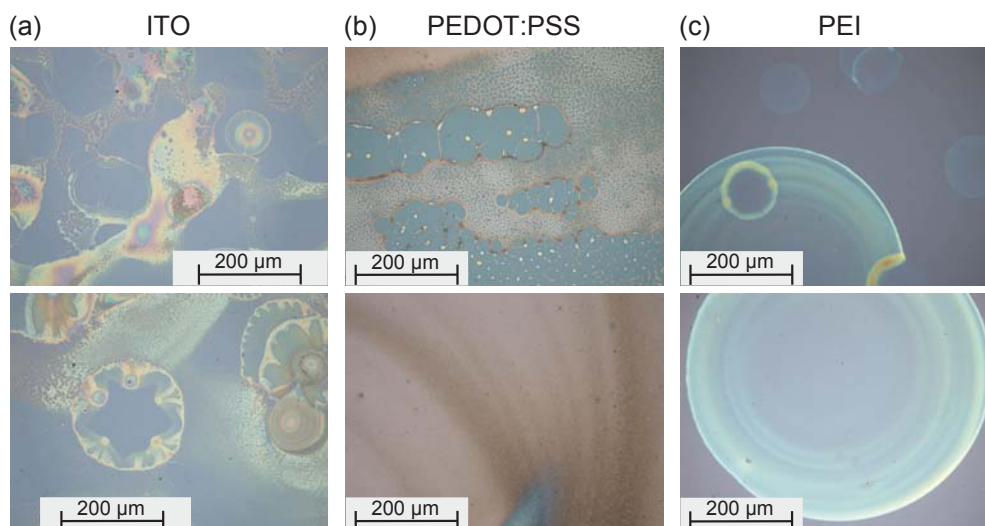


Figure 10.21: (a) PCBM nebulized on ITO. (b) PCBM nebulized on PEDOT:PSS. The pronounced blue substrate color in the top image stems from PEDOT:PSS. The light brownish color in the bottom image indicates complete coverage of the substrate in the image area. (c) PCBM nebulized on PEI. All images were taken at 200x magnification. Top and bottom row exemplify different areas of the respective samples illustrating the inhomogeneous substrate coverages.

10.8 Film Formation Properties

Although the surface tension characterization of ITO and the solvent chlorobenzene showed complete wettability of the substrate, only individual droplets as a result of the nebulizer deposition were observed regardless of the organic molecule. No direct characterization of the droplet size in the nebulae was possible but taking the diameter of the observed individual dry droplets in optical microscopy as a rough measure, the droplet size varies between approximately $50\ \mu\text{m}$ to $500\ \mu\text{m}$ in diameter. Also, the surface energies of PEDOT:PSS and PEI were characterized using contact angle measurements (not shown) and the results including the enclosed area by the wetting envelope are very comparable to the ozone-treated ITO (see section 8.4). Therefore, chlorobenzene should be a suitable solvent to coat these substrate materials. However, in the optical microscopy images in Figure 10.21 complete wetting and homogeneous wetting was not observed. This could be due to the limited amount of liquid reaching the substrates. Additionally, the surface tension is determined in an equilibrium situation. During the nebulizer deposition, kinetic effects especially considering the droplet drying have a significant influence on the formed films.

To test if PCBM might act as a surfactant and thus concentration gradients might influence the wetting behavior, the surface tension of differently diluted PCBM solutions in chlorobenzene were determined using a tensiometer. The values for PCBM concentrations ranging from $0.1\ \text{mg ml}^{-1}$ to $2\ \text{mg ml}^{-1}$ did not differ by more than $0.1\ \text{mN m}^{-1}$ from the surface tension value of $33.1\ \text{mN m}^{-1}$ as obtained for pure chlorobenzene. Therefore, mechanisms related to the Marangoni effect [138] are most likely not responsible for the poor film formation during the nebulizer deposition.

As the outstanding optoelectronic properties of PCBM are best observed for crystalline films a critical discussion of the "layers" formed by the nebulizer method is necessary. It seems that the droplet drying time significantly influences the film formation and the film morphology. For the films produced by the nebulizer method a change in valence structure was observed. While the general position of the intensity maxima are comparable to the spin-coated or drop-cast films the structure is less defined and has a broad valence band feature starting at 6 eV (see Figure 10.19). This could potentially arise from the missing interaction with other PCBM molecules as the droplets dry so quickly that the formation of crystalline domains is not possible. However, gas phase DFT calculations of the eigenval-

ues of one individual PCBM molecule lead to a spectrum of equal shape as for spin-coated and drop-cast PCBM (see Figure 4.3). The change in valence structure could also indicate an orientation effect where the molecules take a more or less upright orientation with respect to the substrate and the side chains pointing upwards. This would then originate in a valence structure dominated by the side chain. Neither of the two hypothesis could be completely excluded or validated in the course of this work. Nonetheless, as the semiconducting properties of the film are connected to a high film crystallinity or at least a high degree of order to allow continuous pathways for charge carriers, the nebulizer process needs to be further optimized to meet these requirements. Slower drying times could be an option as these are likely to be accompanied by increased molecular (re)arrangement but would also promote intermixing with previously deposited material.

One approach to realize more homogeneous films could be at least for the first layer to conduct the deposition process in a solvent saturated argon atmosphere. This could increase the droplet nucleation on the substrate and could lead to a homogeneous wet film formation. The successive drying step could then be performed in a more controlled way in dry argon. This first homogeneous layer could then act as a substrate for the successive droplet deposition. Without orthogonal solvents this would however most likely redissolve the polymer substrate e.g. in the case of targeting the P3HT/PCBM interface. Thus, a successive step-by-step deposition in a saturated environment without redissolving or intermixing of already deposited material seems unlikely.

10.9 Summary

The presented experiments show that organic layers reflecting PCBM properties could be deposited via the nebulization technique. Although there are still some uncertainties how the nebulization process influences the film formation and the obtained photoelectron spectra, different thickness-dependent contact behavior of PCBM on various substrates was directly observed for the first time to the best of my knowledge.

PCBM was deposited on various substrates including polymeric contact materials. Besides varying energy level alignment, also in dependence of the PCBM thickness, a change in the valence structure was measured irrespective of the substrate material. The origin of this behavior is still unclear but a chemical reaction with the substrates or molecular decomposition are tentatively excluded. Possibly, orientation effects could cause the observed

change in the UP spectra. Nonetheless the distinctive core level emissions and HOMO associated features could be observed and an evaluation of the electronic level interaction was still possible.

On the one hand, in the case of PCBM on ozone-treated ITO the representation of energy levels in the order of obtained layer thickness seems to indicate a band bending in PCBM in such a way that the Fermi level shifts downward in the PCBM energy gap. This would mean that electrons are transferred from ITO to PCBM. On the other hand, in the case of PCBM on PEDOT:PSS the trend indicated by the representation of energy levels with respect to layer thickness is not as consistent. While the PCBM energy levels shift downwards in binding energy with increasing coverage after the nebulizer deposition indicating electron transfer from PCBM to PEDOT:PSS, for the drop-cast and spin-coated samples, a similar trend as for PCBM on ITO is observed. In the case of PCBM on ozone-treated ITO and PEDOT:PSS the ICT model predicts vacuum level alignment [20, 46]. However, an interface dipole of around 1 eV was obtained for the lowest coverages in the nebulization processes. Even for the drop-cast and spin-coated samples on these substrate materials no vacuum level alignment was observed. Thus, a predefinition of the energy level positions in PCBM by the substrate material seems unlikely. Only in the case of PCBM on PEI the predicted Fermi level alignment of the ICT model seems to be followed [20, 46]. Interestingly, this is the only case where an efficient electron transfer from PCBM to the substrate is actually intended and necessary for efficient solar cell performance.

11 Evaluation of the Nebulizer Method

The successful deposition of small quantities of dissolved organic semiconductors both on inorganic as well as on organic substrates in a way that is suitable for photoelectron spectroscopy characterization with the newly developed nebulizer technique was studied. Although only individual droplets were deposited in most cases rather than continuous films, the characteristic features of all applied materials could be detected and the determination of the electronic interface properties was possible. In comparison to thicker films deposited also from solution via drop-casting or spin-coating even a dependence of the electronic properties on the film thickness could be shown.

While the nebulizer method has proven to be useful for direct PES characterization of solution-processed interfaces of organic semiconductors, the lack of continuous film formation might be a drawback considering further approaches. For correlating electronic interface properties directly to electric device characteristics, e.g. by building a device out of a PES sample, the requirements for both characterization steps need to be taken into account. In many cases, the optimal film morphology to achieve best device performance involves a high degree of molecular order and homogeneity, which was not reached yet.

To improve film homogeneity but maintain the low film thickness, the nebulization processes must be performed for a prolonged time until already in the liquid state, a continuous film is formed. Performing the deposition in a solvent-saturated environment may increase the drying time and potentially favor better molecular arrangement. This procedure, however, would most likely cancel one of the benefits of this technique which is the almost dry or reduced solvent deposition. Complete liquid films would again increase the probability of redissolving previously deposited layers (of the same or a different material). The use of orthogonal solvents could be beneficial as e.g. in the case of P3HT and PCBM the mixing of the two materials during the nebulizer deposition could be minimized. Yet, this approach would not prevent redissolving already deposited PCBM during the successive nebulized deposition steps in order to achieve thicker layers.

The substrate coverage and possibly the film homogeneity could also be improved through repeatedly moving the substrate through a constant spray produced by the nebulizer unit. Although this might require a constant solution feed to the nebulizer, it should in principle be possible in the current glass cell architecture. By repeated deposition steps, in which only small droplets are deposited, an island like growth mode as possible in PVD processes could be mimicked. But the order and interaction between the subsequently deposited material patches is most likely still very different from films deposited through coating or printing techniques.

Additionally, the current geometric arrangement of the nebulizer unit with respect to the substrate might influence the film quality. In a liquid film facing downward during the deposition hydrodynamic instabilities and gravity effects can significantly alter the film properties. Therefore, different geometric arrangements could improve the nebulizer deposition process. However, this seems to be difficult to realize with the current home-built setup requiring a liquid reservoir on top of the piezo disk of the nebulizer unit. There are, however, commercial systems in which a mist is produced in a nozzle structure via ultrasonic agitation. Such a spray-coating nozzle e.g. from SONO TEK could be incorporated in the glass cell [154] or the complete spray-coating arrangement Exacta Coat [155] could be placed in the glove box attached at the Clustertool. One may expect that these systems allow to form much smaller droplets within the deposition process, which seems to be the most detrimental factor for the deposition of homogeneous films from solution in the given arrangement.

The presented experiments show in principle an alternative pathway to circumvent challenges usually faced when characterizing solution-processed interfaces. Admittedly, this approach is still in the very early stages of development which means there is plenty of room for improvement. The use of orthogonal solvents together with optimized drying conditions e.g. by reduced pressure, solvent-enriched argon atmosphere, increased substrate temperature and last but not least strongly reduced droplet size could improve the film quality and PES results.

12 Concluding Remarks and Outlook

The starting point of this work was the question how donor and acceptor materials interact electronically at the interface of a solution-processed bulk heterojunction solar cell. Therefore, the interface band diagram of thiophene based donors and fullerene based acceptors was characterized with photoelectron spectroscopy using various preparation techniques. For the model system DH6T/PCBM the band energy diagram for evaporated interfaces as well as solution-processed blend structures could be determined. Due to the observed band bending in the donor, this result has important implications on device processes in organic solar cells as charge carrier recombination is possibly increased. Furthermore, an innovative preparation route based on the nebulization of organic solutions was derived from device fabrication processes and adapted to PES requirements. This enabled the determination of band energy diagrams of solution-processed systems relevant for the device performance of printed organic electronics.

The experiments presented in this work show the great opportunities arising from applying PES to derive information on solution-processed systems for knowledge-driven organic optoelectronic device improvements. And although there might still remain some experimental challenges to be overcome, even stepwise interface characterization for (only) soluble organic semiconductors is possible with PES. Especially the glass cell setup has proven to be very powerful and versatile for depositing thin films from solution in an ultra-clean environment and compatible to UHV analysis.

Several direct approaches to the P3HT:PCBM interface were presented and implicit information about the electronic contact formation could be derived. The results indicated a constant Fermi level in the acceptor PCBM and an upward shift of the Fermi level in the energy gap of the donor P3HT. Information about the strength and direction of an interface dipole could not be deduced. However, the results showed the challenges in liquid-based interface preparation as high miscibility and surface tension differences influence the composition especially at the surface (i.e. within the probing depth of PES) and thus accessibility of the interface.

In order to circumvent these challenges, thermal evaporation as a way of stepwise thin film preparation was explored. For PCBM, which is originally designed for solution processing, thin films could be produced although very inefficiently. The PCBM content in the evaporated films is significantly reduced and the residues recovered from the crucible show a high level of impurities containing even C₆₀, which indicates the complete elimination of the PCBM side chain. In the case of DH6T, evaporation is possible and the films obtained through evaporation and drop-casting from chlorobenzene solution have very comparable chemical and electronic properties according to PES. By depth profiling in SXPS measurements an upright molecular orientation of DH6T was observed, which is even more pronounced in the evaporated films.

By combining drop-casting of PCBM and evaporation of DH6T, the acceptor/donor interface was characterized in detail giving an interface dipole of 0.26 eV and band bending in the donor of 0.3 eV. For blends consisting of the same donor:acceptor combination with varying concentration ratios, a DH6T capping layer was observed. Although this again hindered direct access to the solution-processed interface, the varying HOMO-HOMO distance for the different concentration ratios indicated the formation of an interface dipole and band bending also in these experiments. This hybrid approach in combining UHV interface preparation and solution-based layer deposition techniques allows to describe the electronic structure in donor:acceptor systems with a donor capping layer. The observed band bending in the donor is potentially obstructive for solar cell performance as it might lead to hole accumulation at the donor:acceptor interface. This in turn could increase charge carrier recombination. A potential cure for this unfavorable band bending could be doping. In summary, valuable information about the electronic contact formation in organic bulk heterojunctions was obtained in the course of this work.

Considering the establishment of a new deposition technique for organic semiconductor inks to allow stepwise deposition from solution, the nebulizer method was incorporated in the glass cell deposition setup. This way, the possibilities to deposit organic molecules from solution under conditions suitable for PES were expanded. In the case of DH6T, the comparison of nebulized films to drop-cast and evaporated reference samples yielded striking agreement of the spectra and thus confirmed the overall suitability and cleanliness of the glass cell deposition environment as nearly identical chemical and electronic properties were obtained irrespective of the deposition method.

The nebulizer method was also successfully applied with PCBM solutions. By repeated exposure, the PCBM coverage of the ITO substrate could be increased showing the possibility to perform stepwise deposition from solution. In addition, different thickness-dependent electronic properties on different substrate materials were observed for the first time. Although some observations, like the altered valence structure are not yet fully understood, these experiments clearly show the necessity to continue attempts for characterizing solution-processed interfaces. In that regard, the nebulizer setup potentially paves the way for step-by-step interface experiments from solution at atmospheric pressure in inert and contamination-free environment. Generally speaking, in order to be more compatible with desired roll-to-roll processes and thus enable easier knowledge transfer from interface analytics to device production procedures, other solution-based techniques than spin-coating should be employed also at this very fundamental level of research. In this respect, the presented nebulizer method already aims in the right direction as it can potentially be included in roll-to-roll fabrication processes like other spray-coating techniques. This will enable a better up-scaling and comparability to mass produced devices e.g. via printing or other coating techniques.

Future experiments could in principle be directed in two directions:

Step-by-Step Deposition From Solution The presented experiments clearly show the necessity of directly measuring the electronic properties at the relevant interfaces. To achieve this also for solution-processable organic semiconductors including polymers, the development and application of a step-by-step deposition technique should be pursued. While the approach introduced in this work most certainly is a step in the right direction, changes in deposition geometry such as having the substrate facing upward and the mist landing on the substrate from the top could be beneficial in terms of droplet sticking and formation of homogeneous layers. Also the application of commercial spray-coating setups such as the SONO TEK Exacta Coat [155] and/or the nozzles incorporated in this system could be considered to significantly reduce the size of the droplets. Additionally, promising results have been obtained using electrospray thin film deposition in vacuum [27, 28, 156]. The use of orthogonal solvents both in spin-coating as well as in the nebulizer deposition could provide further insight into bulk heterojunctions based on P3HT:PCBM. However, this approach is limited to a certain combination of donor and acceptor materials while the further

development of nebulizer and/or other spray-coating techniques offer a more general access to solution-processed organic semiconductor interfaces.

Curing of Band Bending As the observed band bending in the donor is potentially obstructive for solar cell performance, p-doping of the donor and/or n-doping of the acceptor could be applied to nullify or even reverse the band bending. With the current glass cell setup ideal conditions to explore doping from solution are available. Even co-deposition of matrix and dopant could be possible with an altered nebulizer setup based on two sources. Additionally, the influence of doping on the energy level alignment in polymeric solar cells could be characterized and correlated with device performance taking advantage of the vast knowledge and multiplicity of characterization techniques united at the InnovationLab.

Bibliography

- [1] INTERGOVERNMENTAL PANEL ON CLIMATE CHANGE. Fifth Assessment Report Climate Change 2013: The Physical Science Basis <http://www.ipcc.ch/report/ar5/wg1/#.U15k2V0HuSo>.
- [2] H. SHIRAKAWA, E. J. LOUIS, A. G. MACDIARMID, C. K. CHIANG, and A. J. HEEGER: Synthesis of electrically conducting organic polymers: halogen derivatives of polyacetylene, $(\text{CH})_x$. *Journal of the Chemical Society, Chemical Communications* (1977), p. 578–580.
- [3] R. SONDERGAARD, M. HÖSEL, D. ANGMO, T. T. LARSEN-OLSEN, and F. C. KREBS: Roll-to-roll fabrication of polymer solar cells. *Materials Today* 15 (2012), p. 36–49.
- [4] A. TSUMURA, H. KOEZUKA, and T. ANDO: Macromolecular electronic device: Field-effect transistor with a polythiophene thin film. *Applied Physics Letters* 49 (1986), p. 1210–1212.
- [5] C. W. TANG and S. VAN SLYKE: Organic Electroluminescent Diodes. *Applied Physics Letters* 51 (1987), p. 913–915.
- [6] LG, <http://www.lg.com/global/oledtv>.
- [7] SAMSUNG, <http://www.samsung.com/us/video/tvs/KN55S9CAFXZA>.
- [8] PHILIPS, <http://www.lighting.philips.de/lightcommunity/trends/oled/LumibladeOLEDGL350.wpd>.
- [9] OSRAM, http://www.osram.de/osram_de/produkte/led-technologie/oled-lichtgestaltung/index.jsp.
- [10] C. W. TANG: 2-Layer Organic Photovoltaic Cell. *Applied Physics Letters* 48 (1986), p. 183–185.
- [11] J. J. M. HALLS, C. A. WALSH, N. C. GREENHAM, E. A. MARSEGLIA, R. H. FRIEND, S. C. MORATTI, and A. B. HOLMES: Efficient Photodiodes from Interpenetrating Polymer Networks. *Nature* 376 (1995), p. 498–500.
- [12] G. YU, J. GAO, J. C. HUMMELEN, F. WUDL, and A. J. HEEGER: Polymer Photovoltaic Cells - Enhanced Efficiencies Via a Network of Internal Donor-Acceptor Heterojunctions. *Science* 270 (1995), p. 1789–1791.
- [13] HELIATEK GMBH, http://www.heliatek.com/newscenter/latest_news/neuer-weltrekord-fur-organische-solarzellen-heliatek-behauptet-sich-mit-12-zelleffizienz-als-technologiefuhrer/?lang=en.
- [14] B. P. RAND, D. P. BURK, and S. R. FORREST: Offset energies at organic semiconductor heterojunctions and their influence on the open-circuit voltage of thin-film solar cells. *Physical Review B* 75 (2007), p. 115 327.
- [15] C. HEIN, E. MANKEL, T. MAYER, and W. JAEGERMANN: Engineering the electronic structure of the CuPc/BPE-PTCDI interface by WO_3 doping of CuPc. *Physica Status Solidi a-Applications and Materials Science* 206 (2009), p. 2757–2762.
- [16] L. BRILLSON: The structure and properties of metal-semiconductor interfaces. *Surface Science Reports* 2 (1982), p. 123 – 326.
- [17] H. ISHII, K. SUGIYAMA, E. ITO, and K. SEKI: Energy level alignment and interfacial electronic structures at organic metal and organic organic interfaces. *Advanced Materials* 11 (1999), p. 605–625.

-
- [18] P. SCHILINSKY, C. WALDAUF, and C. J. BRABEC: Recombination and loss analysis in polythiophene based bulk heterojunction photodetectors. *Applied Physics Letters* 81 (2002), p. 3885–3887.
- [19] G. LI, V. SHROTRIYA, J. S. HUANG, Y. YAO, T. MORIARTY, K. EMERY, and Y. YANG: High-efficiency solution processable polymer photovoltaic cells by self-organization of polymer blends. *Nature Materials* 4 (2005), p. 864–868.
- [20] Z. XU, L. M. CHEN, M. H. CHEN, G. LI, and Y. YANG: Energy level alignment of poly(3-hexylthiophene): [6,6]-phenyl C(61) butyric acid methyl ester bulk heterojunction. *Applied Physics Letters* 95 (2009), p. 013 301.
- [21] Z. XU, L. M. CHEN, G. W. YANG, C. H. HUANG, J. H. HOU, Y. WU, G. LI, C. S. HSU, and Y. YANG: Vertical Phase Separation in Poly(3-hexylthiophene): Fullerene Derivative Blends and its Advantage for Inverted Structure Solar Cells. *Advanced Functional Materials* 19 (2009), p. 1227–1234.
- [22] I. G. HILL, A. KAHN, J. CORNIL, D. A. DOS SANTOS, and J. L. BRÉDAS: Occupied and unoccupied electronic levels in organic pi-conjugated molecules: comparison between experiment and theory. *Chemical Physics Letters* 317 (2000), p. 444–450.
- [23] T. MAYER, C. HEIN, E. MANKEL, W. JAEGERMANN, M. M. MÜLLER, and H.-J. KLEEBE: Fermi level positioning in organic semiconductor phase mixed composites: The internal interface charge transfer doping model. *Organic Electronics* 13 (2012), p. 1356–1364.
- [24] Z. L. GUAN, J. B. KIM, H. WANG, C. JAYE, D. A. FISCHER, Y. L. LOO, and A. KAHN: Direct determination of the electronic structure of the poly(3-hexylthiophene):phenyl-[6,6]-C61 butyric acid methyl ester blend. *Organic Electronics* 11 (2010), p. 1779–1785.
- [25] W. OSIKOWICZ, M. P. DE JONG, and W. R. SALANECK: Formation of the Interfacial Dipole at Organic-Organic Interfaces: C60/Polymer Interfaces. *Advanced Materials* 19 (2007), p. 4213–4217.
- [26] J. FRISCH, A. VOLLMER, J. P. RABE, and N. KOCH: Ultrathin polythiophene films on an intrinsically conducting polymer electrode: Charge transfer induced valence states and interface dipoles. *Organic Electronics* 12 (2011), p. 916–922.
- [27] A. J. CASCIO, J. E. LYON, M. M. BEERBOM, R. SCHLAF, Y. ZHU, and S. A. JENEKHE: Investigation of a polythiophene interface using photoemission spectroscopy in combination with electro spray thin-film deposition. *Applied Physics Letters* 88 (2006), p. 062 104.
- [28] J. E. LYON, A. J. CASCIO, M. M. BEERBOM, R. SCHLAF, Y. ZHU, and S. A. JENEKHE: Photoemission study of the poly(3-hexylthiophene)/Au interface. *Applied Physics Letters* 88 (2006), p. 222 109.
- [29] Z. CHEN, Z.-B. DENG, M.-Y. ZHOU, Z.-Y. LÜ, H.-L. DU, Y. ZOU, Y.-H. YIN, and J.-C. LUN: A Poly-(3-Hexylthiophene) (P3HT)/[6,6]-Phenyl-C61-Butyric Acid Methyl Ester (PCBM) Bi-layer Organic Solar Cell Fabricated by Airbrush Spray Deposition. *Chinese Physics Letters* 29 (2012), p. 078 801.
- [30] K. X. STEIRER, M. O. REESE, B. L. RUPERT, N. KOPIDAKIS, D. C. OLSON, R. T. COLLINS, and D. S. GINLEY: Ultrasonic spray deposition for production of organic solar cells. *Solar Energy Materials and Solar Cells* 93 (2009), p. 447–453.
- [31] M. SCHWOERER and H. WOLF: *Organic Molecular Solids*. Wiley-VCH (2007).
- [32] W. BRÜTTING: *Physics of Organic Semiconductors*. Wiley-VCH (2005).
- [33] F. CAREY and R. J. SUNDBERG: *Advanced Organic Chemistry Part A: Structure and Mechanisms*. Springer Science and Business Media, LLC (2007).

-
- [34] A. GASSMANN and C. MELZER: Organic Semiconductors and Devices. Lecture notes (2011).
- [35] E. MANKEL: Elektronische Eigenschaften von Heterosystemen organischer und anorganischer Halbleiter: Präparation, Modifikation und Charakterisierung von Grenzflächen und Kompositen. Ph.D. thesis, Technische Universität Darmstadt (2010).
- [36] W. BRÜTTING and W. RIESS: Grundlagen der organischen Halbleiter. *Physik Journal* 05 (2008), p. 33.
- [37] S. OLTHOF: Photoelectron Spectroscopy on Doped Organic Semiconductors and Related Interfaces. Ph.D. thesis, Technische Universität Dresden (2010).
- [38] C. HEIN: Anpassung der elektronischen Struktur an organischen Heterokontakten. Ph.D. thesis, Technische Universität Darmstadt (2012).
- [39] E. BREITMAIER and G. JUNG: Organische Chemie. 6th edition. Thieme Stuttgart (2009).
- [40] H. BÄSSLER, G. SCHÖNHERR, M. ABKOWITZ, and D. M. PAI: Hopping Transport in Prototypical Organic Glasses. *Physical Review B* 26 (1982), p. 3105–3113.
- [41] S. M. SZE and K. K. NG: Physics of Semiconductor Devices. 3rd edition. John Wiley & Sons, Inc. (2007).
- [42] W. SCHOTTKY: Halbleitertheorie der Sperrschicht. *Naturwissenschaften* 26 (1938), p. 843.
- [43] W. SCHOTTKY: Zur Halbleitertheorie der Sperrschicht- und Spitzengleichrichter. *Zeitschrift für Physik* 113 (1939), p. 367–414.
- [44] R. L. ANDERSON: Germanium-Gallium Arsenide Heterojunctions [Letter to the Editor]. *IBM Journal* 4 (1960), p. 283–287.
- [45] R. L. ANDERSON: Experiments on Ge-GaAs Heterojunctions. *Solid-State Electronics* 5 (1962), p. 341–351.
- [46] M. FAHLMAN, S. BRAUN, and W. R. SALANECK: Energy-Level Alignment at Organic/Metal and Organic/Organic Interfaces. *Advanced Materials* 21 (2009), p. 1450–1472.
- [47] H. VAZQUEZ, W. GAO, F. FLORES, and A. KAHN: Energy level alignment at organic heterojunctions: Role of the charge neutrality level. *Physical Review B* 71 (2005), p. 041 306(R).
- [48] X. CRISPIN, V. GESKIN, A. CRISPIN, J. CORNIL, R. LAZZARONI, W. R. SALANECK, and J.-L. BRÉDAS: Characterization of the Interface Dipole at Organic/ Metal Interfaces. *Journal of the American Chemical Society* 124 (2002), p. 8131–8141.
- [49] H. LI, Y. Q. DUAN, V. COROPCEANU, and J. L. BRÉDAS: Electronic structure of the pentacene-gold interface: A density-functional theory study. *Organic Electronics* 10 (2009), p. 1571–1578.
- [50] H. VAZQUEZ, Y. J. DAPPE, J. ORTEGA, and F. FLORES: Energy level alignment at metal/organic semiconductor interfaces: "Pillow" effect, induced density of interface states, and charge neutrality level. *The Journal of Chemical Physics* 126 (2007): 144703.
- [51] M. A. GREEN, K. EMERY, Y. HISHIKAWA, W. WARTA, and E. D. DUNLOP: Solar cell efficiency tables (version 42). *Progress in Photovoltaics: Research and Applications* 21 (2013), p. 827–837.
- [52] H. HOPPE and N. S. SARICIFTCI: Organic solar cells: An overview. *Journal of Materials Research* 19 (2004), p. 1924–1945.
- [53] J. J. M. HALLS, J. CORNIL, D. A. DOS SANTOS, R. SILBEY, D. H. HWANG, A. B. HOLMES, J. L. BRÉDAS, and R. H. FRIEND: Charge- and energy-transfer processes at polymer/polymer interfaces: A joint experimental and theoretical study. *Physical Review B* 60 (1999), p. 5721–5727.
- [54] L. J. A. KOSTER, V. D. MIHAILETCHI, and P. W. M. BLOM: Ultimate efficiency of polymer/fullerene bulk heterojunction solar cells. *Applied Physics Letters* 88 (2006), p. 093 511.

-
- [55] M. C. SCHARBER, D. MÜHLBACHER, M. KOPPE, P. DENK, C. WALDAUF, A. J. HEEGER, and C. J. BRABEC: Design Rules for Donors in Bulk-Heterojunction Solar Cells: Towards 10% Energy-Conversion Efficiency. *Advanced Materials* 18 (2006), p. 789–794.
- [56] A. GADISA, M. SVENSSON, M. R. ANDERSSON, and O. INGANÄS: Correlation between oxidation potential and open-circuit voltage of composite solar cells based on blends of polythiophenes/fullerene derivative. *Applied Physics Letters* 84 (2004), p. 1609–1611.
- [57] P. M. ALLEMAND, A. KOCH, F. WUDL, Y. RUBIN, F. DIEDERICH, M. M. ALVAREZ, S. J. ANZ, and R. L. WHETTEN: 2 Different Fullerenes Have the Same Cyclic Voltammetry. *Journal of the American Chemical Society* 113 (1991), p. 1050–1051.
- [58] B. C. THOMPSON and J. M. J. FRECHET: Organic photovoltaics - Polymer-fullerene composite solar cells. *Angewandte Chemie-International Edition* 47 (2008), p. 58–77.
- [59] S. GUNES, H. NEUGEBAUER, and N. S. SARICIFTCI: Conjugated polymer-based organic solar cells. *Chemical Reviews* 107 (2007), p. 1324–1338.
- [60] T. B. SINGH, N. MARJANOVIC, P. STADLER, M. AUINGER, G. J. MATT, S. GUNES, N. S. SARICIFTCI, R. SCHWODIAUER, and S. BAUER: Fabrication and characterization of solution-processed methanofullerene-based organic field-effect transistors. *Journal of Applied Physics* 97 (2005), p. 083 714.
- [61] H. LI, B. C.-K. TEE, J. J. CHA, Y. CUI, J. W. CHUNG, S. Y. LEE, and Z. BAO: High-Mobility Field-Effect Transistors from Large-Area Solution-Grown Aligned C60 Single Crystals. *Journal of the American Chemical Society* 134 (2012), p. 2760–2765.
- [62] T. B. SINGH, N. MARJANOVIC, G. J. MATT, S. GUNES, N. S. SARICIFTCI, A. M. RAMIL, A. ANDREEV, H. SITTE, R. SCHWODIAUER, and S. BAUER: High-mobility n-channel organic field-effect transistors based on epitaxially grown C-60 films. *Organic Electronics* 6 (2005), p. 105–110.
- [63] M. J. WINOKUR, D. SPIEGEL, Y. KIM, S. HOTTA, and A. J. HEEGER: Structural and Absorption Studies of the Thermochemical Transition in Poly(3-Hexylthiophene). *Synthetic Metals* 28 (1989), p. C419–C426.
- [64] L. H. JIMISON, M. F. TONEY, I. MCCULLOCH, M. HEENEY, and A. SALLES: Charge-Transport Anisotropy Due to Grain Boundaries in Directionally Crystallized Thin Films of Regioregular Poly(3-hexylthiophene). *Advanced Materials* 21 (2009), p. 1568–1572.
- [65] X. L. XIAO, Z. B. WANG, Z. J. HU, and T. A. B. HE: Single Crystals of Polythiophene with Different Molecular Conformations Obtained by Tetrahydrofuran Vapor Annealing and Controlling Solvent Evaporation. *Journal of Physical Chemistry B* 114 (2010), p. 7452–7460.
- [66] D. CHIRVASE, Z. CHIGUVARE, M. KNIPPER, J. PARISI, V. DYAKONOV, and J. HUMMELEN: Electrical and optical design and characterisation of regioregular poly(3-hexylthiophene-2,5-diyl)/fullerene-based heterojunction polymer solar cells. *Synthetic Metals* 138 (2003), p. 299 – 304.
- [67] D. FICHO: Handbook of Oligo- and Polythiophenes. Wiley-VCH (1999).
- [68] F. PADINGER, R. S. RITTBERGER, and N. S. SARICIFTCI: Effects of postproduction treatment on plastic solar cells. *Advanced Functional Materials* 13 (2003), p. 85–88.
- [69] W. L. MA, C. Y. YANG, X. GONG, K. LEE, and A. J. HEEGER: Thermally stable, efficient polymer solar cells with nanoscale control of the interpenetrating network morphology. *Advanced Functional Materials* 15 (2005), p. 1617–1622.
- [70] Y. SHIGESATO: Handbook of Transparent Conductors. Springer New York Heidelberg Dordrecht London (2010).

-
- [71] Y. GASSENBAUER: Untersuchung der elektronischen und chemischen Oberflächeneigenschaften von Zinn-dotiertem Indiumoxid im Hinblick auf die Funktion in organischen Leuchtdioden. Ph.D. thesis, Technische Universität Darmstadt (2007).
- [72] G. GRECZYNSKI, T. KUGLER, M. KEIL, W. OSIKOWICZ, M. FAHLMAN, and W. SALANECK: Photoelectron spectroscopy of thin films of PEDOT:PSS conjugated polymer blend: a mini-review and some new results. *Journal of Electron Spectroscopy and Related Phenomena* 121 (2001), p. 1–17.
- [73] Y. ZHOU, C. FUENTES-HERNANDEZ, J. SHIM, J. MEYER, A. J. GIORDANO, H. LI, P. WINGET, T. PAPADOPOULOS, H. CHEUN, J. KIM, M. FENOLL, A. DINDAR, W. HASKE, E. NAJAFABADI, T. M. KHAN, H. SOJOUDI, S. BARLOW, S. GRAHAM, J.-L. BRÉDAS, S. R. MARDER, A. KAHN, and B. KIPPELEN: A Universal Method to Produce Low Work Function Electrodes for Organic Electronics. *Science* 336 (2012), p. 327–332.
- [74] H. SIRRINGHAUS, P. J. BROWN, R. H. FRIEND, M. M. NIELSEN, K. BECHGAARD, B. M. W. LANGEVELD-VOSS, A. J. H. SPIERING, R. A. J. JANSSEN, E. W. MEIJER, P. HERWIG, and D. M. DE LEEUW: Two-dimensional charge transport in self-organized, high-mobility conjugated polymers. *Nature* 401 (1999), p. 685–688.
- [75] F. GARNIER, A. YASSAR, R. HAJLAOUI, G. HOROWITZ, F. DELOFFRE, B. SERVET, S. RIES, and P. ALNOT: Molecular Engineering of Organic Semiconductors - Design of Self-assembly Properties in Conjugated Thiophene Oligomers. *Journal of the American Chemical Society* 115 (1993), p. 8716–8721.
- [76] H. S. SEO, Y. ZHANG, Y. S. JANG, and J. H. CHOI: Performance and transport characteristics of alpha,omega-dihexylsexithiophene-based transistors with a high room-temperature mobility of 0.16 cm²/V s. *Applied Physics Letters* 92 (2008), p. 223 310.
- [77] F. F. MUHAMMAD and K. SULAIMAN: Photovoltaic performance of organic solar cells based on DH6T/PCBM thin film active layers. *Thin Solid Films* 519 (2011), p. 5230–5233.
- [78] H. W. KROTO, J. R. HEATH, S. C. O'BRIEN, R. F. CURL, and R. E. SMALLEY: C₆₀: Buckminsterfullerene. *Nature* 318 (1985), p. 162–163.
- [79] W. KRÄTSCHMER, L. D. LAMB, K. FOSTIROPOULOS, and D. R. HUFFMAN: Solid C₆₀: a new form of carbon. *Nature* 347 (1990), p. 354–358.
- [80] J. C. HUMMELEN, B. W. KNIGHT, F. LEPEQ, F. WUDL, J. YAO, and C. L. WILKINS: Preparation and Characterization of Fulleroid and Methanofullerene Derivatives. *Journal of Organic Chemistry* 60 (1995), p. 532–538.
- [81] D. BRIGGS: Surface Analysis of Polymers by XPS and static SIMS. Cambridge University Press, Cambridge (1998).
- [82] T. GLASER: Infrarotspektroskopische Untersuchung der p-Dotierung organischer Halbleiter mit Übergangsmetalloxiden. Ph.D. thesis, Ruprecht-Karls-Universität Heidelberg (2012).
- [83] S. HÜFNER: Photoelectron Spectroscopy: Principles and Applications. 2nd edition. Springer Berlin / Heidelberg (1996).
- [84] J. VICKERMAN and I. GILMORE: Surface Analysis - The Principal Techniques. John Wiley & Sons Ltd. (2009).
- [85] G. BEAMSON and D. BRIGGS: XPS of Polymers Database. Surface Spectra (1992).
- [86] PHI VersaProbe Unique Features www.phil.com.
- [87] D. A. SHIRLEY: High-Resolution X-Ray Photoemission Spectrum of Valence Bands of Gold. *Physical Review B* 5 (1972), p. 4709–4714.

-
- [88] S. TOUGAARD and I. CHORKENDORFF: Differential inelastic electron scattering cross sections from experimental reflection electron-energy-loss spectra: Application to background removal in electron spectroscopy. *Physical Review B* 35 (1987), p. 6570–6577.
- [89] J. F. MOULDER, W. F. STICKLE, P. E. SOBOL, and K. D. BOMBEN: Handbook of X-Ray Photoelectron Spectroscopy. Physical Electronics, Inc. (1995).
- [90] G. FRIEDBACHER and H. BUBERT (editors) : Surface and Thin Film Analysis. 2nd edition. Wiley-VCH, Weinheim (2011).
- [91] J. J. YEH and I. LINDAU: Atomic Subshell Photoionization Cross-Sections and Asymmetry Parameters - 1 Less-Than-or-Equal-to Z Less-Than-or-Equal-to 103. *Atomic Data and Nuclear Data Tables* 32 (1985), p. 1–155.
- [92] A. DECKER: Farbstoffsensibilisierung von Dünnschichtsilizium für photovoltaische Anwendungen. Ph.D. thesis, Technische Universität Darmstadt (2012).
- [93] C. J. POWELL and A. JABLONSKI. NIST Electron Inelastic-Mean-Free-Path Database. Standard Reference Data Program, National Institute of Standards and Technology, Gaithersburg, 1.1 edition (2000).
- [94] S. TANUMA, C. J. POWELL, and D. R. PENN: Calculations of electron inelastic mean free paths. V. Data for 14 organic compounds over the 50-2000 eV range. *Surface and Interface Analysis* 21 (1994), p. 165–176.
- [95] H.-D. DÖRFLER: Grenzflächen und kolloid-disperse Systeme. Springer Berlin/Heidelberg (2002).
- [96] KRÜSS GMBH, <http://www.kruss.de/de/theorie/messungen/kontaktwinkel/einfuehrung.html>.
- [97] ACCU DYNE TEST, http://www.accudynetest.com/polymer_surface_data/ptfe.pdf.
- [98] M. HESSE, H. MEIER, and B. ZEEH: Spektroskopische Methoden in der organischen Chemie. Georg Thieme Verlag (1991).
- [99] WATERS CORPORATION, http://www.waters.com/waters/en_US/HPLC---High-Performance-Liquid-Chromatography/nav.htm?locale=en_US&cid=10048919.
- [100] V. D. MIHAILETCHI, H. X. XIE, B. DE BOER, L. J. A. KOSTER, and P. W. M. BLOM: Charge transport and photocurrent generation in poly (3-hexylthiophene): Methanofullerene bulk-heterojunction solar cells. *Advanced Functional Materials* 16 (2006), p. 699–708.
- [101] G. LI, V. SHROTRIYA, Y. YAO, J. S. HUANG, and Y. YANG: Manipulating regioregular poly(3-hexylthiophene): [6,6]-phenyl-C-61-butyric acid methyl ester blends - route towards high efficiency polymer solar cells. *Journal of Materials Chemistry* 17 (2007), p. 3126–3140.
- [102] G. P. LOPEZ, D. G. CASTNER, and B. D. RATNER: XPS O 1s binding energies for polymers containing hydroxyl, ether, ketone and ester groups. *Surface and Interface Analysis* 17 (1991), p. 267–272.
- [103] J. A. LEIRO, M. H. HEINONEN, T. LAIHO, and I. G. BATIREV: Core-level XPS spectra of fullerene, highly oriented pyrolytic graphite, and glassy carbon. *Journal of Electron Spectroscopy and Related Phenomena* 128 (2003), p. 205–213.
- [104] K. AKAIKE, K. KANAI, H. YOSHIDA, J. TSUTSUMI, T. NISHI, N. SATO, Y. OUCHI, and K. SEKI: Ultraviolet photoelectron spectroscopy and inverse photoemission spectroscopy of [6,6]-phenyl-C-61-butyric acid methyl ester in gas and solid phases. *Journal of Applied Physics* 104 (2008), p. 023 710.

-
- [105] T. SCHWIEGER, X. LIU, H. PEISERT, B. ADOLPHI, N. KIRIY, and M. KNUPFER: Electronic properties of interfaces between different sexithiophenes and gold. *Journal of Applied Physics* 97 (2005), p. 123 712.
- [106] W. R. SALANECK, O. INGANÄS, B. THÉMANS, J. O. NILSSON, B. SJÖGREN, J. E. OSTERHOLM, J. L. BRÉDAS, and S. SVENSSON: Thermochromism in Poly(3-Hexylthiophene) in the Solid-State - a Spectroscopic Study of Temperature-Dependent Conformational Defects. *Journal of Chemical Physics* 89 (1988), p. 4613–4619.
- [107] H. FUJIMOTO, U. NAGASHIMA, H. INOKUCHI, K. SEKI, Y. CAO, H. NAKAHARA, J. NAKAYAMA, M. HOSHINO, and K. FUKUDA: Ultraviolet Photoemission-Study of Oligothiophenes - π -Band Evolution and Geometries. *Journal of Chemical Physics* 92 (1990), p. 4077–4092.
- [108] M. SCHWARZE: Photoelektronenspektroskopie am lösungsprozessierten Donor-Akzeptor-System P3HT:PCBM. Master thesis, Ruprecht-Karls-Universität Heidelberg, Heidelberg (2012).
- [109] A. OPITZ, J. FRISCH, R. SCHLESINGER, A. WILKE, and N. KOCH: Energy level alignment at interfaces in organic photovoltaic devices. *Journal of Electron Spectroscopy and Related Phenomena* (2012).
- [110] M. CAMPOY-QUILES, T. FERENCZI, T. AGOSTINELLI, P. G. ETCHEGOIN, Y. KIM, T. D. ANTHOPOULOS, P. N. STAVRINO, D. D. C. BRADLEY, and J. NELSON: Morphology evolution via self-organization and lateral and vertical diffusion in polymer: fullerene solar cell blends. *Nature Materials* 7 (2008), p. 158–164.
- [111] Y. YAO, J. HOU, Z. XU, G. LI, and Y. YANG: Effects of Solvent Mixtures on the Nanoscale Phase Separation in Polymer Solar Cells. *Advanced Functional Materials* 18 (2008), p. 1783–1789.
- [112] S. DUHM, I. SALZMANN, N. KOCH, H. FUKAGAWA, T. KATAOKA, S. HOSOURI, K. NEBASHI, S. KERA, and N. UENO: Vacuum sublimed α , ω -dihexylsexithiophene thin films: Correlating electronic structure and molecular orientation. *Journal of Applied Physics* 104 (2008), p. 033 717.
- [113] A. KUMAR, G. LI, Z. R. HONG, and Y. YANG: High efficiency polymer solar cells with vertically modulated nanoscale morphology. *Nanotechnology* 20 (2009), p. 165 202.
- [114] A. GOPAL: Effects of Thickness, Morphology and Molecular Structure of Donor and Acceptor Layers in Thermally Interdiffused Polymer Photovoltaics. Ph.D. thesis, Virginia Polytechnic Institute and State University, Blacksburg (2007).
- [115] K. AKAIKE, K. KANAI, Y. OUCHI, and K. SEKI: Influence of side chain of [6,6]-phenyl-C(61)-butyric acid methyl ester on interfacial electronic structure of [6,6]-phenyl-C(61)-butyric acid methyl ester/Ag substrate. *Applied Physics Letters* 94 (2009), p. 043 309.
- [116] M. P. FELICISSIMO, D. JARZAB, M. GORGOI, M. FORSTER, U. SCHERF, M. C. SCHARBER, S. SVENSSON, P. RUDOLF, and M. A. LOI: Determination of vertical phase separation in a polyfluorene copolymer: fullerene derivative solar cell blend by X-ray photoelectron spectroscopy. *Journal of Materials Chemistry* 19 (2009), p. 4899–4901.
- [117] M. H. RICHTER, D. FRIEDRICH, and D. SCHMEISSER: Valence and Conduction Band States of PCBM as Probed by Photoelectron Spectroscopy at Resonant Excitation. *BioNanoScience* 2 (2012), p. 59–65.
- [118] C. ENKVIST, S. LUNELL, B. SJÖGREN, S. SVENSSON, P. A. BRÜHWILER, A. NILSSON, A. J. MAXWELL, and N. MÅRTENSSON: C1s Shakeup Spectrum of C₆₀ - Global Charge-Transfer Satellites and Their Relation to the X-Ray Threshold Singularities in Macroscopic Systems. *Physical Review B* 48 (1993), p. 14 629–14 637.
- [119] N. TRINH TUNG, N. DUC NGHIA, and N. VAN TUYEN: Glass transition of PCBM, P3HT and their blends in quenched state. *Advances in Natural Sciences: Nanoscience and Nanotechnology* 3 (2012), p. 045 001.

-
- [120] HELMHOLTZ ZENTRUM BERLIN, http://www.helmholtz-berlin.de/forschung/grossgeraete/betrieb-beschleuniger/betriebsmodi_en.html (2013).
- [121] S. DUHM, H. GLOWATZKI, J. P. RABE, N. KOCH, and R. L. JOHNSON: Influence of alkyl chain substitution on sexithienyl-metal interface morphology and energetics. *Applied Physics Letters* 88 (2006).
- [122] BTU COTTBUS. Beamline Leaflet U49/2-PGM2, Version: July 2008 .
- [123] M. KNUPFER and X. LIU: Interface electronic properties of oligothiophenes: the effect of chain length and chemical substituents. *Surface Science* 600 (2006), p. 3978–3981.
- [124] S. DUHM, G. HEIMEL, I. SALZMANN, H. GLOWATZKI, R. L. JOHNSON, A. VOLLMER, J. P. RABE, and N. KOCH: Orientation-dependent ionization energies and interface dipoles in ordered molecular assemblies. *Nature Materials* 7 (2008), p. 326–332.
- [125] I. G. HILL, A. KAHN, Z. G. SOOS, and R. A. PASCAL: Charge-separation energy in films of pi-conjugated organic molecules. *Chemical Physics Letters* 327 (2000), p. 181–188.
- [126] M. D. IOSIP, S. DESTRI, M. PASINI, W. PORZIO, K. P. PERNSTICH, and B. BATLOGG: New dithieno[3,2-b : 2',3'-d]thiophene oligomers as promising materials for organic field-effect transistor applications. *Synthetic Metals* 146 (2004), p. 251–257.
- [127] J. MAIBACH, E. MANKEL, T. MAYER, and W. JAEGERMANN: The band energy diagram of PCBM-DH6T bulk heterojunction solar cells: synchrotron-induced photoelectron spectroscopy on solution processed DH6T:PCBM blends and in situ prepared PCBM/DH6T interfaces. *Journal of Materials Chemistry C* 1 (2013), p. 7635–7642.
- [128] J. MAIBACH, E. MANKEL, T. MAYER, and W. JAEGERMANN: Synchrotron induced photoelectron spectroscopy on drop casted donor/acceptor bulk heterojunction: Orbital energy line up in DH6T/PCBM blends. *Surface Science* 612 (2013), p. L9–L11.
- [129] A. L. AYZNER, C. J. TASSONE, S. H. TOLBERT, and B. J. SCHWARTZ: Reappraising the Need for Bulk Heterojunctions in Polymer-Fullerene Photovoltaics: The Role of Carrier Transport in All-Solution-Processed P3HT/PCBM Bilayer Solar Cells. *Journal of Physical Chemistry C* 113 (2009), p. 20 050–20 060.
- [130] Y. B. QI, S. K. MOHAPATRA, S. B. KIM, S. BARLOW, S. R. MARDER, and A. KAHN: Solution doping of organic semiconductors using air-stable n-dopants. *Applied Physics Letters* 100 (2012), p. 083 305.
- [131] D. T. DUONG, C. WANG, E. ANTONO, M. F. TONEY, and A. SALLEO: The chemical and structural origin of efficient p-type doping in P3HT. *Organic Electronics* 14 (2013), p. 1330–1336.
- [132] Y. ZHANG, H. ZHOU, J. SEIFTER, L. YING, A. MIKHAILOVSKY, A. J. HEEGER, G. C. BAZAN, and T.-Q. NGUYEN. MOLECULAR DOPING ENHANCES PHOTOCONDUCTIVITY IN POLYMER BULK HETEROJUNCTION SOLAR CELLS. *Advanced Materials* (2013), available online <http://dx.doi.org/10.1002/adma.201302159>.
- [133] S. NAM, M. SHIN, H. KIM, C.-S. HA, M. REE, and Y. KIM: Improved Performance of Polymer:Polymer Solar Cells by Doping Electron-Accepting Polymers with an Organosulfonic Acid. *Advanced Functional Materials* 21 (2011), p. 4527–4534.
- [134] A. VEYSEL TUNC, A. DE SIO, D. RIEDEL, F. DESCHLER, E. DA COMO, J. PARISI, and E. VON HAUFF: Molecular doping of low-bandgap-polymer:fullerene solar cells: Effects on transport and solar cells. *Organic Electronics* 13 (2012), p. 290–296.
- [135] TDK. Piezoelectronic Products NB Series (Product Data Sheet, 002-03 / 20120316 / ef441_nb) http://www.tdk.co.jp/tefe02/ser_n.htm.

-
- [136] A. L. YARIN: Drop impact dynamics: Splashing, spreading, receding, bouncing... *Annual Review of Fluid Mechanics* 38 (2006), p. 159–192.
- [137] T. GAMBARYAN-ROISMAN: Personal communication (2013).
- [138] M. G. VELARDE and R. K. ZEYTOUNIAN (editors) : Interfacial Phenomena and the Marangoni Effect, *CISM Courses and Lectures*, volume 428. Springer, Wien Ney York (2002).
- [139] M. G. MASON, L. S. HUNG, C. W. TANG, S. T. LEE, K. W. WONG, and M. WANG: Characterization of treated indium-tin-oxide surfaces used in electroluminescent devices. *Journal of Applied Physics* 86 (1999), p. 1688–1692.
- [140] T. OHTA, T. FUJIKAWA, and H. KURODA: Core-Electron Spectra of Monosubstituted Benzenes Obtained by Gas-Phase X-Ray Photoelectron-Spectroscopy. *Bulletin of the Chemical Society of Japan* 48 (1975), p. 2017–2024.
- [141] KRÜSS GMBH. Polare und dispersive Anteile der Oberflächenspannung <http://www.kruss.de>.
- [142] DIVERSIFIED ENTERPRISES. Surface Energy Data for PTFE: Polytetrafluoroethylene, CAS 9002-84-0 <http://www.accudynetest.com/> (2009).
- [143] M. R. LILLIEDAL, A. J. MEDFORD, M. V. MADSEN, K. NORRMAN, and F. C. KREBS: The effect of post-processing treatments on inflection points in current-voltage curves of roll-to-roll processed polymer photovoltaics. *Solar Energy Materials and Solar Cells* 94 (2010), p. 2018–2031.
- [144] H. SCHMIDT, K. ZILBERBERG, S. SCHMALE, H. FLÜGGE, T. RIEDL, and W. KOWALSKY: Transient characteristics of inverted polymer solar cells using titaniumoxide interlayers. *Applied Physics Letters* 96 (2010), p. 243 305.
- [145] S. TROST, K. ZILBERBERG, A. BEHRENDT, A. POLYWKA, P. GÖRRN, P. RECKERS, J. MAIBACH, T. MAYER, and T. RIEDL. OVERCOMING THE "LIGHT-SOAKING" ISSUE IN INVERTED ORGANIC SOLAR CELLS BY THE USE OF AL:ZNO ELECTRON EXTRACTION LAYERS. *Advanced Energy Materials* (2013), available online <http://dx.doi.org/10.1002/aenm.201300402>.
- [146] R. D. DEEGAN, O. BAKAJIN, T. F. DUPONT, G. HUBER, S. R. NAGEL, and T. A. WITTEN: Capillary flow as the cause of ring stains from dried liquid drops. *Nature* 389 (1997), p. 827–829.
- [147] G. GRECZYNSKI, T. KUGLER, and W. R. SALANECK: Characterization of the PEDOT-PSS system by means of X-ray and ultraviolet photoelectron spectroscopy. *Thin Solid Films* 354 (1999), p. 129–135.
- [148] B. L. GROENENDAAL, F. JONAS, D. FREITAG, H. PIELARTZIK, and J. R. REYNOLDS: Poly(3,4-ethylenedioxythiophene) and its derivatives: Past, present, and future. *Advanced Materials* 12 (2000), p. 481–494.
- [149] J. HWANG, F. AMY, and A. KAHN: Spectroscopic study on sputtered PEDOT-PSS: Role of surface PSS layer. *Organic Electronics* 7 (2006), p. 387–396.
- [150] HERAEUS: CLEVIOS™P VP AI 4083 Prdoduct Information (2010).
- [151] N. KOCH, A. ELSCHNER, J. SCHWARTZ, and A. KAHN: Organic molecular films on gold versus conducting polymer: Influence of injection barrier height and morphology on current-voltage characteristics. *Applied Physics Letters* 82 (2003), p. 2281–2283.
- [152] J. S. HUANG, P. F. MILLER, J. S. WILSON, A. J. DE MELLO, J. C. DE MELLO, and D. D. C. BRADLEY: Investigation of the effects of doping and post-deposition treatments on the conductivity, morphology, and work function of poly (3,4-ethylenedioxythiophene)/poly (styrene sulfonate) films. *Advanced Functional Materials* 15 (2005), p. 290–296.

-
- [153] M. BARBER, J. A. CONNOR, M. F. GUEST, I. H. HILLIER, M. SCHWARZ, and M. STACEY: Bonding in some donor-acceptor complexes involving boron trifluoride. Study by means of ESCA and molecular orbital calculations. *Journal of the Chemical Society, Faraday Transactions 2: Molecular and Chemical Physics* 69 (1973), p. 551–558.
- [154] SONO TEK, <http://www.sono-tek.com/mounting-option/>.
- [155] SONO TEK, <http://www.sono-tek.com/>.
- [156] N. DAM, M. M. BEERBOM, J. C. BRAUNAGEL, and R. SCHLAF: Photoelectron spectroscopic investigation of in-vacuum-prepared luminescent polymer thin films directly from solution. *Journal of Applied Physics* 97 (2005).
- [157] M. P. SEAH and W. A. DENCH: Quantitative electron spectroscopy of surfaces: A standard data base for electron inelastic mean free paths in solids. *Surface and Interface Analysis* 1 (1979), p. 2–11.
- [158] W. GEENS, T. MARTENS, J. POORTMANS, T. AERNOUTS, J. MANCA, L. LUTSEN, P. HEREMANS, S. BORGHS, R. MERTENS, and D. VANDERZANDE: Modelling the short-circuit current of polymer bulk heterojunction solar cells. *Thin Solid Films* 451 (2004), p. 498–502.
- [159] SIGMA ALDRICH. MSDS PEI (2012).

Appendix



A Additional Data to the Analysis of Evaporated PCBM

A.1 Difference XP Spectra of the Crucible Residue Sample

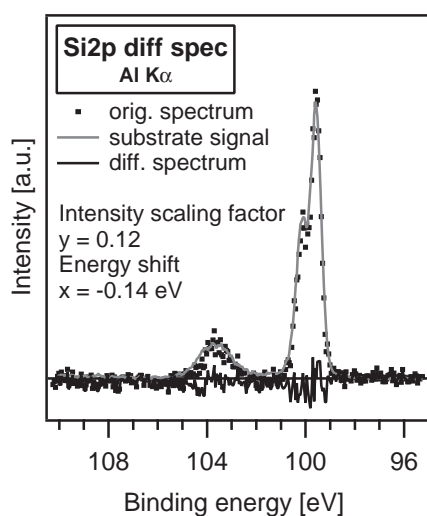


Figure A.1: Difference spectrum of the Si2p emission measured for the crucible residue film. The calculation was performed in such a way as to eliminate the substrate Si2p emission. The intensity and binding energy scaling factors determined in this way were used to calculate the difference spectra of the O1s and C1s emission.

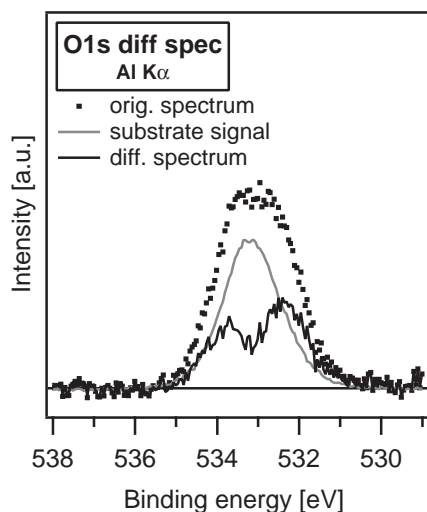
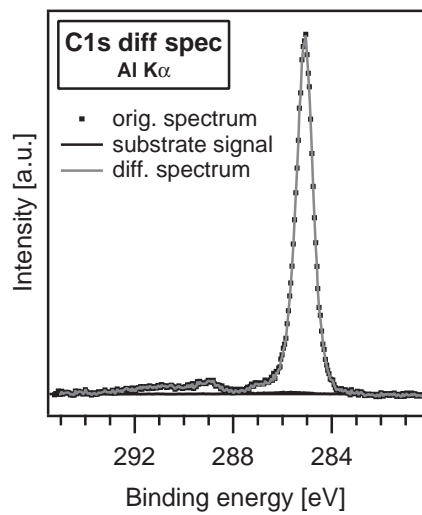


Figure A.2: Difference spectrum of the O1s emission measured for the crucible residue film. The calculation was performed using the intensity and binding energy scaling factors determined as determined for the substrate Si2p emission.

Figure A.3: Difference spectrum of the C1s emission measured for the crucible residue film. The calculation was performed using the intensity and binding energy scaling factors determined as determined for the substrate Si2p emission.



B Inelastic Mean Free Path Calculations

As a measure for the mean escape depth of the photoelectrons ($\lambda(E)$) the inelastic mean free paths (IMFP) were used in this work. These values were calculated using the NIST database [93] in which the TPP-2M [94] equation is implemented to obtain IMFP values from predictive chemical formulas. For these calculations, the stoichiometric formula of the organic compound in question, the number of valence electrons (N_v), the band gap (E_g), and the density (ρ) are needed. If no value for the density was found in literature a value of 1.3 g cm^{-3} was assumed. The following tables summarize the obtained IMFP values for the used organic molecules and give the required input parameters. As from the software only a set of value pairs is given, in the table the IMFP corresponding to the energy closest to the desired energy is given. In general, it should be noted that the combined standard uncertainty is given to be 4.7 \AA or 20.5 % [93].

The obtained values for organic materials are typically higher than for inorganic materials (compare e.g. "universal" curve depicted in Figure 3.8 in section 3.3) but correlate to the compilation of data for attenuation lengths for organic materials by SEAH AND DENCH [157].

Table B.1: Inelastic mean free path of PCBM. $N_v = 314$, $E_g = 2 \text{ eV}$ [24], $\rho = 1.5 \text{ g cm}^{-3}$ [158].

Electron energy [eV]	corresponding emission	excitation energy [eV]	IMFP [\AA]
1024.7	In3d	1486.6	27.8
1202.1	C1s	1486.6	31.53
955.6	O1s	1486.6	26.32
156.1	In3d	600	7.7
315	C1s	600	11.69
69	O1s	600	5.7
75	C1s	360	5.85

Table B.2: Inelastic mean free path of DH6T. $N_v = 218$, $E_g = 2.3$ eV [22, 126], $\rho = 1.3$ g cm⁻³.

Electron energy [eV]	corresponding emission	excitation energy [eV]	IMFP [Å]
1024.7	In3d	1486.6	27.6
1202.1	C1s	1486.6	31.4
1322.6	S2p	1486.6	33.9
955.6	O1s	1486.6	26.2
156.1	In3d	600	7.5
315	C1s	600	11.5
75	C1s	360	5.4
46	S2p	210	4.7

Table B.3: Inelastic mean free path in PEI. $N_v =$, $E_g = 6.2$ eV [73], $\rho = 1.03$ g cm⁻³ [159].

Electron energy [eV]	corresponding emission	excitation energy [eV]	IMFP [Å]
1024.7	In3d	1486.6	33.37

Publications & Conference Contributions

Publications

H. CHEUN, C. FUENTES-HERNANDEZ, J. SHIM, Y. N. FANG, Y. CAI, H. LI, A. K. SIGDEL, J. MEYER, J. MAIBACH, A. DINDAR, Y. H. ZHOU, J. J. BERRY, J. L. BREDAS, A. KAHN, K. H. SANDHAGE, and B. KIPPELEN: Oriented Growth of Al₂O₃:ZnO Nanolaminates for Use as Electron-Selective Electrodes in Inverted Polymer Solar Cells. *Advanced Functional Materials* 22 (2012), p. 1531-1538.

J. MAIBACH, E. MANKEL, T. MAYER and W. JAEGERMANN: Synchrotron Induced Photoelectron Spectroscopy on Drop-Casted Donor/Acceptor Bulk Heterojunction: Orbital Energy Line Up in DH6T/PCBM Blends. *Surface Science* 621 (2013), p. L9-L11.

S. TROST, K. ZILBERBERG, A. BEHRENDT, A. POLYWKA, P. GÖRRN, P. RECKERS, J. MAIBACH, T. MAYER, and T. RIEDL: Overcoming the "Light-Soaking" Issue in Inverted Organic Solar Cells by the Use of Al:ZnO Electron Extraction Layers. *Advanced Energy Materials*, available online, DOI: 10.1002/aenm.201300402.

J. MAIBACH, E. MANKEL, T. MAYER and W. JAEGERMANN: The Band Energy Diagram of PCBM-DH6T Bulk Heterojunction Solar Cells: Synchrotron-Induced Photoelectron Spectroscopy on Solution Processed DH6T:PCBM Blends and In-situ Prepared PCBM/DH6T Interfaces. *Journal of Materials Chemistry C* 1 (2013), p. 7635-7642.

Conference Contributions

DPG Frühjahrstagung, 2011, Dresden

J. MAIBACH, E. MANKEL, T. MAYER and W. JAEGERMANN: Combined Study of Interfaces and Device Properties of a Solid State Dye Sensitized Solar Cell. (Poster).

Winter School Organic Electronics, 2012, Heidelberg

J. MAIBACH, T. GLASER, A. FUCHS, E. MANKEL, T. MAYER, C. LENNARTZ, A. PUCCI and W.

JAEGERMANN: Investigation of the Molecular Stability of PCBM During Thermal Evaporation. (Poster).

MRS Spring Meeting, 2012, San Francisco, USA

J. MAIBACH, E. MANKEL, T. MAYER and W. JAEGERMANN: SXPS characterization of an In-situ Solution Processed Bulk Heterojunction Model System. (Poster).

MSE, 2012, Darmstadt

J. MAIBACH, E. MANKEL, T. MAYER and W. JAEGERMANN: SXPS Characterization of Solution Processed Bulk Heterojunction Model Systems. (Poster).

EU-PVSEC, 2012, Frankfurt

J. MAIBACH, E. MANKEL, T. MAYER and W. JAEGERMANN: Electronic Structure of Solution Processed Bulk Heterojunction Donor/Acceptor Model Systems. (Poster).

ISOE, 2012, Okinawa

J. MAIBACH, E. MANKEL, T. MAYER and W. JAEGERMANN: SXPS Study of the Electronic Structure of Solution Processed Bulk Heterojunction Donor/Acceptor Model Systems. (Poster).

DPG Frühjahrstagung, 2013, Regensburg

J. MAIBACH, E. MANKEL, T. MAYER and W. JAEGERMANN: Electronic Interface Properties of PCBM Using Photoelectron Spectroscopy. (Talk).

MRS Spring Meeting, 2013, San Francisco, USA

J. MAIBACH, E. MANKEL, T. MAYER and W. JAEGERMANN: Towards Photoelectron Spectroscopic Interface Characterization in Printed Electronics. (Poster).

EnMat II, 2013, Karlsruhe

J. MAIBACH, E. MANKEL, T. MAYER and W. JAEGERMANN: Photoelectron Spectroscopic Characterization of Electronic Interfaces Prepared From Inks. (Talk).

Danksagung

An dieser Stelle möchte ich mich herzlich bei allen bedanken, die direkt oder indirekt zum Gelingen dieser Arbeit beigetragen haben.

Besonderer Dank gilt

Prof. Dr. Wolfram Jaegermann für das Ermöglichen dieser Arbeit am Fachgebiet Oberflächenforschung sowie für die interessante Aufgabenstellung, die Unterstützung und für die Freiräume, eigene Ideen zu einwickeln und zu bearbeiten.

Prof. Dr. Heinz von Seggern für die freundliche Übernahme des Zweitgutachtens.

Dr. Thomas Mayer für die gute Betreuung sowie für die intensive Diskussion meiner Messergebnisse und Aufbauten, welche diese Arbeit sehr voran gebracht haben und meinen Blick auf das wissenschaftlich Wesentliche geschärft haben.

Dr. Eric Mankel für die vielen Hilfestellungen bei den Experimenten, sei es nachts bei BESSY oder beim Aufbauen der Anlage in Heidelberg. Durch unsere vielen Diskussionen z.B. auf den unzähligen gemeinsamen Fahrten nach Heidelberg habe ich sehr viel gelernt.

Torben Adermann nicht nur für die detaillierte Charakterisierung des Temperaturverhaltens von PCBM, sondern auch für die daraus resultierende sehr gute Zusammenarbeit und Dr. Manuel Hamburger, welcher zu jeder Frage die passende Antwort hatte, sobald die richtige Strukturformel gefunden war.

Dr. Tobias Glaser, Sebastian Beck, und David Gerbert für die IR-Messungen an PCBM einschließlich der intensiven Diskussion zu den Ergebnissen.

Dr. Andreas Fuchs, Dr. Christian Krekeler und Dr. Christian Lennartz für die theoretischen Berechnungen der Orbitalenergien.

Martin Schwarze und Christian Scichocki, die mit viel Einsatz ihre Master- und Diplomarbeiten bei mir bearbeitet haben und mich dadurch unterstützt haben.

Dr. Eric Shen für die (mutter)sprachlichen Korrekturen.

allen Mitgliedern und Ehemaligen des Organik-Teams für die nette Zeit im Büro und den Austausch über Probleme und Möglichkeiten, wenn Moleküle im Spiel sind. Ebenso möchte ich Marga Lang, dem Admin-Team und allen weiteren Mitgliedern des Fachgebiets danken, die durch ihren Einsatz das Arbeiten in Darmstadt so reibungslos ermöglicht haben.

allen Mitgliedern des A-Teams und den weiteren Kollegen am InnovationLab für die produktive Zusammenarbeit und tolle Arbeitsatmosphäre, welche sicher auch durch unsere zahlreichen Aktivitäten außerhalb des Labors entstanden ist.

der Werkstatt am Fachbereich Materialwissenschaft für die Unterstützung und Umsetzung der Nebulizer-Bauteile.

meiner Familie, ohne deren Vertrauen, Ermunterung und Rückhalt mein Studium und diese Arbeit nicht möglich gewesen wären.

Jens für die vielen Diskussionen und ausführlichen Korrekturen, vor allem aber noch mehr für dein Verständnis, deine Unterstützung und die vielen kleinen und größeren Ablenkungen genau zur richtigen Zeit.

Erklärung zur Dissertation

Hiermit versichere ich, die vorliegende Dissertation ohne Hilfe Dritter nur mit den angegebenen Quellen und Hilfsmitteln angefertigt zu haben. Alle Stellen, die aus Quellen entnommen wurden, sind als solche kenntlich gemacht. Diese Arbeit hat in gleicher oder ähnlicher Form noch keiner Prüfungsbehörde vorgelegen.

Darmstadt, den 05.12.2013

(Julia Maibach)

Lebenslauf

Der Lebenslauf ist in der Online-Version aus Gründen des Datenschutzes nicht enthalten.